Riches, Liza (2023) *Investigating shock metamorphism features in feldspar.* MSc(R) thesis.

http://theses.gla.ac.uk/83651/

Investigating shock metamorphism features in feldspar

Liza Riches

Submitted in fulfilment of the requirements for the
Degree of Master of Science by Research MSc(R)

School of Geographical and Earth Sciences
College of Science and Engineering
University of Glasgow

July 2022
(Amendments Dec 2022)

Abstract

Hypervelocity impact cratering processes are of key importance for the understanding of planetary formation and evolution in our Solar System. The investigation of shock deformation features within impact craters is therefore an invaluable practice that should help in the future identification of impact sites, as well as the general field of planetary materials. Due to the high abundance of feldspar group minerals on planetary surfaces, the study of shock metamorphism in feldspars is crucial. Shock barometry is the process by which certain diagnostic features can be used to determine the level of shock experienced within a mineral and therefore determine the shock conditions experienced by those minerals. The identification of diagnostic shock microstructure features has often focused on studying quartz using a polarising microscope. However, this thesis has instead investigated the use of feldspar, searching for shock features using a range of microanalytical techniques. This thesis has studied samples from the Chicxulub Impact Structure in the Yucatan Peninsula, Mexico using an optical microscope, scanning electron microscopy (SEM), energy dispersive X-ray spectroscopy (EDS), backscatter electron images (BSE), electron backscatter diffraction (EBSD), cathodoluminescence (CL) and electron probe micro-analysis (EPMA) to identify shock deformation features in feldspar and investigate any connection between deformation features and chemical content. This thesis has several key findings.

1. No shock attenuation was observed over the depth interval that these samples covered (55.8m).
2. Typically, more deformation was observed in Na-rich feldspar than K-rich feldspar.
3. The Ca content within Na-rich feldspar was found to have been influenced by deformation within twins. EBSD maps identified deformation features within feldspar twins, specifically, partial amorphisation in alternating twins. These partially amorphised twins contained ~1-2 at. % less Ca than crystalline twins.

Previous research has not always recorded chemical content of feldspars in enough detail to determine if these observations are present in other locations. With further and closer examination of feldspar minerals of various chemical compositions and different impact sites, it is possible that a more exact and detailed shock barometer for feldspar could be made in the future. Finally, it has proven useful in this thesis to use multiple methods of analysis to provide more successful identification of shock deformation features, which is recommended in future when developing shock barometry in feldspars.

Table of Contents

Abstract ii

List of Tables vii

List of Figures ix

Acknowledgements xii

Declaration xiii

Abbreviations xiv

1 Introduction 1

1.1 Project overview 1

1.1.1 Summary 1

1.1.2 Aims and Objectives 3

1.2 Feldspars 3

1.2.1 An introduction to feldspars 3

1.2.2 Shock metamorphic features in feldspar 6

1.2.3 Furthering research in feldspars 11

1.3 Chicxulub 13

1.3.1 Expedition 364 14

1.3.2 Importance of this research 16

1.4 Samples 18

1.5 Outline of this thesis 21

2 Methodology 21

2.1 Collection of samples 21

2.2 Preparation of samples 22

2.3 Optical microscopy 22

2.4 Scanning Electron Microscopy (SEM) 23

2.4.1 Scanning Electron Microscopy (SEM) Backscattered Electron Images (BSE) 24

2.4.2 Scanning Electron Microscopy (SEM) Energy Dispersive X-ray Spectroscopy (EDS) 26

2.4.3 Electron Backscatter Diffraction (EBSD) 27
2.4.4 Cathodoluminescence (CL) 31
2.5 Electron Probe Micro-Analysis (EPMA) 31
3 Results 33
3.1 Sample CHX-1160.7 33
3.1.1 Sample overview 33
3.1.2 Specific deformation features in CHX_1160.7 41
3.2 Sample CHX-1199.6 75
3.2.1 Sample overview 75
3.2.2 Specific deformation features in CHX-1199.6 78
3.3 Sample CHX-1216.5 93
3.3.1 Sample Overview 93
3.3.2 Specific deformation features in CHX-1216.5 96
3.4 Results summary – comparing across samples 104
4 Discussion 107
4.1 No obvious difference in deformation across depth 107
4.2 Feldspar composition and shock effects 108
4.3 Shock barometry 116
4.4 Deformation in twins 121
4.4.1 Alternating twins 121
4.4.2 Relationship between Ca content and deformation 125
5 Conclusion 131
5.1 Main summary 131
5.1.1 Shock attenuation with depth 132
5.1.2 Na-rich vs K-rich feldspar 132
5.1.3 Multiple methods of investigation 133
5.1.4 Partial amorphisation 134
5.2 Research Impact 135

6 Appendices 137

6.1 Appendix A: Image permissions 137

6.2 Appendix B: Additional Cathodoluminescence (CL) images ... 141

6.3 Appendix C: EDS Data 143

6.4 Appendix D: All EBSD Data 145

6.5 Appendix E: EPMA Data 149

6.6 Appendix F: Conference abstracts generated by this project 158

References 163

List of Tables

Table 3.1 - Normalised chemical composition of selected indexed and non-indexed points within Sites 1 and 2 (analysis points seen in Figure 3.4C and Figure 3.6B) in atomic percent (at. %). 42
Table 3.2 - Normalised chemical composition of the selected areas in site 7 in atomic percent (at. %). 55
Table 3.3 - Normalised chemical composition of selected areas of Site 4 (marked by blue boxes in Figure 3.11) in atomic percent (At. %). 58
Table 3.4 - EPMA data showing normalised chemical composition of the selected areas within Na feldspar and the K feldspar in Site 6 in atomic percent (at. %). 58
Table 3.5 - Normalised chemical composition of areas in Site 3 (in atomic percent (at. %). 62
Table 3.6 - Normalised chemical composition (EDS data) of the areas marked by blue box in Figure 3.15A, Figure 3.16A, Figure 3.17A, Figure 3.18A) in atomic percent (At%). 66
Table 3.7 - Normalised chemical composition (EPMA) of areas in Site 11 (in atomic percent (at. %). 74
Table 3.8 - Normalised chemical composition (EPMA) of the selected areas in Site 5 in atomic percent (at. %). 80
Table 3.9 - Normalised chemical composition (EPMA) of the selected areas in Site 7 in atomic percent (at. %). 81
Table 3.10 - Normalised chemical composition (EPMA) of the selected areas in Site 8 in atomic percent (at. %). 82
Table 3.11 - Normalised chemical composition of Na and K-rich feldspar from Site 2 of sample CHX-1199.6. Spectra numbers correlate to areas marked by the blue boxes in Figure 3.27A) in atomic percent (at. %). 86
Table 3.12 - Normalised chemical composition of Na and K-rich feldspar from sample CHX-1199.6 for sites 1, 3, 4, 6, 9. 88
Table 3.13 - Normalised chemical composition (EPMA) of the selected areas in Na-rich and K-rich feldspar in Site 1 in atomic percent (at. %). 99

Table 3.14 - Normalised chemical composition (EPMA) of the selected areas in Na-rich and K-rich feldspar in Site 2 in atomic percent (at. %). 100
Table 3.15 - Normalised chemical composition (EPMA) of the selected areas in Na-rich and K-rich feldspar in Site 3 in atomic percent (at. %). 102
Table 3.16 - Normalised chemical composition of the selected areas in Site 4 of thin section CHX-1216.5 (marked by the blue boxes in Figure 3.36A) in atomic percent (at. %). 103
Table 3.17 - Average EPMA showing overall average composition of Na-rich and K-rich feldspar in all three thin sections. 105
Table 4.1 - Table showing the Ca, Na, and K composition of K-rich feldspars from Site 6 of thin section CHX-1160.7........ 112

List of Figures

Figure 1.1 - Diagram of feldspar twins based on images from Haldar et al., 2014 and Deer, Howie & Zussman et al., 2014. 5

Figure 1.2 - Images taken from Pickersgill et al., 2015 where partial isotropisation in alternating twins is shown in PPL (plane polarised light) in A and XPL (cross polarised light) in B. 11

Figure 1.3 - Map showing location of expedition 364 and location of hole M0077A. These images have been adapted from figures in (Gulick et al., 2017a; Feignon et al., 2021). 13

Figure 1.4 - Log of hole M0077A with stars marking the location fo the samples studied in this thesis. Log on the left is a close up of a selected area from the right log. Images modified from Guilick et al., 2017. 14

Figure 2.1 - Diagram showing incident electron beam and its interactions with the sample surface. Image based off diagram from https://serc.carleton.edu/17272 (Henry, 2021). 24

Figure 2.2 - Diagram showing the diffraction of electrons onto a phosphor screen where Kikuchi patterns will then be made. Image based on image from (Naresh-Kumar et al., 2017). 28

Figure 3.1 - Full thin section images of samples CHX-1160.7. A, B are optical microscope images, C, D are scanning electron microscopy (SEM) images 36

Figure 3.2 - K-Na-Ca ternary plot showing the average composition of Crystal 1 (C1) in Figure 3.1 37

Figure 3.3 - EBSD images of Area 1 (A1) from sample CHX-1160.7 39

Figure 3.4 - BSE, EDS, EBSD and CL images of Site 1 44

Figure 3.5 - Site 1 Band Contrast (BC) map, Ca EDS map, Kikuchi patterns and pole figures 45

Figure 3.6 - Site 2 imaged with BSE with selected areas within Site 2 investigated further with BSE, EDS, GROD Angle, and Euler maps 50

Figure 3.7 - Site 2 BC map, Ca EDS map, Kikuchi patterns and pole figures 51

Figure 3.8 - EPMA At. % Ca vs Na content for indexed and non-indexed points at Sites 1 and 2 53

Figure 3.9 - BSE and EDS images of Site 7. 56

Figure 3.10 - Graph showing At. % Ca, Na, K, Si and Al content at each EPMA point spectra collected at Site 7....................................56
Figure 3.11 - Site 4 BSE image and EDS map 59
Figure 3.12 - Site 6 BSE image and EDS map 60
Figure 3.13 - Graph showing At. % Ca vs Na content at each EPMA point spectra collected at Site 6.. 61
Figure 3.14 - Site 3 BSE images and EDS maps 65
Figure 3.15 - Site 5 BSE images and EDS map 69
Figure 3.16 - Site 8 BSE image and EDS map. 69
Figure 3.17 - Site 9 BSE image and EDS map. 71
Figure 3.18 - BSE maps of Site 10 72
Figure 3.19 - CL images and an EDS map of an area of Site 1. 73
Figure 3.20 - BSE and EDS maps of Site 11................................75
Figure 3.21 - Full thin section BSE image and EDS map of sample CHX-1199.6.. 77
Figure 3.22 – A K-Na-Ca ternary plot showing the composition of feldspars in Figure 3.21A 78
Figure 3.23 - BSE images of Site 5. Both images are of the same area and are as separate panels so as to make all annotations clear to see83
Figure 3.24 - BSE images and an EDS map of Site 7. Both BSE images are of the same field of view 84
Figure 3.25 - BSE image of Site 8...84
Figure 3.26 - Graph showing Na and Ca content in Na-rich feldspar from Sites 5, 7, and 8..85
Figure 3.27 - BSE image and EDS map of Site 2 86
Figure 3.28 - BSE image of CHX-1199.6 Site 1.............................89
Figure 3.29 - BSE images of CHX-1199.6. Sites 4, 6, and 9. 91
Figure 3.30 - BSE image of Site 3...92
Figure 3.31 - BSE and EDS map of sample CHX-1216.5. 95
Figure 3.32 - K-Na-Ca ternary plot showing the composition of feldspars in sample CHX-1216.5 (as seen in Figure 3.31A) 96
Figure 3.33 - BSE and EDS map of Site 1 in thin section CHX-1216.5. 101
Figure 3.34 - BSE and EDS map of Site 2 from thin section CHX-1216.5 101
Figure 3.35 - BSE image of Site 3 from thin section CHX-1216.5 103
Figure 3.36 - BSE and EDS maps of Site 4 sample CHX- 1216.5. 104
Figure 4.1 - BSE image of Site 1 from thin section CHX-1216.5 109
Figure 4.2 - BSE image of Site 2 from thin section CHX-1199.6....... 110
Figure 4.3 - BSE image from site 6 of sample CHX-1160.7 113

Figure 4.4 - BSE image of Site 3 from thin section CHX-1199.6....... 115
Figure 4.5 - Optical microscope images of sample CHX-1160.7, Site 1. 117
Figure 4.6 - BSE and Euler maps of Site 1 from thin section CHX-1160.7. 118
Figure 4.7 - Example of 010 boundaries (red pixels) being detected using Aztec Crystal on an all-Euler map. Example from sample CHX-1160.7 Site 2. 123
Figure 4.8 - BSE image of Sample CHX-1160.7 Site 1.................. 125
Figure 4.9 - False colour EDS map showing distribution of Ca in sample CHX-1160.7 Site 1. 126
Figure 4.10 - False colour EDS map showing distribution of C (yellow) in sample CHX-1160.7 Site 1. 130
Figure 6.1 CL image showing part of Site 2 of thin section CHX-1160.7. Area of EBSD for Site 2 can be seen in the grey rectangle. 141
Figure 6.2 CL image of another part of Site 2 (thin section CHX-1160.7). Grey rectangle is area over which EBSD has been carried out. 142

Acknowledgements

I would like to thank my two supervisors, Dr Luke Daly and Dr Annemarie Pickersgill for all their help and support throughout this project. I would also like to thank Peter Chung and Dr Liene Spruzeniece for their assistance in the lab and Dr Chris Hayward for collecting EPMA data.

For Chicxulub samples I thank the participating scientists from IODP-ICDP Expedition 364, as well as the drilling team, and the crew of the LB Myrtle. Expedition 364 was implemented by the European Consortium for Ocean Research Drilling (ECORD) with funding from the International Ocean Discovery Program (IODP) and the International Continental scientific Drilling Project (ICDP).

Declaration

All the material presented in this thesis is the result of work carried out between January 2021 and June 2022 (unless otherwise stated) at the School of Geographical and Earth Sciences (GES), College of Science and Engineering, University of Glasgow, under the supervision of Dr Annemarie Pickersgill and Dr Luke Daly. This thesis is based on the authors own independent research and any work by other authors has been acknowledged in the text.

Liza Riches

14/07/2022

Abbreviations

Al	Aluminium
At. %	Atomic percent
BSE	Backscatter electron
Ca	Calcium
CL	Cathodoluminescence
EBSD	Electron Backscatter Diffraction
EBSP	Electron Backscatter Pattern
EDS	Energy-dispersive X-ray Analysis
EPMA	Electron probe micro-analyser
GPa	Gigapascal
K	Potassium
KV	Kilovolts
MBSF	Metres below the Seafloor
Na	Sodium
O	Oxygen
PPL	Plane-polarised light
SEM	Scanning electron microscope
Si	Silicon
Wt. %	Weight percent
XPL	Cross-polarised light
μm	micrometre

Chapter 1

1 Introduction

1.1 Project overview

1.1.1 Summary

Shock metamorphism is a term used to describe the deformation of rocks and minerals after a hypervelocity impact produces a high-pressure shock wave. This impact, for example from a meteorite, will result in a range of effects, from large-scale (such as crater formation) to the small, microscopic changes to minerals (French & Koeberl, 2010).

Researching shock metamorphism in impact craters can provide important insights into planetary formation and evolution. For example, Glikson, (2013) discusses how the study of both lunar craters and impact ejecta found on Earth provide more information about the proposed late heavy bombardment period in the Earth and the Moon's history (estimated to be from ~3.9 - ~3.81 Ga (Ryder, 1990)). There are however still limitations when using terrestrial craters to infer details about, for example, Lunar craters as factors such as gravity can influence the size of the crater formed (Cintala & Grieve, 1998). Not only does research into terrestrial craters give information that can be applied to extra-terrestrial bodies throughout the Solar System (Morgan et al., 2016), but they can also have a large ecological significance, for example, the Chicxulub impact was a key cause of the K-Pg mass extinction (L. W. Alvarez et al., 1980; DePalma et al., 2019).

Studying the microstructural effects produced in minerals in response to shock is key to establishing the shock pressure and shockwave propagation through an impacted rock unit and may even be the only evidence that an impact took place due to erosion or burial of the crater. There has been much previous research into the shock metamorphism features of quartz as it is a common mineral on the Earth's surface and exhibits a range of microstructures under different shock pressures (Chao, 1966; Goltrant et al., 1991; Langenhorst and Deutsch, 1994; Stöffler and Langenhorst, 1994; Grieve et al., 1996; Trepmann, 2008; French and Koeberl, 2010). However, there has not been the same level of research into feldspars, despite feldspar being a highly abundant mineral both on Earth (MacKenzie & Adams, 1994), Mars, Earth's Moon, and in many meteorites (Zolensky et al., 2018). Although there has been some research into feldspar deformation (e.g., Ostertag, 1983; Jaret et al., 2014, 2018; Pickersgill et al., 2015; Fritz et al., 2019; Yin & Dai, 2020), it is noticeably less than research into quartz. Thus, further investigation into the deformation features of feldspar can help develop the use of this mineral when identifying diagnostic features of an impact crater and understanding cratering processes. Sometimes features resembling impact craters in appearance can be created by endogenic processes and this has resulted in some impact structures being originally misidentified. For example, the Boltysh impact crater was misidentified as both a caldera and a feature from tectonic movement before identification as an impact crater (Grieve et al., 1987 and references within). This is why diagnostic features are needed to confirm that certain landscape features are in fact impact craters. This in turn is important as the more impact craters that are found the greater the statistical information and accuracy will be for determining past impact rates on Earth (Trefil & Raup, 1990a; French & Koeberl, 2010). It may be in turn that this information on impact rates can then be applied to research into impact rates across the Solar System. It is hoped that in future, diagnostic features of both quartz and feldspar may be used together in this identification process. The development of shock barometry helps to identify more precisely the shock conditions experienced in the sample (i.e. shock pressure and temperature) and so by furthering the use of shock barometry in feldspars, more precise information about shock conditions in a structure may be derived. This will be specifically relevant to samples that are lacking in quartz.

1.1.2 Aims and Objectives

The main aim of this project is to help further investigate shock metamorphic features in feldspars in order to contribute to the development of the use of feldspars in shock barometry.

This was achieved using the following objectives: 1) to identify and study deformation features in feldspars within selected samples from the Chicxulub impact structure through the use of electron microscope images; 2) to analyse the chemistry of these deformed feldspars and compare features across different types of feldspar; 3) to investigate chemical changes within these deformed areas; 4) to analyse these deformed areas further at a crystallographic level using EBSD in order to investigate the relationship between feldspar crystal structure and shock.

Chicxulub has been chosen for this study firstly because it is a known impact site and secondly because the granitic/dacitic rock samples contain both feldspar and quartz which allows for some comparison to be made between the two minerals. The investigation into chemical context should help to make a future feldspar-based shock barometer more precise and more relevant to a large number of impact structures.

1.2 Feldspars

1.2.1 An introduction to feldspars

Feldspar is a triclinic or monoclinic mineral which consists of two solid solution series. These are the plagioclase feldspar (endmembers are albite ($NaAlSi_3O_8$) and anorthite ($CaAl_2Si_2O_8$)) and alkali feldspar series (endmembers orthoclase ($KAlSi_3O_8$) and albite ($NaAlSi_3O_8$)) (MacKenzie & Adams, 1994). Feldspar is a framework silicate mineral which is made up of SiO_4 tetrahedra and four membered rings of AlO_4 with Na^+, Ca^{2+}, or K^+ within the framework (Okrusch & Frimmel, 2020). Feldspar is a prominent rock forming silicate mineral, one of the most abundant minerals in the Earth's crust and is common both in meteorites and other planetary bodies (Duff, 1993). In lunar samples, there is often a greater abundance of plagioclase feldspar compared to alkali feldspar (Levinson & Taylor, 1971).

Plagioclase feldspar is a triclinic mineral that often contains multiple twinning, the most common of which is albite twinning (MacKenzie & Adams, 1994). Alkali feldspars can be either triclinic or monoclinic depending on the exact chemistry due to the K^+ cation having a larger atomic radius than Na^+ or Ca^{2+} (Okrusch & Frimmel, 2020).

In granitic rock, feldspar along with quartz are the most abundant minerals. The typical microstructures that would be seen (not including shock features) are summarised below. These features may give an insight into the original formation conditions and geological history, for example cooling rates and crystal growth (Parsons et al., 2015).

Twinning is one of the key features in feldspar. In plagioclase feldspar polysynthetic twins are very common (though twins can also be found in alkali feldspar), these are twins that are repeating. There are various different types of twins that can appear, examples of which are shown in Figure 1.1.

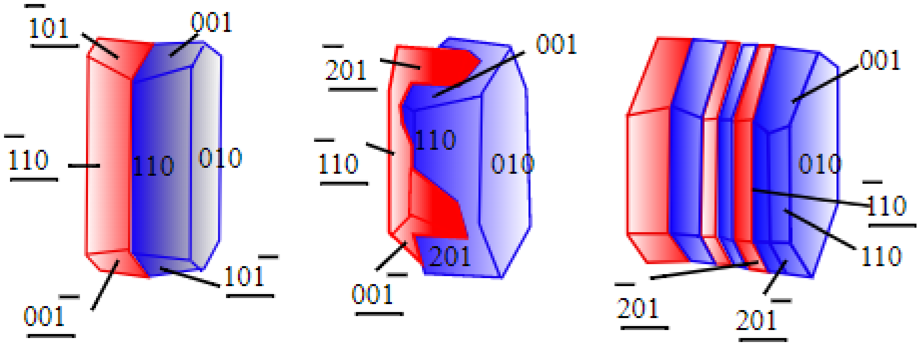

Carlsbard twin

Carlsbad interpenetrant twin

Albite twin

Figure 1.1 - Diagram of feldspar twins based on images from Haldar et al., 2014 and Deer, Howie & Zussman et al., 2014.

During cooling, both alkali and plagioclase feldspars can react as closed systems in which Na and K can diffuse and create exsolution textures (Okrusch & Frimmel, 2020). In these feldspars, the perthitic and anti-perthitic textures can also be often seen as a different feldspar composition appears in the main crystal body as an intergrowth. Perthite is K-rich feldspar with albite intergrowths and antiperthite is albite with K-feldspar intergrowths (Haldar & Tišljar, 2014). If there is a fairly even mix of plagioclase and alkali feldspar, then the term mesoperthite can be used (Parsons et al., 2005). Perthite and antiperthite can form in various different textures, for example, patch perthite, braid perthite, film perthite and vein perthite. Patch perthite has irregular intergrowths that appear ‘blobby’ or ‘patchy’, braid perthite is when the albite intergrowth appears to cross over and form diamond or braided patterns, film perthite occurs when the albite appears as stretched out flattened lenses, and vein perthite shows these intergrowths as interconnecting bands(Parsons et al., 2005, 2015). Perthite can be particularly seen in this thesis in the K-rich feldspar where a perthitic texture is present in some locations. Typically this has formed as patch perthite.

Feldspars are at risk of weathering and alteration by other hydrothermal processes which may disrupt the features that would have previously been seen. Additionally, shock effects which are discussed below in 1.2.2 can also disrupt the features seen.

1.2.2 Shock metamorphic features in feldspar

Feldspar minerals have been investigated in this thesis to help further develop shock barometry. Shock barometry is a way of estimating the pressures experienced by a rock based on the deformation features present in the minerals studied (Holm et al., 2011; Holm-Alwmark et al., 2017a). Most commonly, previous research into shock barometry has focused on quartz (e.g., Chao, 1966; Goltrant et al., 1991; Langenhorst and Deutsch, 1994; Stöffler and Langenhorst, 1994; Grieve et al., 1996; Trepmann, 2008; French and Koeberl, 2010). This is due to quartz being both a very common mineral on the Earth's surface and one which has a simple structure that responds to increasing shock pressures with a range of distinct microstructural features (R. A. F. Grieve et al., 1996).

By focusing mainly on just one mineral however research becomes limited and so the investigation into multiple minerals (e.g. using quartz and feldspar together) may help to prove useful in shock barometry. There are also other minerals which are used in shock barometry, but are typically minor-trace minerals. Zircon for example displays planar microstructures at pressures above 20 GPa (Wittmann et al., 2006). Another example is olivine which has been used before in comparison with feldspar at the Sudbury Igneous Complex (Wang et al., 2018) and in meteorites (Stöffler et al., 2018). At Chicxulub, shock features in apatite have also been investigated (Cox et al., 2020).

Comparisons of shock effects in quartz and feldspar have been carried out in previous research at other impact sites. For example, the Tenoumer impact structure in Mauritania has been investigated by studying both shocked quartz and feldspar (Jaret et al., 2014). In this research it was suggested that feldspar may have value as a mineral for researching deformation features as it starts to deform at lower shock pressures than quartz. This resulted in shock features being identified in feldspars in areas where there was no shocked quartz (Jaret et al., 2014). Another paper, Pittarello et al., 2013) also found that plagioclase contained shock features such as planar deformation features (PDFs) (which have been identified before, for example in (Stöffler & Langenhorst, 1994; Grieve et al., 1996)) and could be used as an indicator of shock scale in lithologies that contain little quartz.

The deformation features that may be identified in feldspar can be divided into two main groups. The first of these are diagnostic shock deformation features. Diagnostic features are those which have definitely (and only) formed from passage of a shockwave during a hypervelocity impact event. The second is non-diagnostic shock deformation features which may have also been created by endogenic processes and so could not be used on their own to identify an impact site. Diagnostic shock metamorphic features include planar deformation features (PDFs) and diaplectic glass (French & Koeberl, 2010) which are described below.

Diagnostic shock features have previously been used in quartz to confirm structures as hypervelocity impact craters. For example, the Siljan impact structure in Sweden has been identified as such using identified planar deformation features (PDFs) in quartz as well as shatter cones (Svensson, 1971; Holm et al., 2011). It is hoped that feldspar could be used as extensively as quartz in this maner.

In some research, (Ostertag, 1983; Stöffler et al., 2018), five features are listed as shock metamorphic microstructure in both plagioclase and alkali feldspar. These are undulatory extinction, mosaicism, PDFs, diaplectic glass (and the formation of various PDFs) and melting. There are however other features that are also recorded in specific samples such as shock darkening or partial isotropisation (French & Koeberl, 2010; Stöffler et al., 2018; Yin & Dai, 2020).

Research suggests that these main five features form in a specific order as shock pressure (and temperature) increases. Typically, at low pressures (<10 GPa), fractures are the first feature to be found, followed by undulatory extinction (~5-14 GPa) mosaicism (18-26 GPa), transformation to diaplectic glass (26–34 GPa) and at the greatest pressures (~>42 GPa), melt glass forms as the feldspar melts (Ostertag, 1983; Stöffler et al., 2018). Note the pressure slightly varies between references and different shock pressure are required depending on the type of feldspar.

1.2.2.1 Fracturing

Fracturing starts to occur at lower pressures than most other features (<10 GPa (Ostertag, 1983)). Fractures are not considered a shock diagnostic feature as they can be created through endogenic processes. However, at a known impact site, the investigation of fractures may prove useful as they typically start to form at a lower pressure than other microstructures and therefore can be used as an indicator of pressure in samples where other shock features are not available.

1.2.2.2 Undulatory Extinction

Undulatory extinction is when a mineral appears to have a wave of extinction that is seen in cross polarised light through a petrographic microscope when the stage is rotated (MacKenzie & Adams, 1994). This feature forms from bending of the crystal lattice rather than fracturing. This is a microstructure that can form as a result of an impact however, it is not a diagnostic shock feature as it can also form from other processes.

1.2.2.3 Mosaicism

Mosaicism is an optical effect where the crystal lattices of sub grains become disorientated from those surrounding them (French & Koeberl, 2010). According to previous feldspar shock experiments of Ostertag (1983), mosaicism occurs at pressures ranging from 18 to 26 GPa. It is suggested from previous observations that as pressure increases, so does the level of mosaicism. However, once the pressure allows for the formation of diaplectic glass (1.2.2.5), mosaicism disappears (Stöffler et al., 2018). In cross polarised light mosaicism is seen as an odd and irregular extinction pattern (Ostertag, 1983; Langenhorst & Deutsch, 1994; Stöffler et al., 2018).

1.2.2.4 Planar deformation features (PDFs)

PDFs are a type of planar microstructure that are known to be diagnostic of shock metamorphism (French & Koeberl, 2010). They often occur along with other deformation microstructures such as mosaicism (Goltrant et al., 1992).

PDFs have been identified and extensively researched in quartz (e.g. Bohor, 1990; Stöffler and Langenhorst, 1994). In quartz they have been described as "remarkably straight, sharp and continuous under the optical microscope" (Goltrant et al., 1992). They have been identified to some extent in feldspars as well. One study by Pittarello et al., (2013) investigated both plagioclase and alkali feldspar samples from the El'gygytgyn impact structure and found evidence of PDFs particularly within the plagioclase.

Some planar microstructures can also be found on unshocked samples, so it is important to determine the difference between shock induced planar features such as PDFs and other planar features unrelated to shock when carrying out such an investigation.

1.2.2.5 Diaplectic Glass

Diaplectic glass is formed at higher pressures than the deformation features mentioned previously (Stöffler et al., 2018). For plagioclase to form diaplectic glass pressures of ~24 – 45 GPa have been suggested and for alkali feldspar higher pressures may be required (~32–45 GPa) ((Stöffler et al., 2018) and references within). Shock experiments on single feldspar crystals (sanidine, orthoclase, microcline, oligoclase, labradorite, and polycrystalline bytownite) indicate that diaplectic glass forms at pressures of 26-34 GPa (Ostertag, 1983). Diaplectic glass has been described as having morphological and textural features preserved and not containing signs of vesiculation or flow within (Stöffler, 1984; Chen & el Goresy, 2000; Stöffler et al., 2018). An example of diaplectic glass being present in alternating twins in feldspar is shown in Figure 1.2. Diaplectic glass is isotropic, and so it appears extinct when rotated between crossed polarisers. There has been more focussed research on diaplectic feldspar glass in comparison to others deformation features of feldspar that form at lower pressures.

Chemical composition of the precursor mineral can strongly influence the pressures required for the formation of diaplectic glass (Stöffler et al., 2018). Fritz et al., (2019) found that feldspars in the plagioclase series (albite to anorthite) will require higher temperatures to become diaplectic glass as the anorthite (Ca) content in the sample increases and thus suggested the possibility of a greater pressure also being required. However, Fritz et al., (2019) go on to state that other studies have found the opposite trend between anorthite content and pressure (Daniel et al., 1997; Kubo et al., 2010; J. R. Johnson, 2012), suggesting that the relation between feldspar composition and shock deformation pressures is something that needs to be researched further.

In past research the term maskelynite has often been used to refer to diaplectic plagioclase glass (Fritz et al., 2019) however it is important to note that the terms “diaplectic glass” and “maskelynite” do have different meanings (Chen & el Goresy, 2000) despite sometimes being used synonymously in regards to isotropic plagioclase. Maskelynite forms from the high-pressure quenching and melting of meteoritic plagioclase (Chen & el Goresy, 2000).

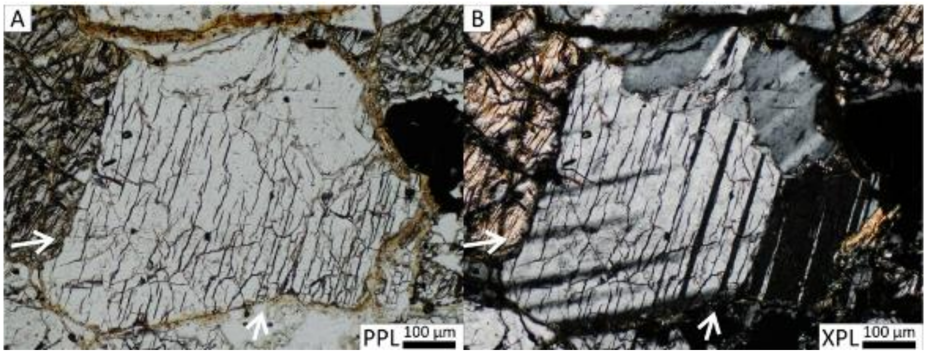

Figure 1.2 - Images taken from Pickersgill et al., 2015 where partial isotropisation in alternating twins is shown in PPL (plane polarised light) in A and XPL (cross polarised light) in B. In B the black twins remain extinct if the stage is rotated. These isotropic twins have been transformed into diaplectic glass.

1.2.2.6 Melting

Melting of feldspar occurs as the pressure increases to above ~42 GPa (Ostertag, 1983). At this point melt glass forms and all other features of the original crystal are now destroyed (Stöffler, 1984; Stöffler et al., 2018). Instead, the melt may show a flow structure. Some examples of this can be seen in Chapter 3 (for example 3.2.2.2 **Error! Reference source not found.**C). This type of monomineralic melt is different to impact melt rock. In this thesis, half of sample CHX-1216.5 was made up of clast-rich impact melt rock.

1.2.3 Furthering research in feldspars

As shock metamorphic features in feldspars are relatively under-researched in comparison to minerals such as quartz, there are areas that still need further investigation. One of these is the effect of the chemical composition of feldspars on the formation of shock features. Some research has investigated this phenomenon however we still do not have a complete understanding of the effect of composition on shock microstructure and there are varying views on the level of influence chemical composition has. For example, Stöffler et al., (2018) suggests that alkali and plagioclase feldspar will require different pressures for certain shock deformation features to form. Another investigation into experimentally shocked feldspars suggests that although the chemical composition has an impact, other factors such as the presence of inclusions may be more influential (Ostertag, 1983). Therefore, even when comparing the shock features in feldspars of different compositions it is important to make note of any other factors present and consider the influence these factors may have had.

Typically, plagioclase feldspars have been researched more than alkali feldspars, however, there has still been some research into alkali feldspars. For example, an investigation by Yin & Dai, (2020) into feldspars from the Xiuyan impact crater did study alkali feldspars (both albite and orthoclase), and a range of shock metamorphic features were found. Weakly shocked features (irregular fractures and undulatory extinction) were found near both endmembers of the alkali series (albite and orthoclase) however more strongly shocked features (melt glass) were found mostly in albite (Na-rich).

Another issue that has recently been addressed is the need for a clear and defined shock pressure scale. In some literature (Dressler, 1990; Stöffler, 1971; Yin & Dai, 2020) deformation features are divided into different stages of shock metamorphism (4 to 6 stages in total depending on the paper). This issue of different researchers using different divisions of deformation features into a shock scale has since been identified in Stöffler et al., (2018) which discusses the confusion of many different classification systems describing progressive shock metamorphism. Stöffler et al., (2018) suggests seven progressive stages of shock metamorphism for felsic rocks. This starts at what is described as S1 where the minerals are unshocked and there are no optical features to be seen and ends with S7 where the whole sample has melted. This particular shock scale involves the use of multiple minerals (mostly quartz and feldspar as well as biotite, pyroxene and amphibole) however, it is only related to features identified using optical microscopy.

1.3 Chicxulub

The Chicxulub impact structure is located in the Yucatan Peninsula, Mexico (as seen in **Error! Reference source not found.**). The crater was discovered in the late 1970s. Its diameter has been debated to range in size from 130 to 300 km (Pope et al., 1996; Urrutia-Fucugauchi et al., 1996; Kring, 2005) however many studies have concluded that the diameter is most likely to be ~180 km (Hildebrand et al., 1991, 1995; Stöffler et al., 2004). The crater is buried under 1 km of tertiary carbonates and is comparatively well preserved for a crater of this size (Morgan et al., 1997). As this crater is so large and well preserved, plenty of research has been carried out here with the knowledge gathered being applied to less accessible craters (e.g., on extra-terrestrial bodies (Vermeesch & Morgan, 2004)).

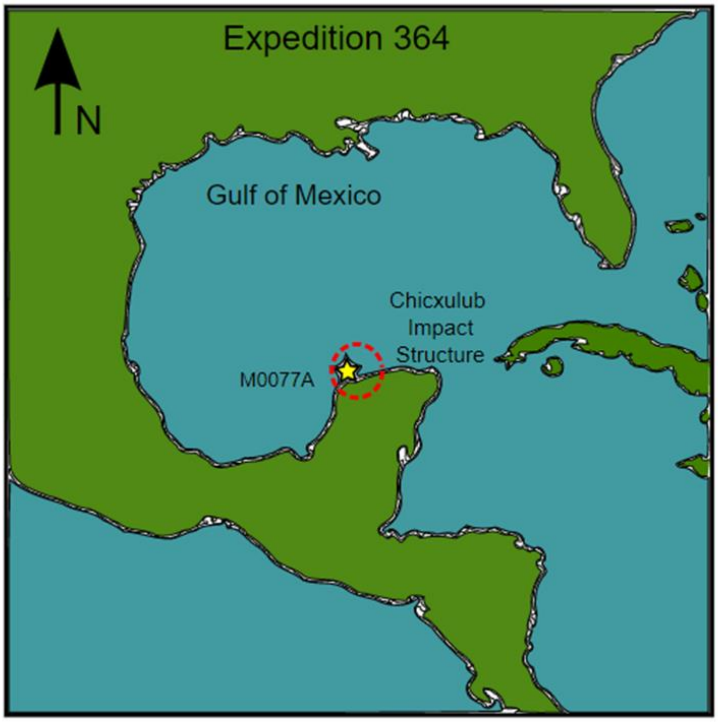

Figure 1.3 - Map showing location of expedition 364 and location of hole M0077A. These images have been adapted from figures in (Gulick et al., 2017a; Feignon et al., 2021).

Since its discovery, there has been a lot of interest in the crater and it has since been dubbed the dinosaur killer crater as this meteor impact is closely tied to the K-Pg mass extinction (L. Alvarez et al., 1980). The most robust age of the impact determined using $^{40}Ar/^{39}Ar$ of associated glass spherules yielded an age of 66.038 ± 0.098 Ma (Renne et al., 2013). This age is indistinguishable from the age of the K-Pg boundary (66.043 ± 0.086 Ma, (Renne et al., 2013)).

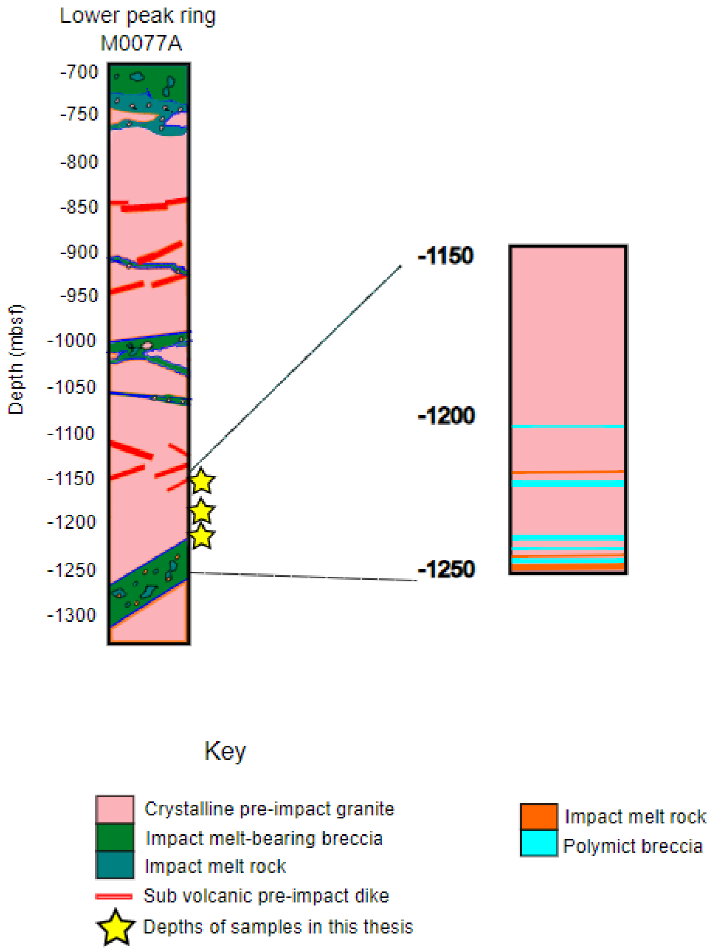

Figure 1.4 - Log of hole M0077A with stars marking the location fo the samples studied in this thesis. Log on the left is a close up of a selected area from the right log. Images modified from Guilick et al., 2017.

1.3.1 Expedition 364

An expedition in 2016 (Expedition 364) was carried out by the International Ocean Discovery Program (IODP) and the International Continental Scientific Drilling Program (ICDP) to collect samples from the peak ring of the Chicxulub impact crater.

Between the 8th and the 26th of May 2016, Expedition 364 drilled a single hole (hole M0077A) down to a depth of 1500 m below seafloor (Gulick et al., 2017). The core samples collected from 505.70 m below seafloor (mbsf) and deeper were able to be used in multiple studies (Gulick et al., 2017). The expedition itself was carried out in order to investigate several Science Plan Goals set out by the IODP (International Open Discovery Program). These goals ranged from the nature of impact melt rock to the global climatic effects of the impact (Gulick et al., 2017).

Expedition 364 recovered samples of varying lithologies. From a depth of 505.70 mbsf to 617.33 mbsf the core mostly consists of post impact sediments including claystone, siltstone and limestone (Gulick et al., 2017). The next section known as the upper peak ring (617.33 - 747.02 mbsf) is described as consisting mostly of suevite and impact melt rock and the lower peak ring (747.02 - 1334.69 mbsf) consists of shocked granitoids as well as suevite and impact melt rock. This project focuses on samples from the lower peak ring. The main composition of the samples collected are alkali feldspar, quartz, plagioclase, and small quantities of biotite (Gulick et al., 2017).

The samples collected from Expedition 364 have been used to investigate shock metamorphism in minerals other than quartz and feldspar. For example, an investigation into shock microstructures in titanite by Timms et al., (2019) identified certain twins in Chicxulub's shocked samples that have not been observed in endogenically deformed titanite. This means that it is possible for the features identified to be used in the future as diagnostic indicators of shock metamorphism. The more diagnostic features identified from minerals, the more likely these features can be used to help successfully identify hypervelocity impact structures in the future. This highlights the importance of investigating shock deformation in multiple minerals in addition to quartz.

1.3.2 Importance of this research

1.3.2.1 Importance of research at Chicxulub

The research being carried out on Chicxulub can have many different uses and implications. For example, as Chicxulub is the only crater on Earth with a full and intact peak ring it is ideal for comparisons to impact craters with peak rings on other planetary bodies (Morgan et al., 2016). Chicxulub is one of the three largest known impact craters on Earth (Grieve & Therriault, 2000). As such a large crater with an intact peak ring, it has a great value when researching deformation features formed from an impact site and so the knowledge gained from this study can be applied to other less intact impact craters. One limitation however is that the crater is well buried, however Expedition 364 (from which the samples in this study were obtained) overcame this through extensive drilling.

1.3.2.2 Importance of studying shock metamorphism and the future identification of impact structures

The identification of diagnostic features of shock metamorphism is key as it allows more potential structures to be identified as impact craters. This in turn will help give a better statistical overview of the impact rate on Earth in the past (French & Koeberl, 2010). Estimates in the past have proved difficult with the small percentage of craters discovered and accurately dated. For example, Trefil & Raup, (1990b) suggested that only 16% of impact craters over 20 km in diameter have been discovered which makes estimations of impact rates difficult. It is important to note that the use of impact craters to estimate bombardment rates may be biased to both newer craters and larger structures as these may be easier to find and are less likely to have been subsequently destroyed by tectonic processes (Grieve & Robertson, 1979). Some have suggested using distal impact ejecta layers for helping to determine bombardment rates (Johnson & Bowling, 2014) but this in turn has its own limitations as it is also dependant on the continuing discovery of these layers. It may be that the use of both known impact craters, ejecta layers and knowledge of lunar impact rates together may help to further improve estimated impact rates on Earth. This in turn can help research in other areas such as what the early Earth was like and the formation of the Solar System (Grieve & Robertson, 1979).

1.3.2.3 – Importance of researching feldspars

Quartz is often chosen instead of feldspar as the main mineral of choice when investigating shock deformation. For example, when early research was being carried out at Chicxulub, quartz was used to help create models and theories about the events during and after impact and the spread of ejected material (Alvarez et al., 1995). The uneven distribution of the abundance of shocked quartz across the crater site was used to suggest a steeper angle of trajectory (steeper than 65°) when modelling (Alvarez et al., 1995). By furthering knowledge of the shock metamorphism of feldspars, it is more likely that feldspars could be used at other craters in future research.

By developing feldspar shock barometry, it is more likely that formation details such as pressure and temperature will be more precisely determined in feldspar-rich impact structures, which will be particularly useful in samples that are lacking in quartz.

It has been noted in previous studies that shock metamorphism can lead to lower seismic velocity and density of felsic basement samples (Morgan et al., 2016). It is suspected that processes such as fracturing as a result of shock can lead to a decrease in density and an increase in pore space. An investigation at Haughton, Canada, suggested that this change in density is influenced by the lithology of the site (Singleton et al., 2011). This study showed that felsic rocks have a greater decrease in density as shock level increases due to the minerals starting to melt at a lower pressure than in mafic rocks. It also suggests that the specific composition in a felsic rock may further influence this due to the melting points of specific minerals. For example, a felsic sample with less quartz (but higher levels of feldspar and mica) will require less pressure to decrease in density after being shocked. This is due to quartz requiring a higher melting pressure than the feldspar (Singleton et al., 2011). The decreasing density of naturally shocked quartz has been investigated in previous studies (Stöffler & Langenhorst, 1994) but it appears likely that the melting pressure of feldspar may also have an influence in this matter (Singleton et al., 2011).

1.3.2.4 Other fields of research relating to impact structures

Furthering knowledge of impact craters may also assist future projects in other disciplines. For example, the decreasing density of samples with higher levels of shock metamorphism can allow for different microbial habitats to be created (Cockell et al., 2002). This demonstrates how research into shock metamorphism has been applied to a more ecological discipline.

1.4 Samples

The samples that are studied in this investigation are from the Chicxulub impact structure, collected during IODP-ICDP Expedition 364 (see section 1.3). Three samples were selected which were collected from the following depths: 1160.7 mbsf, 1199.6 mbsf, and 1216.5 mbsf.

The samples have been analysed using the following methods: optical microscopy, scanning electron microscopy (SEM) backscatter electron (BSE) images, energy dispersive X-ray spectrometry (EDS), with additional areas of interest from sample CHX-1160.7 being investigated further using electron backscatter diffraction (EBSD), electron probe micro-analysis (EPMA) and cathodoluminescence (CL). Specific operating conditions for these methods are discussed in Chapter 2.

An overview of these samples was generated using a petrographic microscope. Samples were examined for shock effects such as fractures, mosaicism, PDFs, and undulatory extinction. Optical microscopy has been often used in the past for the purposes of shock barometry (e.g., Stöffler et al., 2018) and in this thesis has been used alongside other analytical methods.

The use of SEM BSE images in this investigation allowed specific deformation features to be identified (such as fractures and planar features which will be discussed in Chapter 3). This was coupled with SEM-EDS data which allowed the chemical distribution of selected elements to be identified. Which in turn allowed deformation features to be correlated with chemical context.

EPMA data has also been used in this thesis for more specific point spectral analysis of selected locations. This method of chemical analysis has been used previously to investigate variations in mineralogical compositions, for example in Lewis & Jones, (2019) where EPMA was used (alongside other methods) to identify the composition of plagioclase in the chondrules of Semarkona LL3.00 chondritic meteorite.

Specific deformation features were analysed using EBSD. This has been used in previous research to identify shock deformation features in feldspar (Pittarello et al., 2020a). An investigation into shock events in the nakhlite meteorites used EBSD to create grain-relative orientation distribution angle maps (GROD) and was able to identify the deformed regions within the sample (Daly et al., 2019). Daly et al., (2019) detected shock generated mechanical twins in pyroxene using EBSD which highlights the invaluable use of the method when investigating shock microstructures. Another example of the use of EBSD to investigate shocked minerals is Timms et al., (2020) in which EBSD (along with other methods) was used to study shocked titanite from Chicxulub and was able to identify shock twins within a crystal.

Using EBSD it is possible to identify features of shock and to use this information to determine different levels of deformation and post shock annealing that samples experienced. An example of this can be found in a study of olivine grains within ordinary chondrite meteorites (Ruzicka & Hugo, 2018). Ruzicka & Hugo, (2018) used EBSD to create average values of deformation using Mean Grain Orientation Spread (GOS) as well as Lattice Preferred Orientation (LPO) data. Using this data they were able to infer that the different meteorites studied experienced different conditions of temperature and varying levels of post shock annealing were found. In samples with strong olivine LPO's it was inferred that there had been strong deformation (Ruzicka & Hugo, 2018).

Feldspar is not one of the main minerals that has been investigated with EBSD as the literature is mostly dominated by research into quartz, olivine, pyroxenes, calcite and garnet (Prior et al., 2009). For example, the LPO of olivine was investigated in a study to investigate the anisotropy of the upper mantle (Karato et al., 2008). In another study pole figures were created using EBSD to demonstrate the influence of water on the LPO of olivine suggesting that the slip systems in olivine change dramatically depending on water content (Jung et al., 2006). One reason that feldspar may not have been investigated as much using EBSD is because feldspar is susceptible to beam damage when attempting to get high resolution data (Prior et al., 2009). There have however been some previous investigations into feldspars using EBSD. One study investigating plagioclase feldspar across a shear zone found that intergrowths within the plagioclase (~An_{50}) had retained a matching crystallographic orientation with the parent feldspar (Mukai et al., 2014). Further, Mukai et al.,

(2014) were then able to identify differences within this intergrowth resulting from chemical composition as it was found that the Ca-rich domains had low angle grain boundaries. Another study details the use of EBSD to find orientation microstructures in alkali feldspar to investigate the relationship between argon age and orientation microstructure (McLaren & Reddy, 2008). Another study used EBSD to investigate feldspar shock deformation in a shatter cone form the Manicouagan Structure, Canada (Pittarello et al., 2020a). In this study of the Manicouagan Structure, the amorphous nature of lamellae in planar microstructures of plagioclase were investigated and a more detailed analysis was made possible through the use of EBSD. The study found amorphous alternating thin lamellae that were identified as shock induced micro twins.

1.5 Outline of this thesis

This thesis is divided into five chapters (including Chapter 1: Introduction (this chapter)). Chapter 2 discusses the methodology with specific instrument operating conditions used for this thesis as well as an overview of the workings and use of each method. Chapter 3 discusses the results from this study, and the findings of which are then interpreted and put into context with current literature in Chapter 4. The whole thesis is then summarised in the conclusion in Chapter 5.

Chapter 2

2 Methodology

2.1 Collection of samples

The three samples in this project are labelled CHX_1160.7, CHX_1216.5 and CHX_1199.6. Sample numbers correspond to sample depth in metres below sea floor (mbsf). These samples were collected in 2016 during the IODP-ICDP Expedition 364 from hole M0077A (Gulick et al., 2017). A single hole drill was used to extract the samples, starting with open hole drilling (using a starting drill diameter of 12 ½ inches). In stages, the hole was drilled and then cased and cemented and drilled again at a greater depth with a drill of a smaller diameter. Once the hole reached 505.7 mbsf, coring took place and the base of the hole reached 1334.69 mbsf (Gulick et al., 2017). The samples for this research project were all collected from the recovered core.

2.2 Preparation of samples

Pre-made thin sections were prepared for EBSD by polishing in stages. First, they were polished using 1 μm aluminium oxide spheres, suspended in glycol for 5 minutes. Then they were polished using 0.3 μm aluminium spheres in glycol for a further 5 minutes. Then the sample was placed in colloidal silica (with a grain size of 100 nm) suspended in sodium hydroxide solution on a Vibromet polisher. The sample was left on the polisher for 4 hours and then removed and the colloidal silica was washed off in warm water and fairy liquid before being placed in distilled water in an ultrasonic bath for 2 minutes and then gently wiped dry with a chem wipe.

For analysis using EBSD, the sample needed to be carbon coated after polishing. This is done to create a conductive surface for the electrons that are fired at the sample. The carbon coating was applied using a sputter coater to a thickness of 7 nm. The sample was then attached to an aluminium stub with a double-sided carbon tab. Aluminium tape was used to secure the sample in place and to ground the sample.

2.3 Optical microscopy

Samples were analysed using a petrographic microscope to identify deformation features. The images obtained using a petrographic microscope were then also compared with SEM BSE images (section 2.4.1) to compare what features could be seen with each method and identify any differences. In some cases, these differences were attributed to different magnification but there are also features which can only be detected using certain methods. Optical microscopy also provides an overview of the sample whereas other methods (such as EBSD) focus in on smaller areas.

The optical microscope used was the Leica ICC50 W microscope and images were captured and analysed using LAS E2 software. Samples were imaged using both plane-polarised light (PPL) and cross-polarised light (XPL).

A full thin section map of one of the samples (CHX-1160.7) was also created using a Zeiss Axio Imager M2 automated using ZEN imaging software.

2.4 Scanning Electron Microscopy (SEM)

The samples were analysed using a Zeiss Sigma Variable pressure field emission gun scanning electron microscope (equipped with an Oxford Instruments X-Max 8- mm^2 silicon drift X-ray detector) at the University of Glasgow Imaging Spectroscopy and Analysis Centre (ISAAC). Using the SEM backscatter electron images (BSE) and energy dispersive X-ray spectrometry (EDS) maps were created. BSE images allow microstructures to be seen and EDS maps show chemical distribution. The BSE images and EDS maps were used to select areas for further analysis using EBSD (using the SEM equipped with a NordlysMax^2 EBSD detector) and Cathodoluminescence (CL) (for which data was collected on the FEI Quanta environmental SEM). EBSD can be used to determine crystallographic deformation. BSE, EDS and EBSD data were collected and interpreted using the Aztec (version 5.1) software from Oxford Instruments. Aztec crystal (version 2.1) software also from Oxford Instruments Nanoanalysis was used for further EBSD analysis to create maps and pole figures.

The SEM releases a beam of electron that hit the sample as shown in **Error! Reference source not found.**. Further details of each technique can be found in the following sections.

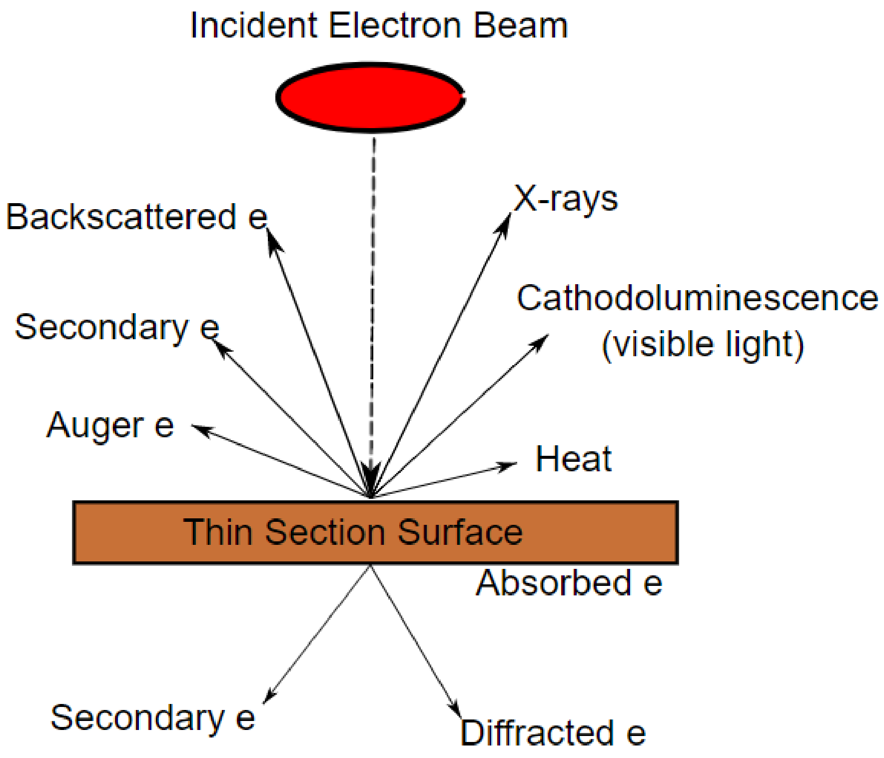

Figure 2.1 - Diagram showing incident electron beam and its interactions with the sample surface. Image based off diagram from https://serc.carleton.edu/17272 (Henry, 2021).

2.4.1 Scanning Electron Microscopy (SEM) Backscattered Electron Images (BSE)

Backscattered electron images show mean atomic number density (z), with areas of higher atomic number appearing brighter, and areas with lower atomic number appearing darker (Reed, 2005b). In this project the samples had to be well polished to reduce the effect of topographical interference on the BSE signal (Reed, 2005b).

BSE images are created by the backscattering of electrons off a sample onto a detector. An electron beam strikes the sample and these electrons are reflected off (Figure 2.1) the sample and then are recorded by the detector (Reed, 2005a). From this detector a greyscale BSE image is then created based on the energy from individual electrons. The atomic number (Z) contrast is the predominant factor that influences the image created by the detector (Reed, 2005b). Atomic number is not the only influence as factors such as density, topography and crystallographic orientation also influence the image that is created. The greater the atomic number (larger Z value), the greater the number of high-energy electrons backscattered. This results in higher Z phases forming brighter regions within an image in contrast to lower Z phases which appear darker (Reed, 2005b). The resulting greyscale images can be used to see certain features across the sample surface such as the outline of different crystals and deformation features. Different minerals can appear lighter or darker (depending on their elemental composition) (Qin & Beckingham, 2019) and very dark regions can also indicate fractures, weathering, or holes in the sample. For the purposes of this thesis, it is important to note that the feldspars of differing composition have a different appearance with K-rich feldspar appearing brighter on a BSE image than the Na-rich feldspar.

It is recommended that an accelerating voltage of above 15 kV is used as the BSE signal is energy sensitive and so may not detect electrons at a lower voltage as easily. However, it is also recommended not to use too high a voltage as the spatial resolution is reduced at high accelerating voltages (Reed, 2005b). For this study an accelerating voltage of 20 kV was used.

SEM-BSE images were collected for the full thin section of samples CHX_1160.7, CHX_1199.6 and CHX_1216.5. This was done using the Zeiss Sigma VP-FEG-SEM as described in section 2.4. These images were montaged into full thin section maps and were used to find areas containing potential deformation features in each section.

2.4.2 Scanning Electron Microscopy (SEM) Energy Dispersive X-ray Spectroscopy (EDS)

Energy dispersive X-ray spectroscopy data is used to determine elemental compositional data from the samples. This is done by recording energy from X-rays that are released from the sample after an electron beam has released high energy electrons onto the sample (Figure 2.1). These x-rays are produced through the following process: as an electron beam interacts with a sample it imparts energy to the atoms within the sample, this energy then causes an electron in the outer shell of the atom to move to a heightened energy state. This energy is then released from the electron as it returns to its ground state in the form of X-rays (Goldstein et al., 1992). This X-ray is then measured by the EDS detector (*Reed 2010)*. Each element emits a series of X-rays with a specific energy. By measuring the abundance of X-rays measured across the energy window a spectrum is produced that can be used to identify the elements found at that specific point and measure their relative abundance (Goldstein et al., 1992).

EDS data can then be used to produce elemental maps showing the distribution of elements across the sample site (Qin & Beckingham, 2019). Also, from these EDS maps point or area spectra data can be collected from specific regions within the respective sample point or area on the EDS map.

Attached to the Zeiss sigma VP-FEG-SEM is the Oxford instrument X-Max 8 - mm^2 silicon drift X-ray detector that was used to collect EDS data for this thesis. The composition of the selected region is calculated in atomic percent (at. %) focussing on the elements that are commonly associated with feldspar (K, Na, Ca, O, Si, Al). From these elemental abundance data, the type of feldspar can be calculated by the relative abundance in at. % of Na, Ca, and K present. It is important to note that the data in these EDS spectra have been normalised. In some cases compositional data from EDS spectra were confirmed by EPMA (see section 2.5).

2.4.3 Electron Backscatter Diffraction (EBSD)

Electron Backscatter Diffraction (EBSD) is used to investigate crystallographic orientation and in this thesis to investigate deformation within the microstructure of feldspar crystals. EBSD data is collected by firing a beam of electrons from an electron gun at a sample that is inclined at a 70° angle to the horizontal (as shown in **Error! Reference source not found.**). Hitting the sample at this angle helps to deflect electrons along the crystal lattice. A phosphor screen is present which collects the diffracted electrons in the form of Kikuchi bands and this image is then captured by a camera behind the screen. There are some electrons that have been elastically scattered and some inelastically scattered meaning that they lose a small amount of energy and thus change wavelength (Hammond, 2015). It is through this elastic-inelastic scattering that Kikuchi bands form and a series of these Kikuchi bands combine to form a Kikuchi pattern. This Kikuchi pattern can then be matched to a specific crystal structure in a database and then determine the crystallographic orientation and deformation. One thing that needed to be carefully considered when analysing feldspars is the exposure time. Feldspars can be beam sensitive and may slowly become amorphous when exposed to a high energy electron beam for a long period of time (Luu et al., 2021). The exposure time for EBSD collection in this thesis was 50 ms.

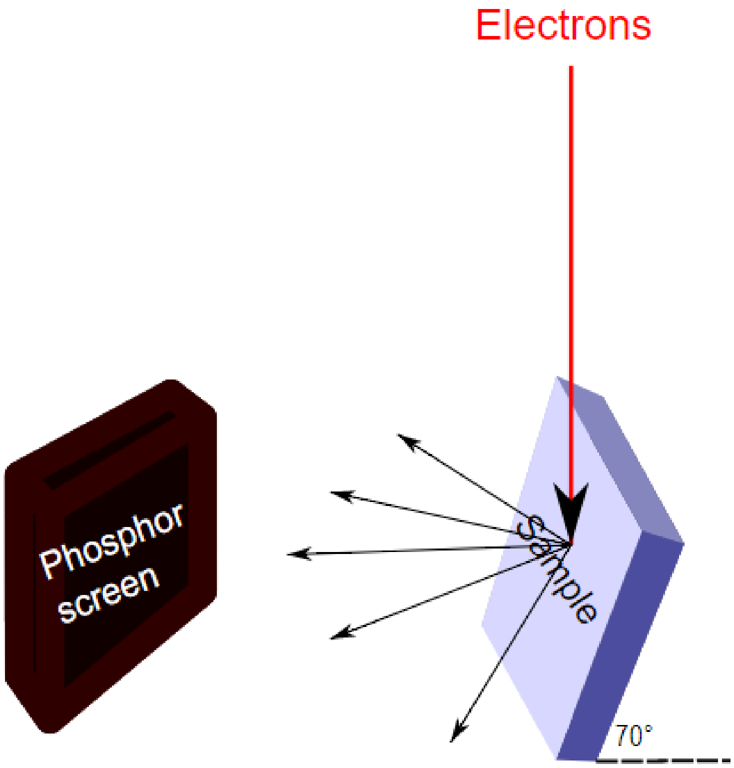

Figure 2.2 - Diagram showing the diffraction of electrons onto a phosphor screen where Kikuchi patterns will then be made. Image based on image from (Naresh-Kumar et al., 2017).

EBSD data can be presented in a variety of ways as a range of different maps can be created. In this thesis data is commonly presented in the form of band contrast, phase, grain reference orientation deviation (GROD) angle, inverse pole figure (IPF), and Euler maps.

Band contrast maps give an indication of the detected pattern quality over the sample. If an area is darker then the quality of the electron backscatter pattern (EBSP) collected is lower with less distinct Kikuchi bands visible. This type of map can be used to visualise crystallinity of the sample. Band contrast maps are often added as a layer beneath other EBSD maps to help with visualisation.

Phase maps show the different mineral phases matched by software. When a Kikuchi pattern was found that matched a mineral selected from the database then it was recorded as that mineral phase on the phase map. This type of map can be used to determine mineral abundances.

Grain reference orientation deviation (GROD) angle maps are used to investigate internal misorientation within a crystal, (Oxford Instruments Plc, 2021). This gives a visual indication of the deformation experienced within the crystal structure. This is done by determining the average orientation of pixels within a grain and then colour coding the variations of crystallographic orientations away from that mean orientation.

Inverse Pole Figure (IPF) maps show the crystallographic orientation of crystals within the sample relative to the plane that the EBSD map was acquired in (Oxford Instruments NanoAnalysis, 2020). This can be done relative to any direction (x, y, z). Sometimes it is helpful to have two IPF maps presenting orientation data relative to different directions to compare as features may be apparent in one orientation and not in the other.

Euler maps are another way to give a visual representation of crystallographic orientation and are used to show details of the crystal microstructure (Oxford Instruments NanoAnalysis, 2020). Euler maps are created using Euler angles which are a set of three rotation angles around an axis which give crystal coordinates (Nolze, 2015). These have then been plotted on an ‘euler all’ which has all three angles represented by colours red, green, and blue.

Although Euler maps do help to show crystallographic orientation, IPF maps are also used due to the fact that the colour scheme on an Euler map does not show some very slight variations in orientation as well as IPF maps do (Oxford Instruments NanoAnalysis, 2020). This can be confusing in samples were much of the area shows a similar orientation but not exactly the same. IPF maps however can show these slight changes more clearly. In this project Euler maps have mostly been used to show large changes in crystallographic orientation (for example to show the presence of twins) whereas IPF maps have been used more to investigate small changes in crystallographic distortion in more detail.

EBSD data was collected using the same Zeiss SEM as for BSE and EDS data, with a Nordlys Max^2 EBSD detector. A voltage of 20 kV was used and an exposure time of 25 ms. Electrons passed through a 100 µm aperture and the beam current was 4.1 nA. For the first set of EBSD maps, the step size was set to 3 µm. Additional high resolution EBSD maps were collected using a step size of 0.5 µm.

For EBSD phase identification, several match units were selected from the mineral database. The best match unit for feldspar in our samples, which was defined by the lowest mean angular deviation and largest amount of bands used, was bytownite. Bytownite was then selected to match electron backscatter patterns (EBSP).

EBSD data was then analysed using Aztec Crystal (version 2.1). The data was cleaned by first removing wild spikes and then correcting to 6 neighbours surrounding a pixel (and iterating this 10 times). Several different EBSD maps were generated and investigated to highlight distinct microstructures. Aztec Crystal was also used to detect the grain boundaries of individual crystals.

For phase maps (as seen in Appendix D) it is important to note that certain mineral phases were used in EBSD as proxy for the correct mineral phase. For example, from EDS data most of the plagioclase feldspar was identified as albite however the best EBSD match unit in the database was bytownite, thus bytownite was used as a proxy for albite. In the same way, microcline is used as a proxy for K-feldspar and Quartz-new for quartz.

All scale bars on GROD angle maps were limited to a range of 1-10° misorientation and coloured so that blue colours indicate regions of low internal misorientation 0-3° through green, yellow and red indicating increasing degrees of internal misorientation where red is 8-10° internal misorientation.

The most common direction used for the IPF maps in this thesis is z (a line perpendicular to map plane) however this is specified for each of the maps.

2.4.4 Cathodoluminescence (CL)

Cathodoluminescence (CL) images show a greyscale image of the surface of a sample. From these images different minerals and features within individual minerals such as zoning can be seen (Götze & Kempe, 2009).

CL images are produced by the bombardment of electrons onto a sample producing luminescence (Figure 2.1). Luminescence varies depending on the composition of the sample and can be used to detect features such as growth zoning and alteration (Lee et al., 2007). The variation in emissions from cathodoluminescence have also been reported to be influenced by crystallographic defects allowing these features to be visualised due to both these defects and the change in composition as new crystals form or are altered (Reed, 2005a). CL was carried out using Edax Centarus SEM-CL with the FEI Quanta environmental SEM. The voltage was 20kV and a 15.5 mm working distance was used.

2.5 Electron Probe Micro-Analysis (EPMA)

Electron Probe Micro-Analysis (EPMA) allows more precise and accurate quantitative compositional data to be collected at specific points than EDS. This has provided a more accurate measure of composition relative to EDS (which has been used to give a more general view of composition over a wider area). EPMA works by using wavelength dispersive X-ray spectroscopy (WDS) (rather than for example EDS which uses a scanning electron microscope). This works by focussing an electron beam on a very small area of a sample, this then produces diagnostic X-rays of specific energies, to produce a spectrum from which different elements can be detected from their different wavelengths. EPMA measures the quantitative abundance of specific selected elements and so studies energy difference (recorded from X-rays) in a smaller part of the energy spectra (compared to EDS). The concentration of these elements can be determined by observing their intensity in the spectrum and comparing them to samples of known composition (standards) (Reed, 2005a).

EPMA data was collected by Dr Chris Hayward at the University of Edinburgh in December 2021. 15 keV was used and both 4 nA and 100 nA were used as conditions for detecting various elements (full details of which can be found in the Appendix E). Quantitative chemical abundances in wt. % for Si, Al, Na, Ca, K, Mg, Fe, Sr, Ti, Mn, and Ba were collected. O content was calculated using stoichiometry. These values were later converted into at. %. Conversion to at. % was calculated using the equation: $at\% = \frac{(wt.\%\,X/at.wt.X)}{\Sigma \text{ of all elements in the sample } (wt.\%/at.wt.)} * 100$ where X is the element value being converted and at.wt. is the atomic weight as adapted from (Plasmaterials, 2016). Standards used are recorded in Appendix E.

Analytical uncertainty of EPMA measurements was calculated from % uncertainty which was originally determined using wt. % and standard deviation (which are recorded in the Appendix E) and then converted into at. %. In some cases, averages and standard deviation were calculated for specific sets of data as seen in Chapter 3.

3 Results

3.1 Sample CHX-1160.7

3.1.1 Sample overview

Sample CHX_1160.7 was taken from 1160.7 mbsf (metres below seafloor).

CHX_1160.7 comprises Na-rich feldspar (~60%), K-rich feldspar (~15%) and quartz (~15%). Other minerals (e.g., biotite, titanite) make up the remaining 10%.

There is one large euhedral albite crystal, ~35 mm long and ~15 mm wide dominating the thin section, this crystal has been labelled "C1" (as shown in **Error! Reference source not found.**A and 3.1C). The remainder of the crystals in the thin section are smaller including feldspars (~100 μm to 9000 μm), quartz (~100 μm to 3500 μm), biotite (~1 mm), and titanite (~660 μm).

Optical microscopy

Most areas of interest found by polarising light microscopy were better imaged by other methods. As a result, these petrographic microscope images are not always discussed in the results below unless there is a specific point of interest. An overall montage image for sample CHX_1160.7 has been included in **Error! Reference source not found.**. The main things that can be seen is the main minerals present (plagioclase, alkali feldspar, and quartz) with basic features such as twins in the plagioclase feldspar being seen. **Error! Reference source not found.**A and **Error! Reference source not found.**B show the one large plagioclase crystal.

Energy Dispersive X-ray Spectroscopy (EDS)

The false colour red, green, blue (RGB) EDS map shown in **Error! Reference source not found.**D visualises the chemical distribution of feldspars three endmembers Na, Ca, and K-rich, helping to highlight which feldspars are Na or K-rich (there is no Ca-rich feldspar in these samples). The main crystal (C1) is mostly Na-rich (red), with some K-rich (blue) zones. There is a higher K content in the centre of the crystal with very little around the edge of C1 (as seen in blue in **Error! Reference source not found.**B). These small but concentrated areas of K-rich feldspar within the Na-rich C1 are regions of patch perthite and similar smaller patches can be found throughout the crystal.

Electron Probe Micro-Analysis (EPMA)

EPMA point spectral analysis yielded precise compositional data for specific locations. These data can reveal compositional variation within minerals and microstructures. Each sample point also has a calculated standard deviation (SD) which can been found in the Appendix E. Calculated at. % uncertainty was used for error bars where data has been displayed graphically (**Error! Reference source not found.**, **Error! Reference source not found.**, **Error! Reference source not found.**).

The average Ca, Na, and K content for each of the selected sites within crystal 1 (C1) for which EPMA data was collected are reported in a ternary plot (**Error! Reference source not found.**). From this it is clear that C1, although containing some K-rich inclusions, is overall an Na-rich plagioclase feldspar (**Error! Reference source not found.**).

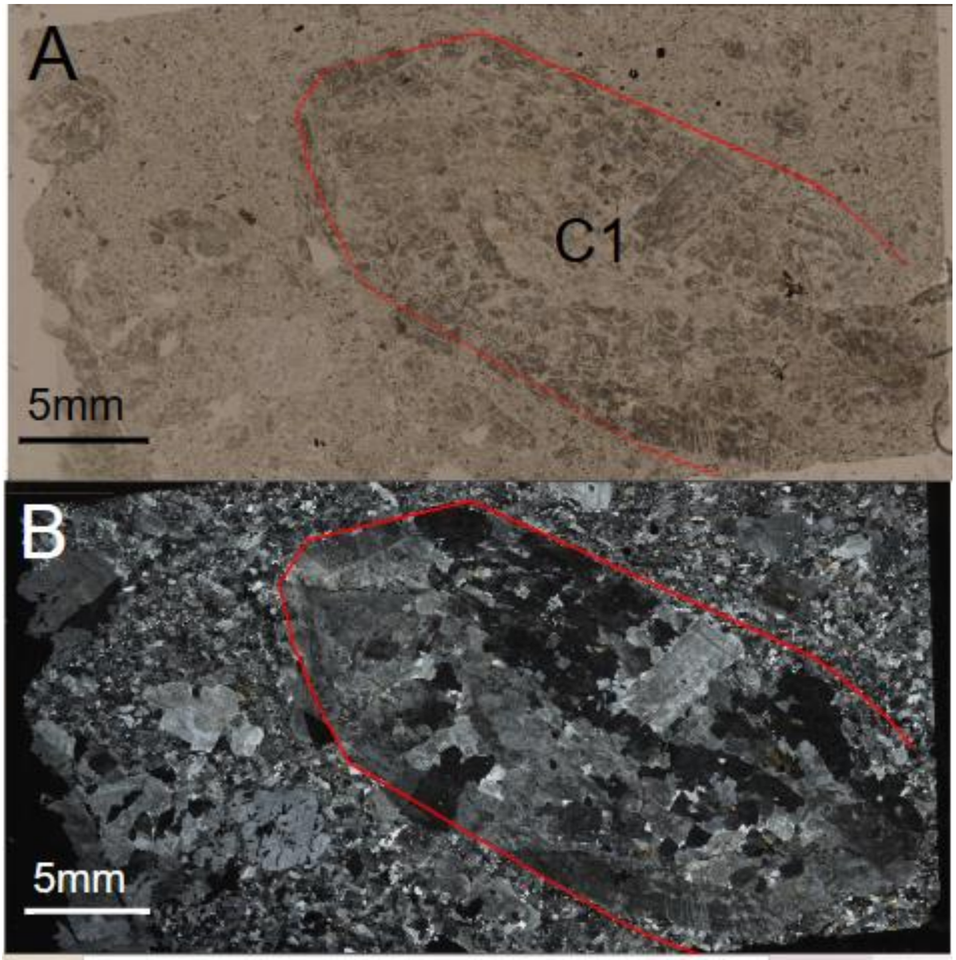
A
C1
5mm
B
5mm

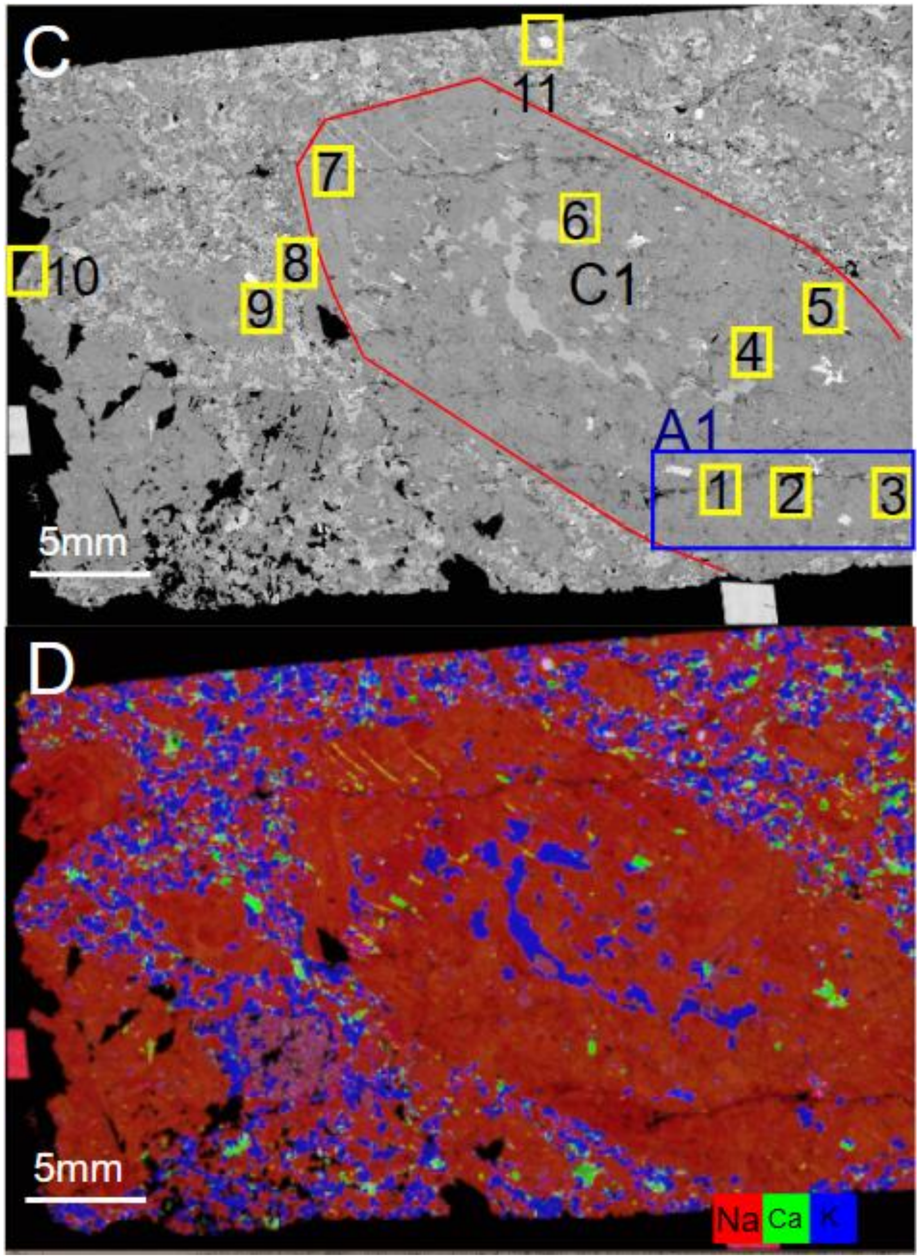

Figure 3.1 - Full thin section images of samples CHX-1160.7. A, B are optical microscope images, C, D are scanning electron microscopy (SEM) images. A) Plane Polarised Light (PPL) image with large euhedral crystal outlined in red and labelled as C1. B) Cross Polarised Light (XPL) montage image of the entire sample. Red line outlines C1. C) Backscatter electron (BSE) image with large euhedral crystal outlined in red and labelled as C1. Individual sites where more detailed analyses were conducted are highlighted in yellow boxes and numbered. The yellow boxes have all been analysed using BSE and EDS with some areas also being analysed using higher resolution BSE and/or cathodoluminescence (CL). The blue box highlights the area investigated using EBSD (labelled A1). D) False coloured energy dispersive X-ray spectroscopy (EDS) map with Na, Ca, and K in red, green, and blue respectively.

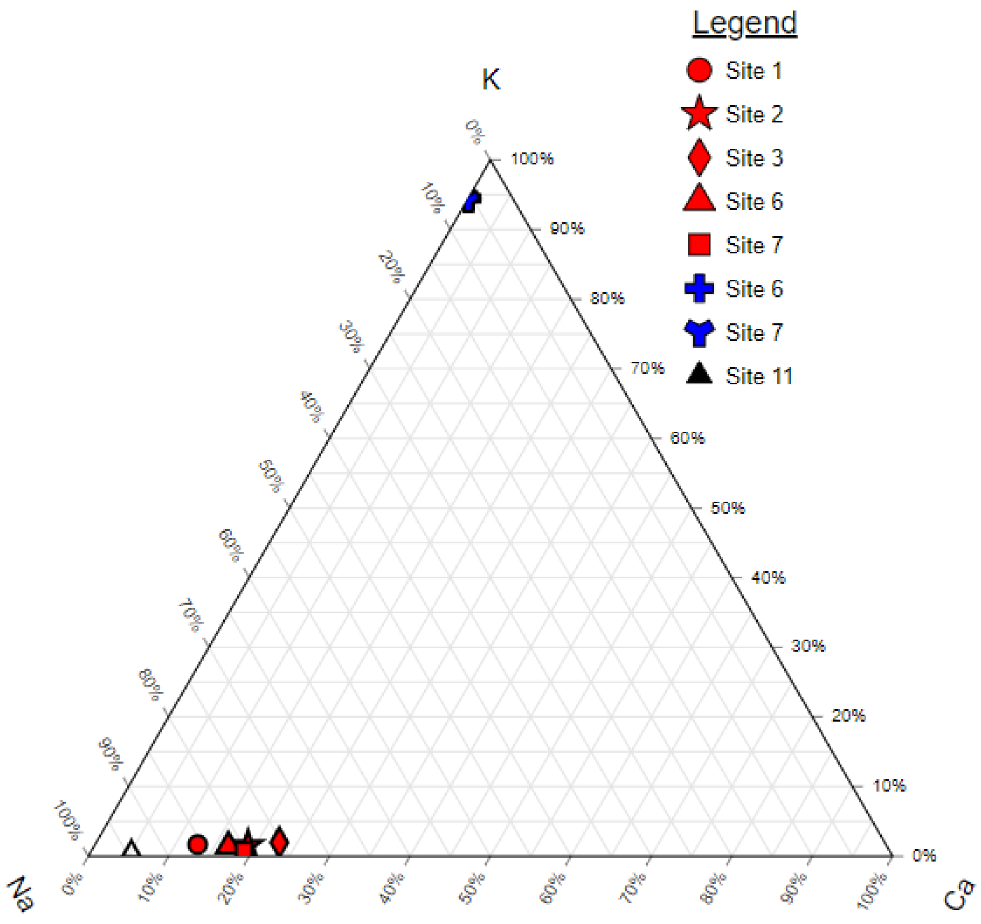

Made with TernaryPlot.com

Figure 3.2 - K-Na-Ca ternary plot showing the average composition of Crystal 1 (C1) in Figure 3.1. Those points marked in red (circle, star, diamond, triangle, square) are Na-rich parts of the crystal (which are the typical of the crystal as a whole). Those marked in blue (+ and Y signs) are K-rich zones in the overall Na-rich C1. Site 11 (marked with the black triangle) is an Na-rich crystal (not C1 but still from this thin section) that has been placed on as a comparison. Plot points are from EPMA point spectral analysis calculated averages.

Electron Backscatter Diffraction (EBSD)

An area of sample CHX_1160.7 within C1 was selected for further analysis using EBSD due to the interesting features highlighted using previous analytical methods (these features are discussed in section 3.1.2). This area is highlighted and labelled in **Error! Reference source not found.**C as A1 (Area 1). **Error! Reference source not found.** shows a range of maps (IPF, GROD angle, etc.) that were generated using the collected EBSD data. Each map also shows band contrast to indicate the quality of the Kikuchi patterns produced by electron beams, this is shown as a greyscale image underlying the other data.

Error! Reference source not found.B shows that the area is mostly Na-rich feldspar and the Inverse Pole Figure (IPF) map (**Error! Reference source not found.**C) shows that much of this albitic plagioclase has the same crystallographic orientation, with the green areas showing {100} in the z direction (perpendicular to the plane of the section). Some twins can be seen within these albite regions in the all-Euler map of A1 (**Error! Reference source not found.**D). The IPF map (**Error! Reference source not found.**C) reveals that closer to the large horizontal fracture the albite varies in crystallographic orientation compared to the majority of the albite elsewhere in the area as evidenced by different IPF colourings.

In order to investigate deformation, GROD angle maps were created so that the misorientation within each grain could be seen. All of the maps in this investigation have been set to the same scale with a maximum misorientation angle of 10°.

Error! Reference source not found.E is a GROD angle map for the entirety of Area 1 (**Error! Reference source not found.**C). In **Error! Reference source not found.**E a range of internal deformation is observed within grains. Some grains contain little internal misorientation evidenced by blue colouration (~1-3° of misorientation) whereas other areas (particularly on the right half of the image) appear to have greater amounts of internal misorientation, evidenced by green (~5°), yellow (~7°), and red (~8-10°) colouration of the GROD angle map.

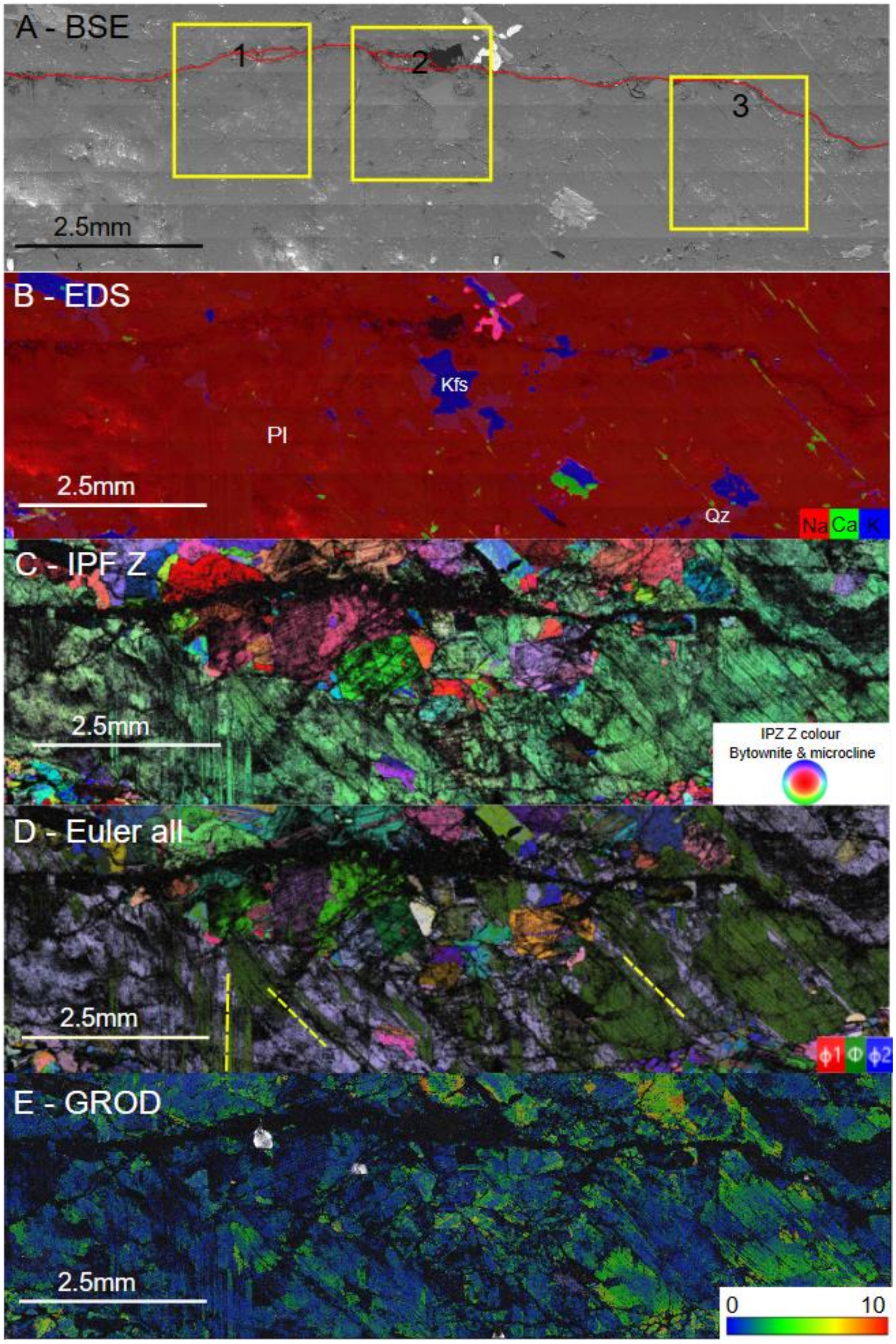

Figure 3.3 - EBSD images of Area 1 (A1) from sample CHX-1160.7. A) BSE image. Red line highlights fracture going horizontally across the top of A1. Yellow boxes outline areas for Sites 1 to 3. B) False coloured EDS map showing Na, Ca, and K in red, green, and blue respectively. A1 is Na-rich feldspar with some K-rich feldspar. There are some regions that are high in Ca (green) but these are not feldspar and are more likely pyroxene, nor is the pink coloured phase a feldspar (is a form of iron copper sulphide). C) IPF map (z-direction) showing the crystallographic orientations of Bytownite (the best phase match for this area and so used as proxy for all Na-rich feldspar) relative to the plane of the section. D) All Euler map of the area. Yellow lines highlight the orientation of different sets of twins. E) Grain reference orientation deviation (GROD) angle map showing the internal misorientation within each grain relative to

the average orientation of each grain. More intense internal misorientation can be seen on the right-hand side (greener tones) of the area than the left (bluer tones).

The majority of Area 1 has been successfully indexed as feldspar by EBSD using the match units of bytownite (as proxy for albite) and microcline (as proxy for K-feldspar), some quartz was also identified. However, some areas (estimated around 15% of the area) provided ‘zero solutions’ meaning the phase has not been indexed in those pixels as a result of low band contrast or a lack of Kikuchi patterns. Often if material has not been indexed this indicates that the phase is amorphous and could therefore be interpreted as diaplectic glass. However, there are other reasons for an area to not be indexable by EBSD. For example, an area that is not polished well enough may not yield Kikuchi patterns. Another reason for non-indexed areas could be either the presence of a void or fracture (meaning there is no signal to be detected) or due to mixed Kikuchi pattern signals at a grain boundary or nanocrystalline region.

In many cases these non-indexed regions (black in band contrast and other maps) still contain a faint Kikuchi pattern (not defined enough to be indexed). Non-indexed regions frequently appear to be contained within specific lamellae, often alternating with crystalline lamellae next to them.

In some examples (as will be discussed in Section 3.1.2.1) EDS and EPMA analysis indicated a distinct chemistry in the non-indexed regions different from the more crystalline material, although the chemistry is still overall albite. From the EPMA data, the average composition of Na-rich feldspar in thin section CHX-1160.7 is 6.49 at. % Na, 1.2 at. % Ca, and 0.11 at. % K and the average composition of K-rich feldspar is 0.38 at. % Na, 0.01 at. % Ca, and 6.5 at. % K. The EDS data also yielded the same composition.

3.1.2 Specific deformation features in CHX_1160.7

3.1.2.1 Partial amorphisation in alternating twins and change in Ca levels

One of the main features that has been found in this sample is the partial amorphisation of alternating twins. This can be seen within Area 1 at Sites 1 and 2 (as labelled in **Error! Reference source not found.**C). As both sites are located within the large plagioclase crystal C1, both are Na-rich. Site 1 also contains an inclusion of quartz (around 570 μm long) in the centre (**Error! Reference source not found.**A). Site 2 also contains a large K-rich feldspar crystal in the top left of the image in **Error! Reference source not found.**A which is ~755 μm wide. There are also some quartz crystals (ranging from ~300–550 μm long) containing fractures just below the K-rich feldspar.

The Na-rich feldspar at Sites 1 and 2 contain very little K (ranging from ~0.09--~0.17 at. % K) and Ca (ranging from ~0.35 -~1.8 at. % Ca) but more Na (ranging from ~5.85--~7.1 at. % Na). This ~1.25 at. % Na and ~1.44 at. % Ca chemical variation can be seen in the EPMA point spectral analysis data (Table 3.1) collected within the area shown in **Error! Reference source not found.**C. The location of the EPMA point spectra in this table have been correlated with the EBSD maps to determine whether the EPMA spectra were acquired from indexed or non-indexed electron backscatter patterns (EBSP). There is a clear 0.95 at. % Ca and 0.87 at. % Na variation in average Ca and Na content between indexed and non-indexed regions within the EBSD data with indexed points containing an average 1.61 at. % Ca and 6.10 at. % Na and non-indexed points containing 0.66 at. % Ca and 6.97 at. % Na (based on the difference between the average at. % for indexed and non-indexed points for each element, (Table 3.1). This chemical variation will be discussed later in this section.

Table 3.1 - Normalised chemical composition of selected indexed and non-indexed points within Sites 1 and 2 (analysis points seen in Figure 3.4C and Figure 3.6B) in atomic percent (at. %). Chemical compositions are only given for major elements. These values have been converted from weight % and re-normalised. The point number correlates to the point locations labelled in ***Error! Reference source not found****.C and* ***Error! Reference source not found****.B. These have been correlated with the EBSD maps to determine whether the EPMA spectra were acquired from indexed or non-indexed electron backscatter patterns (EBSP) pixels. The average and SD have been calculated for both the indexed and non-indexed data set. Non-normalised weight percent measurements can be found in Appendix E. This table only records data for the points where it was possible to line up the EPMA point with the indexed or un-indexed regions of the EBSD dataset, in other places this was not possible.*

		At. % at indexed points						
Site #	Point #	Ca	Na	K	Si	Al	O	Other
1	5	1.47	6.32	0.11	21.62	8.97	61.46	0.05
1	6	1.60	6.16	0.17	21.43	9.12	61.43	0.09
1	7	1.29	6.44	0.15	21.78	8.79	61.46	0.08
1	8	1.49	6.16	0.14	21.61	9.06	61.51	0.03
2	1	1.57	6.13	0.11	21.41	9.24	61.47	0.07
2	2	1.76	6.00	0.09	21.21	9.41	61.45	0.08
2	3	1.78	5.89	0.08	21.25	9.44	61.51	0.05
2	4	1.80	5.85	0.19	21.20	9.41	61.46	0.09
2	5	1.70	5.93	0.19	21.31	9.31	61.47	0.09
Average		**1.61**	**6.10**	**0.14**	**21.43**	**9.20**	**61.47**	**0.07**
SD		**0.170**	**0.199**	**0.043**	**0.207**	**0.227**	**0.027**	**0.024**

		At. % at non-indexed points						
Site #	Point #	Ca	Na	K	Si	Al	O	Other
1	1	0.35	7.13	0.09	22.79	8.01	61.61	0.02
1	2	0.51	7.06	0.09	22.49	8.27	61.54	0.03
1	3	0.61	6.88	0.15	22.38	8.40	61.55	0.04
1	4	0.62	7.04	0.13	22.34	8.33	61.48	0.06
2	6	0.92	6.79	0.10	22.03	8.66	61.48	0.03
2	7	0.93	6.91	0.10	22.03	8.58	61.42	0.03
Average		**0.66**	**6.97**	**0.11**	**22.35**	**8.37**	**61.51**	**0.03**
SD		**0.229**	**0.131**	**0.024**	**0.290**	**0.234**	**0.066**	**0.015**

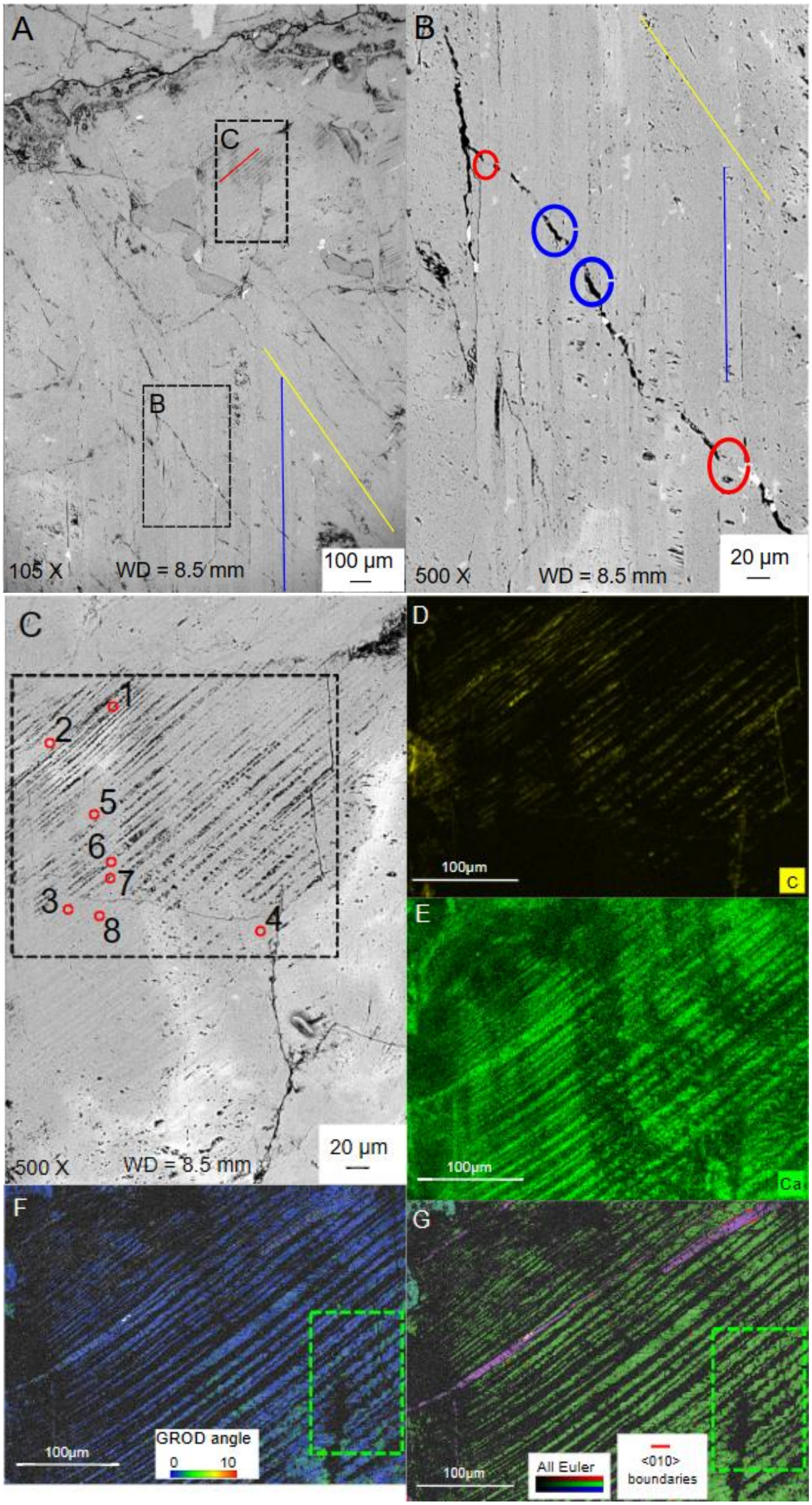
A
C
B
105 X
WD = 8.5 mm
100 µm
B
500 X
WD = 8.5 mm
20 µm
C
1
2
5
6
7
3
8
4
500 X
WD = 8.5 mm
20 µm
D
100µm
C
E
100µm
Ca
F
100µm
GROD angle
0
10
G
100µm
All Euler
<010>
boundaries

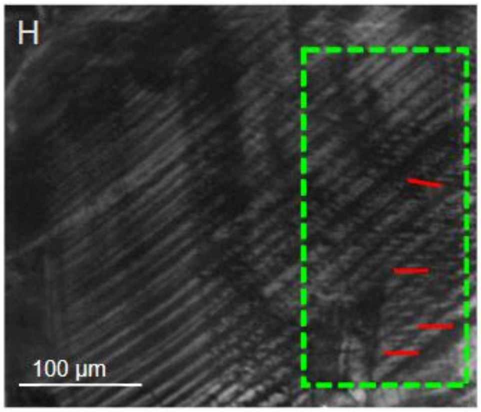

Figure 3.4 - BSE, EDS, EBSD and CL images of Site 1. A) An overview BSE image with planar features highlighted in red, blue and yellow lines. Areas for images B and C have been highlighted in black dashed boxes. B) Close up image of blue and yellow planar features. Note that the lamellae alternate darker and lighter. The fracture going across the image appears to be infilled in some areas (examples shown in red circles) and not in other areas (examples shown in blue circles). Upon closer inspection, these infilled parts of the fracture are within the lighter coloured lamellae. C) Close up image of red planar feature. Note the alternating darker and lighter lamellae. Exact points where EPMA point spectra were acquired marked by red dots. Numbers related to those noted in Table 3.1. Black box in C highlights the area for images D, E, F, G, H. Note, the diffuse bright markings to the lower right of C are produced by charging effect of the electron beam sample. D) False colour EDS map showing the distribution of C (in yellow) in selected area for image C. This indicates regions where there is a lack of material. E) False colour EDS map showing the distribution of Ca (green). Note that variation in Ca can be seen between alternating lamellae. F) EBSD GROD angle map showing misorientation within the crystal in this area. Note there is very little misorientation along the individual lamellae, but alternating lamellae are non-indexed (appearing black) due to partial amorphisation. Green box highlights step texture. G) Euler angle EBSD map. Green box highlights step texture. <010> boundaries help to highlight that these alternating planar features are twins. All the green planar features are of the same orientation. H) CL image, green box highlights step texture. Red lines show horizontal dashes that form a step like texture. Images C – H all show to varying degrees a dark swooping curve which will be discussed more in section 3.1.2.4.

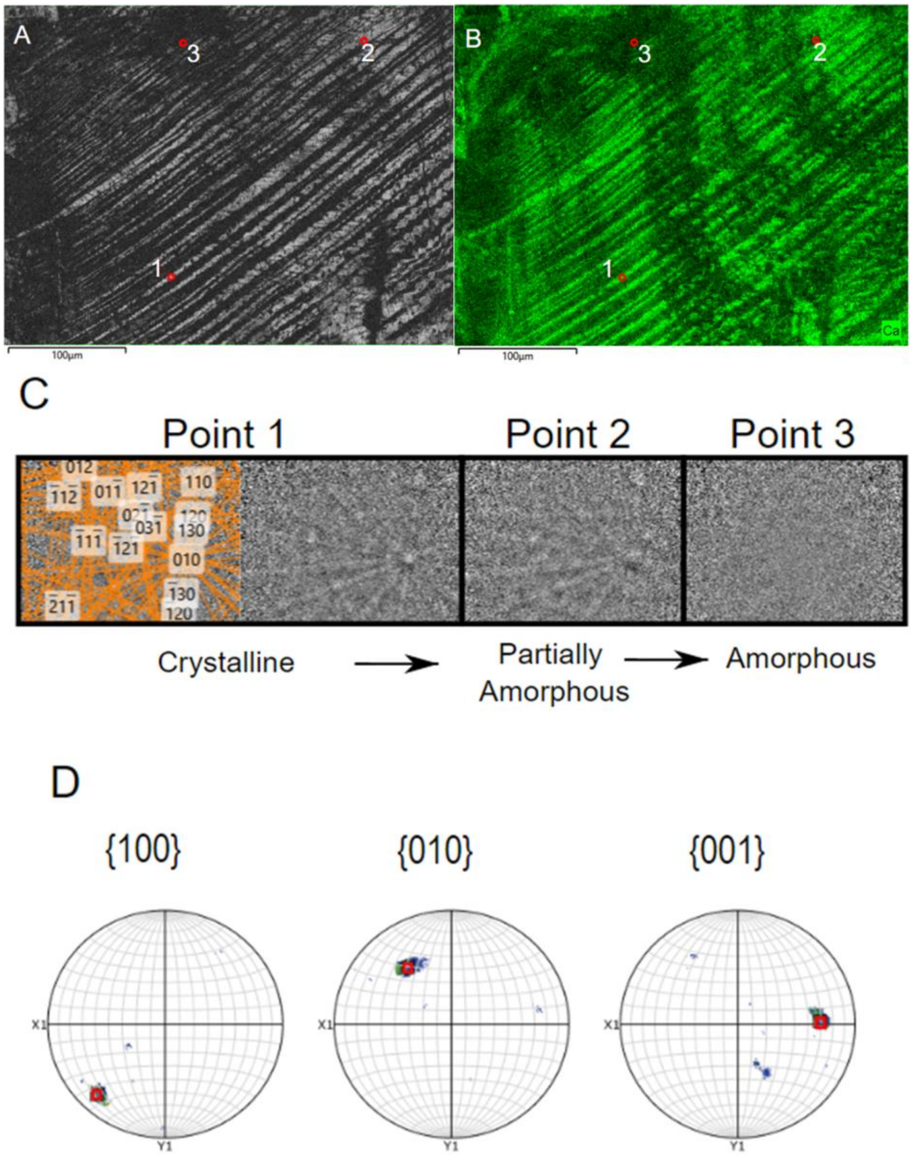

Figure 3.5 - Site 1 Band Contrast (BC) map, Ca EDS map, Kikuchi patterns and pole figures. A) Band contrast map showing a region of Site 1, red circles 1, 2 and 3 refer to the points discussed in B and C. B) False colour EDS map showing the distribution of Ca (green) in Site 1. Note that point 1 on maps A and B are on an indexed location with higher Ca compared to point 2 and 3. C) Kikuchi patterns of an indexed point (point 1) (shown both with orange simulation pattern overlay and without), non-indexed point 2 (which still shows a slight Kikuchi pattern but not clear enough to be indexed) and point 3 which is completely amorphous with no obvious Kikuchi pattern to be seen. Note that points 1 and 2 have Kikuchi patterns with the same crystallographic orientation. D) Pole figure for this site. Red box indicates data from point 1. Plotted data outside of the red box is for the rest of the area. As the red box for point 1 is with the main collection of data this suggests that point 1 has a similar orientation to many of the crystalline parts of this region of Site 1.

Within Site 1 part of the large irregular fracture mentioned previously can be seen to the top left of **Error! Reference source not found.**A. Using the images in **Error! Reference source not found.**, three different planar features (labelled in red, blue, and yellow) can be seen in high-resolution BSE each with distinct orientations and with differing thicknesses. These are referred to as the red, blue, and yellow planar features respectively and the 'lines' within these features are referred to as lamellae. The red planar features appear to consist of two different lamellae alternating, one of which is dark in backscatter images and approximately 5 µm thick and the other set are wider (~10 µm) and appear less weathered (**Error! Reference source not found.**C). The darker lamellae are suspected to have experienced more post shock alteration (likely water-mediated alteration) based on a slight increase in C seen on EDS maps of this area, this suggests that there is a lack of material as seen in **Error! Reference source not found.**D and this void space has instead been filled by resin (detected as C by EDS). The planar features marked by the blue line also demonstrate some variance in thickness of lamellae and some areas appear more weathered than others (**Error! Reference source not found.**D). Overall, however these planar features highlighted by the blue lines are less well defined than those highlighted by the red line (**Error! Reference source not found.**A).

The third set of planar features (yellow line in **Error! Reference source not found.**A and **Error! Reference source not found.**B) are less visible than the other two labelled features (red and blue features). This yellow set of planar features appear to curve slightly, and they crosscut the planar features marked by blue lines. In these high-resolution BSE images this third set of planar features appear to be made up of both darker and lighter coloured lamellae. Some of the lighter coloured lamellae in the blue planar features do contain planar features at an orientation matching those of the yellow set (**Error! Reference source not found.**B) showing that the yellow lamellae cross through the blue planar features. **Error! Reference source not found.**B also shows an interaction between the blue planar features and the fracture that crosses the centre of the image. The fracture appears to have been infilled where lighter coloured lamellae in BSE images intersect the fracture but where darker lamellae meet the fracture, the fracture remains open. Further examination of the planar features highlighted in red (**Error! Reference source not found.**C) in high-resolution BSE images also shows that the darker lamellae (potentially weathered regions) appear to be ‘contained’ within an area made by a fracture. Beyond the fracture (labelled in **Error! Reference source not found.**C) the planar features continue however they appear less weathered beyond this point suggesting fracturing occurred before alteration.

Site 1 was then investigated using EBSD. An all-Euler map of a region (**Error! Reference source not found.**G) of the area seen in **Error! Reference source not found.**C shows that the planar features marked by the red line in **Error! Reference source not found.**A and **Error! Reference source not found.**C are twins, many of which are non-indexed and appear black on EBSD maps (interpreted as amorphous, unless they are also visibly absent from BSE/SE images in which case they are voids filled by resin). These planar features can be identified as twins because in areas where they are crystalline they show a 180 ° rotation around the <010> boundaries (as seen at some locations in **Error! Reference source not found.**G). Examination of the Kikuchi patterns within these non-indexed regions reveals some faint patterns centres and Kikuchi bands within the EBSP, but these are not strong enough to be indexed by the software (**Error! Reference source not found.**). Therefore, these areas are described as partially amorphised (as also described at Site 2). A GROD angle map (**Error! Reference source not found.**F) of this region shows partially amorphised twins but also shows that there is very little misorientation along the crystalline twins. Therefore, this EBSD analysis allows the red planar features to be identified as alternating partially amorphous twins and it is suspected that on closer analysis, the blue planar features may be also. Additionally, both this GROD angle map and the IPF map show a region with a ‘step-like’ texture in the bottom right of **Error! Reference source not found.**F and **Error! Reference source not found.**G running along some of the partially amorphous twins. A CL image of the same area also shows planar features in this region however, here they are more like dark horizontal dashes rather than steps (**Error! Reference source not found.**H).

At Site 2 there are several features of interest including at least three sets of planar features at different orientations. These have been labelled with red, blue, and yellow lines and thus will be referred to as the red, blue, and yellow features. Firstly, there are potential planar deformation features marked by the red line in **Error! Reference source not found.**A, these planar features appear to contain lamellae that alternate in size with varying thickness (estimated at 14 µm and 5 µm thick). These look to be held within fractures which appear to be forming a large-scale diamond pattern which may be the cleavage of the feldspar. Examining the red planar features more closely reveals that these features are contained by some of the surrounding fractures, as these features stop particularly abruptly at the border with the upper fracture drawn in **Error! Reference source not found.**C in purple. There are also some perpendicular features which can be seen within the lamellae. The other two sets of planar features are less defined and have been marked in **Error! Reference source not found.**A with blue and yellow lines. The blue planar features also show that in some areas, some alternating lamellae appear to have been weathered more than the others (**Error! Reference source not found.**D). The yellow planar features are less visible and from BSE images, very little can be determined aside from their near vertical orientation.

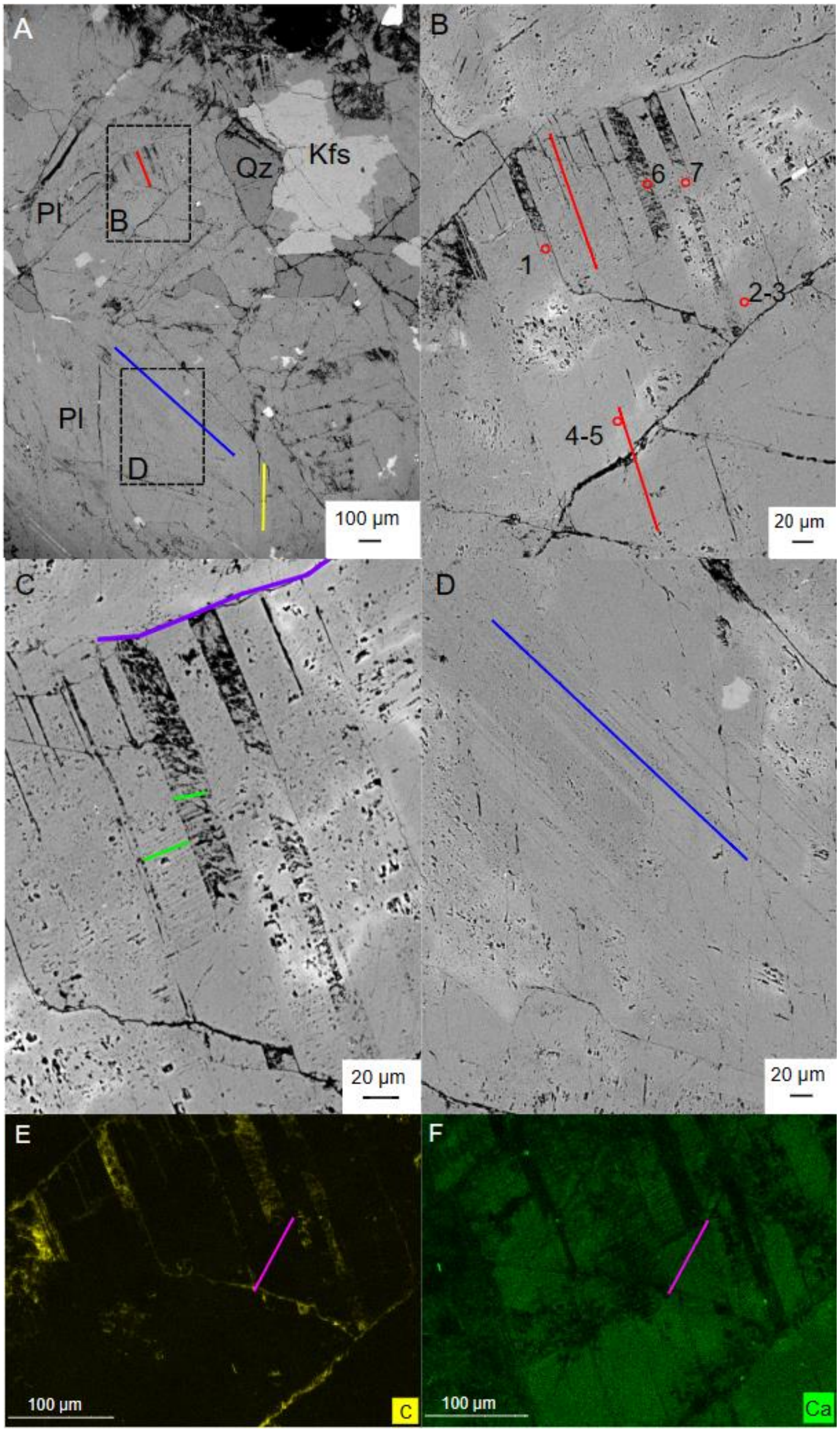
A
Pl
B
Qz
Kfs
Pl
D
100 µm
B
1
6
7
2-3
4-5
20 µm
C
20 µm
D
20 µm
E
100 µm
C
F
100 µm
Ca

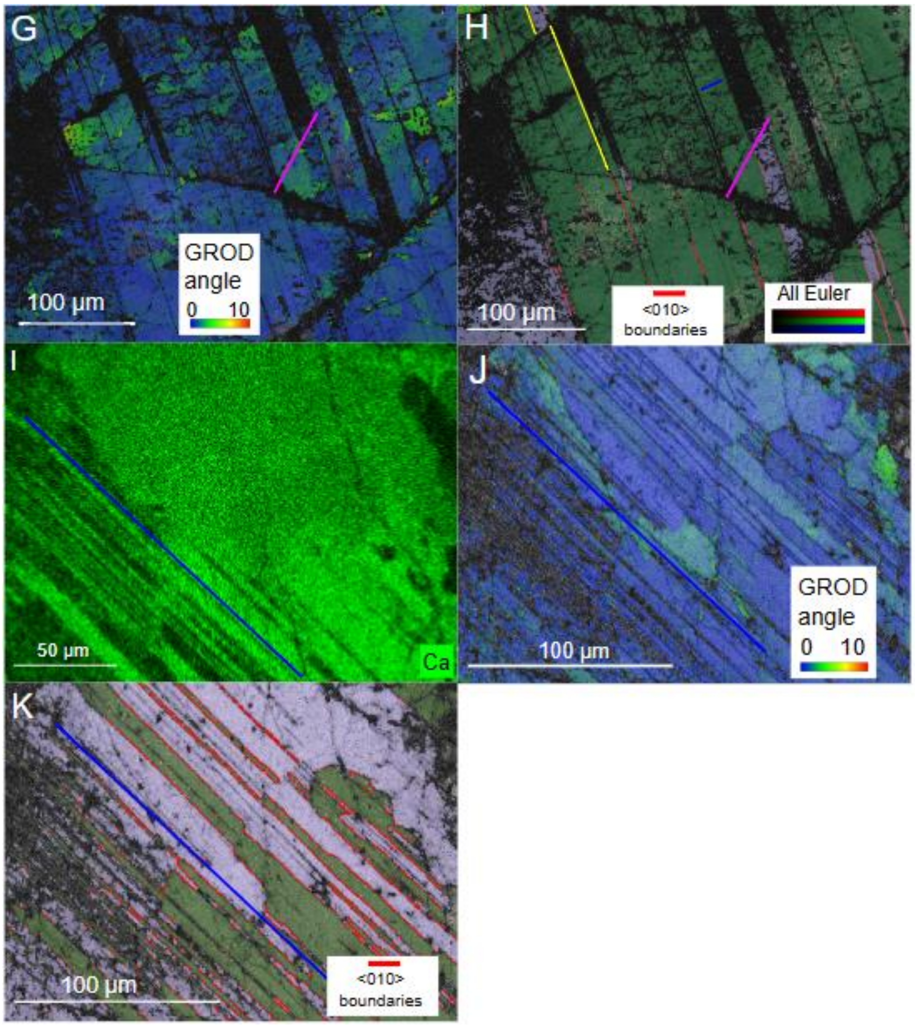

Figure 3.6 - Site 2 imaged with BSE with selected areas within Site 2 investigated further with BSE, EDS, GROD Angle, and Euler maps. A) BSE image highlighting three different sets of planar features with red, blue, and yellow lines. Pl = plagioclase, Kfs = Potassium feldspar, Qz = quartz. Black boxes label areas then shown in images B and D. B) Image of red planar features. The lower red line shows that planar features continue either side of the fracture present but with less obvious deformation on the lower side of the fracture. Red dots relate to exact points where EPMA point spectra were acquired (Table 3.1). C) Higher magnification BSE image of red planar features reveals perpendicular planar features (green lines). Purple line indicates upper fractures where planar features then abruptly stop. D) Magnified image of blue planar feature. E) False colour EDS map of same area as C (red planar feature) showing the distribution of carbon (yellow). Yellow areas indicate regions where holes in the sample have been infilled by resin. F) False colour EDS map of same area showing the distribution of Ca. Note that variation in Ca can be seen between alternating lamellae. G) GROD angle map showing misorientation. Pink line indicates fracture cutting across twins, below which the twins are no longer partially amorphised. H) Euler map of same area. Yellow lines show displacement of twins across a fracture and blue line shows direction of perpendicular lines within twins. Red lines show <010> boundaries that were detected using Aztec crystal, note the boundaries do not continue to the black non-indexed regions as this partial amorphisation has meant that the boundaries cannot be detected in this region. I-K show area of blue planar feature. I) False colour EDS map showing distribution of Ca. Note the blue planar features can only be seen on the lower half. J) GROD angle map showing misorientation. K) Euler map with grain boundaries showing that these planar features are twins.

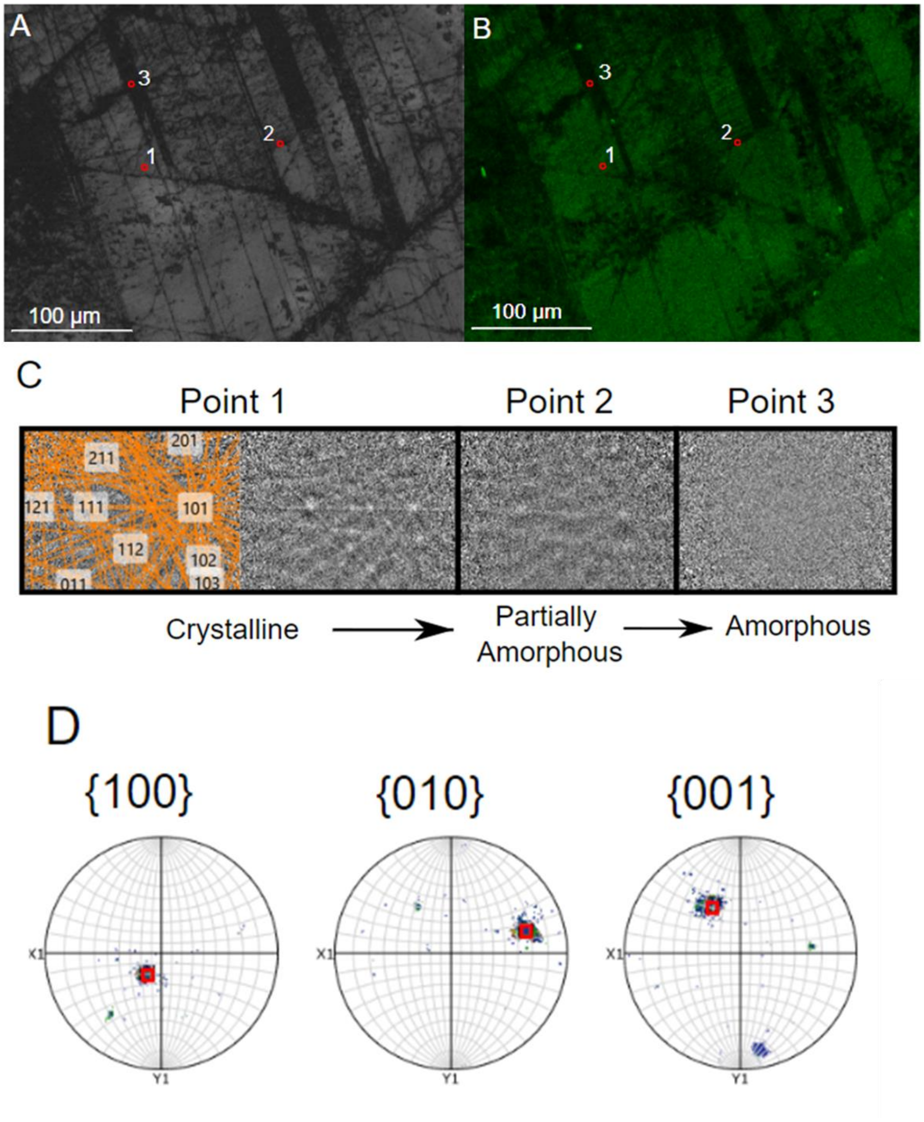

Figure 3.7 - Site 2 BC map, Ca EDS map, Kikuchi patterns and pole figures. A) Band contrast map showing a region of Site 1, red circles 1, 2 and 3 refer to the points discussed in B and C. B) False colour EDS map showing the distribution of Ca (green) in Site 2, red circles 1, 2, and 3 refer to the points discussed in C and D. C) Kikuchi patterns of an indexed point (point 1) (shown both with orange simulation pattern overlay and without), non-indexed point 2 (which still shows a slight pattern but not clear enough to be indexed) and point 3 which is completely amorphous with no obvious Kikuchi pattern to be seen. Note that points 1 and 2 have Kikuchi patterns with the same orientation. D) Pole figures for this site. Red box indicates exact point 1. Plotted data outside of the red box is for the rest of the area. As the red box for point 1 is with the main collection of data this suggests that point 1 has a similar orientation to many of the crystalline parts of the region of Site 2.

All these features have been found in the Na-rich area (as labelled in **Error! Reference source not found.**A) in contrast, the K-rich area does not appear to contain as many features only a few irregular fractures.

An area of Site 2 was also investigated using EBSD (marked in **Error! Reference source not found.**A) which revealed that the red planar features are 010 twins. These twins continue (although displaced) either side of the fracture (**Error! Reference source not found.**H). On one side of the fracture some of these twins have become partially amorphised but in many cases not the other side of the fracture. This amorphisation has been detected by the presence of non-indexed areas within the twins (**Error! Reference source not found.**G) however, when viewing the EBSP images (**Error! Reference source not found.**) a poorly defined Kikuchi pattern can still be seen in the non-indexed areas (much like at Site 1) meaning that these regions have retained a degree of crystallinity. In some of these twins, amorphisation appears to decrease (Kikuchi patterns become clear and more areas are crystalline and able to be properly indexed using EBSD) as you move along the twin away from the fracture (**Error! Reference source not found.**G). Amorphisation stops completely when it reaches another (smaller) fracture. In the neighbouring crystalline twin to each of these amorphised twins there are some planar features perpendicular to the twin boundary (**Error! Reference source not found.**C).

The blue planar features highlighted in the BSE images (**Error! Reference source not found.**D) also are identified as twins using Euler maps (**Error! Reference source not found.**K) and the partial amorphisation appears to have occurred here as well. The high-spatial resolution Ca EDS map of Site 1 (**Error! Reference source not found.**E) collected simultaneously with the EBSD data shows that the Ca content at this site varies between the partially amorphous (unindexed) and crystalline regions of the EBSD maps. EPMA and EDS data agree that the partially amorphised twins contain ~1 at. % less Ca than those twins that are crystalline. There is also variation in Ca content that follows a curving pattern that can be seen in the EDS map (**Error! Reference source not found.**E) which is a curved region of lower Ca content (tentatively identified as chemical zoning and discussed more in section 3.1.2.4). When investigating Ca trends in both twins and zoning with EPMA data, not only are these Ca trends confirmed, but also the opposite trend occurs with Na content. So as Ca content increases, Na content decreases and vice versa. This same trend can be seen at Site 2 where the areas with partial amorphisation also have less calcium by ~1 at. %. This trend can be seen with the EPMA data (Table 3.1) and the relationship between Na and Ca is shown graphically in (**Error! Reference source not found.**).

The same relationship also occurs with Al and Si content (as seen in Table 3.1). It is worth noting that this relationship is evident in both normalised (at. %) data and un-normalised (wt. %) data, so it is not just an artefact of data processing.

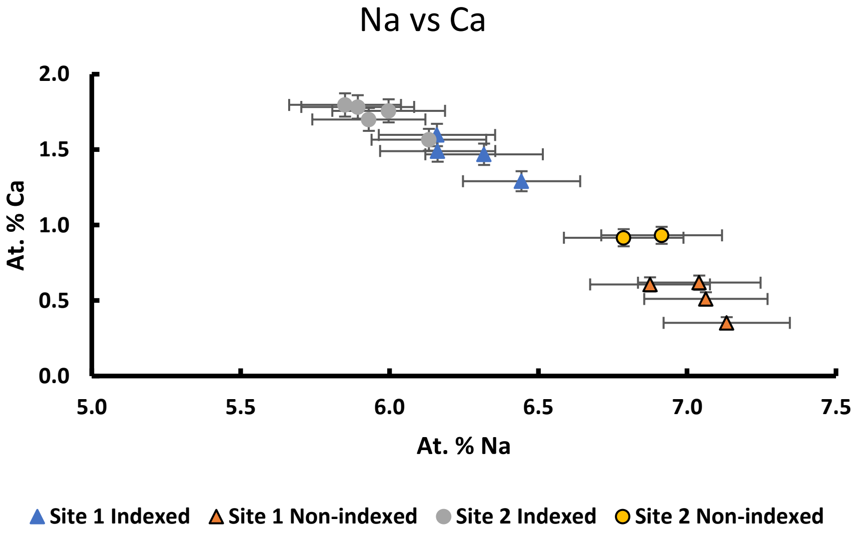

Figure 3.8 - EPMA At. % Ca vs Na content for indexed and non-indexed points at Sites 1 and 2. The indexed points from these sites contain noticeably more Ca and less Na than the non-indexed points. Error bars have been plotted based on calculated % uncertainty for individual points (see Appendix).

Partial amorphisation is suspected to have occurred in other sites where EBSD has not been used to confirm due to time constraints. For example, Site 7 which is located along the left side of the top horizontal fracture seen in C1 (**Error! Reference source not found.**C). Below the main horizontal fracture Site 7 consists of mostly Na-rich feldspar as well as one quartz crystal around 500 µm long (**Error! Reference source not found.**A). The area above the fracture also mostly contains Na-rich feldspar but also contains a few small regions of K-rich feldspar and some regions rich in Ca and Fe (**Error! Reference source not found.**A and **Error! Reference source not found.**B). Selected regions in this Na-rich feldspar (as well as two K-rich feldspar areas) were selected for EPMA spectral analysis and show an overall average composition of 6.17 at. % Na and 1.46 at. % Ca for the Na rich feldspar that makes up most of this area (Table 3.2 and Figure 3.9).

Site 7 contains two sets of planar features in the Na-rich feldspar below the fracture (as labelled in **Error! Reference source not found.**A). These have been labelled with red and blue lines and so will be referred to as the blue and red planar features. The red planar features appear to be made of alternating dark and lighter lamellae ranging in width from (~40-90 µm for both the lighter and darker lamellae). The blue planar features appear to be present in the same location as the red planar features and so the two sets of lamellae can be seen to cross over each other in some regions.

The red planar features, have darker lamellae which alternate with lighter lamellae (**Error! Reference source not found.**A), these also appear to have varying Ca levels with the darker lamellae appearing to have less Ca than the neighbouring lighter lamellae (lighter lamellae example with more Ca circled in **Error! Reference source not found.**B).

Table 3.2 - Normalised chemical composition of the selected areas in site 7 in atomic percent (at. %). Chemical compositions are only given for major elements. These values have been converted from weight % and re-normalised. The point number correlates to the blue boxes in Figure 3.9A.

		At. %						
Point #	Na or K-rich	Ca	Na	K	Si	Al	O	Other
1a	Na-rich	1.37	6.16	0.03	21.64	9.16	61.58	0.00
1b	Na-rich	1.50	6.10	0.04	21.61	9.12	61.57	0.00
1c	Na-rich	1.70	6.01	0.11	21.40	9.21	61.49	0.00
2a	K-rich	0.02	0.42	6.42	23.39	7.73	61.92	0.19
2b	K-rich	0.01	0.44	6.42	23.32	7.84	61.92	0.18
2c	K-rich	0.02	0.43	6.43	23.39	7.75	61.93	0.27
3a	Na-rich	1.55	6.15	0.02	21.62	9.07	61.55	0.55
3b	Na-rich	1.19	6.20	0.04	21.96	8.89	61.66	0.32
3c	Na-rich	1.44	6.20	0.05	21.65	9.07	61.55	0.33
4a	Na-rich	1.85	5.85	0.06	21.21	9.45	61.51	0.18
4b	Na-rich	0.35	7.21	0.10	22.70	8.04	61.55	0.20
5a	Na-rich	1.42	6.21	0.04	21.60	9.14	61.54	0.24
5b	Na-rich	1.25	6.39	0.04	21.81	8.92	61.55	0.06
5c	Na-rich	1.89	5.78	0.06	21.28	9.38	61.54	0.13
6a	Na-rich	1.60	6.07	0.09	21.56	9.09	61.53	0.20
6b	Na-rich	1.67	6.08	0.04	21.55	9.07	61.53	0.17
6c	Na-rich	1.63	6.03	0.14	21.54	9.07	61.51	0.23
7a	K-rich	0.02	0.33	6.49	23.35	7.80	61.93	0.23
7b	K-rich	0.01	0.27	6.64	23.35	7.77	61.89	0.25
7c	K-rich	0.01	0.45	6.46	23.28	7.84	61.88	0.27
K-rich average		**0.01**	**0.39**	**6.48**	**23.35**	**7.79**	**61.91**	**0.23**
K-rich SD		0.007	0.073	0.085	0.041	0.049	0.021	0.038
Na-rich average		**1.46**	**6.17**	**0.06**	**21.65**	**9.05**	**61.55**	**0.19**
Na-rich SD		0.377	0.333	0.034	0.357	0.327	0.041	0.152

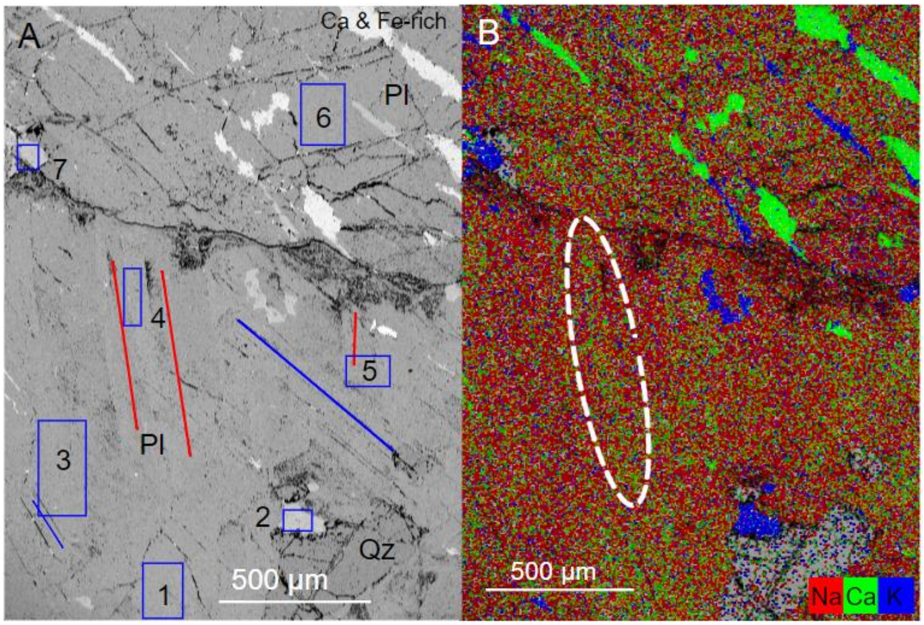

Figure 3.9 - BSE and EDS images of Site 7. A) BSE image of site 7. Pl=plagioclase, Kfs = K feldspar and Qz= quartz. Red and blue lines highlight two sets of planar features. Blue boxes show the location of EPMA point spectra areas, numbers correlate to location numbers seen in table 3.2. B) False colour EDS map showing the distribution of Ca, Na, and K in green, red, and blue respectively. White circle highlights a region containing more Ca than its neighbouring lamellae. Note that the Ca-rich regions above the fracture are not feldspar but a mineral rich in Ca and Fe (as labelled in A).

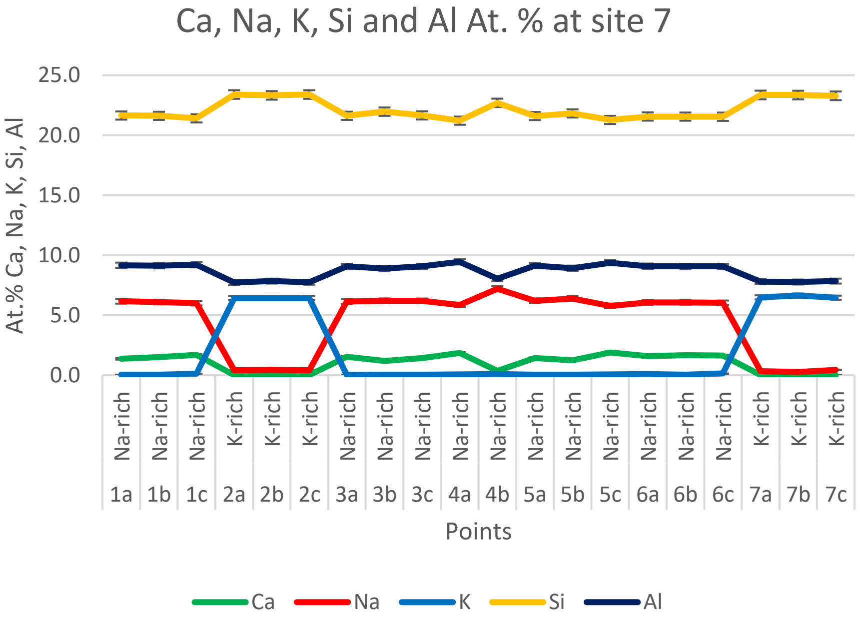

Figure 3.10 - Graph showing At. % Ca, Na, K, Si and Al content at each EPMA point spectra collected at Site 7. Points relate to EPMA points labelled in boxes in ***Error!***

***Reference source not found.**A. At many points analytical uncertainty bars are too small to see. Analytical uncertainty bars calculated from % uncertainty.*

3.1.2.2 K-rich feldspar vs Na-rich feldspar

Sample CHX-1160.7 although containing more Na-rich feldspar, does still contain some K-rich feldspar within it. In some sites, Na-rich and K-rich feldspar can be found together in the same location, allowing direct comparisons to be made between the shock deformation features which can be found on both types of feldspar.

Sites 4 and 6 are good examples of this. Site 4 is located within C1 (**Error! Reference source not found.**C). The site mainly comprises Na-rich feldspar, however it also contains some quartz (largest around 400 μm long) and areas of K-rich feldspar (the largest areas of which continue beyond the edge of the site) which are seen in **Error! Reference source not found.**B. Site 6 is located within the centre of C1 (**Error! Reference source not found.**C). This site contains both Na-rich and K-rich feldspar as well as a quartz crystal (~490 μm wide by ~930 μm long). Most of the Na and K-rich feldspar continues beyond site 6 however there are also smaller inclusions of K-rich feldspar ~230 μm long.

EDS analysis of Site 4 shows the Na rich areas contain ~6.0 at. % Na and ~0.1 at. % K (Spectrum 1, Table 3.3 in contrast to the small areas of K-rich feldspar which contain ~9.2 at. % K and no Na (Spectrum 2, Table 3.3). No EPMA data was collected at Site 4 however EPMA data was collected for Site 6. The Na-rich feldspar in Site 6 is contains an average of 6.8 at. % Na and 1.3 at. % Ca and the K-rich feldspar contains an average 6.5 at. % K and only 0.4 at. % Na and 0.01 at.% Ca (**Error! Reference source not found.**). Within the Na-rich feldspar, the Ca content appears to be heterogeneous across the mineral, which can be seen in the EDS map where Ca distribution is represented in green (**Error! Reference source not found.**B). This irregular distribution of Ca is also noticeable in **Error! Reference source not found.** where the at. % Ca is noticeably lower at point 5. Point 5 is the location at which Na content is highest and Ca content is lowest, once again a negative correlation can be seen between Na and Ca content (as illustrated Figure 3.12).

Table 3.3 - Normalised chemical composition of selected areas of Site 4 (marked by blue boxes in Figure 3.11) in atomic percent (At. %). These values have been normalised and have a 10% relative uncertainty. EDS data.

	At. %						
	Ca	Na	K	Si	Al	O	Other
Spectrum 1 (Na-rich)	1.6	6.0	0.1	23.9	9.7	58.3	0.5
Spectrum 2 (K-rich)	0.1	0	9.2	28.2	10.8	51.4	0.3

Table 3.4 - EPMA data showing normalised chemical composition of the selected areas within Na feldspar and the K feldspar in Site 6 in atomic percent (at. %). Chemical compositions are only given for major elements. These values have been converted from weight % and re-normalised. The point number correlates to the point locations labelled in Figure 3.12C.

		At. %						
	Point #	Ca	Na	K	Si	Al	O	Other
Na-rich feldspar	1a	1.70	5.77	0.16	21.44	9.30	61.58	0.07
	1b	1.54	5.88	0.19	21.63	9.11	61.59	0.06
	1c	1.59	6.10	0.14	21.43	9.21	61.47	0.06
	3a	1.25	6.29	0.11	21.87	8.85	61.57	0.06
	3b	1.52	6.11	0.12	21.60	9.07	61.53	0.06
	3c	1.47	6.16	0.10	21.60	9.09	61.53	0.06
	5a	1.33	6.44	0.09	21.70	8.90	61.46	0.08
	5b	0.66	6.65	0.07	22.40	8.49	61.66	0.07
	5c	0.48	7.13	0.05	22.57	8.19	61.55	0.04
	Average	**1.28**	**6.28**	**0.11**	**21.80**	**8.91**	**61.55**	**0.06**
	SD	**0.43**	**0.42**	**0.04**	**0.41**	**0.36**	**0.06**	**0.01**
K-rich feldspar	2a	0.03	0.43	6.44	23.40	7.69	61.91	0.13
	2b	0.01	0.39	6.51	23.30	7.84	61.89	0.10
	2c	0.01	0.30	6.62	23.30	7.83	61.89	0.06
	4a	0.01	0.29	6.62	23.32	7.79	61.89	0.10
	4b	0.01	0.37	6.56	23.24	7.88	61.86	0.09
	4c	0.01	0.47	6.44	23.41	7.69	61.91	0.09
	6a	0.01	0.27	6.57	23.37	7.81	61.94	0.04
	6b	0.01	0.36	6.47	23.46	7.70	61.96	0.06

6c	0.01	0.45	6.45	23.36	7.76	61.91	0.07
Average	**0.01**	**0.37**	**6.52**	**23.35**	**7.78**	**61.91**	**0.08**
SD	**0.01**	**0.07**	**0.07**	**0.07**	**0.07**	**0.03**	**0.03**

In Site 4, plagioclase feldspar contains a range of deformation features within it. Firstly, there are fractures across the site which although not diagnostic of shock, are likely still a result of shock deformation. Secondly there are planar features (marked in **Error! Reference source not found.**A by the red line) which are almost perpendicular to several fractures below (the direction of which are marked by the green line). One region of K-rich feldspar in Site 4 also contains fractures (marked by the yellow lines) however, these are not as defined as those found in the neighbouring plagioclase. These fractures however do appear to join with one main irregular fracture. Despite the presence of a few fractures, it is still clear that the surrounding plagioclase contains far more deformation features than the areas of K-rich feldspar.

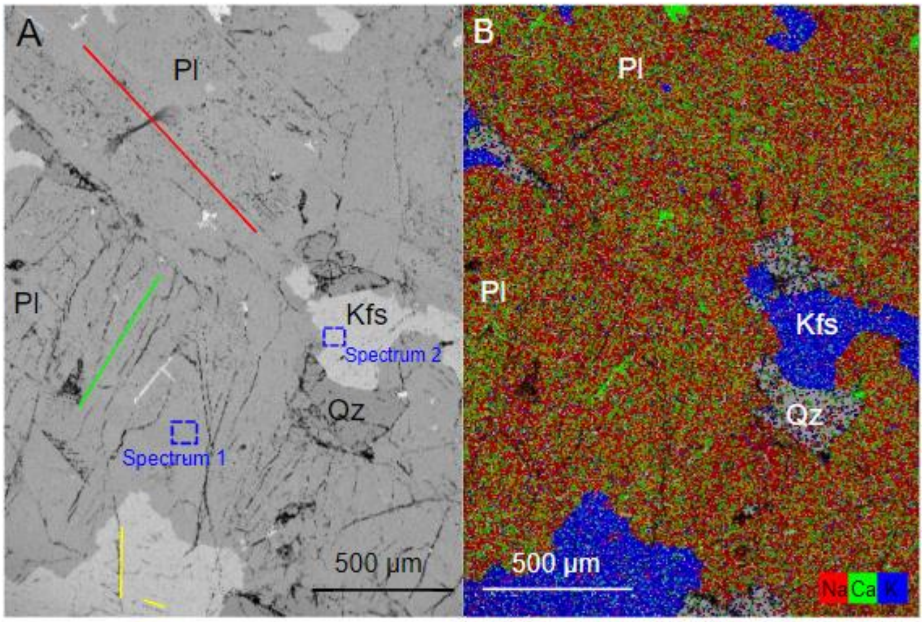

Figure 3.11 - Site 4 BSE image and EDS map. A) BSE image of Site 4. Red line highlights planar features and the green line helps to highlight the fractures that are at an almost perpendicular angle to the planar features. The yellow lines highlight fractures in K-rich feldspar. Blu boxes outline areas of EDS spectra recorded in Table 3.3. Pl = plagioclase, Kfs = K-rich feldspar and Qz = Quartz. B) False colour EDS maps showing the distribution of Na (red), Ca (green), and K (blue). This illustrates the division between the K-rich and Na-rich feldspar. Note that the Ca and Na within plagioclase regions is unevenly distributed. Pl = plagioclase, Kfs = K-rich feldspar and Qz = Quartz.

In Site 6 the quartz contains more defined fractures than the feldspars, although the feldspars do still contain some fractures. The plagioclase feldspar has multiple fractures and a planar feature marked by the blue line in **Error! Reference source not found.**A. There are two types of K rich feldspar which can be seen here. The small amount seen on the left (circled in red in **Error! Reference source not found.**A) is very rounded in shape. This suggests that this sample is likely to be recrystallised feldspar. The larger K-rich feldspar seen on the bottom left contains more angular grain boundaries making it more likely a primary feldspar. Both these alkali feldspars contain little to no features other than the odd fracture in the primary feldspar on the right.

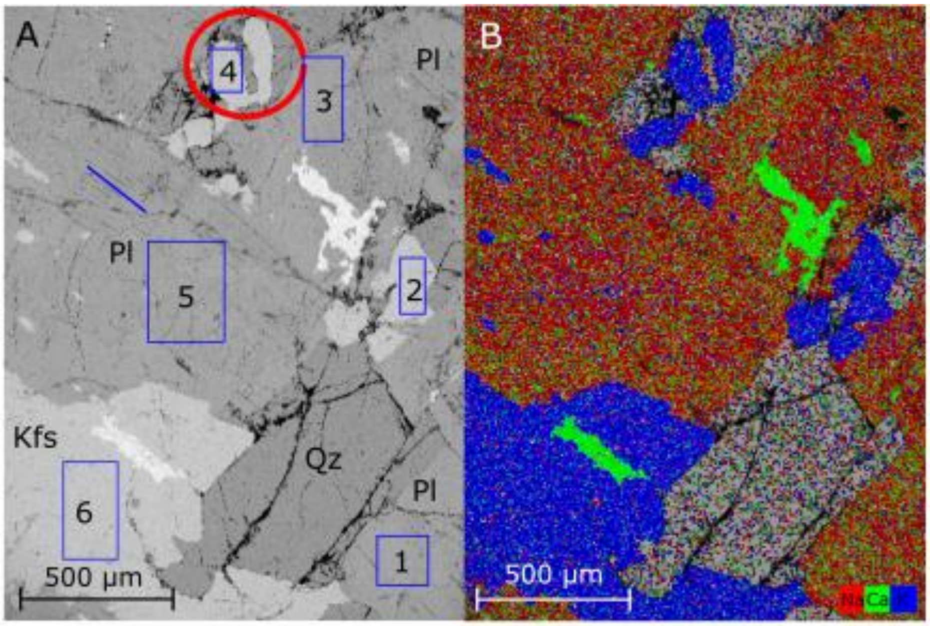

Figure 3.12 - Site 6 BSE image and EDS map. A) BSE image of Site 6. Blue line highlights planar features. Red circle highlights secondary K-rich feldspar. Blue boxes show location of EPMA spectra areas. Three measurements were taken from each box (labelled A-B for each box in Table 3.4). Pl = plagioclase, Kfs = K feldspar and Qz = Quartz. B) False colour EDS map showing the distribution of Na (red), Ca, (green) and K (blue). Note that the Ca-rich regions are not feldspar but most likely a pyroxene.

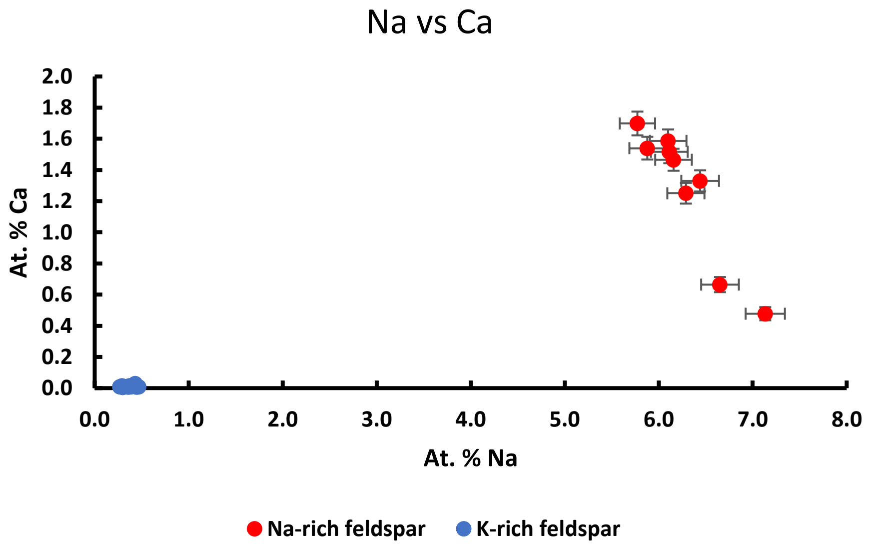

Figure 3.13 - Graph showing At. % Ca vs Na content at each EPMA point spectra collected at Site 6. Note the Na-rich feldspar shows a negative correlation between Na and Ca content. Error bars have been plotted based on calculated % uncertainty (see Appendix E).

Na-rich and K-rich feldspar have been compared further using EBSD. This has been done at Site 3 which is located within C1, in the far right of the images in **Error! Reference source not found.**C. Site 3 has two visible feldspar phases, a Na-rich and K-rich phase, with a small amount of quartz (as labelled in **Error! Reference source not found.**). The Na-rich feldspar has a average Na content of 5.93 at.% and an average Ca content of 1.79 at.% (Table 3.5). Data in Table 3.5 show that as Na increases, Ca decreases, with the same trend exhibited by Si and Al (as mentioned in section 3.1.2.1).

Table 3.5 - Normalised chemical composition of areas in Site 3 (in atomic percent (at. %). Chemical compositions are only given for major elements. These values have been converted from weight % and re-normalised. The point number correlates to the point locations labelled in Figure 3.14B. These data have been correlated with the EBSD maps to determine whether the EPMA spectra were acquired from indexed or non-indexed electron backscatter patterns (EBSP) pixels and have all been confirmed to be indexed. The average and SD have been calculated for these points.

	At. % at Indexed points						
Point #	Ca	Na	K	Si	Al	O	Other
1	1.48	6.16	0.11	21.64	9.03	61.53	0.06
2	1.76	5.74	0.21	21.30	9.40	61.53	0.06
3	1.95	5.92	0.12	21.18	9.34	61.43	0.07
4	1.97	5.84	0.12	21.12	9.44	61.45	0.07
5	1.88	5.85	0.12	21.15	9.46	61.46	0.07
6	1.69	6.00	0.19	21.33	9.27	61.45	0.08
7	1.86	5.90	0.13	21.16	9.43	61.45	0.07
8	1.86	5.88	0.15	21.28	9.28	61.47	0.08
9	1.87	5.87	0.16	21.15	9.44	61.44	0.07
10	1.62	6.16	0.38	21.26	9.17	61.30	0.11
11	1.99	5.59	0.13	21.09	9.59	61.53	0.07
12	1.59	6.31	0.05	21.46	9.10	61.43	0.06
Average	**1.79**	**5.93**	**0.16**	**21.26**	**9.33**	**61.46**	**0.07**
SD	**0.16**	**0.20**	**0.08**	**0.16**	**0.16**	**0.06**	**0.01**

Site 3 contains a mix of features including irregular fractures and planar features. The irregular fractures are randomly distributed. There are two different sets of planar features which can be seen. The first of which is highlighted in blue in **Error! Reference source not found.**A and consists of some near vertical lamella which appear to connect with some smaller lamellae on the right-hand side (this is therefore suspected to be the same planar feature with a sharp bend on the left (marked in **Error! Reference source not found.**A)). The second set of planar features are highlighted in green in **Error! Reference source not found.**A. These are a series of lamellae that have a very slight curve to them (when compared to the straight line drawn in green next to them).

This particular planar feature labelled in green appears to be more defined at the upper left than at the lower right. The K-rich feldspar in this area appears to be curved and irregular in shape, the quartz is also rounded and mixed in amongst the K-rich feldspar. The quartz is fractured, whereas the K-rich feldspar is not.

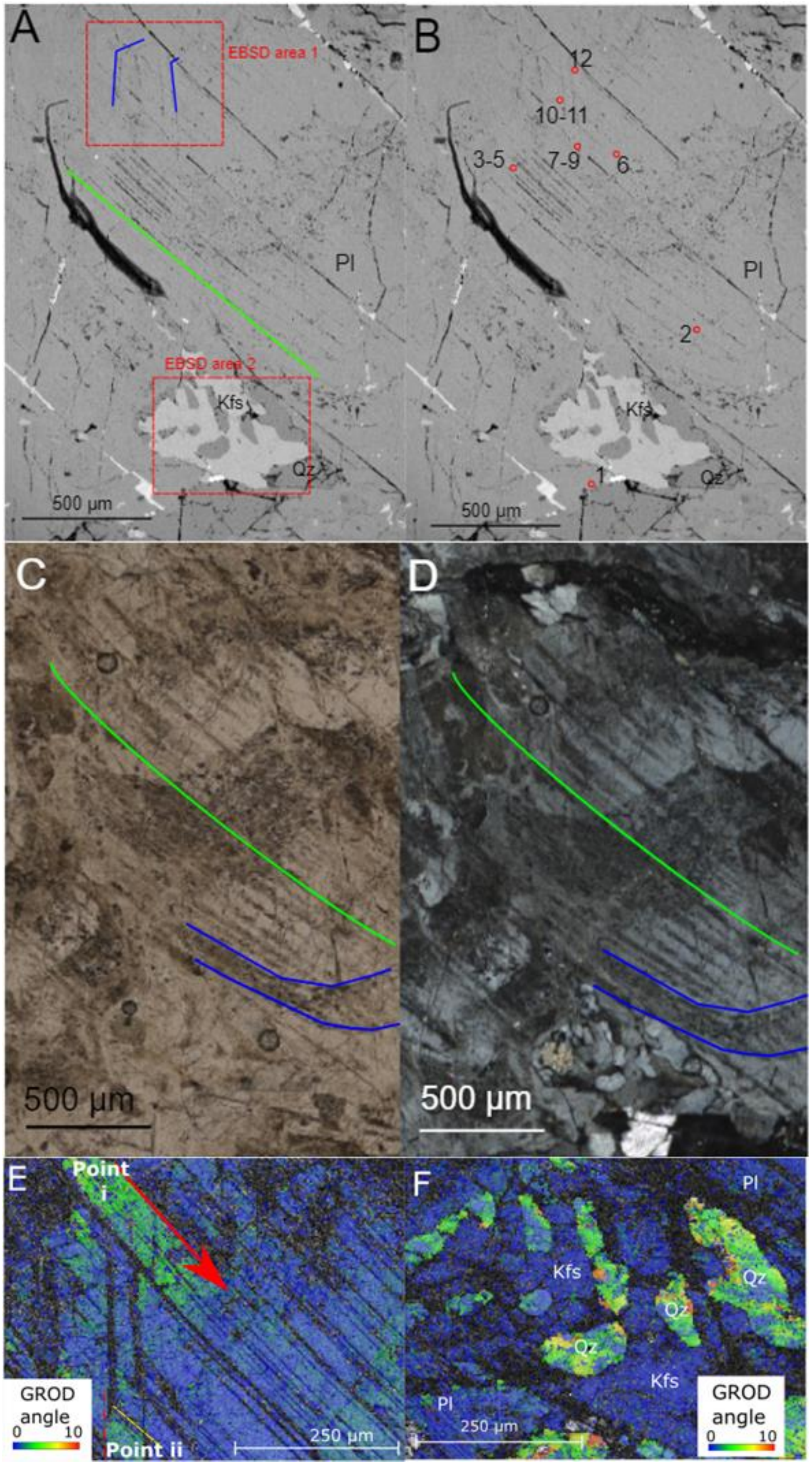
A
EBSD area 1
EBSD area 2
Kfs
Qz
Pl
500 µm
B
12
10-11
3-5
7-9
6
Pl
2
Kfs
1
Qz
500 µm
C
500 µm
D
500 µm
E
Point i
Point ii
GROD angle
0
10
250 µm
F
Pl
Kfs
Qz
Qz
Qz
Kfs
Pl
250 µm
GROD angle
0
10

Figure 3.14 - Site 3 BSE images and EDS maps. A) BSE image of Site 3. Red boxes indicate areas shown in E and F. Planar features with a kink (or sharp bend) are labelled with blue lines. Planar features with a slight curve are highlighted by the straight green line. B) Exact points where EPMA point spectra were acquired at this site. Data for specific numbered points in Table 3.5. C) PPL image of green planar features which appear curved particularly at the bottom. D) XPL image of green planar feature showing them as twins. E) GROD angle map of Area 1 from ***Error! Reference source not found.****A. Points i and ii are regions of greater internal misorientation (~6-7°). Arrow indicates direction of decreasing misorientation (following planar features). At point ii the red and yellow dashed lines indicate the planar features that appear to contain the region of greater misorientation. F) GROD angle map of Area 2 from* ***Error! Reference source not found.****A showing greater misorientation in quartz than feldspar. Pl = plagioclase feldspar, Kfs = K rich feldspar, Qz = Quartz.*

The images collected using a polarising microscope help to give some context to the planar features found in **Error! Reference source not found.**A. The green planar features line up with the twins seen in XPL (also highlighted green in **Error! Reference source not found.**D) which appear slightly curved. The blue planar features are less clear in the optical images however, in surrounding areas, regions of zoning can be seen.

EBSD analysis was carried out at both a Na-rich area and over the area with K-rich feldspar and quartz in Site 3. The GROD angle map (**Error! Reference source not found.**E) shows misorientation in a Na-rich area of Site 3. The points marked i and ii highlight two regions with greater misorientation (up to ~7°), constrained by the surrounding fractures and planar features. Point i appears to have the greatest misorientation (~7°) in the top left. Moving away from this region following the edge of lamella in a SE direction the degree of misorientation decreases. Directly to the left of the of greatest misorientation there are non-indexed points indicating amorphous material (the black regions). Point ii contains an area of ~5° misorientation and appears to be constrained by planar features in two different orientations (marked by dotted lines in **Error! Reference source not found.**E). The GROD angle map for the K-rich feldspar region however in **Error! Reference source not found.**F shows a greater degree of misorientation in the quartz rather than the K-rich feldspars and there are no planar features observed within the K-rich feldspar. There are however some planar features in the albite in the top right and bottom left (these are a continuation of the features identified in the Na-rich feldspar area. These planar features are believed to be twins.

3.1.2.3 Additional Planar features

A range of other planar features which are potentially deformation features have been identified in CHX-1160.7. Site 5 for example, which is in the right side of the large crystal (C1) (**Error! Reference source not found.**C). The site mainly consists of Na-rich feldspar however there are some quartz crystals (**Error! Reference source not found.**A) up to 0.5 mm long. The composition of the Na-rich phase (6.1 at. % Na) is shown in spectrum 1 in **Error! Reference source not found.**. There is also a mineral in the top of **Error! Reference source not found.**A approximately 300 µm wide which contains Ti, Fe and K. Circled in red in **Error! Reference source not found.**A there is a set of dark coloured lamellae (magnified view in **Error! Reference source not found.**C marked by the red line and referred to as the red lamellae) which appear to have smaller perpendicular planar features (marked in yellow and referred to as the yellow lamellae) within. It is possible that these are another form of alternate twin deformation (see section 3.1.2.1) as both the yellow features and the red features appear to have alternating darker and lighter lamellae within.

Table 3.6 - Normalised chemical composition (EDS data) of the areas marked by blue box in Figure 3.15A, Figure 3.16A, Figure 3.17A, Figure 3.18A) in atomic percent (At%). These values have been normalised and have a 10% relative uncertainty.

Site #	Spectra #	At. %						
		Ca	Na	K	Si	Al	O	Other
5	1 (Na-rich)	1.9	6.1	0.1	23.6	10.3	57.9	0.2
8	1 (Na-rich)	1.6	5.7	0.2	23.9	9.95	58.6	0.1
9	1 (Na-rich)	1.5	6.5	0.2	23.2	9.7	58.9	0.0
	2 (K-rich)	-	1.4	7.3	24.2	8.1	58.7	0.4
	3 (Na-rich)	0.8	6.3	1.2	22.5	9.9	58.5	0.8

10	1 (Na-rich)	1.3	6.6	0.3	24.8	10.1	56.8	0.2
	2 (K-rich)	0.1	0.5	8.1	23.7	7.9	59.3	0.3

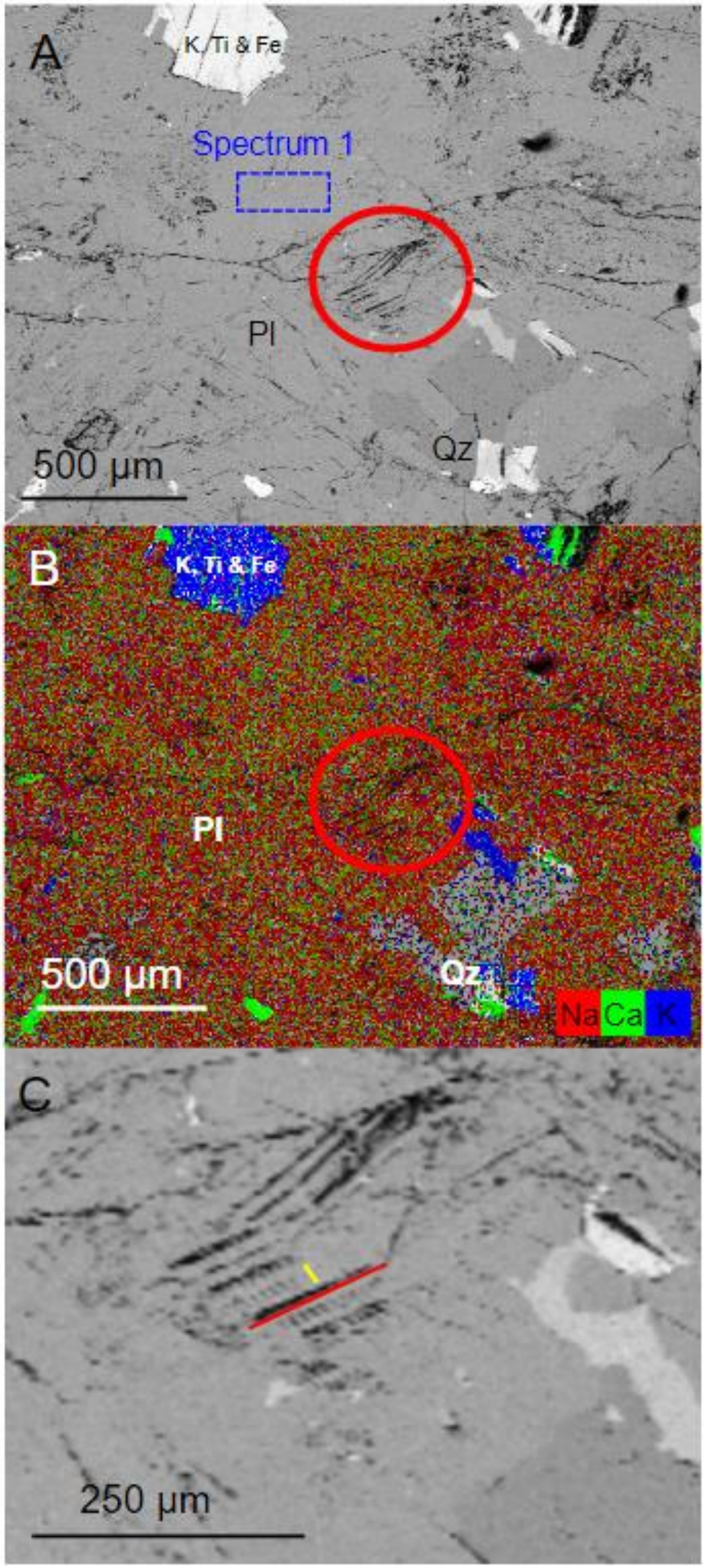
A
K, Ti & Fe
Spectrum 1
Pl
Qz
500 µm
B
K, Ti & Fe
Pl
500 µm
Qz
Na Ca K
C
250 µm

Figure 3.15 - Site 5 BSE images and EDS map. A) BSE image of Site 5. Ladder texture in red circle. Blue box highlights the area where the chemical composition has been acquired and reported in Table 3.6. Pl = plagioclase feldspar, Qz = Quartz. B) False colour EDS maps showing Na, Ca and K in red, green, and blue respectively. This map demonstrates that this area is predominantly Na-rich feldspar. C) Ladder texture with planar features highlighted by the red and yellow lines.

Another example of a different planar feature can be found at Site 8 which is located on the left edge of C1 (**Error! Reference source not found.**C). It contains mostly Na-rich feldspar as well as some small areas of quartz and K-rich feldspar (~200-400 µm). The edge of C1 can be seen on the left side of the image were the groundmass starts (**Error! Reference source not found.**A). The composition of the Na rich phase is 5.7 at. % Na, 1.6 at. % Ca, and 0.1 at. % K (spectrum 1 in **Error! Reference source not found.**). An EDS map of the site is also shown in **Error! Reference source not found.**B. Two sets of planar features can be seen here at Site 8. One set is very faint (marked by the blue line in **Error! Reference source not found.**A) and one set is prominent and bends slightly in the middle (marked by the red line in **Error! Reference source not found.**A. These two planar features appear to cross over each other at the edge of the crystal.

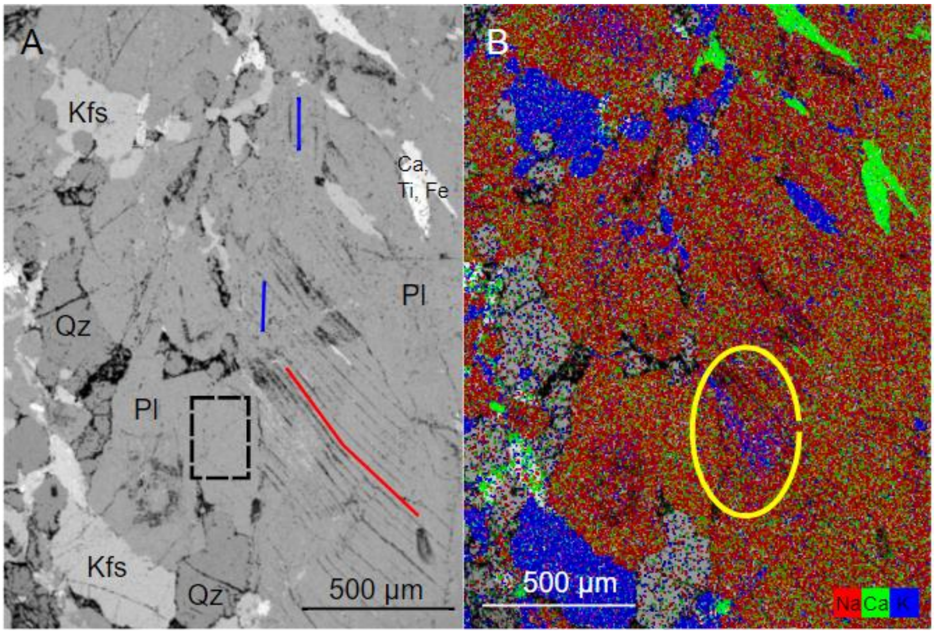

Figure 3.16 - Site 8 BSE image and EDS map. A) BSE image of Site 8. Red and blue lines indicate labelled planar features and EDS spectra area highlighted by black dashed box for compositional data reported in Table 3.6. Pl=plagioclase, Kfs = K feldspar and Qz= quartz. B)

False colour EDS map showing the distribution of Ca, Na, and K in green, red, and blue respectively. The K and Ca distribution within the Na-rich regions (plagioclase) is not evenly distributed, the yellow circle indicates a region of increased K in a Na-rich feldspar. Note the Ca-rich areas in the top right are not feldspar, they are also rich in Ti and Fe.

Another site with planar features is Site 9. Site 9 is located in the bottom right-hand edge of a Na-rich plagioclase crystal (the overall crystal is about 6.5 mm long) (**Error! Reference source not found.**C). This site also covers part of the groundmass of the sample containing a mix of Na and K-rich feldspar as well as quartz and small amounts of other minerals containing Ca (not feldspar) which have a slight flow texture (**Error! Reference source not found.**A). The Na-rich feldspar typically contains around 6.5 at. % Na, 1.5 at. % Ca and 0.2 at. % K whereas the K-rich feldspar contains around 1.4 at. % Na, 7.3 at. % K, and no Ca. This chemical content was taken from EDS spectra marked in **Error! Reference source not found.**B and reported in **Error! Reference source not found.**.

From the BSE images at this site (circled in red **Error! Reference source not found.**A) a planar feature can be seen in the bottom right. This planar feature is curved, with the appearance of a wavy line. Interestingly, the EDS map of this area shows an increase of K in the region where this wavy feature can be seen **Error! Reference source not found.**B. The area is overall Na-rich rather than K rich (spectrum 3 in **Error! Reference source not found.**) and is the only such example that has been found in these samples. This region (spectrum 3) also exhibits a slight decrease in Ca compared to the other EDS spectrum (spectrum 1 in **Error! Reference source not found.**) which is more of the typical composition when compared to the Na-rich feldspar composition recorded from other sites in **Error! Reference source not found.**. A Ca decrease associated with deformation has been found in other sample site locations with other deformation features (the partial amorphisation of alternating twins discussed in section 3.1.2.1).

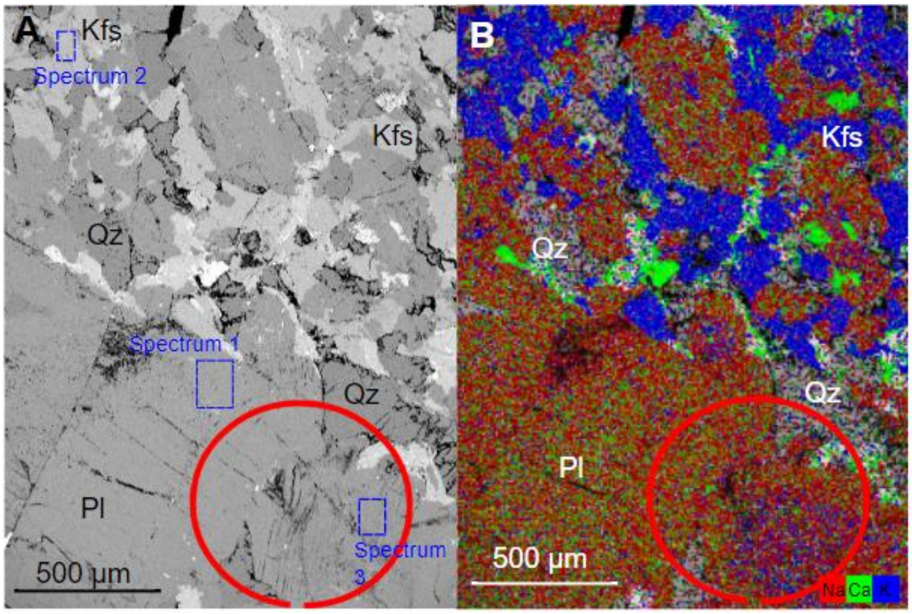

Figure 3.17 - Site 9 BSE image and EDS map. A) BSE image of Site 9. Wavy feature circled in red and EDS spectra area highlighted by blue boxes for chemical data quoted in Table 3.6. Pl=plagioclase, Kfs = K feldspar and Qz= quartz. B) False colour EDS map showing the distribution of Ca, Na, and K in green, red, and blue respectively.

Finally, Site 10 which is located on the far-left hand side of thin section CHX-1160.7 (**Error! Reference source not found.**C). The site covers an area of groundmass with a mix of Na-rich and K-rich feldspar as well as quartz (**Error! Reference source not found.**A). Grain size ranges from ~50-700 µm. Chemical composition has been taken from EDS data of selected regions for Na-rich and K-rich feldspar as seen in **Error! Reference source not found.**. The Na-rich feldspar (spectrum 1) contains approximately 6.6 at. % Na, 1.3 at. % Ca and 0.3 at. % K whereas the K-rich feldspar (spectrum 2) contains around 0.5 at. % Na, 0.1 at. % Ca and 8.1 at. % K, (**Error! Reference source not found.**). An interesting set of planar features can be seen in an area of Na-rich feldspar (circled in red in **Error! Reference source not found.**A magnified in **Error! Reference source not found.**B). These features are alternating dark lamellae (marked in **Error! Reference source not found.**B by the yellow line) ~14.5 µm wide with much thinner lighter coloured lamellae (~6 µm wide). These darker lamellae appear to be made up of additional lines (marked by the red line in **Error! Reference**

source not found.B forming a feather like pattern. No notable features can be seen in the K-rich feldspar, and the quartz at the site only shows some fracturing (see 3.1.2.2 for detailed comparison between deformation in different types of feldspar).

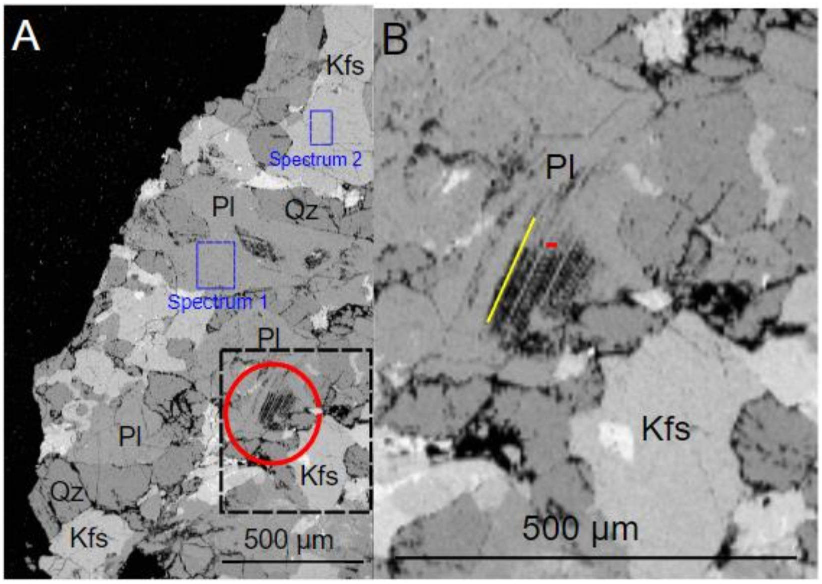

Figure 3.18 - BSE maps of Site 10. A) BSE image of Site 10. Planar feature circled in red and EDS spectra area highlighted by blue boxes for chemical data reported in Table 3.6. Black box highlights area shown in B. Pl=plagioclase, Kfs = K feldspar and Qz= quartz. B) Magnified BSE image of area in black box and feature circled in red in image A. Red and yellow lines highlight lamellae of interest with the smaller red lamellae occurring within the yellow lamellae. Both the red and yellow lamellae have alternating dark and light lamellae.

3.1.2.4 Zoning

Although compositional zoning is not a deformation feature, it is important to note that it is present in some locations as it may affect the deformation features that are present. This is seen for example in Site 1 where partial amorphisation in alternating twins has been identified (see section 3.1.2.1) and varying Ca levels across the alternating twins could be found. In the same region areas of potential zoning can be seen with decreased levels of Ca (**Error! Reference source not found.**C). This potential zoning feature seen in Ca EDS maps is also observed using cathodoluminescence (CL) where the curved features of lower Ca (suspected zoning) show as darker regions (**Error! Reference source not found.**A and **Error! Reference**

source not found.B) that appear to be a type of distorted compositional zoning. This distortion may be attributed to variations in crystal growth-rate between the crystal axes.

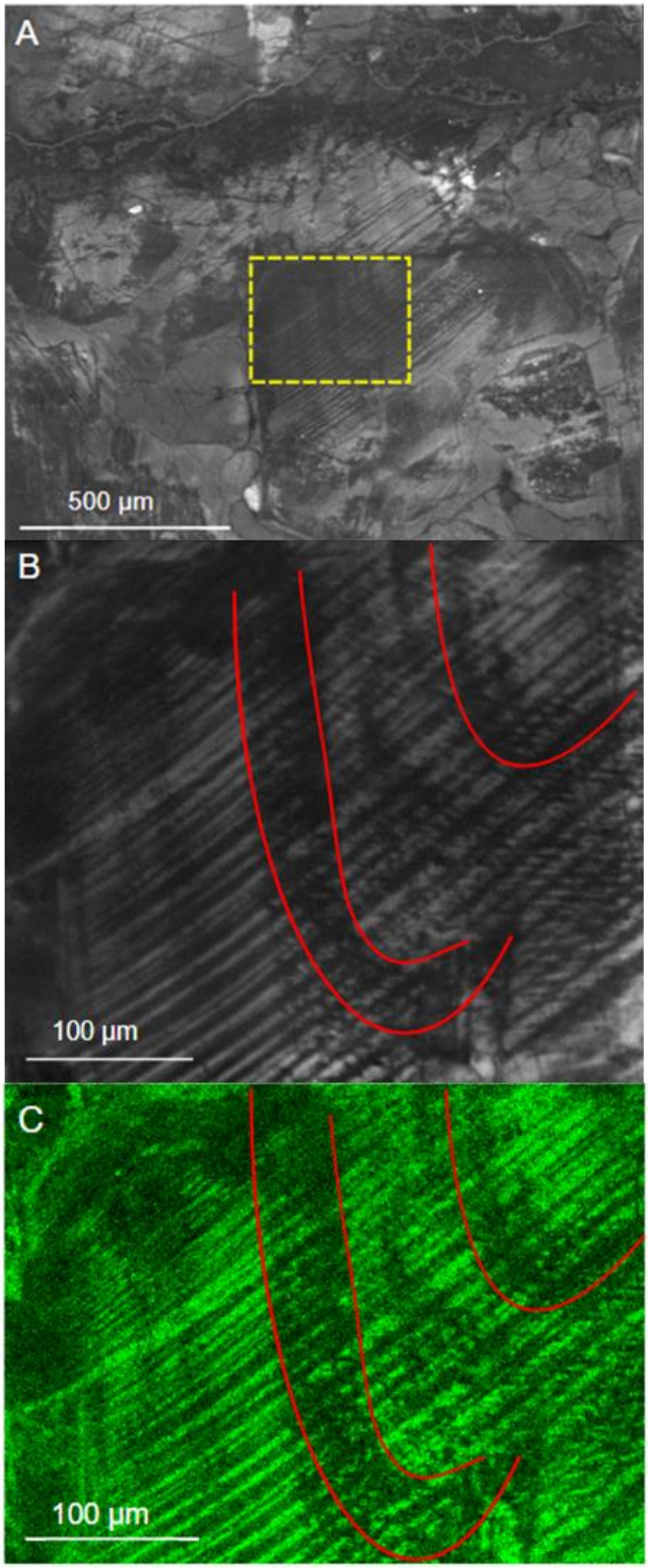

Figure 3.19 - CL images and an EDS map of an area of Site 1. A) CL image with yellow box highlighting the region investigated using EBSD. B) CL image of area of zoning. The red lines

highlight the outline of zoned areas. C) EDS map showing the distribution of Ca (green) for the same area of zoning. When comparing B and C, the same zoned bands can be seen both through the distribution of Ca content and as a feature on CL.

Compositional zoning is also evident at Site 11, located within the groundmass of CHX-1160.7 **Error! Reference source not found.**C, along the top edge of the thin section. This site contains a mixture of quartz and feldspar (both Na-rich and K-rich) in varying sizes from ~50–700 µm (**Error! Reference source not found.**A), as well as a mineral that is rich in Fe (approximately 500 µm) with Ca and Ti around the edge. In one of the Na-rich feldspars (around 340 µm long) there appears to be a decrease in Ca content in the centre of the sample. Selected points in this specific crystal (circled in blue in **Error! Reference source not found.**B) have been analysed using EPMA point spectra selection to determine composition of the location (**Error! Reference source not found.**). EPMA data confirms a noticeable decrease in Ca in the centre. It is, however, unclear whether this is zoning or water-mediated alteration resulting in a loss of Ca in the centre.

Table 3.7 - Normalised chemical composition (EPMA) of areas in Site 11 (in atomic percent (at. %). Chemical compositions are only given for major elements. These values have been converted from weight % and re-normalised. The point number correlates to the point locations in Figure 3.20B. The average and standard deviation (SD) have been calculated for these points.

				At. %			
Point #	Ca	Na	K	Si	Al	O	Other
1	0.58	7.36	0.07	22.28	8.29	61.37	0.05
2	0.01	7.91	0.01	23.01	7.61	61.44	0.01
3	0.17	7.44	0.09	22.65	8.09	61.48	0.08
4	0.03	7.83	0.01	23.05	7.59	61.48	0.01
5	1.19	6.74	0.08	21.86	8.67	61.41	0.05
Average	**0.40**	**7.46**	**0.05**	**22.57**	**8.05**	**61.44**	**0.04**
SD	**0.50**	**0.47**	**0.04**	**0.51**	**0.46**	**0.05**	**0.03**

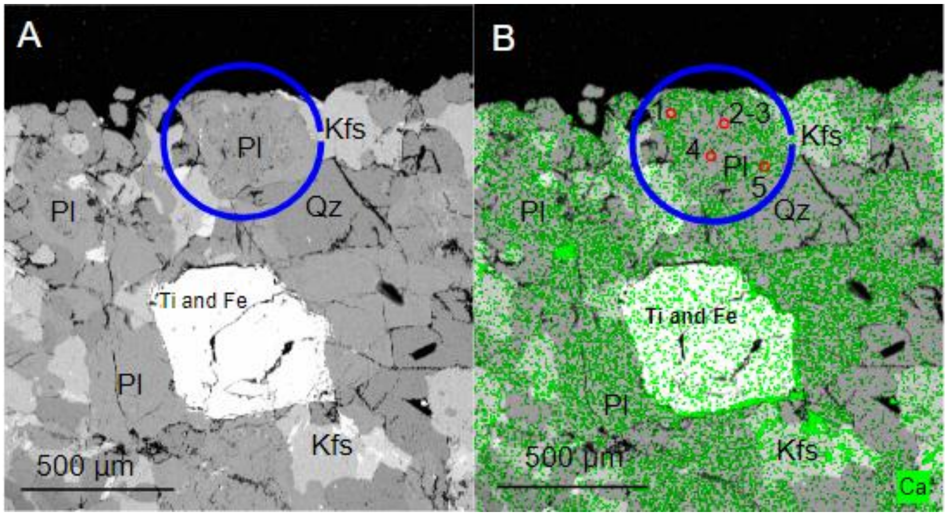

Figure 3.20 - BSE and EDS maps of Site 11. A) BSE image of Site 11. Blue circle highlights specific Na-rich feldspar which has appears in this image darker in the centre than around the rim. Pl=plagioclase, Kfs = K feldspar and Qz= quartz. B) False colour EDS map showing the distribution of Ca in green and showing the location of EPMA point spectra areas (numbers correlate to point numbers seen in Table 3.7). Note the irregular distribution of Ca.

3.2 Sample CHX-1199.6

3.2.1 Sample overview

Sample CHX-1199.6 was taken from a depth of 1199.6 mbsf. The sample is a granite containing relatively equal amount of K-rich (~35%) and Na-rich feldspar (~40%) as well as quartz (~20%). There are small amounts of other minerals including titanite, augite, and biotite which make up an estimated 5% of the sample. From the BSE image of this sample (**Error! Reference source not found.**A) a large gap can be seen to split the sample into two parts referred to as the upper and lower halves. Although the lower half is smaller than the upper, both contain the same lithologies. Most crystal boundaries for the minerals are irregular and, in some areas, unclear, and most crystals range in size from ~150 µm – 14 mm.

The sample was viewed under an optical microscope and definite shock features could not be seen. The main petrographic features that could be seen was twinning in the plagioclase feldspar, exsolution in the alkali feldspar and various fractures throughout the sample.

This sample was investigated using BSE and EDS maps as well as EPMA point spectral data from selected areas (methods discussed in sections 2 and 3.1.1). An EDS map (**Error! Reference source not found.**B) of the whole thin section shows areas rich in K (blue) and Na (red) as well as showing Ca content in green.

The EPMA data has been plotted in a ternary plot (**Error! Reference source not found.**) which shows the average Na-rich and K-rich feldspar compositions for each EPMA site (all sites including those used in EPMA are indicated in **Error! Reference source not found.**A). From this EPMA data, the Na-rich feldspar in thin section CHX-1199.6 has an average composition of 6.97 at. % Na, 2.12 at. % Ca, and 0.14 at. % K and the K-rich feldspar has an average composition of 0.45 at. % Na, 0.02 at. % Ca, and 7.38 at. % K. The SD for each sample point has been recorded in Appendix E. In cases where data is shown graphically (**Error! Reference source not found.**), calculated at. % uncertainty has been used for error bars (these error bars are sometimes smaller than the data point).

This sample was also examined using a polarising microscope but no notable features were observed and so these images have not been included in this thesis.

The sample shows signs of alteration or damage however some deformation features have been preserved. Much of the K-rich feldspar found in this sample appears to have exsolution. In some sites deformation features have been found in both K-rich and Na-rich feldspar as well as quartz (for example, Sites 1 and 3) however in other sites (such as Site 4) the feldspars (particularly Na-rich feldspar) contain more deformation features than the neighbouring quartz. These sites are all discussed in more detail in the following sections.

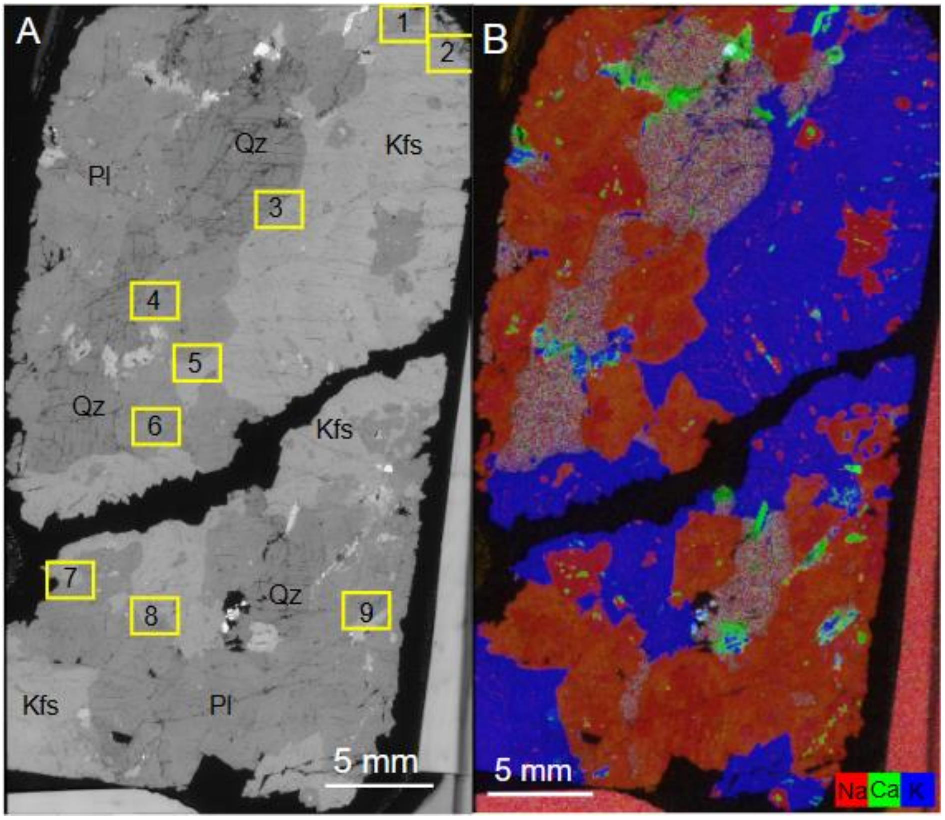

Figure 3.21 - Full thin section BSE image and EDS map of sample CHX-1199.6. A) BSE image of sample CHX-1199.6 with sample site locations labelled. Pl=plagioclase, Kfs = K feldspar and Qz= quartz. B) False coloured energy dispersive X-ray spectroscopy (EDS) map with Na, Ca, K in red, green, and blue respectively.

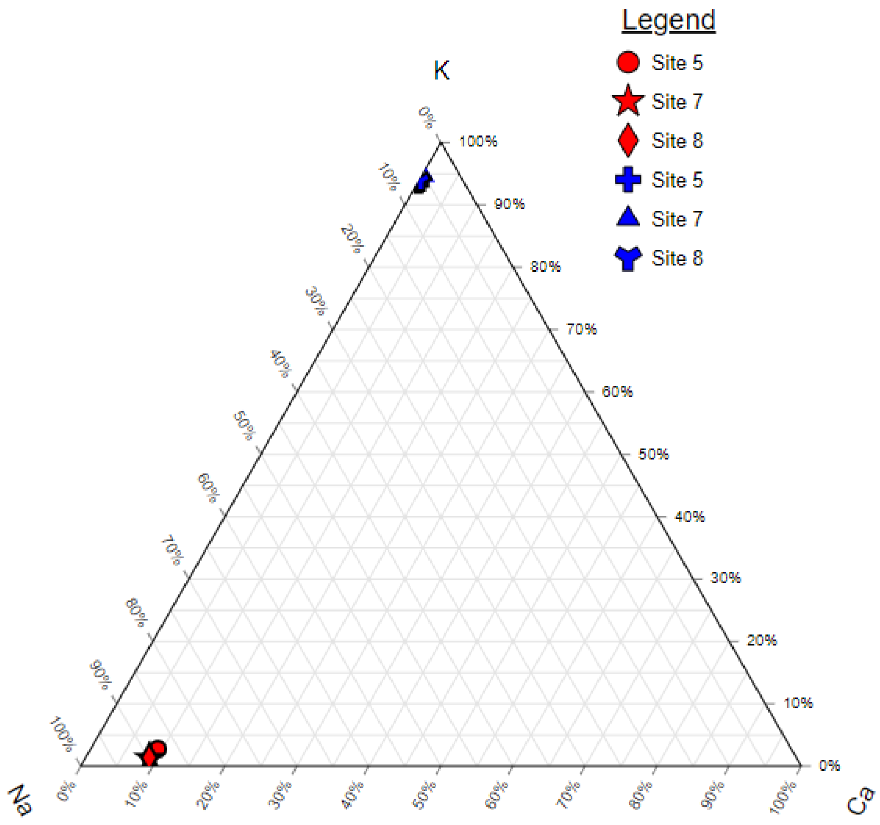

Made with TernaryPlot.com

Figure 3.22 - K-Na-Ca ternary plot showing the composition of feldspars in Figure 3.21A. Those points marked in red (circle, star, diamond) are Na-rich areas and those marked in blue (+, triangle and Y sign) are K-rich areas. Plot points are from EPMA point spectral analysis calculated average of Na-rich and K-rich feldspars per site. Full data recorded in Table 3.8, Table 3.9, and Table 3.10.

3.2.2 Specific deformation features in CHX-1199.6

3.2.2.1 K-rich vs Na-rich feldspar

Sample CHX-1199.6 contains both Na-rich and K-rich feldspar together comprising ~75% of the whole thin section. This has allowed these two types of feldspar to be compared side by side to determine whether one type contains more shock deformation features than the other.

Three locations that were selected to investigate deformation in different feldspars in sample CHX-1199.6 are Sites 5, 7, and 8. All three sites contain both Na-rich and K-rich feldspar. Site

5 is located near the bottom of the upper half of sample CHX-1199.6 (see **Error! Reference source not found.**) and the composition of both Na-rich and K-rich feldspar has been recorded in Table 3.8 as determined by EPMA (obtained from the selected regions in **Error! Reference source not found.**B). The K-rich feldspar comprises 7.36 at. % K and the Na-rich feldspar comprises 6.73 at. % Na. Site 7 is located in the top left of the lower half of sample CHX-1199.6 (**Error! Reference source not found.**). The chemical composition of both types of feldspar is reported in Table 3.9. The K-rich feldspar has an average of 7.49 at. % K and the Na-rich feldspar has an average of 7.10 at. % Na. An RGB EDS map of site 7 (**Error! Reference source not found.**B) shows the distribution of Na, Ca, and K and shows an uneven distribution of Ca across the Na-rich feldspar with more Ca being seen in the lower region of the image than the top right. Site 8 is located in the mid left of the lower half of sample CHX-1199.6 (see **Error! Reference source not found.**). One crystal of K-rich feldspar is about 600 µm long and the other feldspars are larger than the site. The chemical composition has been determined using EPMA data from selected sites (Table 3.10). In the Na-rich feldspar, there is a variation in Ca content across different areas of the site with boxes 1 and 6 containing >1 at. % Ca and other boxes containing <1 at. % Ca (Table 3.10).

Table 3.8 - Normalised chemical composition (EPMA) of the selected areas in Site 5 in atomic percent (at. %). Chemical compositions are only given for major elements. These values have been converted from weight % and re-normalised. The point number correlates to the point locations labelled in Figure 3.23B. Average and SD have been calculated from these points. Raw data (un-normalised wt.%) are reported in Appendix E.

	Point #	At. %						
		Ca	Na	K	Si	Al	O	Other
Na-rich feldspar	1a	0.79	7.06	0.06	22.11	8.50	61.42	0.06
	1b	0.34	7.30	0.04	22.64	8.10	61.53	0.05
	1c	0.46	7.18	0.22	22.37	8.24	61.41	0.13
	2a	1.26	6.57	0.13	21.70	8.89	61.41	0.04
	2b	1.21	6.69	0.15	21.74	8.81	61.38	0.03
	2c	0.87	6.58	0.19	22.17	8.59	61.56	0.03
	2d	1.07	6.72	0.14	21.91	8.70	61.43	0.03
	2e	0.98	6.78	0.12	22.17	8.43	61.48	0.04
	3a	0.12	6.15	0.08	23.60	7.80	62.21	0.05
	3b	0.70	7.21	0.06	22.38	8.19	61.44	0.02
	3c	0.03	7.30	1.87	22.37	7.60	60.81	0.02
	3d	0.30	7.52	0.07	22.74	7.87	61.46	0.04
	3e	0.41	7.47	0.07	22.57	8.03	61.43	0.03
	3f	0.48	7.29	0.13	22.50	8.12	61.44	0.04
	6a	0.93	5.61	0.08	22.66	8.60	62.08	0.04
	6b	1.02	5.54	0.09	22.48	8.76	62.04	0.07
	6c	1.17	5.37	0.08	22.36	8.91	62.06	0.04
Average		**0.71**	**6.73**	**0.21**	**22.38**	**8.36**	**61.56**	**0.04**
SD		**0.39**	**0.69**	**0.43**	**0.44**	**0.40**	**0.35**	**0.02**
K-rich feldspar	4a	0.02	0.51	7.21	23.07	7.64	61.53	0.03
	4b	0.01	0.43	7.36	23.01	7.67	61.49	0.02
	4c	0.01	0.32	7.42	23.02	7.69	61.51	0.03
	5a	0.01	0.85	7.27	22.86	7.66	61.33	0.03
	5b	0.01	0.48	7.38	23.09	7.54	61.48	0.03
	5c	0.01	0.41	7.50	23.00	7.62	61.44	0.03
Average		**0.01**	**0.50**	**7.36**	**23.01**	**7.64**	**61.46**	**0.03**
SD		**0.00**	**0.18**	**0.10**	**0.08**	**0.06**	**0.07**	**0.00**

Table 3.9 - Normalised chemical composition (EPMA) of the selected areas in Site 7 in atomic percent (at. %). Chemical compositions are only given for major elements. These values have been converted from weight % and re-normalised. The point number correlates to the point locations labelled in Figure 3.24. Averages and SD have been calculated from these points. Raw data (un-normalised wt.%) are reported in Appendix E.

		At. %						
	Point #	Ca	Na	K	Si	Al	O	Other
Na-rich feldspar	3a	0.35	7.47	0.25	22.65	7.88	61.38	0.04
	3b	0.23	7.53	0.06	22.79	7.87	61.48	0.03
	3c	0.14	7.78	0.04	22.88	7.71	61.43	0.03
	3d	0.24	7.63	0.06	22.74	7.83	61.42	0.09
	4a	1.14	6.70	0.17	22.05	8.47	61.44	0.04
	4b	1.11	6.72	0.17	21.92	8.63	61.41	0.04
	4c	1.12	6.52	0.19	22.00	8.63	61.50	0.04
	4d	1.13	6.64	0.23	22.01	8.52	61.43	0.04
	5a	1.43	6.42	0.05	21.66	8.93	61.46	0.04
	5b	1.36	6.50	0.05	21.69	8.91	61.45	0.04
	5c	1.45	6.25	0.11	21.56	9.10	61.48	0.06
	5d	1.47	6.44	0.07	21.64	8.89	61.44	0.05
	6a	0.30	7.39	0.08	22.64	8.04	61.48	0.07
	6b	0.74	7.09	0.07	22.12	8.52	61.42	0.05
	6c	0.36	7.51	0.05	22.63	7.99	61.44	0.04
	6d	0.14	7.64	0.05	22.83	7.83	61.47	0.04
	7a	0.26	7.60	0.06	22.67	7.94	61.42	0.05
	7b	0.36	7.41	0.11	22.58	8.03	61.43	0.08
	7c	0.43	7.31	0.07	22.55	8.10	61.47	0.08
	7d	0.43	7.48	0.08	22.52	8.04	61.40	0.07
Average		**0.71**	**7.10**	**0.10**	**22.31**	**8.29**	**61.44**	**0.05**
SD		**0.50**	**0.51**	**0.06**	**0.45**	**0.44**	**0.03**	**0.02**
K-rich feldspar	1a	0.02	0.31	7.55	23.05	7.54	61.46	0.07
	1b	0.02	0.26	7.53	23.09	7.56	61.50	0.05
	1c	0.01	0.29	7.55	23.07	7.56	61.48	0.04
	1d	0.01	0.20	7.75	23.03	7.54	61.43	0.05
	2a	0.03	0.34	7.39	23.02	7.67	61.51	0.04
	2b	0.04	0.41	7.44	22.96	7.65	61.44	0.06
	2c	0.02	0.91	7.36	22.85	7.57	61.26	0.03
	2d	0.01	0.47	7.36	23.09	7.55	61.49	0.03
Average		**0.02**	**0.40**	**7.49**	**23.02**	**7.58**	**61.45**	**0.05**
SD		**0.01**	**0.22**	**0.13**	**0.08**	**0.05**	**0.08**	**0.01**

Table 3.10 - Normalised chemical composition (EPMA) of the selected areas in Site 8 in atomic percent (at. %). Chemical compositions are only given for major elements. These values have been converted from weight % and re-normalised. The point number correlates to the point locations labelled in Figure 3.25. Averages and SD have been calculated from these points. Raw data (un-normalised wt.%) are reported in Appendix E.

		At. %						
	Point #	Ca	Na	K	Si	Al	O	Other
Na-rich feldspar	1a	1.37	6.35	0.10	21.63	9.03	61.48	0.05
	1b	1.11	6.83	0.07	21.96	8.59	61.42	0.03
	1c	1.15	6.66	0.09	21.92	8.69	61.46	0.04
	1d	1.20	6.58	0.12	21.92	8.67	61.47	0.05
	3a	0.33	7.56	0.05	22.69	7.91	61.44	0.03
	3b	0.22	7.74	0.10	22.69	7.84	61.36	0.06
	3c	0.10	7.71	0.07	22.93	7.70	61.46	0.05
	3d	0.15	7.43	0.15	22.56	8.19	61.45	0.07
	4a	0.24	7.58	0.07	22.81	7.79	61.46	0.07
	4b	0.22	7.44	0.05	22.78	7.92	61.51	0.08
	4c	0.29	7.42	0.09	22.68	7.96	61.47	0.10
	4d	0.22	7.47	0.21	22.63	7.95	61.40	0.11
	5a	0.89	7.04	0.08	22.04	8.52	61.39	0.05
	5b	0.50	7.26	0.10	22.47	8.17	61.45	0.05
	5c	0.69	7.23	0.09	22.34	8.20	61.41	0.05
	5d	0.90	6.87	0.12	22.10	8.50	61.44	0.06
	6a	0.91	6.86	0.16	22.10	8.49	61.44	0.04
	6b	1.09	6.48	0.21	22.12	8.52	61.53	0.05
	6c	1.24	6.52	0.10	21.90	8.69	61.48	0.07
	6d	1.11	6.61	0.11	21.96	8.69	61.49	0.05
Average		**0.70**	**7.08**	**0.11**	**22.31**	**8.30**	**61.45**	**0.06**
SD		**0.44**	**0.45**	**0.04**	**0.39**	**0.38**	**0.04**	**0.02**
K-rich feldspar	2a	0.01	0.23	7.51	22.91	7.80	61.48	0.09
	2b	0.01	0.37	7.40	23.06	7.60	61.50	0.06
	2c	0.02	0.52	7.35	23.09	7.50	61.47	0.05
	2d	0.02	0.52	7.39	23.03	7.56	61.44	0.04
	7a	0.01	0.45	7.28	23.12	7.57	61.53	0.04
	7b	0.02	0.59	6.63	23.30	7.64	61.77	0.06
	7c	0.02	0.56	7.29	22.99	7.64	61.46	0.04
	7d	0.04	0.41	7.55	23.02	7.50	61.41	0.08
Average		**0.02**	**0.46**	**7.30**	**23.06**	**7.60**	**61.51**	**0.06**
SD		**0.01**	**0.12**	**0.29**	**0.12**	**0.10**	**0.11**	**0.02**

Clear grain boundaries can be seen between the Na-rich and K-rich feldspars of Site 5 (**Error! Reference source not found.**A). The Na-rich feldspar at this site contains abundant fractures, some of which appear to be partially filled in with Ca-rich material. The K-rich feldspar by comparison shows little other than several irregular, faint narrow fractures and areas of exsolution. At Site 7 (**Error! Reference source not found.**A), the Na-rich feldspar contains a similar abundance of fractures to those seen at Site 5 and a set of planar features (marked by the yellow line) in the bottom area (which on the EDS map contained more Ca). The other Na-rich feldspar area, which contains less Ca, appears to be more weathered. The K-rich feldspar contains fractures and areas of exsolution. The BSE image for Site 8 (**Error! Reference source not found.**A) shows fractures in both Na and K-rich feldspar, however the Na rich feldspar also shows some planar features (labelled in yellow in **Error! Reference source not found.**A). The boundaries between the two different types of feldspar are angular in some regions but in other regions have become rounded and irregular. This suggests that parts of some of the crystals have recrystallised whereas other areas have maintained their original shape. There are also some small Ca and Fe rich minerals within the smaller Na-rich feldspar. These Ca-Fe phases (largest of which is 277 μm long) are rounded and irregular in shape, these are the brighter phases in **Error! Reference source not found.**.

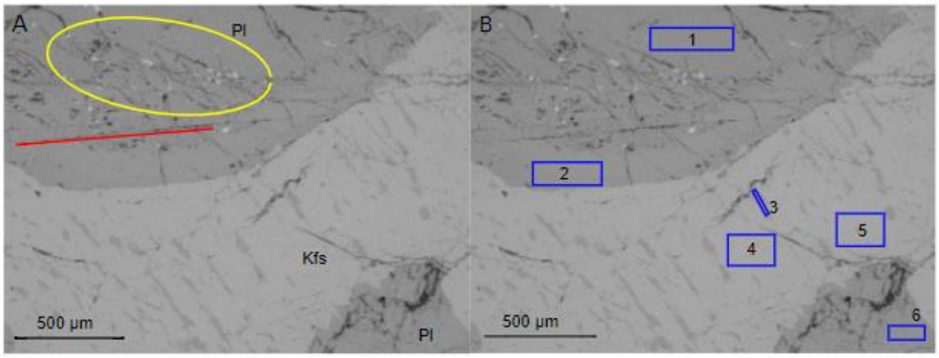

Figure 3.23 - BSE images of Site 5. Both images are of the same area and are as separate panels so as to make all annotations clear to see. A) BSE image of Site 5. Red line highlights planar feature and yellow circle shows fractures with infilled areas. Pl = plagioclase feldspar,

Kfs = K rich feldspar, Qz = Quartz. B) Locations of EPMA points spectral analysis. 3 points were analysed per area. Note box 3 is over an area of Na-rich exsolution. Data from these locations is reported in Table 3.8.

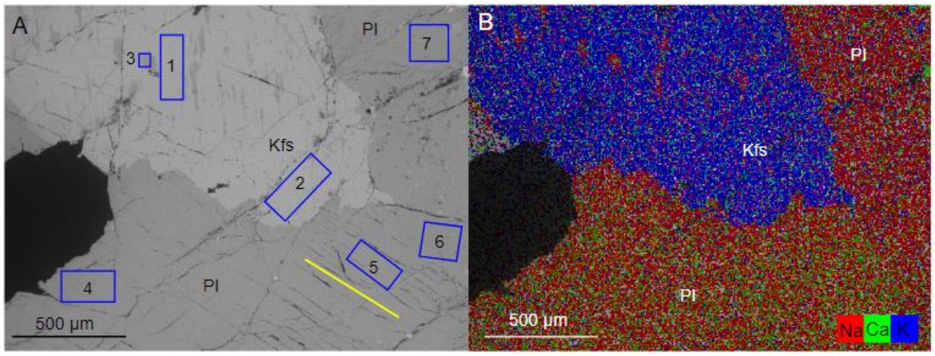

Figure 3.24 - BSE images and an EDS map of Site 7. Both BSE images are of the same field of view. A) BSE image of Site 7. Yellow line highlights planar feature. Pl = plagioclase feldspar, Kfs = K rich feldspar, Qz = quartz. B) A false colour EDS image showing the distribution of Na, Ca, and K content in red, green, and blue respectively. Note that there is more Ca in the Na-rich feldspar along the bottom of the image than in the top right. C) Locations of EPMA points spectral analysis. 4 spots analysed per area. Note box 3 is over an area of Na-rich exsolution. Data from these locations is recorded in Table 3.9.

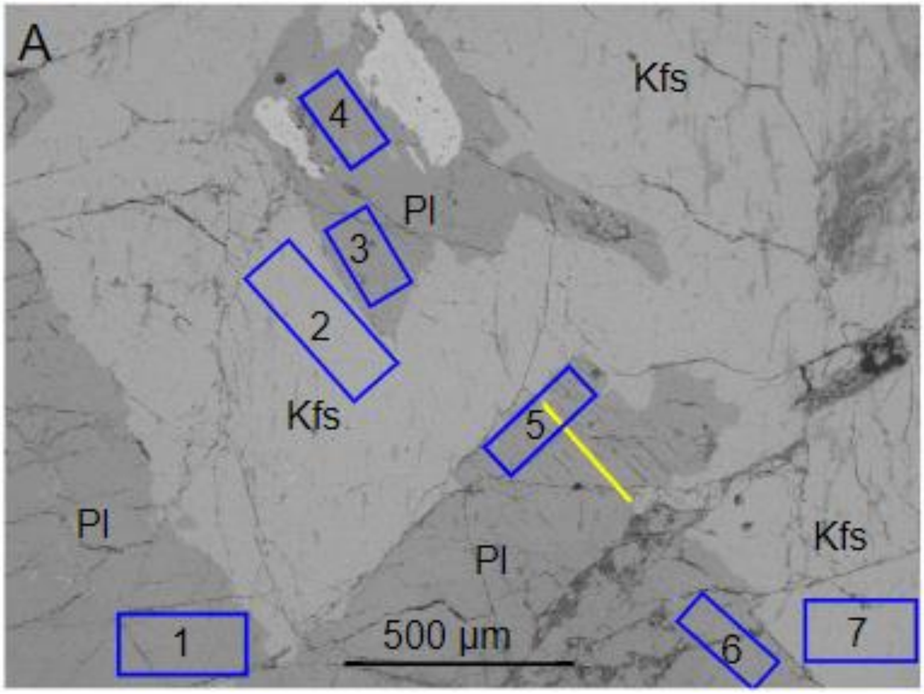

Figure 3.25 - BSE image of Site 8. A) BSE image of Site 8. Yellow line highlights planar feature in Na-rich feldspar. Pl = plagioclase feldspar, Kfs = K rich feldspar, Qz = Quartz. B) Locations of EPMA points spectral analysis. 4 spots analysed per area. Data from these locations is recorded in Table 3.10.

EPMA data is shown for a few areas of irregularity aswell from Site 5, for example box 3 (e.g point 3a) (**Error! Reference source not found.**). This is likely due to the fact that box 3 (as seen in **Error! Reference source not found.**C) is taken from a small area of exsolution and so may be differernt to the typical chemical compositions of Na rich feldspar recorded.

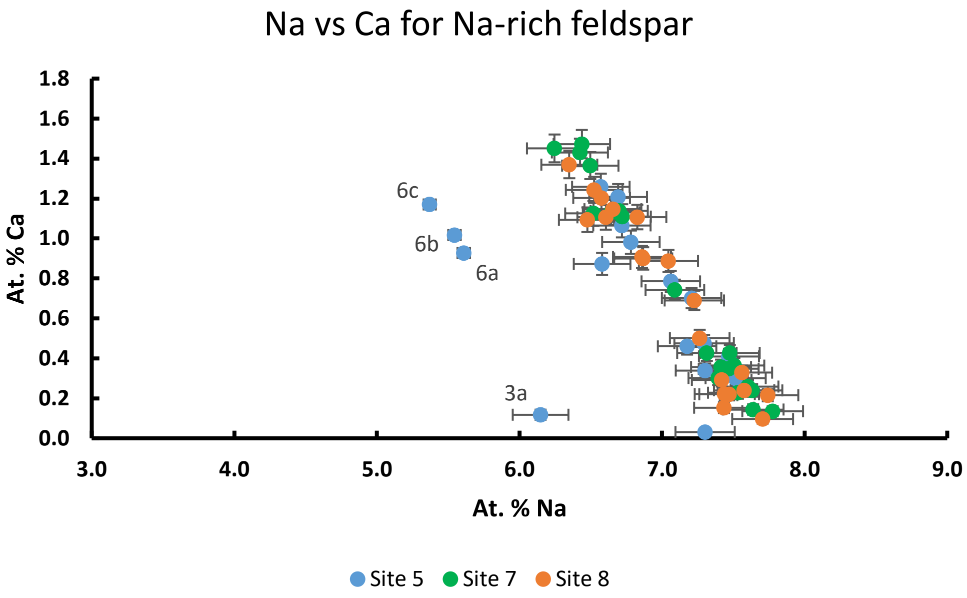

Figure 3.26 - Graph showing Na and Ca content in Na-rich feldspar from Sites 5, 7, and 8. Error bars have been made from calculated at. % for each point (Appendix E). See Table 3.8, Table 3.9, and Table 3.10 for the individual EPMA points data. Three points from Site 5 appear separate from the main group, point 3a is from an area of Na-rich exsolution in a K-rich area and points 6a, 6b, and 6c are from box 6 (Figure 3.23B), a different Na-rich crystal to the others recorded at Site 5.

One question that comes up when considering the differences between the deformation features found in Na and K-rich feldspar is whether the K-rich feldspar is lacking in features because less have formed or because deformation features have been lost post shock. A location that can help provide further insight into this is Site 2 of CHX-1199.6. Site 2 is located in the top right of the thin section. This site is mostly K-rich feldspar (estimated ~85%) (the composition is reported in Table 3.11). This K-rich feldspar contains around 7.4 at. % K, 1.1 at. % Na and 0.2 at. % Ca (Table 3.11). There are also regions of exsolution that are more Na-rich (spectrum 2 of Table 3.11).

Table 3.11 - Normalised chemical composition of Na and K-rich feldspar from Site 2 of sample CHX-1199.6. Spectra numbers correlate to areas marked by the blue boxes in Figure 3.27A) in atomic percent (at. %). These values have been normalised and have a 10% relative uncertainty. Data collected by EDS. Totals can be seen in Appendix C.

	At. %						
	Ca	Na	K	Si	Al	O	Other
Spectrum 1 (K-rich)	0.2	1.1	7.4	24.7	8.9	57.6	-
Spectrum 2 (Na-rich)	0.6	4.9	1.8	24	8.7	59.8	0.2

The BSE image at Site 2 shows K-rich feldspar with many areas of exsolution (**Error! Reference source not found.**A). This can also be seen in the EDS map which highlights the Na-rich regions of exsolution in the predominantly K-rich area (**Error! Reference source not found.**B). It also shows severe damage (perhaps water-mediated alteration) at the edge of the sample (top right). Despite this, a set of planar features can still be seen labelled by red lines in **Error! Reference source not found.**A. Large fractures can also be seen across this site, cutting across both exsolution patches and planar features. This indicates these fractures formed after exsolution and planar features.

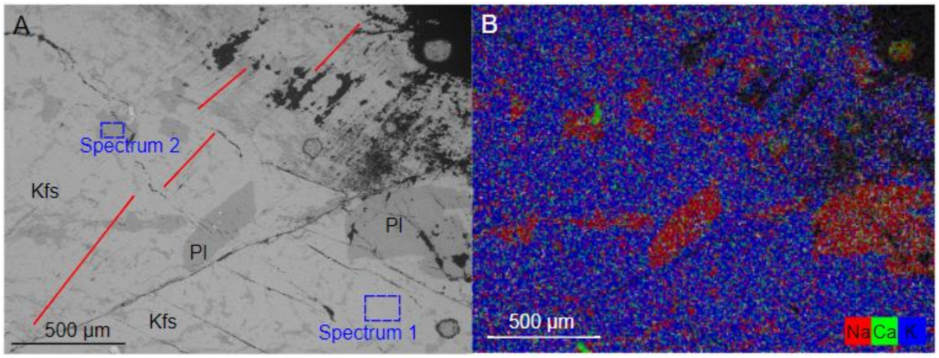

Figure 3.27 - BSE image and EDS map of Site 2. A) BSE image of Site 2. Red lines highlight orientation of planar features. Locations of EDS spectra are highlighted by blue boxes (results in Table 3.11). Pl = plagioclase feldspar, Kfs = K rich feldspar, Qz = Quartz. B) A false colour EDS image showing the distribution of Na, Ca, and K content in red, green, and blue respectively helps to further highlight the Na-rich and K-rich areas.

Therefore, overall, it can be observed that although there are some examples of deformation features being detected in K-rich feldspar (for example, Site 2), deformation features have formed more frequently in Na-rich feldspar.

3.2.2.2 Comparing feldspar to quartz

In some Sites in sample CHX-1199.6, there are different types of feldspar and quartz present. This allows direct comparisons to be made between shock deformation in feldspar and quartz from minerals that have experienced the same shock conditions. In sample CHX-1199.6, Sites 1, 3, 4, 6 and 9 all allow these comparisons to be made.

Site 1 for example contains both Na-rich and K-rich feldspar directly next to quartz. This site is located in the top right of sample CHX-1199.6 (**Error! Reference source not found.**A). The quartz crystal is ~1.37 mm long and up to 566 µm wide and there is a region that appears melt like ~1 mm wide containing Fe, Ca, and Mg. EDS data yields a K-rich feldspar composition of approximately 8.1 at. % K, 0.3 at. % Ca and 0.2 at. % Na and the Na-rich feldspar contains approximately 6.4 at. % Na, 1.3 at. % Ca and 0.7 at. % K (Table 3.12).

When examining the BSE image of this site, deformation features can be found in the different minerals with both types of feldspar and quartz containing fractures, some of which continue across crystal boundaries, and others remain within single crystals. The Na-rich feldspar shows some planar features (suspected twins) which are for the most part faint but in some areas are darker, more defined lamellae. Many of the fractures in this Na-rich feldspar are also in the same orientation as these suspected twins (red line in **Error! Reference source not found.**). In the neighbouring quartz there are also some fractures matching that orientation, the largest and most prominent of which have dark lines (blue line in **Error! Reference source not found.**) which emerge from these large fractures and are almost perpendicular to them. This may be a form of feather feature and a potential deformation feature. The K-rich feldspar contains many areas of exsolution as well as areas containing fractures. Some of these fractures cross-cut the exsolution. In some areas, the fractures appear to have been altered or infilled (particularly in the region highlighted by the yellow circle in **Error! Reference source not found.**) where they cross a region of exsolution. The K-rich feldspar also appears to have regions with very faint planar features (green circle in **Error! Reference source not found.**).

Table 3.12 - Normalised chemical composition of Na and K-rich feldspar from sample CHX-1199.6 for sites 1, 3, 4, 6, 9. Spectra numbers correlate to areas marked by the boxes in Figure 3.28, Figure 3.29, Figure 3.30) in atomic percent (at. %). These values have been normalised and have a 10% relative uncertainty. Data collected by EDS. Totals can be found in Appendix C.

		At. %						
Site	Spectrum	Ca	Na	K	Si	Al	O	Other
1	1 (Na-rich)	1.3	6.4	0.7	23.8	9.7	58.1	0.1
	2 (K-rich)	0.3	0.2	8.1	25.4	7.9	58	0.1
3	1 (K-rich)	0.3	0.8	7.1	24.5	7.8	59.4	0.2
	2 (Na-rich)	1.1	4	2.8	26.4	7.1	58.7	-
4	1 (Na-rich)	1.3	5.9	0.3	24.6	9.7	57.9	0.3
	2 (K-rich)	0.6	0.4	6.9	18.9	11.2	60.7	1.3
6	1 (Na-rich)	1.6	5.4	0.4	23.2	10.3	59.1	0.2
9	1 (Na-rich)	1.7	6.8	-	24	8.8	58.2	0.6

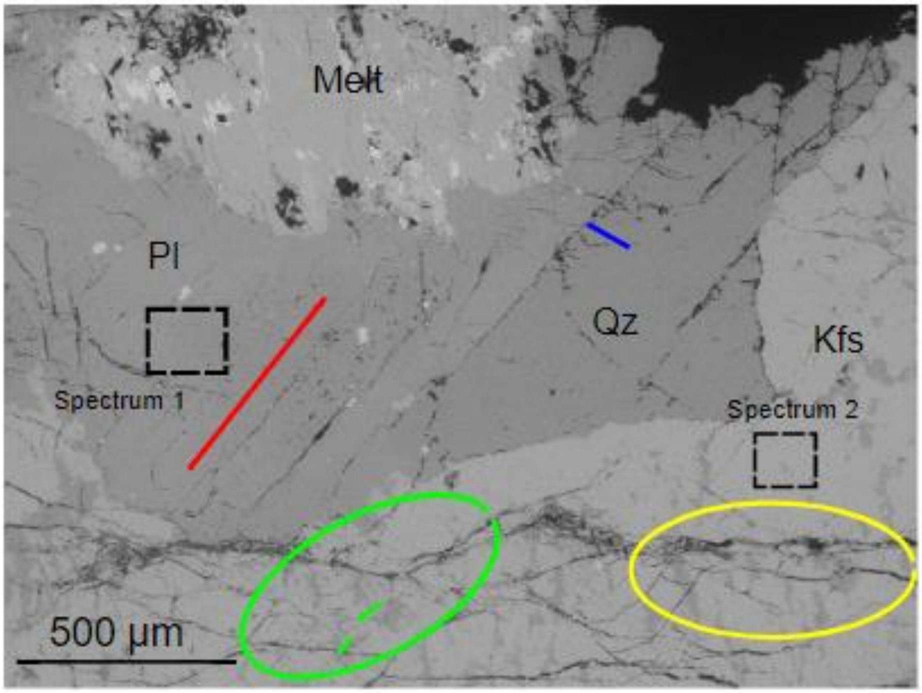

Figure 3.28 - BSE image of CHX-1199.6 Site 1. Red and blue lines highlight orientation of planar features and green circle highlights some faint planar features (orientation marked by green lines). Yellow circle highlights fracture where areas of Na-rich exsolution appear to fill in fractures slightly. Pl = plagioclase feldspar, Kfs = K-rich feldspar, Qz = quartz. Areas where EDS spectra were collected are highlighted by black boxes for chemical data quoted in Table 3.12.

Comparisons specifically between Na-rich feldspar and quartz have been made at Sites 4, 6, and 9. Site 4 is located in the middle left of the upper half of thin section CHX-1199.6 (**Error! Reference source not found.**). Most of this site comprises Na rich feldspar, with a region of quartz to the left as seen in **Error! Reference source not found.**A. The chemical composition of the Na-rich feldspar has been determined using EDS spectra from a selected area of Site 4 and contains 5.9 at. % Na, 1.3 at. % Ca, and 0.4 at. % K (spectrum 1 in Table 3.12). There is also a small area of K-rich feldspar which has angular boundaries and so is probably primary with a composition of 0.4 at. % Na, 0.6 at. % Ca, and 6.9 at. % K (spectrum 2 in Table 3.12). Both the quartz and the feldspar contain fractures however these fractures appear to be wider in the quartz than in the feldspar (**Error! Reference source not found.**A). The Na-rich feldspar also contains a set of planar features which are labelled by the red line, from which another set of planar features emanate (yellow line in **Error! Reference source not**

found.A). Much of this area appears to be weathered which may influence the deformation features seen.

Site 6 is located near the bottom of the upper half of thin section CHX-1199.6 (**Error! Reference source not found.**). The Na-rich feldspar and quartz in this Site both continue outside of the site field of view (**Error! Reference source not found.**B). The Na-rich feldspar contains around 5.4 at. % Na, 1.6 at. % Ca, and 0.4 at. % K based on EDS data (Table 3.12, spectrum 1). The BSE image (**Error! Reference source not found.**B) at this site shows a mostly undeformed quartz crystal, directly next to a large region of Na-rich feldspar which contains numerous fractures. Although fractures are not diagnostic of shock, the lack of fractures in the quartz still indicates that potential deformation features in this case have formed more readily in feldspar than quartz.

Site 9 is located in the mid right of the lower half of sample CHX-1199.6 (**Error! Reference source not found.**). This site contains Na-rich feldspar and quartz, as well as a melt like region containing Mg and Fe (**Error! Reference source not found.**C).

The quartz grain is about 7 µm wide and all other minerals are larger than the site field of view. The chemical composition has been determined using EDS data (Table 3.12). The Na-rich feldspar contains ~6.8 at. % Na and 1.7 at. % Ca (and no K). The Na-rich feldspar in this region contains multiple fractures, as does the quartz however the feldspar also contains an area of planar features in which alternate lamellae appear dark (and so may have been weathered). This alternating planar feature (marked yellow in the BSE image (**Error! Reference source not found.**C)) may be a form of deformation across alternating twins.

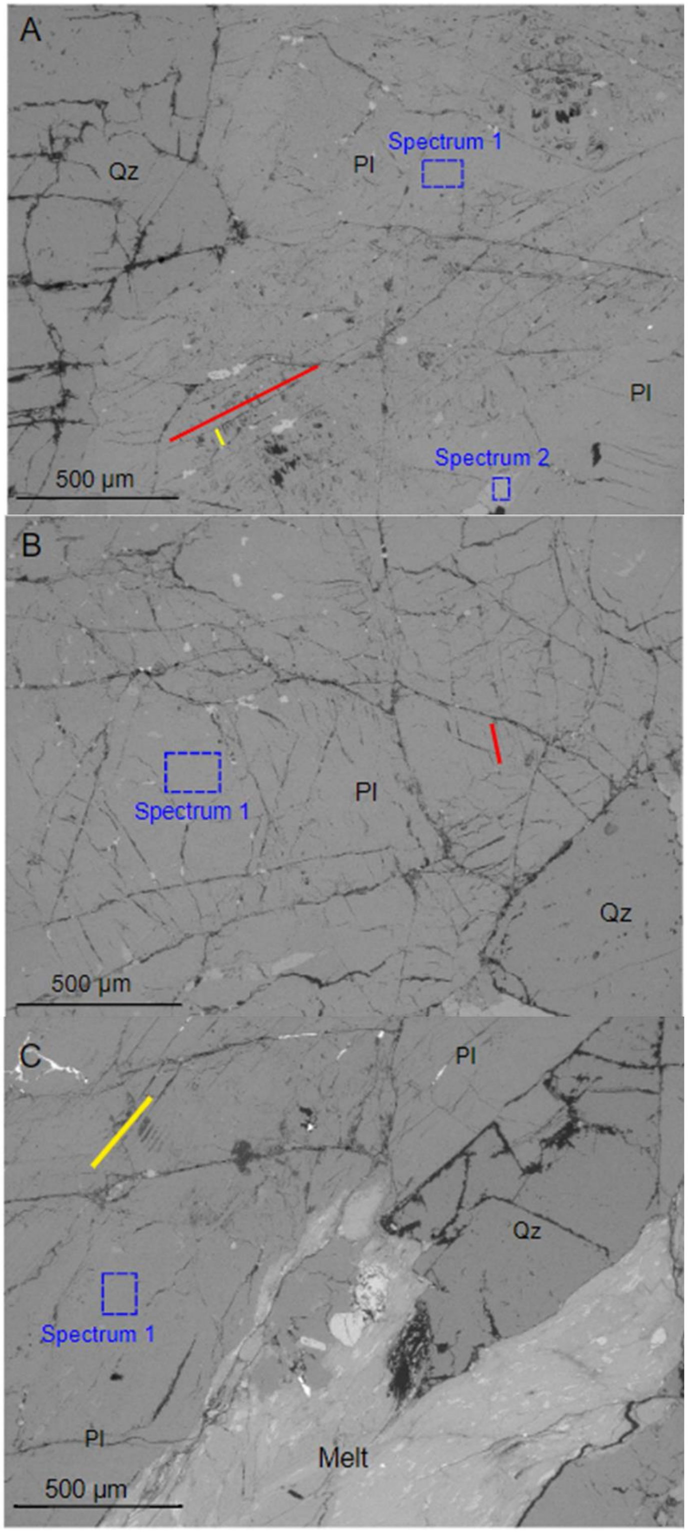

Figure 3.29 - BSE images of CHX-1199.6. Sites 4, 6, and 9. A) BSE image of CHX-1199.6 Site 4. Red and yellow lines highlight orientation of planar features in Na-rich feldspar. EDS spectra area highlighted by blue boxes for chemical data reported in Table 3.12. B) BSE image of Site 6. Red line highlights planar feature in Na-rich feldspar. Blue box highlights area for EDS spectra in Table 3.12. C) BSE image of Site 9. Yellow line highlights planar feature in Na-rich

feldspar. EDS spectra area highlighted by blue boxes for chemical data reported in Table 3.12. Pl = plagioclase feldspar, Kfs = K rich feldspar, Qz = Quartz.

At Site 3 a comparison can be made between K-rich feldspar and quartz. Site 3 is located in the upper half of sample CHX-1199.6 and shows part of a large grain boundary between quartz and K-rich feldspar grains that continue on beyond the field of view (**Error! Reference source not found.**). The chemical composition of the K-rich feldspar has been determined using EDS spectra from a selected area of Site 3 and contains 0.8 at. % Na, 0.3 at. % Ca, and 7.1 at. % K (spectrum 1 Table 3.12).

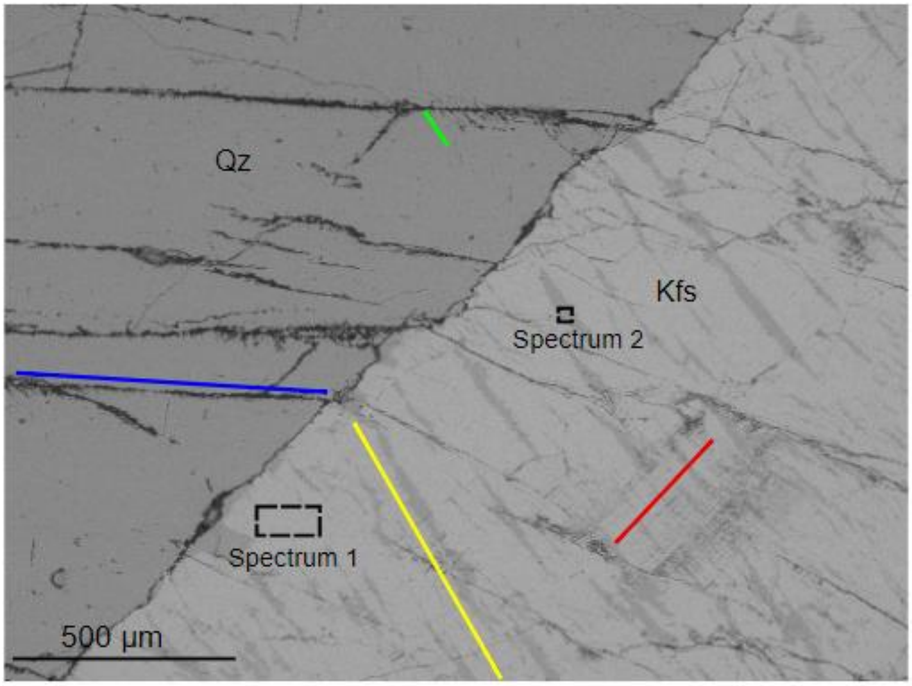

Figure 3.30 - BSE image of Site 3. Red and green lines highlight orientation of planar features in K-feldspar and quartz respectively. Blue line shows direction of fracture and yellow line shows orientation of elongated exsolution. Pl = plagioclase feldspar, Kfs = K rich feldspar, Qz = Quartz. EDS spectra area highlighted by black boxes for EDS spectra reported in Table 3.12.

The BSE image in **Error! Reference source not found.** shows fractures going across both the quartz and K-rich feldspar towards the grain boundary. Those fractures on the quartz side are likely planar fractures that have smaller planar features coming off them. The K-rich feldspar contains areas of exsolution which are all elongated in the same direction (yellow line in **Error! Reference source not found.**). Also seen in the K-rich feldspar is an area highlighted by the red line in **Error! Reference source not found.** which contains two sets of planar features at different orientations which appear to crosscut each other in an irregular order. Additionally, both sets of planar features appear to be controlled and contained by surrounding fractures.

3.3 Sample CHX-1216.5

3.3.1 Sample Overview

Sample CHX-1216.5 was taken from 1216.5 mbsf and a full BSE image and EDS map of the thin section can be seen in **Error! Reference source not found.**A. The sample was also analysed using a polarising microscope but due to the small size of the features investigated, most optical images do not provide sufficient spatial resolution and therefore have not been included in this thesis. A few examples of optical microscope images have been included in the Appendix. In which both plagioclase and alkali feldspar can be seen. The most obvious features that can be seen is twinning, exsolution and fracturing (and in some cases movement along these fractures). The large fracture down the centre divides the sample into two parts. The left part is mostly clast-rich impact melt rock and is often too altered to identify feldspars. The right-hand part of the thin section is granite, in which the feldspar contains many irregular fractures. This right-hand part of the thin section comprises an estimated 40% Na-rich feldspar, 30% K-rich feldspar, 20% quartz and 10% other minerals or regions of melt. Fractures appear more prevalent in the feldspars that are plagioclase than those that are alkali feldspar in composition. The alkali feldspar contains exsolution textures.

Some of the sites within CHX-1216.5 have been analysed using EPMA point spectral analysis (as highlighted in **Error! Reference source not found.**A). Full EPMA results including standard deviation (SD) are reported in Appendix E. Calculated at. % uncertainty has been used as error bars when data has been displayed graphically. These data have also been plotted on a ternary diagram (**Error! Reference source not found.**) in order to show the composition of Na-rich and K-rich feldspars found in the sample. From the EPMA data recorded, the average composition of the Na-rich feldspar in thin section CHX-1216.5 is 6.81 at. % Na, 0.62 at. % Ca, and 0.25 at. % and for K-rich feldspar is 0.54 at. % Na, 0.02 at. % Ca, and 6.55 at.% K.

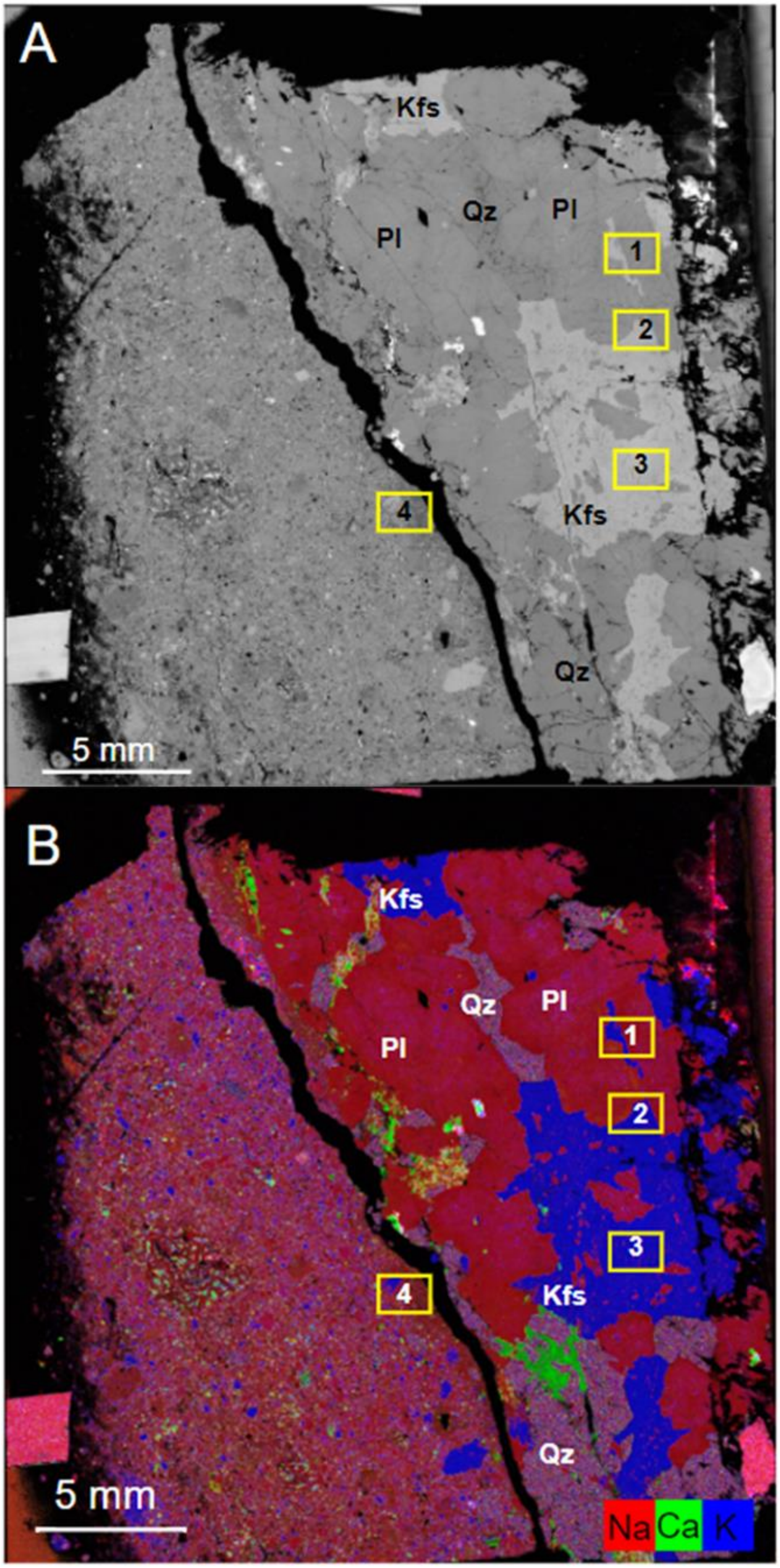

Figure 3.31 - BSE and EDS map of sample CHX-1216.5. A) BSE image of sample CHX-1216.5. Sample Site locations labelled with yellow boxes. B) False coloured energy dispersive X-ray

spectroscopy (EDS) map with Na, Ca, and K in red, green, and blue respectively. Pl = plagioclase feldspar, Kfs = K-rich feldspar, Qz = quartz.

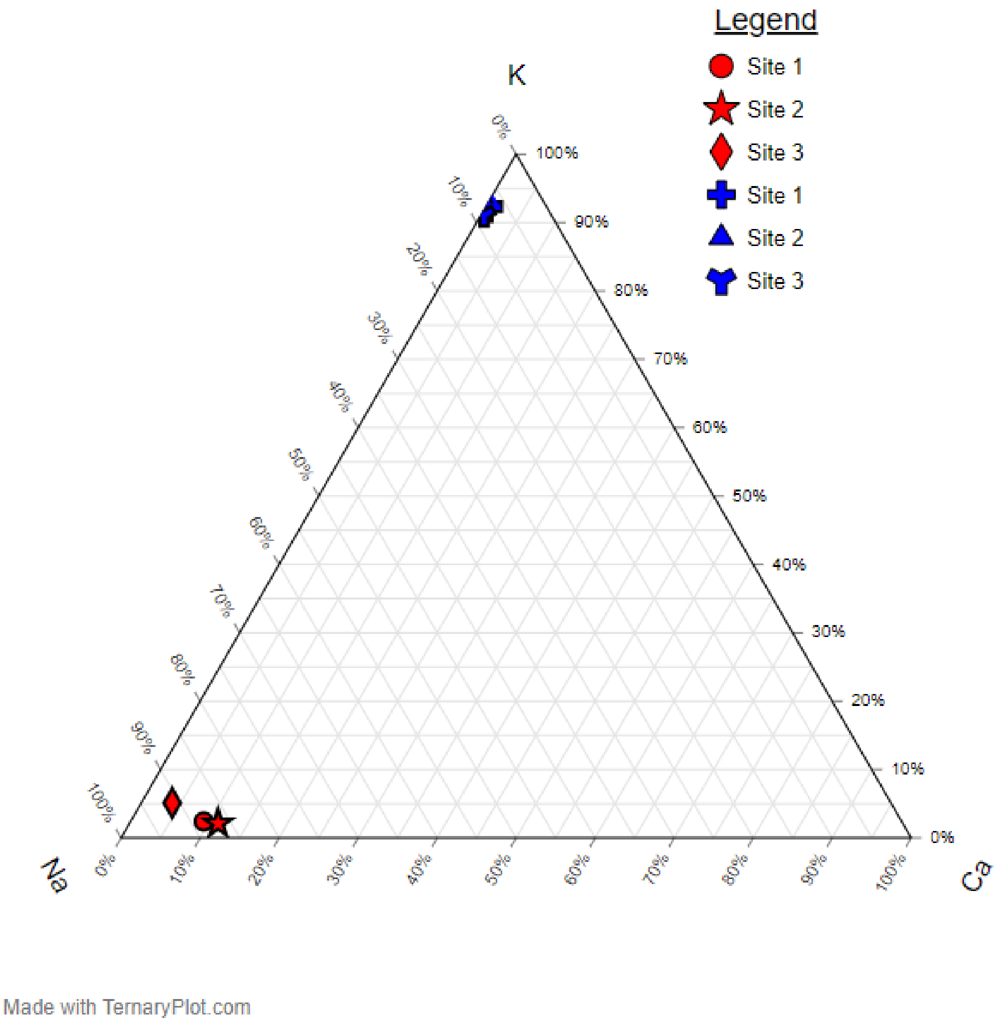

Figure 3.32 - K-Na-Ca ternary plot showing the composition of feldspars in sample CHX-1216.5 (as seen in Figure 3.31A). Those points marked in red (circle, star, diamond) are Na-rich areas and those marked in blue (+, triangle, Y) are K-rich areas. Plot points are from EPMA point spectral analysis calculated averages for sites that were analysed using EPMA. Note the Na-rich feldspar from Site 3 is exsolution.

3.3.2 Specific deformation features in CHX-1216.5

3.3.2.1 K-rich vs Na-rich feldspar

Much like sample CHX-1199.6, sample CHX-1216.5 is useful for comparing shock deformation features between K-rich and Na-rich feldspar because all four sites contain both types of feldspar. Sites 1 and 2 for example both contain Na-rich feldspar containing more evidence of deformation than the neighbouring K-feldspar. Site 1 is located in the upper right-hand side of sample CHX-1216.5 (**Error! Reference source not**

found.A). Both the Na-rich and K-rich feldspar grains continue beyond the site area (**Error! Reference source not found.**). Chemical composition has been observed using EPMA point spectral analysis and from this the Na-rich feldspar can be seen to contain an average of 6.73 at. % Na, 0.70 at. % Ca, and 0.18 at. % K (Table 3.13). The K-rich feldspar contains an average of 0.55 at. % Na, 0.01 at. % Ca, and 6.77 at. % K (Table 3.13). Additionally, the chemical distribution can be seen in an EDS map (**Error! Reference source not found.**B). EPMA data also shows that Ca content varies across the Na-rich feldspar areas, with points 1 and 4 (Table 3.13) containing around 1 at. % Ca greater than in other Na-rich samples. This can also be seen in **Error! Reference source not found.**B where an increase in Ca can be seen around the boundary between the right-hand Na-rich feldspar and the neighbouring K-rich feldspar. The K-rich feldspar (shown in **Error! Reference source not found.**A) has no obvious deformation features at all, whereas the Na-rich feldspar contains a large number of fractures. Some of these fractures appear to have a consistent orientation (marked by the red and yellow lines in **Error! Reference source not found.**A) and overlap to form a criss-cross pattern in the Na-rich feldspar on the right-hand side, these may be part of the mineral cleavage. There are also irregular fractures in this Na-rich feldspar. The K-rich feldspar in this site contains both angular and rounded boundaries.

Site 2 is located on the right-hand side of thin section CHX-1216.5 (**Error! Reference source not found.**A). The site contains both Na-rich and K-rich feldspar (**Error! Reference source not found.**A) and has been analysed using EDS (**Error! Reference source not found.**B) and EPMA point spectral analysis (Table 3.14). The K-rich feldspar contains an average of 0.49 at. % Na, 0.02 at. % Ca, and 6.65 at. % K, the Na-rich feldspar contains 6.62 at. % Na, 0.86 at. % Ca, and 0.16 at. % K (Table 3.14). At this site the K-rich feldspar shows areas of exsolution (yellow circle in **Error! Reference source not found.**A) but the only potential deformation features which can be seen are two small fractures where the K-rich feldspar meets the Na-rich feldspar. The Na-rich feldspar contains considerably more fractures as well as two sets of planar features at different orientations (marked by red and blue lines in **Error! Reference source not found.**A).

Table 3.13 - Normalised chemical composition (EPMA) of the selected areas in Na-rich and K-rich feldspar in Site 1 in atomic percent (at. %). Chemical compositions are only given for major elements. These values have been converted from weight % and re-normalised. The point number correlates to the point locations labelled in Figure 3.33A. Average and SD have been calculated from these points. Raw data (un-normalised wt.%) are reported in Appendix E.

	Point #	At. %						
		Ca	Na	K	Si	Al	O	Other
Na-rich feldspar	1a	1.25	6.34	0.14	21.69	9.02	61.49	0.07
	1b	1.32	6.59	0.05	21.64	8.95	61.42	0.03
	1c	1.32	6.64	0.10	21.59	8.95	61.36	0.04
	2a	0.32	7.52	0.03	22.60	8.04	61.44	0.05
	2b	0.21	5.18	0.67	21.56	10.34	61.92	0.12
	2c	0.25	6.92	0.82	22.15	8.45	61.27	0.14
	4a	1.38	6.33	0.15	21.65	8.97	61.47	0.05
	4b	1.24	6.41	0.14	21.88	8.78	61.52	0.04
	4c	1.26	6.40	0.16	21.85	8.80	61.50	0.04
	6a	0.28	7.33	0.13	22.71	8.00	61.50	0.05
	6b	0.18	6.37	0.09	22.17	9.29	61.81	0.09
	6c	0.45	7.06	0.04	22.56	8.29	61.60	0.02
	8a	0.46	7.36	0.08	22.41	8.17	61.40	0.12
	8b	0.30	7.26	0.05	22.67	8.09	61.55	0.08
	8c	0.35	7.24	0.12	22.59	8.13	61.50	0.08
Average		**0.70**	**6.73**	**0.18**	**22.11**	**8.69**	**61.52**	**0.07**
SD		**0.51**	**0.61**	**0.23**	**0.44**	**0.63**	**0.16**	**0.04**
K-rich feldspar	3a	0.00	0.65	6.81	23.12	7.74	61.64	0.05
	3b	0.00	0.60	6.78	23.08	7.83	61.67	0.04
	3c	0.00	0.52	6.90	23.14	7.74	61.66	0.03
	5a	0.01	0.61	6.57	23.24	7.74	61.78	0.04
	5b	0.01	0.61	6.68	23.22	7.71	61.73	0.04
	5c	0.02	0.62	6.47	23.21	7.83	61.80	0.05
	7a	0.03	0.47	7.00	23.10	7.73	61.63	0.04
	7b	0.02	0.47	6.77	23.16	7.81	61.74	0.03
	7c	0.01	0.40	6.92	23.25	7.66	61.73	0.03
Average		**0.01**	**0.55**	**6.77**	**23.17**	**7.75**	**61.71**	**0.04**
SD		**0.01**	**0.09**	**0.17**	**0.06**	**0.06**	**0.06**	**0.01**

Table 3.14 - Normalised chemical composition (EPMA) of the selected areas in Na-rich and K-rich feldspar in Site 2 in atomic percent (at. %). Chemical compositions are only given for major elements. These values have been converted from weight % and re-normalised. The point number correlates to the point locations labelled in Figure 3.34A. Averages and SD have been calculated from these points. Raw data (un-normalised wt.%) are reported in Appendix E.

		At. %						
	Point #	Ca	Na	K	Si	Al	O	Other
Na-rich feldspar	1a	1.30	6.17	0.14	21.78	8.99	61.58	0.04
	1b	1.29	6.15	0.27	21.84	8.86	61.54	0.05
	1c	1.30	6.42	0.09	21.75	8.90	61.49	0.04
	3a	1.31	6.09	0.19	21.74	9.05	61.58	0.04
	3b	1.34	6.20	0.19	21.69	9.01	61.52	0.04
	3c	1.09	6.19	0.20	21.87	9.00	61.60	0.04
	4a	0.47	6.49	0.11	22.27	8.87	61.72	0.06
	4b	1.31	6.27	0.14	21.76	8.93	61.52	0.05
	4c	1.34	6.16	0.18	21.66	9.08	61.53	0.05
	6a	0.11	7.32	0.22	22.88	7.88	61.54	0.06
	6b	0.12	7.40	0.13	22.87	7.89	61.54	0.05
	7a	0.06	7.56	0.12	22.93	7.80	61.51	0.03
	7b	0.10	7.63	0.11	22.81	7.87	61.46	0.02
Average		**0.86**	**6.62**	**0.16**	**22.14**	**8.63**	**61.55**	**0.04**
SD		**0.58**	**0.61**	**0.05**	**0.53**	**0.54**	**0.06**	**0.01**
K-rich feldspar	2a	0.03	0.68	6.53	23.22	7.75	61.76	0.03
	2b	0.02	0.67	6.52	23.23	7.76	61.77	0.03
	2c	0.01	0.53	6.66	23.30	7.68	61.79	0.04
	5a	0.01	0.30	6.78	23.32	7.73	61.83	0.03
	5b	0.03	0.47	6.55	23.22	7.86	61.84	0.03
	5c	0.01	0.31	6.83	23.29	7.72	61.81	0.04
Average		**0.02**	**0.49**	**6.65**	**23.26**	**7.75**	**61.80**	**0.03**
SD		**0.01**	**0.17**	**0.13**	**0.04**	**0.06**	**0.03**	**0.00**

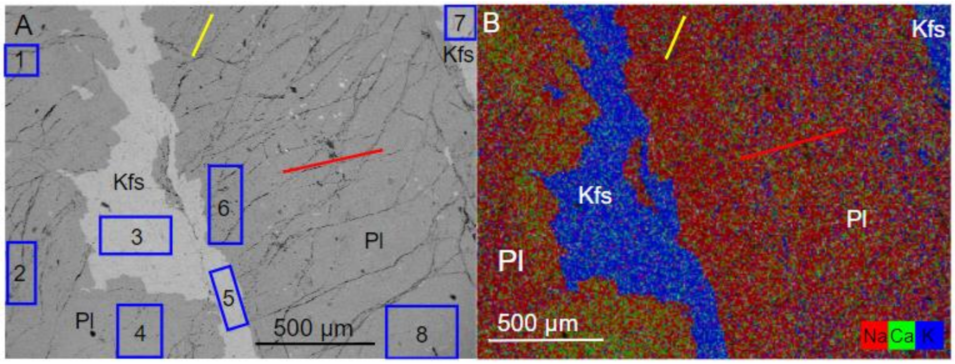

Figure 3.33 - BSE and EDS map of Site 1 in thin section CHX-1216.5. A) BSE image of Site 1. Red and yellow lines highlight orientation of features. Note that in comparison to the Na-rich feldspar, the K-rich feldspar contains few features. Locations of EPMA point spectral analysis marked with blue boxes (3 points analysed per box). Data from these locations is reported in Table 3.13. Pl = plagioclase feldspar, Kfs = K-rich feldspar, Qz = quartz. B) A false colour EDS image showing the distribution of Na, Ca, and K content in red, green, and blue respectively. The distribution of Ca in the Na-rich feldspar is uneven with greater Ca content (increased green) seen in the left-hand side Na-rich feldspar along the boundary with the K-rich feldspar.

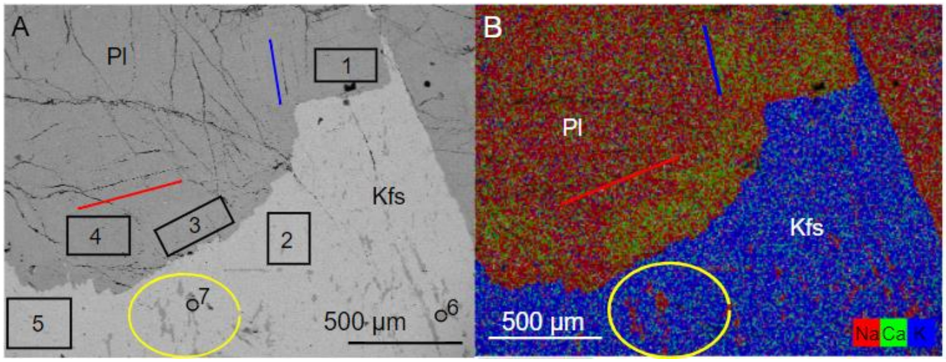

Figure 3.34 - BSE and EDS map of Site 2 from thin section CHX-1216.5. A) BSE image of Site 2. Red and blue lines highlight orientation of planar features. Yellow circle highlights some regions of exsolution. Locations of EPMA point spectral analysis marked by black boxes. Data from these locations is reported in Table 3.14. B) A false colour EDS image showing the distribution of Na, Ca, and K content in red, green, and blue respectively. Note that there is an increase in Ca in the Na-rich feldspar near the boundary with K-rich feldspar. Pl = plagioclase feldspar, Kfs = K-rich feldspar, Qz = Quartz.

Site 3 is located in the right-hand side of sample CHX-1216.5 (**Error! Reference source not found.**A). The site is made up of mostly K-rich feldspar with areas of Na-rich feldspar exsolution (**Error! Reference source not found.**). This K-rich feldspar contains an average of 0.58 at. % Na, 0.03 at. % Ca and 6.23 at. % K based on EPMA point spectral analysis (Table 3.15). The compositional data for areas of exsolution is recorded in Table 3.15. There is also a large fracture going across this site (marked by the red line in **Error! Reference source not found.**) along which the areas of exsolution appear to be displaced, suggesting that the fracturing occurred after exsolution occurred.

Table 3.15 - Normalised chemical composition (EPMA) of the selected areas in Na-rich and K-rich feldspar in Site 3 in atomic percent (at. %). Chemical compositions are only given for major elements. These values have been converted from weight % and re-normalised. The point number correlates to the point locations labelled in Figure 3.35. Average and SD have been calculated from these points. Raw data (un-normalised wt.%) are reported in Appendix E.

		At. %						
	Point #	Ca	Na	K	Si	Al	O	Other
Na-rich feldspar	1a	0.20	6.18	0.96	22.04	8.93	61.49	0.20
	1b	0.17	7.56	0.05	22.85	7.81	61.49	0.08
	1c	0.17	6.78	1.00	22.11	8.50	61.25	0.19
	3a	0.21	7.44	0.20	22.60	8.06	61.42	0.07
	3b	0.40	7.34	0.12	22.48	8.17	61.43	0.05
	3c	0.67	7.15	0.07	22.29	8.34	61.44	0.03
Average		**0.30**	**7.07**	**0.40**	**22.40**	**8.30**	**61.42**	**0.10**
SD		**0.20**	**0.52**	**0.45**	**0.31**	**0.39**	**0.09**	**0.07**
K-rich feldspar	2a	0.02	0.79	5.99	23.10	8.01	61.83	0.26
	2b	0.01	0.46	6.31	23.04	8.09	61.82	0.25
	2c	0.02	0.56	6.37	23.05	7.98	61.76	0.27
	4a	0.03	0.71	6.18	23.18	7.89	61.82	0.18
	4b	0.05	0.47	6.27	23.05	8.08	61.85	0.22
	4c	0.04	0.50	6.25	23.13	8.02	61.87	0.19
Average		**0.03**	**0.58**	**6.23**	**23.09**	**8.01**	**61.82**	**0.23**
SD		**0.01**	**0.14**	**0.13**	**0.05**	**0.07**	**0.04**	**0.04**

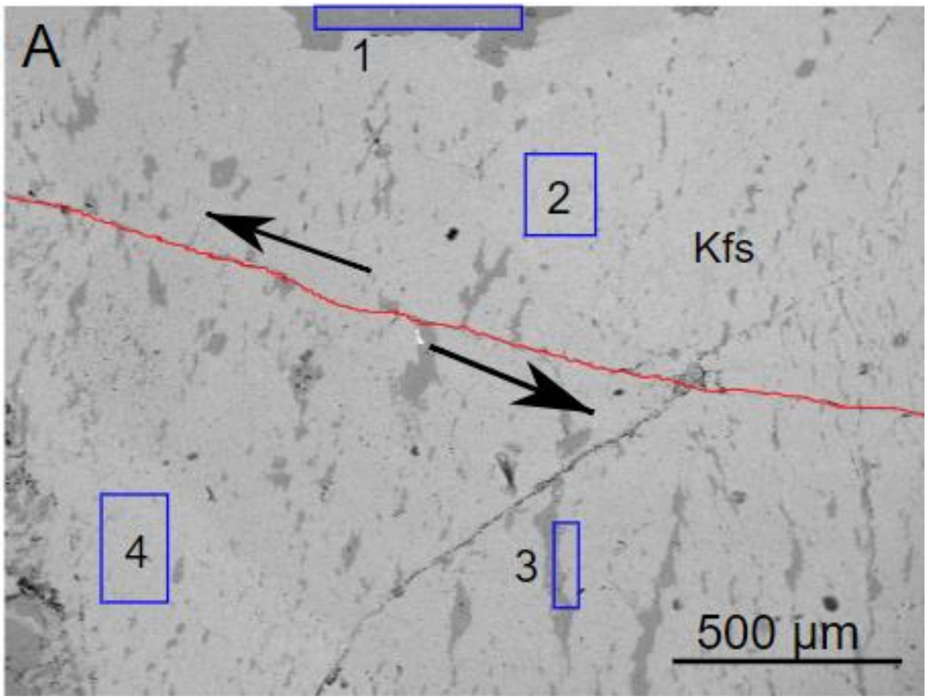

Figure 3.35 - BSE image of Site 3 from thin section CHX-1216.5. Red line follows fracture along which areas of exsolution have been shifted away from each other (shifting direction illustrated by arrows). Locations of EPMA point spectral analysis in blue boxes (3 points analysed per box). Data from these locations is recorded in Table 3.15. Pl = plagioclase feldspar, Kfs = K-rich feldspar, Qz = quartz.

Site 4 is from the left side (impact melt side) of sample CHX-1216.5 (**Error! Reference source not found.**A). It shows a K-rich feldspar crystal with a reasonably intact crystal shape surrounded by groundmass with melt material. Joined to this K-rich feldspar is a bit of Na-rich feldspar which appears to be devoid of features, which is in contrast to most other Na-feldspar observations in this thesis. This crystal demonstrates similar fractures and areas of exsolution to the alkali feldspar found in the granite (right) side of the sample (**Error! Reference source not found.**A). Compositional data has been reported using EDS (Table 3.16).

Table 3.16 - Normalised chemical composition of the selected areas in Site 4 of thin section CHX-1216.5 (marked by the blue boxes in Figure 3.36A) in atomic percent (at. %). These values have been normalised and have a 10% relative uncertainty. Data collected by EDS.

	At. %						
	Ca	Na	K	Si	Al	O	Other
Spectrum 1 (Na-rich)	0.7	6.7	0.5	24.9	9.3	57.7	0.1

Spectrum 2 (K-rich)	0.1	0.3	6.9	25.5	9.4	57.6	0.2

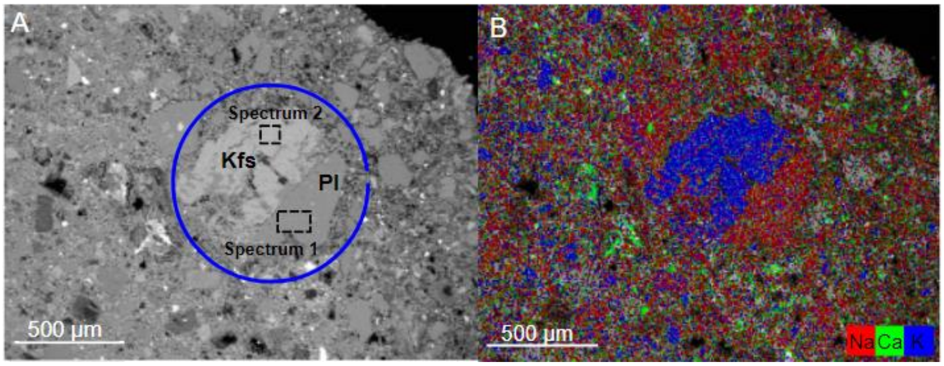

Figure 3.36 - BSE and EDS maps of Site 4 sample CHX- 1216.5. A) BSE image of Site 4. Blue circle around main feldspar crystal. Black boxes highlight area for EDS spectra in Table 3.16. B) A false colour EDS image showing the distribution of Na, Ca, and K content in red, green, and blue respectively. Pl = plagioclase feldspar, Kfs = K-rich feldspar.

3.4 Results summary – comparing across samples

When comparing samples CHX-1060.7, CHX-1199.6, and CHX-1216.5, it is clear that deformation features have formed more in Na-rich feldspar rather than K-rich feldspar. While areas of Na-rich feldspar have shown regions of potential planar deformation features as well as numerous fractures, K-rich feldspar appears in some regions to be largely lacking in deformation features. Both primary K-rich feldspar and recrystallised K-rich feldspar have been detected across the different samples however, both types are noticeably lacking in shock deformation features.

EBSD shows that in some Na-rich regions, alternating twins have become partially amorphised (as determined by the faintly present but unindexed Kikuchi patterns) whilst their neighbouring twins have remained crystalline. At the same partially amorphised areas, the Ca content appears to be even lower (~1 at. % less) than the lowest amount (~1.5 - 2 at. %) recorded in the crystalline regions.

CHX-1060.7 has been investigated using a wider range of methods than the other two samples because preliminary investigations revealed more deformation features within the large plagioclase crystal known as C1. It is from here that deformation in alternating twins was identified and the associated change in Ca and Na content detected.

Table 3.17 - Average EPMA showing overall average composition of Na-rich and K-rich feldspar in all three thin sections.

		Average compositions from EPMA data (at. %)		
Thin section	Na or K-rich feldspar	Na	Ca	K
CHX-1160.7	Na-rich	6.49	1.2	0.11
CHX-1160.7	K-rich	0.38	0.01	6.5
CHX-1199.6	Na-rich	6.97	2.12	0.4
CHX-1199.6	K-rich	0.45	0.02	7.38
CHX-1216.5	Na-rich	6.81	0.62	0.25
CHX-1216.5	K-rich	0.54	0.02	6.55

The average chemical compositions of the Na-rich and K-rich feldspar from each thin section is recorded in **Error! Reference source not found.**. From this table it is clear that all three thin sections had feldspar had both K-rich feldspars of similar compositions and Na-rich feldspars of similar compositions, however CHX-1199.6 has Na-rich feldspar which contains a slightly higher average level of Ca (2.12 at. % Ca) compared to that of the other two thin sections (1.2 at. % Ca and 0.62 at. % Ca). The compositions of these three samples are close enough to each other to allow for reasonable comparisons to be made across the different thin sections as they form the same types of feldspars.

One of the samples (sample CHX-1216.5) is divided into two parts; granite and clast rich impact melt rock. Most of this thesis has focused on the granite half of this sample (as this project has been studying feldspars). It is worth pointing out however that the fact that the granite in this sample shows similar shock features to the other two samples. This suggests that the granite in CHX-1216.5 does not appear to have been affected by being next to impact melt rock.

4 Discussion

This study examined shocked feldspar samples from the Chicxulub impact structure and examined these samples using a range of different methods (optical microscopy, scanning electron microscopy (SEM) backscatter electron images (BSE), energy dispersive X-ray spectroscopy (EDS), electron backscatter diffraction (EBSD), cathodoluminescence (CL) and electron probe micro-analysis (EPMA). From this thesis four main discussion points were identified: 1) no obvious variation in shock deformation features across depth, 2) variation in shock deformation features based on the feldspar composition, 3) shock barometry, and 4) deformation within alternating twins. These points are discussed below.

4.1 No obvious difference in deformation across depth

When comparing across the three samples examined in this thesis qualitative visual evaluation of the density of shock deformation features revealed that there was no trend between the density or type of shock deformation features with depth in the drill core. This finding would be expected as there is only a small depth interval. Any difference in the abundance of deformation features that was found across these three samples was also connected to a change in composition of the host mineral (see sections 4.2 and 4.4.2) rather than depth. The samples examined in this thesis were all relatively close in depth within the core, ranging from 1160.7 mbsf to 1216.5 mbsf, covering a distance of 55.8 m. Previous research, for example, both at the Chicxulub and Bosumtwi impact structures, has suggested a change in shock pressure and associated deformation with depth within an impact crater (Ferrière et al., 2008; Feignon et al., 2020). However, these studies occurred over a much larger depth interval (~567.5 m at Chicxulub and ~179.8 m at Bosumtwi) than the depth range covered by the samples in this thesis (~55.8 m). A study that specifically looked at shocked quartz in Chicxulub, covered a depth range of 567.5 m (Feignon et al., (2020)) (from 743.6 mbsf to 1311.1 mbsf, using samples from Expedition 364 – the same expedition from which the samples in this thesis were obtained). Feignon et al., (2020) found that, as depth increased, there was a slight shock attenuation (with pressure estimates falling from ~18 to ~16 GPa). This reduction of shock effects with increasing depth was found through the observation of the number of sets of PDFs in quartz (with PDFs of specific orientations being found indicating higher shock pressures) in samples ranging from 743.6 mbsf to 1311.1 mbsf. This sampling range overlaps the depths at which the samples in this thesis were collected, however only shows a trend over a distance of ~500 m approximately ten times greater than examined in this thesis (~50 m). Thus, previous studies suggest that the shock wave attenuated at a rate of ~1 GPa/ 280 m (Feignon et al., 2020). Therefore, it is unsurprising that no variation in shock pressure and associated microstructure was observed in this thesis. It is therefore recommended that the literature quoted above are a more accurate source of referral for considering variation in shock features across depth.

4.2 Feldspar composition and shock effects

There are fewer deformation features in the K-rich feldspar than in the Na-rich feldspar. This is particularly noticeable in samples CHX-1199.6 and CHX-1216.5 which both contain Na and K-rich feldspar that are adjacent to each other. These two feldspars are likely to have experienced the same shock conditions (pressure, temperature). However, EBSD, BSE optical microscopy and SEM-EDS data show that they record different shock features. This is seen for example in **Error! Reference source not found.** from sample CHX-1216.5 where both Na-rich and K-rich feldspar can be seen, the K-rich feldspar is noticeably lacking deformation features. There are two possible explanations for this: 1) K-rich feldspar does not contain many deformation features because they did not form, or 2) deformation features have been lost due to water-related alteration.

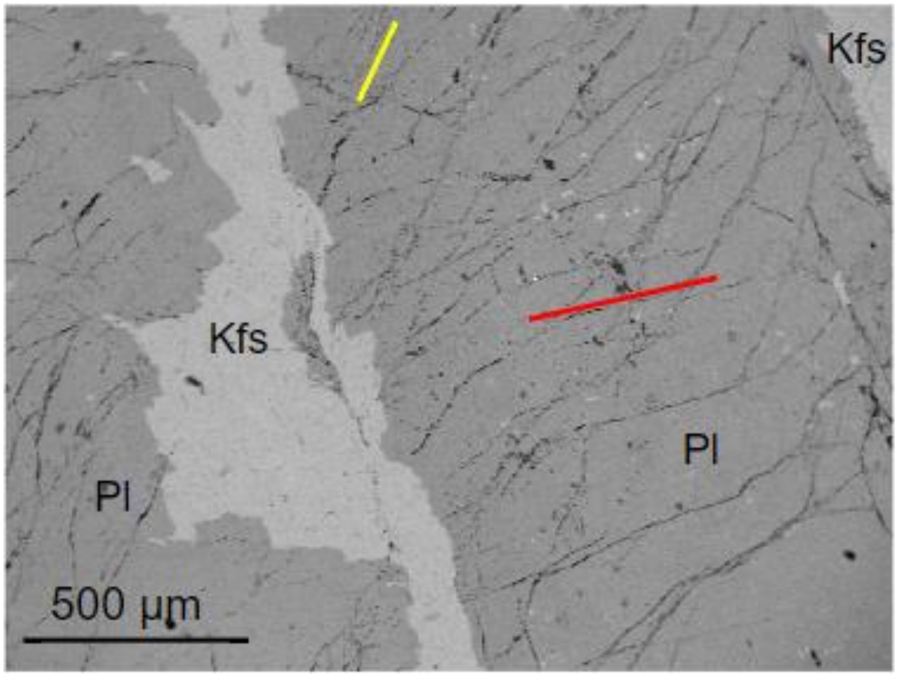

Figure 4.1 - BSE image of Site 1 from thin section CHX-1216.5. Red and yellow lines highlight orientation of fractures. Randomly oriented fractures are also present in Na-rich feldspar. The Na rich feldspar has noticeably more fractures than the K-rich feldspar neighbouring it. Pl = plagioclase feldspar, Kfs = K-rich feldspar.

There are a few examples of deformation in K-rich feldspar, one example is from Site 2 of thin section CHX-1199.6 which contains planar features in K-rich feldspar **Error! Reference source not found.**. Site 2 still shows its features despite alteration in this area, suggesting water-mediated alteration cannot be attributed to the lack of features at other sites in these thin sections.

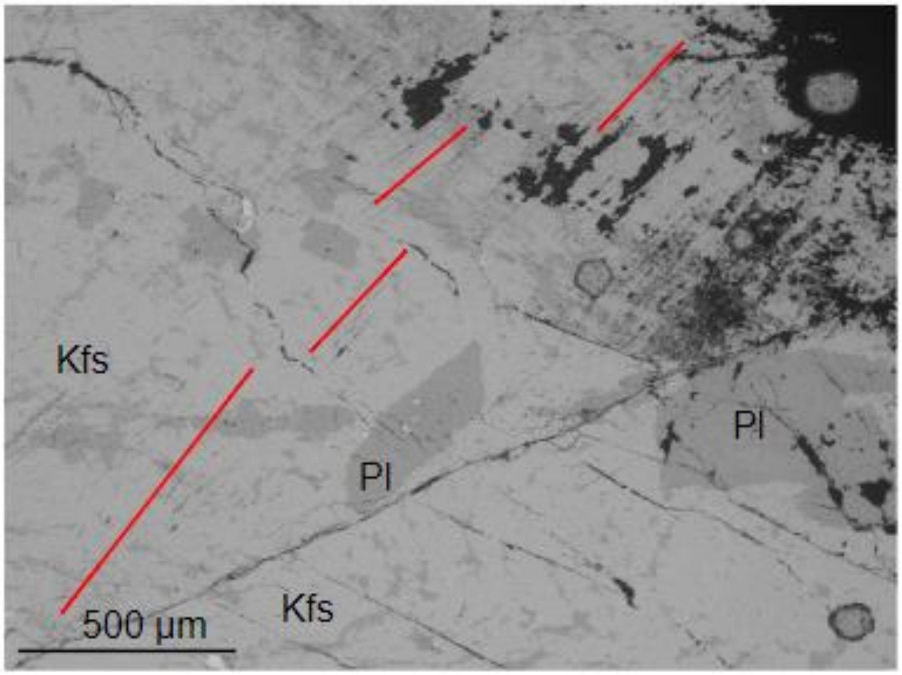

Figure 4.2 - BSE image of Site 2 from thin section CHX-1199.6. Red lines show faint planar features in K-rich feldspar. Alteration can be seen in top right of image however the red planar feature can still be seen. Pl = plagioclase feldspar, Kfs = K-rich feldspar.

There are two different types of K-rich feldspar which have been described in these samples, primary and secondary feldspars, which are found together in some sites. The first type of K-rich feldspars which are interpreted to be primary feldspars that formed during igneous crystallisation of the granite. These primary feldspars are typically more angular at grain boundaries and euhedral. The second type of K-feldspar, which are interpreted to be secondary (forming after igneous crystallisation), are recrystalised feldspars which typically have a more rounded crystal shape. An example of both types of feldspar can be seen in Site 6, thin section CHX-1160.7 (**Error! Reference source not found.**). In Site 6, the compositions of these two types of K-rich feldspar appear to be very similar to each other as demonstrated in Table 4.1 which shows the Ca, Na and K content of both primary and secondary feldspar. For example, K content in primary feldspar ranges from 6.45-6.57 at. % K and ranges from 6.44-6.62 at. % K in secondary feldspar (Table 4.1). In Site 6, Na-rich feldspar can also be seen which contains noticeably more deformation features than either type of K-rich feldspar at the site, with Na-rich feldspar containing PDFs and K-rich feldspar in most cases showing only fractures. The formation of secondary feldspar is not necessarily an impact process as there are other processes that could have formed this secondary feldspar. For example, the secondary feldspar could have formed during previous hydrothermal alteration (Larsson et al., 2002). This secondary feldspar could also be a result of a post-impact hydrothermal process, a study by Timms et al., (2020) used titanite to try and date hydrothermal alteration at the Chicxulub impact structure and found evidence for hydrothermal alteration processes that resulted in a loss of Pb after the impact event. It is important to note that even the primary K-rich feldspar contains noticeably fewer shock metamorphic features than the neighbouring Na-rich feldspar (**Error! Reference source not found.**). This suggests that the K-rich feldspar did genuinely record fewer shock effects, compared to Na-rich feldspar, rather than just losing these features during recrystallisation (an argument that could have been used if only recrystallised feldspar was found and not primary feldspar).

There is also the possibility that shock features could have been disrupted by annealing. For example, K-rich feldspar could of have some features that were subsequently lost due to annealing. Some previous discussions into post shock annealing have highlighted that there can be a change in the distribution of the local chemical composition, with Ostertag & Stöffler, 1982 suggesting thermal annealing can result in a more heterogeneous distribution of Al and Si in feldspars and increased diffusivity of the Na, Ca and K. This study also found that plagioclase feldspar recrystallised more rapidly than alkali feldspar and suggests that this may be due to viscosity (plagioclase has a lower viscosity than feldspar) (Ostertag & Stöffler, 1982). Some research specifically discusses effects of shock annealing in impact melt (Bischoff & Stöffler, 1984).

However, the sample that contains some impact melt rock (CHX-1216.5) did not appear to contain a difference in shock features based on proximity to melt (most feldspars were found in the granite half of the sample rather than the melt side) when compared to the other two samples. It should be noted however due to the small sample size in this thesis that this finding may not be significant. Differences between how these different feldspars respond post shock may therefore help to explain why there was a difference in the shock features observed. However, further research may be needed to help determine to what level this could have influenced the results found here. It may be recommended that shock experiments on feldspars of similar compositions to those in this study were carried out to try and resolve this.

Table 4.1 - Table showing the Ca, Na, and K composition of K-rich feldspars from Site 6 of thin section CHX-1160.7. Data was collected using EPMA and compares the composition of primary K-rich feldspar and secondary K-rich feldspar. See Figure 4.3 to see the primary and secondary feldspars for Site 6 marked by blue and red boxes respectively.

	Ca	Na	K
Primary - 1	0.01	0.27	6.57
Primary – 2	0.01	0.36	6.47
Primary – 3	0.01	0.45	6.45
Secondary - 1	0.01	0.29	6.62
Secondary – 2	0.01	0.37	6.56
Secondary - 3	0.01	0.47	6.44
Primary average	**0.01**	**0.36**	**6.5**
Primary SD	**0**	**0.09**	**0.06**

Secondary average	**0.01**	**0.38**	**6.54**
Secondary SD	**0**	**0.09**	**0.09**

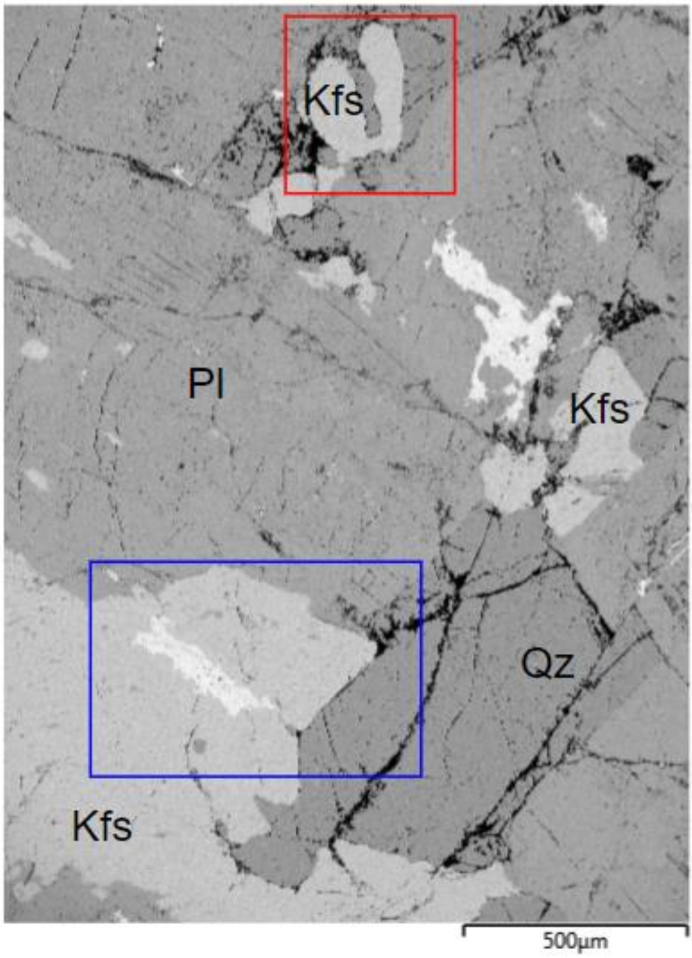

Figure 4.3 - BSE image from site 6 of sample CHX-1160.7. Red box highlights oddly shaped K feldspar with curved edges indicating this feldspar is recrystallised. Blue box highlights part of K feldspar with straighter, more angular edges, suggesting feldspar is a primary feldspar. Pl = plagioclase feldspar, Kfs = K-rich feldspar, Qz = Quartz.

Samples CHX-1199.6 and CHX-1216.5 both have many examples of K-rich feldspar containing areas of exsolution forming a patch perthite texture (for example, **Error! Reference source not found.**) (as identified with diagrams in (Parsons et al., 2015)). In a few regions, these areas of exsolution appear more elongated and aligned (for example CHX_1199.6 Site 3, (**Error! Reference source not found.**) and although still most similar to patch perthite, bear some resemblance to braid perthite. This may suggest that a braid to patch perthite reaction took place (as described in (Parsons & Lee, 2009)), this is not directly related to the shock effects as exsolution is not a shock deformation feature. The presence of fractures cross-cutting exsolution in some samples (most common in sample CHX-1216.5) suggest exsolution likely occurred pre-impact. It is, therefore, worth considering the effect that the presence of exsolution may have had on the shock features recorded in the sample. It has already been established that the chemical composition strongly influences the shock deformation microstructures formed in a sample. For example, Fritz et al., (2019) discuss this influence of composition across the plagioclase series using shock experiments to investigate the formation of diaplectic glass (in this paper also described as maskelynite). Fritz et al., (2019) suggests that the minimum pressure required for the formation of diaplectic glass is less when a feldspar contains less albite and more anorthite.

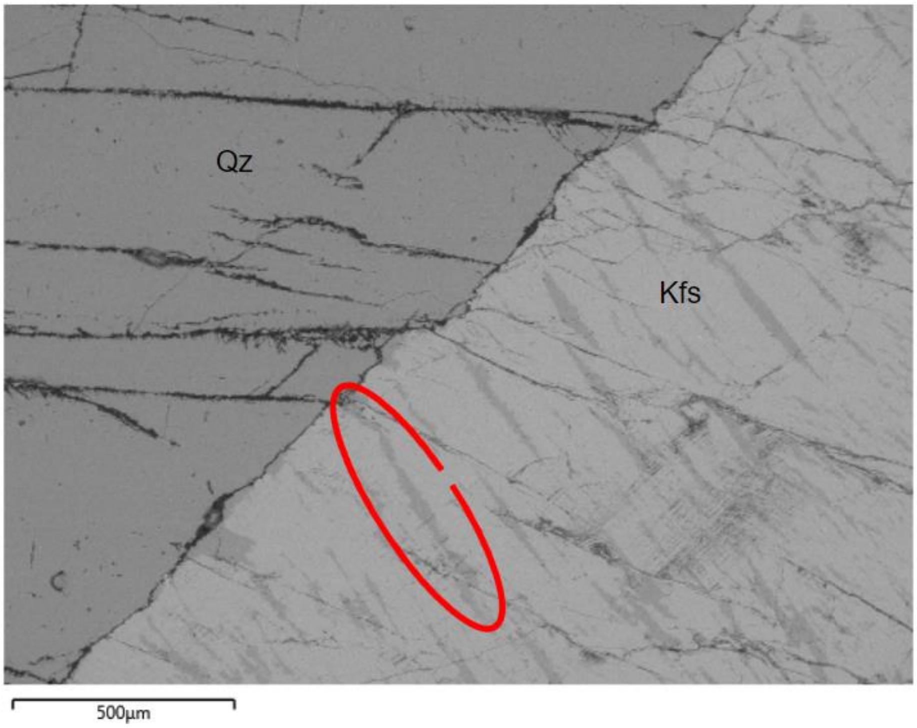

Figure 4.4 - BSE image of Site 3 from thin section CHX-1199.6. Red circle highlights one area (among many seen) of exsolution in Kfs area. Kfs = K rich feldspar, Qz = Quartz.

Generally, it has been observed in this thesis that there has been more research into plagioclase than alkali feldspar, something which has also been pointed out previously, for example by Pickersgill et al., (2021) who noted far fewer reports of the quantified differences in shock response in alkali feldspars. There may be less recorded research into shock deformation features in alkali feldspar due to the scarcity of deformation features, as observed in this thesis. However, it must also be considered that there are also very few examples where a lack of deformation features in alkali feldspar have been recorded as there are unlikely to be reports of negative findings. Therefore, it is unclear whether less research in the past into deformation features in alkali feldspar means there are fewer features to report. More research looking at feldspar with a range of chemical compositions from the same locations is needed in order to compare more directly different types of feldspar.

4.3 Shock barometry

The identification of diagnostic (and non-diagnostic) features of shock deformation is crucial for shock barometry. Previous research investigating the use of feldspar (and other minerals) in shock barometry has been primarily carried out using optical microscope observations (e.g., (Stöffler et al., 2018). This is due to the fact that optical microscopy is a readily accessible tool for most laboratories while many other analytical techniques, for example, electron backscatter diffraction (EBSD) are more specialist and not available in all laboratories to apply to geological samples (Prior et al., 2009). For the purposes of shock barometry, Stöffler et al., (2018) discusses a range of shock classification systems and maintains that optical microscopy should be the primary observational technique, with other techniques such as scanning electron microscopy (SEM) only being used as supporting techniques. While it is generally accepted that optical investigations are carried out earlier on when studying a thin section, this thesis maintains that it is important to augment optical microscopy investigations with the use of a range of other methods rather than just using a polarising microscope and only using other methods in specific circumstances. A stance that is supported by, for example, by the discovery and use of FRIGN zircon, which is only detectable via EBSD (Cavosie et al., 2018).

When considering the findings in this thesis, most deformation microstructures were identified using BSE or EBSD images along with EDS and EPMA chemical analysis, rather than polarising microscope images. For example, Site 1 of thin section CHX-1160.7 (as discussed in Section 3.1.2.1) was investigated using BSE and then with EBSD, and deformation features were identified, specifically in this instance the identification of partially amorphised alternate twins. The same sample site (Site 1) was also investigated optically, however, optical microscopy did not show definitive alternate twin amorphisation (**Error! Reference source not found.**)). Although the site can be seen to be slightly darker and the irregular vertical fracture can still be seen in both plane polarised light and between crossed polarisers, the twins are not as easy to see as in EBSD images. The quartz in this region does have some planar deformation features, therefore if this site was classified using Stöffler et al., (2018) shock metamorphism classification system for felsic rocks (so only using the polarizing microscope observations) then it could be classified S3 (meaning conditions similar to ~5-10 GPa and ~100°C). Whereas, if features identified via other methods (e.g. partial amorphisation of feldspar via EBSD, as seen in **Error! Reference source not found.**B were also considered for the Stöffler et al., (2018) classification (although this is not the purpose of their classification system), then the shock stage for the same area could be S5 (~35 GPa and ~300°C). Thus, an optical only approach may underestimate the peak shock pressure inferred for impact rocks.

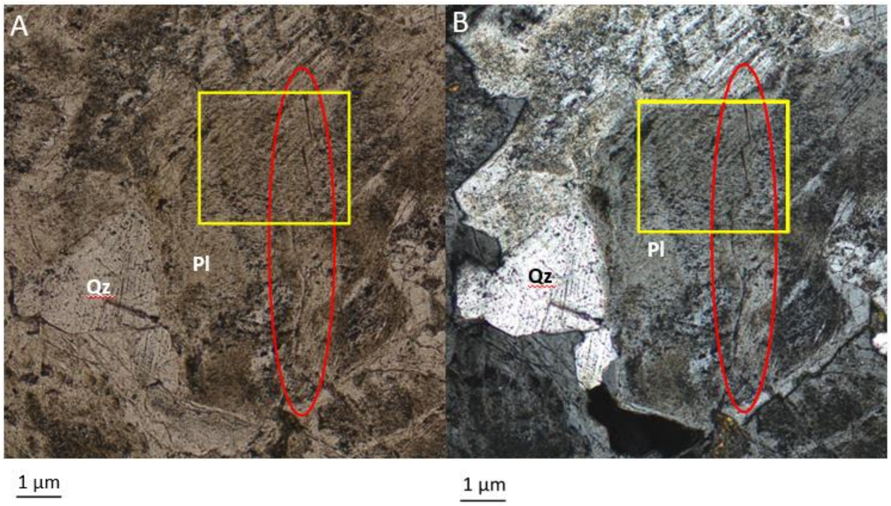

Figure 4.5 - Optical microscope images of sample CHX-1160.7, Site 1. A) Plane polarised light (PPL). B) Cross polarised light (XPL). Red circle highlights large fracture and yellow box labels area of deformation that was analysed further in section 3.1.2.1. Note twins in yellow box are hard to see. Pl = plagioclase feldspar, Qz = quartz.

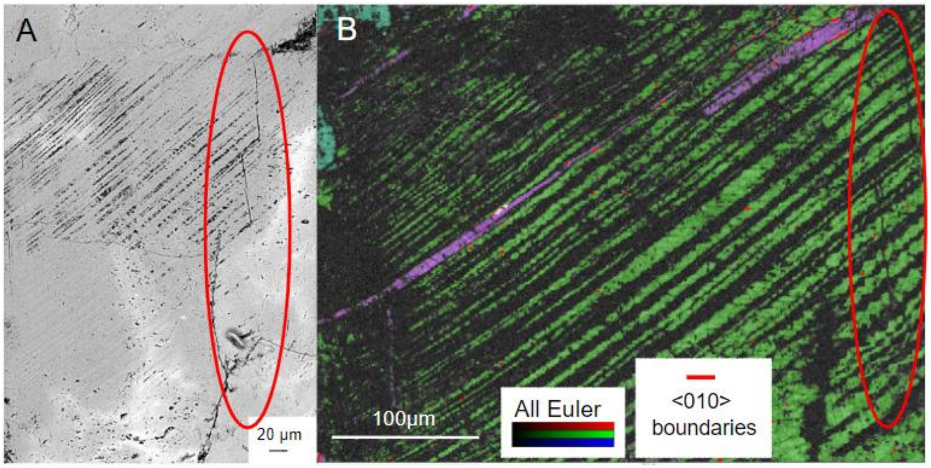

Figure 4.6 - BSE and Euler maps of Site 1 from thin section CHX-1160.7. A) BSE image of part of Site 1, area seen in yellow box of Figure 4.5. Red circle highlights fracture as point of reference. Here twins can be more easily seen than in Figure 4.5. B) Euler angle EBSD map showing same area of Site 1. Red lines indicate 010 boundaries (not shown in many areas due to partial amorphisation). Black twins have become sufficiently amorphised so that they can no longer be confidently indexed using EBSD, indicating diaplectic glass.

The identification of diaplectic glass using only a polarizing microscope proved difficult during this project as in many instances the diaplectic glass could not clearly be seen. This could be attributed to the both the small scale of some of the twins (within which diaplectic glass had formed) and also water-related alteration in some areas. This difficulty has been highlighted in previous research, for example, a study into shock experiments on maskelynite-bearing anorthosite struggled to identify signs of multiple shock effects in amorphised plagioclase (in that paper described as maskelynite and diaplectic glass interchangeably) using only ‘simple petrographic or textural observations’ (Lambert & Grieve, 1984). In that study, the challenge was addressed by studying the experimentally re-shocked samples using a microphotometer. A clear difference was found in the refractive indices between re-shocked maskelynite and singularly shocked maskelynite. Although this example did not use techniques such as EBSD, it does highlight the benefit of using additional methods instead of just optical microscope observations. However, it is worth noting that there are examples of features (in this case isotropisation in alternating lamellae) being recorded without the additional use of methods such as EBSD, for example, Stöffler, (1966) identified these alternating features using ‘microscope and x-ray examination’ (the exact methodological details of which are not fully specified). Other examples include Albin et al., (2009) (and references within) which discuss the alternating deformation features of feldspar twins (including isotropisation of alternating twins and presence of PDFs within twins) but do not mention the use of methods such as EBSD.

Other researchers have also identified the utility of using multiple techniques to investigate shock barometry in a variety of minerals. For example, Kovaleva & Habler, (2019) investigated micro twins in zircons using a variety of methods including optical microscopy, BSE, EDX, and EBSD and found that in some areas of the samples, micro-twins were so small that they could only be seen using EBSD mapping with small step sizes (0.08–0.29 µm). These micro-twins were therefore undetectable using an optical microscope alone. FRIGN (former reidite in granular neoblastic) zircon is a form of zircon that was transformed into reidite (due to the high pressure from a shock event) and then reverted back (due to high temperature) to zircon. Due to its formation by both high pressure and high temperatures, it is considered a valuable diagnostic mineral of shock deformation (Cavosie et al., 2018) and was not discovered without the use of EBSD.

Shock effects have been detected using a mix of both optical microscope work and other methods, for example Bischoff & Stöffler, (1984) used optical microscope images, SEM images, and microprobe data to investigate thermal annealing within shocked feldspars in impact melt rock from the Lappajärvi crater and found chemical, structural and textural changes compared to parent crystalline samples from basement rock. Another example used single-crystal X-ray diffraction (XRD) to identify fragmentation features in a range of minerals before any signs of deformation were detectable optically (Hörz & Quaide, 1973). Hörz & Quaide, (1973) used the term fragmentation to describe the breakdown of single crystals into increasingly smaller block sizes. This fragmentation is identified through the presence of broader diffraction peaks using XRD (although it is important to note that line broadening may also depend on crystallographic orientation in relation to incident beam). These examples further highlight the benefits of a multiple method approach to shock barometry.

When considering the use of feldspar as a main record of shock pressure on par with the more commonly used quartz, this thesis has helped to show the value of feldspars, particularly plagioclase. One of the more commonly quoted challenges with the use of feldspars is that the more complex crystal structure may make identification of shock deformation features more difficult (McLaren & Reddy, (2008)), however one of the main results found in this thesis was deformation in alternating twins (as discussed in 4.4), a feature that is only present in a more complex structure that contains twins (as opposed to quartz for example). Other research has previously discussed this alternating deformation in feldspar twins (e.g., Stöffler, (1966); Pickersgill et al., (2015)) and it has been interpreted as a diagnostic shock feature. This emphasizes that the use of feldspar for shock barometry is valuable, showing features that would not be seen in other minerals.

Another way that this project has highlighted the use of feldspars (and by extension, other minerals than quartz) is the observation that Na-rich feldspar contained more evidence of shock deformation than nearby K-rich feldspar or quartz. What this suggests is that by purely assessing shock scale on the basis of observations from one mineral phase alone, or from optical microscopy alone, many observations may be missed and thus result in a less accurate understanding of shock conditions or even a misidentification of a potential impact site. Therefore, when using minerals for shock barometry, it will be more accurate to use a range of mineral phases and a range of different analytical methods to place the sample in question on an appropriate shock scale. This multiple method and/or multiple mineral phases approach has been done before (examples include (Pickersgill et al., 2015; Fritz et al., 2019; Pittarello, et al., 2020a; Yin & Dai, 2020)) and is an approach that is more likely to yield more accurate results.

4.4 Deformation in twins

4.4.1 Alternating twins

A key feature that was found using EBSD was the partial amorphisation of alternating twins in sample CHX-1160.7.

These partially amorphous twins show as non-indexed areas where faint Kikuchi patterns can still be made out (but are not clear enough to be indexed). The presence of non-indexed regions could be attributed to several causes; amorphisation (resulting in a loss of crystal structure preventing the production of Kikuchi patterns, a loss of material, poor polish, nano crystallization, and the replacement of feldspar with a phase that does not indexed well such as zeolite. After some consideration, these twin have been confirmed as the result of partial amorphisation, however these other explanations will be discussed below.

Both loss of material and poor polish could result in a lack of clear of any Kikuchi patterns being produced. While it is true that some areas have experienced some loss in material, there are non-indexed regions where material has been confirmed to be present for example by the use of SE images and Carbon EDS maps (an example of which is seen in section 4.4.2). If the non-indexed regions were due to a poor polish then it would be expected that surrounding regions would also be non-indexed however the surrounding mineralogy has remained crystalline and has been indexed using EBSD. There are even examples of twins that are crystalline (and therefore indexed that have become non-indexed further along the same twin (for example, Site 2 in Sample CHX-1160.7). Therefore neither poor polish, nor loss of material can fully explain these non-indexed regions with faint Kikuchi patterns.

Another potential explanation would be nano crystallization which if present would result in multiple patterns creating a mixed signal of Kikuchi patterns. It is expected however that is if this was what was producing these non-indexed twins, the faint Kikuchi patterns that have been seen would be more confused and would look like multiple patterns overlaid whereas what they actually look like is one Kikuchi pattern that is just very faint (see section 3.1.2.1). In future research the use of TEM would confirm whether or not nano crystallization was present in these twins.

The final alternative hypothesis would be that these twins that are non-indexed are not actually feldspar. For example, there has been examples in previous literature of feldspar in twins being replaced by zeolite (Pickersgill et al., 2015). Zeolite is a weathering product of feldspar which would be difficult to index using EBSD and very hard to polish.

Out of these potential reasons for these non-indexed twins, partial amorphisation was confirmed to be the most likely reason. This partial amorphisation was confirmed by the presence of Kikuchi patterns in ‘non-indexed’ twins which although weakly visible were not clear enough to be indexed correctly using a database, suggesting that although some amorphisation has taken place, it was not enough to result in the complete loss of crystal structure. This partial amorphisation makes it difficult to fully determine the type of twin boundary but examination in more crystalline regions using Aztec Crystal software helped to determine some 010 twin boundaries (see results, section 3.1.2.1, also example shown in **Error! Reference source not found.**).

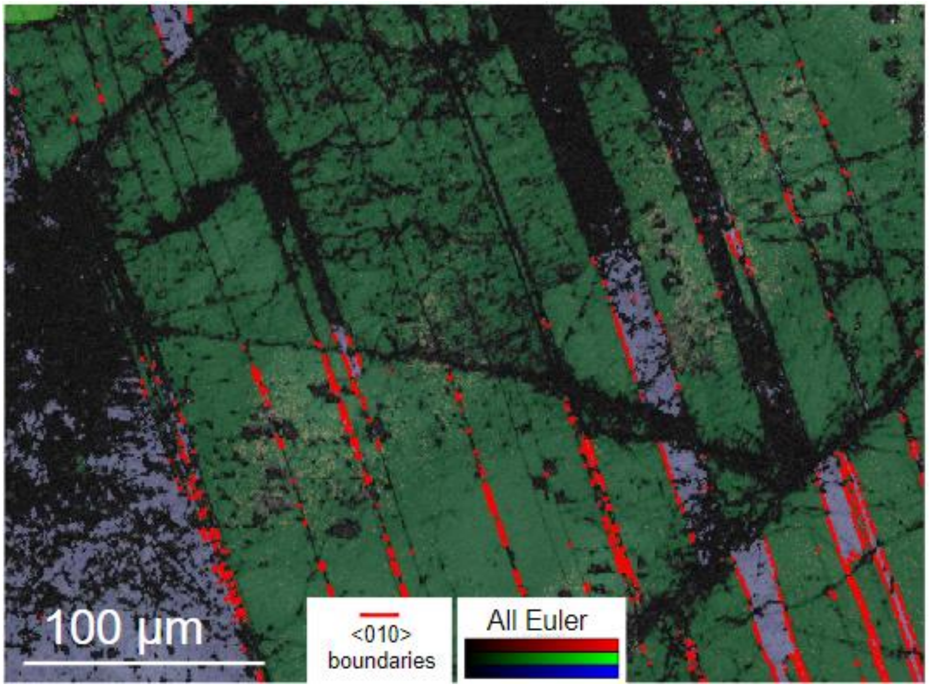

Figure 4.7 - Example of 010 boundaries (red pixels) being detected using Aztec Crystal on an all-Euler map. Example from sample CHX-1160.7 Site 2.

This alternating deformation of twins in feldspar has been identified previously e.g., (Stöffler, 1966; Pickersgill et al., 2015; Pittarello, et al., 2020a) and has been suggested to have been caused by deformation being affected by the orientation of the lamellae in relation to the direction of the shock wave (Stöffler, 1966). This is because the albite-twins mentioned in Stöffler, (1966) will consist of multiple twins with alternating different orientations (i.e., each twin (lamellae) will have a different (but symmetrical) orientation to those either side). These different alternating orientations can be seen back in Figure 1.1.

Another example of where shock features were noted to have a preferred orientation is (Pittarello et al., 2020b), where both feldspar and quartz from shatter cones were investigated. Pittarello et al., 2020b describes PDFs in both quartz and feldspar and notes shock related micro twins in plagioclase feldspar. Pittarello et al., 2020b goes on to talk about the possibility relating this preferred orientation to the propagating shock wave but does note that this would be very difficult to achieve due to the complexities of crater formation and subsequent modifications.

As well as using EBSD to identify these partially amorphous alternating twins, high-resolution BSE images showed some strange interactions between fractures and twins. For example, in Site 1 of sample CHX-1160.7 (section 3.1.2.1) there is a fracture cross cutting several twins with alternating twins appearing to fill in this fracture. The fracture appears to be infilled with the same material already contained in the twin (see **Error! Reference source not found.**), suggesting a fluidity across the selected twin possibly as a result of melting (or plastic deformation) in these alternating twins. This may be another example of alternate twin deformation. It may also help to give an indication of order of events as the fracture could have formed before the deformation of the alternating twins. An alternative explanation however is that the deformation of alternating twins occurred, after which areas were weathered away and caused fracturing in the damaged area. Further analysis across more samples may help to make sequence of events clearer as identification of features that cross cut each other would help to reveal the order of deformation features forming.

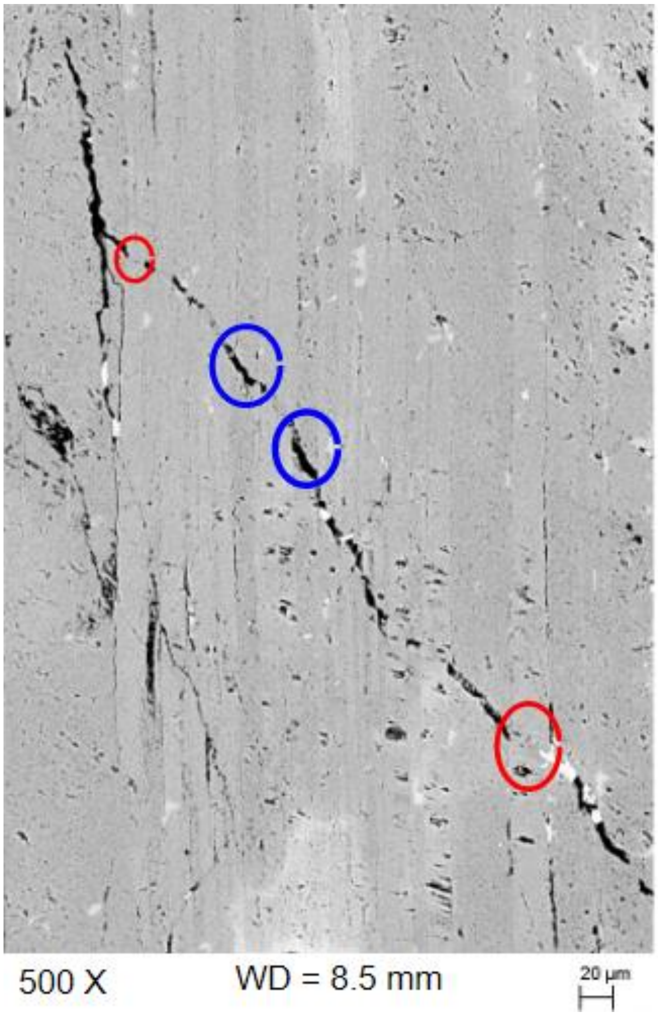

Figure 4.8 - BSE image of Sample CHX-1160.7 Site 1. Fracture that has been infilled in some twins (as highlighted in the red circles) but not in others (see blue circles).

4.4.2 Relationship between Ca content and deformation

Although all of the plagioclase feldspar studied in this thesis is Na-rich rather than Ca-rich, there is still a small amount of Ca contained within them (as described in Chapter 3). This small amount of Ca content (<2.5 at.% Ca (results Chapter 3)) appears to have a strong connection with some of the deformation features highlighted in Chapter 3. In particular, in the areas from sample CHX-1160.7 the partially amorphous twins contain a lower Ca content (less than ~1 at. % Ca) than twins which have remained crystalline, this can be seen in

Error! Reference source not found. where the twins can be seen through the varying Ca levels shown in the EDS map. It should be noted that although all the data in this thesis is quoted in at. %, this compositional difference could also be seen in the raw data in wt.% and so this trend in Ca content was not just created by the normalisation of data. The wt.% of EPMA data has been recorded in Appendix E.

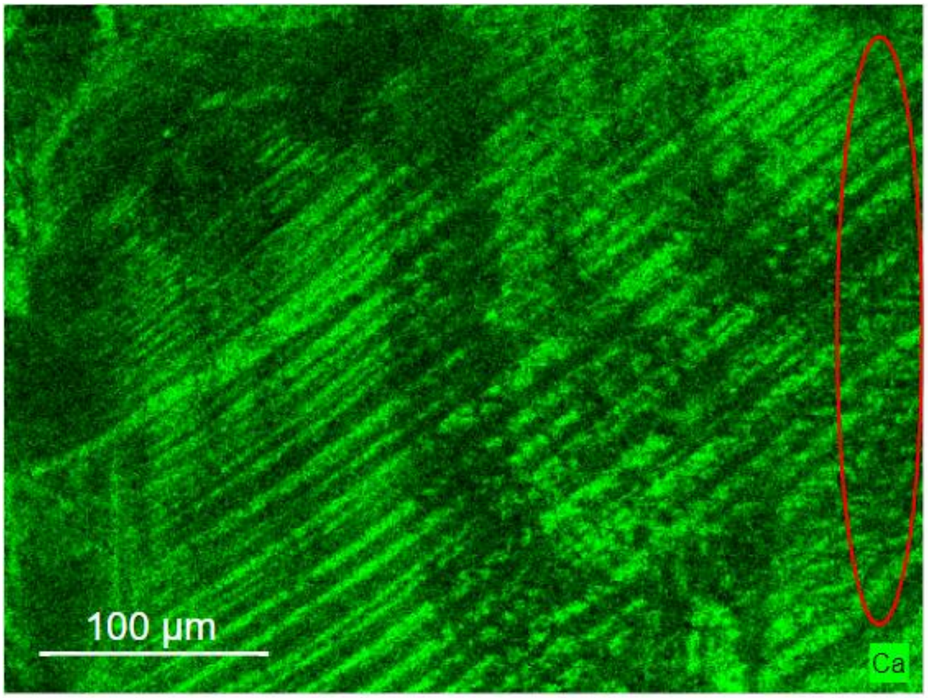

Figure 4.9 - False colour EDS map showing distribution of Ca in sample CHX-1160.7 Site 1. Area covered is the same as Figure 4.6B. Red circle highlights fracture as point of reference. The twins can be seen in this map and line up with the alternating partially amorphised twins seen in Figure 4.6.

Some microprobe areas with less Ca in them also have slightly more Na instead. These same regions also have slightly reduced Al but slightly increased Si. This is due to plagioclase feldspar maintaining charge balance with Ca^{2+} exchanging for Na^{+} and Al^{3+} exchanging for Si^{4+} (Walther, 2005).

When considering the relationship between variation in Ca content and deformation features there appear to be two possible explanations: 1) The Ca content in Na-rich feldspars influences deformation (lower Ca = more readily deformed) or

2) deformation has influenced the distribution of Ca content in the Na-rich feldspars.

For the hypothesis that Ca content influences deformation, it has been reported that factors such as crystal structure and chemical content do have an impact on formation of shock deformation features (e.g., (Stöffler, 1966)). An investigation into shocked lunar samples records a lack of PDFs in the Ca-rich plagioclase studied (Xie et al., 2021) and goes on to point out that earlier research examples where PDFs were found, the feldspars were often Na-rich, as also observed in other studies (e.g., references in Pickersgill et al., (2021)). There are some reports of Ca content influencing the pressure needed for the formation of maskelynite Rubin, (2015), however this again focuses on Ca content greater than that which is recorded in this thesis. In this thesis there were no Ca-rich feldspars however, the variation in Ca content found in the Na-rich feldspars still indicates a connection between the Ca/Na ratio and the prevalence of shock deformation features. The twins containing less Ca (less than ~1 at.%) are the regions that have partially amorphised. Whereas the twins that contain 1-2.5 at.% Ca have remained crystalline. This observation does therefore support the idea that increased Na and decreased Ca are related to the presence of more shock deformation features being found. It has been discussed earlier (in section 4.2) that there is a difference for example in the deformation features found in K-rich feldspar compared to Na-rich feldspar. However, one thing that has not been clearly observed before, is the influence of chemical composition over such a small range. The Ca differences found in these samples are only about a <2 at.% difference and are generally low quantities (section 3.1.2.1). A challenge to the hypothesis that lower Ca content results in higher levels of deformation is that the difference in Ca content is found to be in alternating twins. The twins observed here are lamellae twins that likely formed during growth of the crystal in an igneous setting and thus, twins in the same crystal are unlikely to be of different chemical composition unless they have been altered in some way (Van Der Plas, 1966).

The second hypothesis is that the chemical content in alternating twins in the feldspar crystal has been influenced by deformation, which has been suggested in previous research (i.e., (Xie et al., 2020)). A crystal structure that has been deformed is more likely to experience chemical breakdown and loss or replacement of some elements. As the change in Ca noted in this thesis is a decrease in Ca in the amorphised twins (therefore the more shock deformed twins), this hypothesis appears more likely than explanation 1. Jaret et al., (2014) suggested that change in Na content may be a result of post shock alteration (however they do not discuss Ca). It is worth considering that the Ca content may be a loss of Ca from the partially amorphous twins or that alternatively, there may have been diffusion of Ca from one twin into another. It has been suggested in previous research that the diffusion of Ca in plagioclase feldspar is relatively fast (compared to in K-rich feldspar, with albite diffusing Ca at around 3 orders of magnitude faster than K-rich feldspar), potentially due to the similar size of Na and Ca compared to K (Cherniak and Watson, 2019 and references within). In addition, diffusion or movement of Ca ions may be facilitated by the partial amorphisation of the crystal structure. This idea of diffusion may be supported by the presence of a 'ladder texture' described in section 3.1.2.1 which could be argued to have occurred as a means of allowing a change in chemical content across this region. Ladder texture can be seen in **Error! Reference source not found.**B within the lower half of the red circle highlighting the fracture. If diffusion has occurred as a result of shock metamorphism, this may also help to explain why more deformation features have been found in Na-rich feldspar than K-rich feldspar as slower diffusion rates in K-rich feldspar (Cherniak & Watson, 2019) may have prevented features such as this ladder texture from forming. However, to counterbalance this argument that Ca was transferred through diffusion, microprobe data from other regions (section 3.1.2.1) of the crystal (C1) suggest that Ca content in regions without this alternating twin deformation is similar to that of the indexed (and so less shocked) twins, suggesting that it is the original (pre-shock) composition of the plagioclase. This unshocked composition contains ~1.5-2.5 at. % Ca (compared to the less than ~1 at. % Ca found in the shocked partially amorphous twins). This therefore supports the argument that Ca was lost from amorphous or partially amorphous regions more likely.

It is also worth noting that in some areas, the non-indexed and therefore amorphised or partially amorphised twins appear to be more susceptible to material loss during mechanical polishing during sample preparation than their crystalline counterparts. This can be seen in some carbon EDS maps where carbon from either the sputter coater has concentrated in recesses in the sample or carbon from the resin of the thin section can be seen (for example, **Error! Reference source not found.**). Although this could arguably be the cause of some of the loss of Ca from these regions, there are other areas in the same twins where carbon EDS maps do not suggest there has been much loss of material but Ca content is still lower than in the neighbouring crystalline twins. Therefore, this loss of material during sample preparation is unlikely to be the cause of the change in Ca content but instead may suggest that the partially amorphised regions have become more susceptible to alteration post shock. BSE images also support this idea with alternating twins in some areas appearing darker and more weathered out than the lighter coloured twins each side of them (for example, 3.1.2.2).

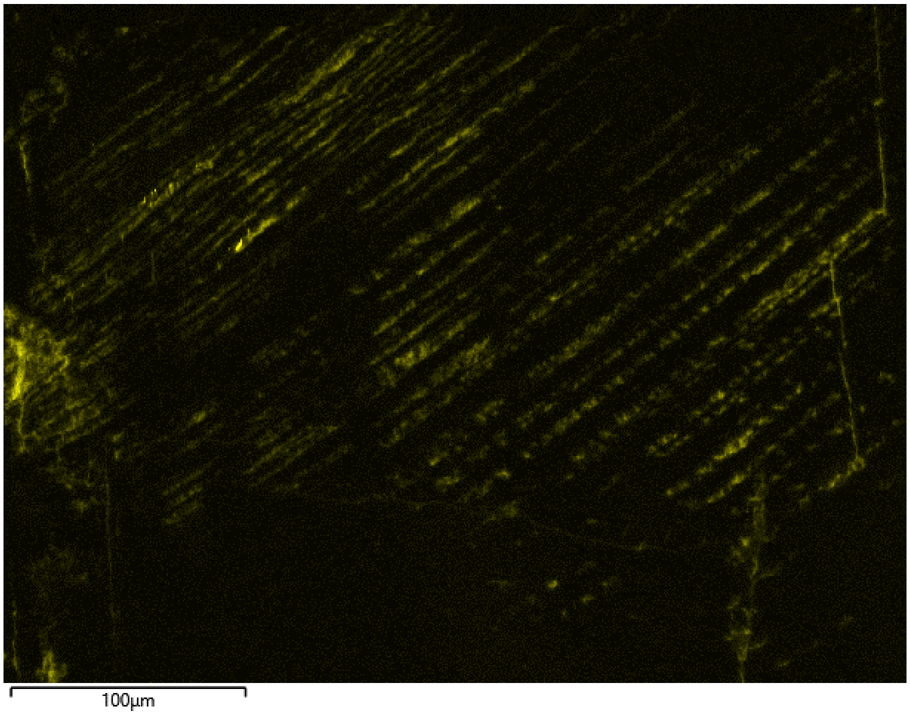

Figure 4.10 - False colour EDS map showing distribution of C (yellow) in sample CHX-1160.7 Site 1. Field of view is the same as Figure 4.6B.

Out of these two explanations, the most likely conclusion based on the findings in this thesis is that deformation has influenced the distribution of Ca content within Na-rich feldspar by the loss of Ca from amorphous (or partially amorphous) twins. The trends showing variation of Ca content mostly relate to deformation involving twins and it is unlikely that alternating twins in an unshocked feldspar (pre-impact) would have any difference in chemical composition without some alteration process taking place. However, there is perhaps also the possibility that other alteration processes occurred before the shock deformation event which could have caused chemical variation, however there is not enough evidence in the features found in this thesis to suggest such an event occurred. Another thing to consider when investigating these Ca trends is that in some of these sample sites (for example, Site 1, section 3.1.2.1) there is evidence for chemical zoning which may influence how easily deformation features can form and make features harder to see. A comparison of these samples in this thesis with some unshocked samples from the same (or more likely, nearby) location may provide further enlightenment in the future.

Typically, Ca content in Na rich feldspars has not often been reported in previous research, so further investigation at multiple impact locations would be beneficial in the future. The more feldspar samples studied from different locations, the greater range of endmember (Ca, Na, and K) content can be recorded. Thus, the trend between deformation features and Ca content could be more confidently confirmed across the plagioclase feldspar series and the increased deformation in Na-rich rather than K-rich feldspar could be confirmed. When investigating Ca content and deformation features in the future, further analysis of internal crystal structure would provide more insight into the formation process of partially amorphised alternate twins.

5 Conclusion

5.1 Main summary

This investigation into shock deformation in feldspars from the Chicxulub structure has produced several key conclusions:

1) No shock attenuation was observed over the depth interval sampled;
2) Na-rich feldspars record more shock microstructures than K-rich feldspars in the same thin section;
3) The use of multiple analytical methods provides a more successful identification of deformation features within feldspars and suggests that the use of multiple methods of analysis is advantageous for the purposes of shock barometry;
4) Partial amorphisation in alternating twins in Na-rich feldspar contains variations in low levels of Ca content with partially amorphous twins containing ~1-2 at. % less Ca than their crystalline counterparts.

5.1.1 Shock attenuation with depth

Variation in type or density of shock derived microstructures cannot be seen in samples over a depth range of 55.8 m. This 55.8 m difference in depth across the samples studied leads to the conclusion that shock attenuation is not measurable over that distance. A recommendation for future study would therefore be to investigate samples from the Chicxulub drill core covering a greater distance in depth than the 55.8 m covered in this thesis and to use more than three samples. Feignon et al., (2020) noted shock attenuation with depth at Chicxulub over 11 samples and a depth range of 567.5 m (743.6 to 1311.1 mbsf), but they were focused on deformation features within quartz. It would be invaluable in the future to investigate how closely deformation features in feldspar follow the observations in quartz that Feignon et al., (2020) used to demonstrate shock attenuation with depth. Such a direct comparison with quartz would help to develop the use of shock barometry with feldspars and help establish how these two minerals could better be used together.

5.1.2 Na-rich vs K-rich feldspar

In this thesis shock deformation features were found to be more abundant in Na-rich feldspar than in K-rich feldspar. In particular, the Na-rich feldspar contained partially amorphised material in alternating twins indicating that Na-rich feldspars were more susceptible to shock. In a previous study by Pittarello, et al., (2020c) experimentally shocked plagioclase was recorded to transform to diaplectic glass at 28 GPa in some cases. However, in many grains only partial amorphisation was recorded (Pittarello, et al., 2020c). In contrast, the K-rich feldspar studied in this thesis contained mostly fractures which may have formed due to the impact event, although these fractures are not actually a diagnostic feature of shock deformation. In the samples studied in this thesis a few areas contained planar features in K-rich feldspar (for example in 3.2.2.2) which could possibly be PDFs (but have not been confirmed as they would require further analysis with higher resolution EBSD and/or TEM) however these are comparatively rare (with only one or two examples found in K-rich feldspar across a single thin section CHX-1199.6) compared to the abundance of potential deformation features found in Na-rich feldspar (although it must be noted that many of these interact with the twins in Na-rich feldspar). Furthermore, although both primary and recrystallised K-rich feldspars were identified, both types still showed a significant lack of deformation features when compared with Na-rich feldspar. This finding is interesting as it means that if these Chicxulub samples had only contained either Na-rich or K-rich feldspar (but not both), then the interpretation that would be made from the samples as to the level of shock experienced would have been different. This highlights the need for a more in-depth shock barometer to be calibrated for feldspars of different compositions and highlights the shock features produced at varying shock pressures for feldspars of differing chemical composition. The creation of a more in-depth feldspar-based shock barometer could be achieved by using experimentally shocked feldspars (with known shock conditions) with a range of chemical compositions to further investigate shock effects across different feldspars. Alongside this it would be beneficial to compare samples from various impact craters and compare deformation features in shocked feldspars with previous research into other shocked minerals.

5.1.3 Multiple methods of investigation

The use of multiple methods of analysis has proved more beneficial in the investigation of feldspar to shock barometry than just the use of a polarising microscope, in particular high resolution electron microscope methods. While the use of almost exclusively a polarising microscope has been popular in the past (e.g., (Stöffler et al., 2018)), the use of multiple methods has proven a more effective way of finding shock deformation features, as has been proven both in this study and in prior research which has successfully used multiple methods for investigating shock deformation (examples include (Jaret et al., 2014; Daly et al., 2019; Pittarello, et al., 2020a; Pittarello, et al., 2020c)). Therefore, I propose that further research investigating deformation in feldspars should use a range of different methods, beyond just those used in this thesis, in order to help to create a more definitive system for using feldspars in shock barometry. Although it is also important to note the importance of all methods used in this thesis, EBSD has, in particular, proved a valuable method for identifying diagnostic shock deformation features in feldspar and so its use in future research into shock metamorphism would be incredibly valuable. Through EBSD the partial amorphisation of alternating twins was readily identified in some sample locations, and so further analysis into the crystal structure may prove useful, particularly at an atomic scale. A recommendation for additional techniques to include in future studies therefore includes transmission Kikuchi diffraction (Daly et al., 2017) (similar to EBSD but with a higher spatial resolution applied to electron transparent samples) or atom probe tomography (White et al., 2018).

5.1.4 Partial amorphisation

The last key finding in this thesis was the relationship between partial amorphisation of alternating twins in Na-rich feldspar, and the slight variation in Ca between the (partially) amorphised twins and the crystalline twins. Ca content was found to be ~1-2 at. % lower in twins that have been partially amorphised than in those that have remained crystalline. The most likely explanation for this is that deformation has resulted in a change in distribution of Ca content within the Na-rich feldspar via diffusion. Although in past research there have been examples focusing on minerals of certain composition (for example, research has been carried out into the shock effects in plagioclase (Kubo et al., 2010; Pickersgill et al., 2015; Xie et al., 2020)), comparisons across feldspars of different compositions are rare and chemical changes within an individual crystal have not often been recorded or discussed. As chemical content has not always been reported in past research it is unclear how common a feature this Ca content variation within partial amorphisation of alternating twins is and so further research at different impact sites with feldspars of varying Ca, Na, and K composition is needed to investigate this using high resolution techniques e.g. SEM BSE, EDS and EBSD analysis.

5.2 Research Impact

The ongoing improvement and development of research into shock deformation in feldspars is useful for three main reasons. The first is the further understanding of individual impact structures as shock barometry can help to provide information on impact conditions (temperature and pressure). While shock barometry has more often relied on predominantly quartz for the identification of diagnostic shock features on a microscopic scale (e.g., (Goltrant et al., 1992; French & Koeberl, 2010; Holm-Alwmark et al., 2017b; Feignon et al., 2020)), the developing use of feldspar is not only beneficial in samples lacking quartz but also to provide additional constraints in samples where quartz has already been used. This thesis has found examples of shock deformation features being found in Na-rich feldspar where they are less visible in the neighbouring quartz (although there are also other examples of quartz showing more deformation features) highlighting the benefits of using multiple minerals and methods together in shock barometry investigations.

The second is that the increased identification and understanding of diagnostic features of shock metamorphism in feldspar will help in the future identification of hypervelocity impact structures. Terrestrial impact structures are often hard to identify because they have been altered by past geological processes (erosion, tectonics, burial, etc. (French & Koeberl, 2010)). The identification of shock deformation features that can only be formed by a hypervelocity impact event (diagnostic features) can help to identify these less obvious impact structures and even confirm more obvious impact structures. The more impact structures that are found and correctly identified as such, the greater statistical overview of past impact rates that can be produced (Trefil & Raup, 1990b; French & Koeberl, 2010).

The third main use of this research is to help contribute to the understanding of feldspar structure by exploring the deformation of feldspar during shock metamorphism. It is clear from this research that different types of feldspar respond to shock differently and that the shockwave produced from impact interacts with for example, feldspar twins resulting in the deformation features that have been found within said twins. These above points (the different microstructural response in different types of feldspar and deformation in selected parts of a feldspar crystal (twins)) indicate that chemical content and crystallographic orientation both have a large influence on the deformation features formed. This supports previous work where the effect of chemical content in plagioclase feldspars on the formation of diaplectic glass was investigated (Fritz et al., 2019). The influence of crystallographic orientation has also been identified in previous research. For example, Pittarello, et al., (2020b) discusses the shock related planar microstructures in quartz and feldspar and determined that the crystallographic orientation of individual crystals in relation to the shock wave controlled the distribution of these features. The partial amorphisation in alternating twins found in this thesis also indicates that the crystallographic orientation of feldspars influences deformation and thus further investigation based on this research may help to provide information on the behaviour of feldspars from different orientations.

In addition to these main three points, this study focused on samples from the Chicxulub impact structure and so the results and interpretations within this thesis help to add to the large collection of information about this site. Chicxulub is an important site for research, both for its use as a large, intact impact structure and for its role in the K-Pg mass extinction. Notably it is the only confirmed peak-ring structure on earth, providing useful insight into the structure of massive impact craters on other planetary bodies (Morgan et al., 2016).

Overall, this investigation has helped provide more information on shock deformation in feldspars and has helped highlight the need in future for a refined shock barometer that takes into account more precise chemical content within individual feldspar crystals.

6 Appendices

6.1 Appendix A: Image permissions

Image permissions for which Figure 1.1 is based off.

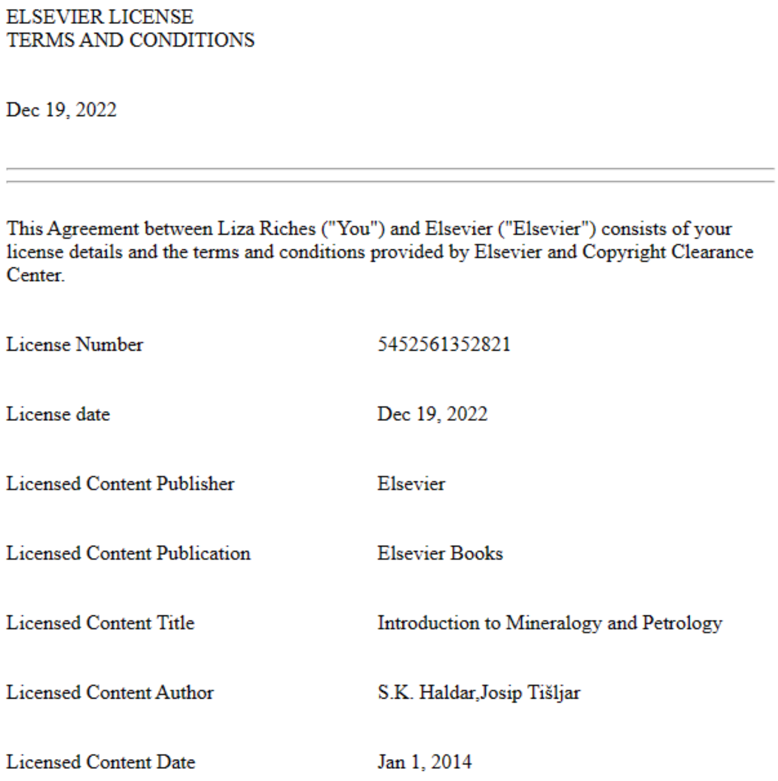

ELSEVIER LICENSE
TERMS AND CONDITIONS

Dec 19, 2022

This Agreement between Liza Riches ("You") and Elsevier ("Elsevier") consists of your license details and the terms and conditions provided by Elsevier and Copyright Clearance Center.

License Number	5452561352821
License date	Dec 19, 2022
Licensed Content Publisher	Elsevier
Licensed Content Publication	Elsevier Books
Licensed Content Title	Introduction to Mineralogy and Petrology
Licensed Content Author	S.K. Haldar,Josip Tišljar
Licensed Content Date	Jan 1, 2014

Image permissions for which Figure 1.2 is based off.

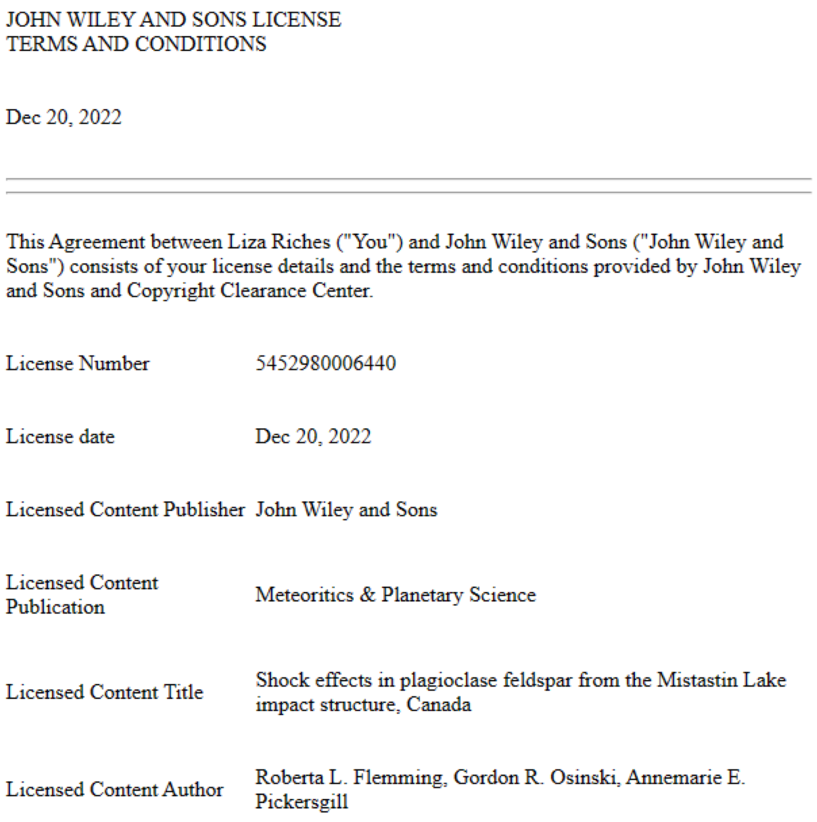

JOHN WILEY AND SONS LICENSE
TERMS AND CONDITIONS

Dec 20, 2022

This Agreement between Liza Riches ("You") and John Wiley and Sons ("John Wiley and Sons") consists of your license details and the terms and conditions provided by John Wiley and Sons and Copyright Clearance Center.

License Number	5452980006440
License date	Dec 20, 2022
Licensed Content Publisher	John Wiley and Sons
Licensed Content Publication	Meteoritics & Planetary Science
Licensed Content Title	Shock effects in plagioclase feldspar from the Mistastin Lake impact structure, Canada
Licensed Content Author	Roberta L. Flemming, Gordon R. Osinski, Annemarie E. Pickersgill

Image permissions for image which **Error! Reference source not found.** is based off.

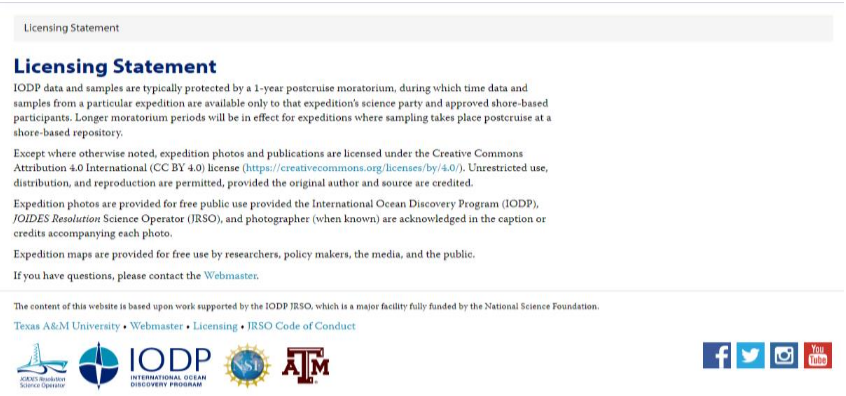

Licensing Statement

Licensing Statement

IODP data and samples are typically protected by a 1-year postcruise moratorium, during which time data and samples from a particular expedition are available only to that expedition's science party and approved shore-based participants. Longer moratorium periods will be in effect for expeditions where sampling takes place postcruise at a shore-based repository.

Except where otherwise noted, expedition photos and publications are licensed under the Creative Commons Attribution 4.0 International (CC BY 4.0) license (https://creativecommons.org/licenses/by/4.0/). Unrestricted use, distribution, and reproduction are permitted, provided the original author and source are credited.

Expedition photos are provided for free public use provided the International Ocean Discovery Program (IODP), *JOIDES Resolution* Science Operator (JRSO), and photographer (when known) are acknowledged in the caption or credits accompanying each photo.

Expedition maps are provided for free use by researchers, policy makers, the media, and the public.

If you have questions, please contact the Webmaster.

The content of this website is based upon work supported by the IODP JRSO, which is a major facility fully funded by the National Science Foundation.

Texas A&M University • Webmaster • Licensing • JRSO Code of Conduct

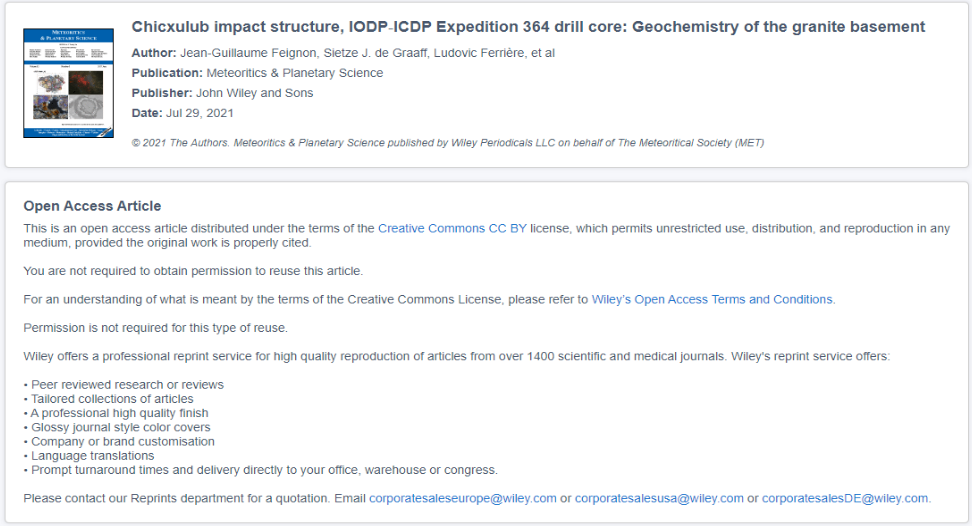

Chicxulub impact structure, IODP-ICDP Expedition 364 drill core: Geochemistry of the granite basement

Author: Jean-Guillaume Feignon, Sietze J. de Graaff, Ludovic Ferrière, et al

Publication: Meteoritics & Planetary Science

Publisher: John Wiley and Sons

Date: Jul 29, 2021

© 2021 The Authors. Meteoritics & Planetary Science published by Wiley Periodicals LLC on behalf of The Meteoritical Society (MET)

Open Access Article

This is an open access article distributed under the terms of the Creative Commons CC BY license, which permits unrestricted use, distribution, and reproduction in any medium, provided the original work is properly cited.

You are not required to obtain permission to reuse this article.

For an understanding of what is meant by the terms of the Creative Commons License, please refer to Wiley's Open Access Terms and Conditions.

Permission is not required for this type of reuse.

Wiley offers a professional reprint service for high quality reproduction of articles from over 1400 scientific and medical journals. Wiley's reprint service offers:

- Peer reviewed research or reviews
- Tailored collections of articles
- A professional high quality finish
- Glossy journal style color covers
- Company or brand customisation
- Language translations
- Prompt turnaround times and delivery directly to your office, warehouse or congress.

Please contact our Reprints department for a quotation. Email corporatesaleseurope@wiley.com or corporatesalesusa@wiley.com or corporatesalesDE@wiley.com.

6.2 Appendix B: Additional Cathodoluminescence (CL) images

Figure 6.1 CL image showing part of Site 2 of thin section CHX-1160.7. Area of EBSD for Site 2 can be seen in the grey rectangle.

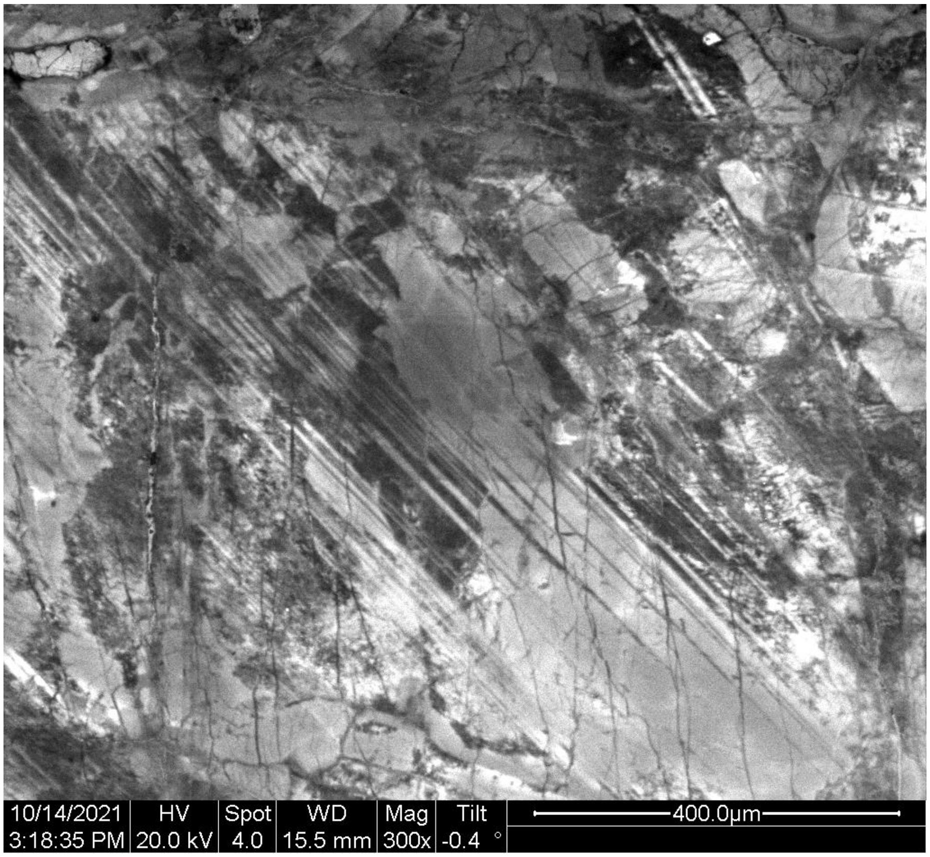

Figure 6.2 CL image of another part of Site 2 (thin section CHX-1160.7). Grey rectangle is area over which EBSD has been carried out.

6.3 Appendix C: EDS Data

EDS full spectra data

Table A - Thin Section CHX-1160.7 EDS data (at. %) with totals

Site	4		5	8	9			10	
Spectrum	1	2	1	1	1	2	3	1	2
Element									
O	58.25	51.38	57.89	58.59	58.8	58.67	58.53	56.79	59.26
Na	6.04	0	6.1	5.71	6.51	1.36	6.26	6.57	0.54
Mg	0	0.06	0.08	0.1	0	0.35	0.46	0	0
Al	9.72	10.82	10.28	9.95	9.72	8.07	9.87	10.09	7.96
Si	23.88	28.17	23.57	23.86	23.24	24.23	22.54	24.81	23.71
K	0.06	9.24	0.09	0.16	0.19	7.31	1.2	0.31	8.07
Ca	1.59	0.12	1.85	1.63	1.53	0	0.82	1.27	0.14
Fe	0.19	0.18	0.14	0	0	0	0.31	0.05	0.32
Ba	0.26	0.02	0	0	0.01	0	0	0.11	0
Total	99.99	99.99	100	100	100	99.99	99.99	100	100

Table B - Thin Section CHX-1199.6 EDS data (at. %) with totals

Site	1		2		3		4		6	9
Spectrum	1	2	1	2	1	2	1	2	1	1
Element										
O	58.07	57.99	57.61	59.79	59.35	58.73	57.87	60.67	59.06	58.22
Na	6.39	0.24	1.13	4.96	0.79	3.96	5.87	0.36	5.37	6.77

Mg	0.1	0.13	0	0.18	0	0	0.06	0.73	0.16	0.44
Al	9.66	7.88	8.94	8.65	7.77	7.1	9.73	11.23	10.27	8.78
Si	23.78	25.4	24.68	23.97	24.48	26.41	24.63	18.88	23.21	23.99
K	0.72	8.08	7.44	1.84	7.11	2.76	0.31	6.92	0.37	0
Ca	1.29	0.3	0.2	0.62	0.28	1.04	1.34	0.64	1.56	1.67
Ti	0	0	0	0	0.1	0	0	0.44	0	0.07
Fe	0	0	0	0	0.11	0	0.19	0.13	0	0.06
Total	100.01	100.02	100	100.01	99.99	100	100	100	100	100

Table C - Thin Section CHX-1216.5
EDS data (at. %) with totals

Site	4	
Spectrum	1	2
Element		
O	57.73	57.64
Na	6.65	0.3
Mg	0.13	0
Al	9.33	9.36
Si	24.94	25.52
K	0.5	6.87
Ca	0.72	0.13
Ba	0	0.18
Total	100	100

6.4 Appendix D: All EBSD Data

Table A - Analysis details and maps for example Dataset 1 from Sample CHX-1160.7

Dataset 1 details

Pixel Count	31775
Raster	205x155
Step Size	3 µm
Acquisition Time	00:26:57
Speed of Acquisition	19.65 Hz
Zero Solution Count	17222
Hit Rate	45.80%

Phases in Dataset 1

Phase	Fraction
Zero solution	54.20%
Chromite	0%
Sanidine	1.50%
Microcline	2.60%
Bytownite	17.70%
Quartz-new	24.10%
Pyrite	0%

Example maps:

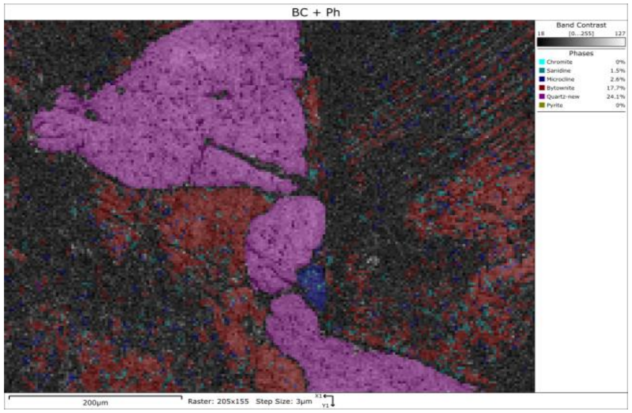

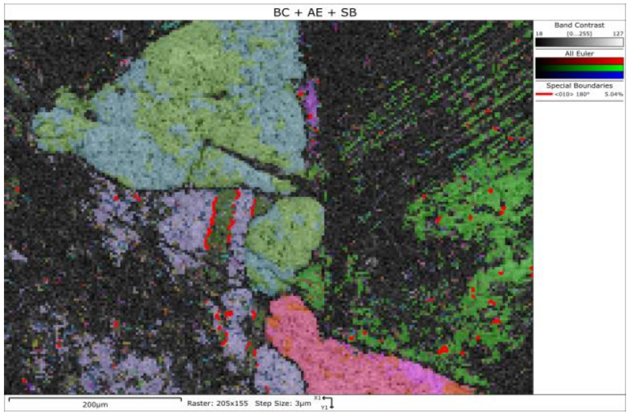

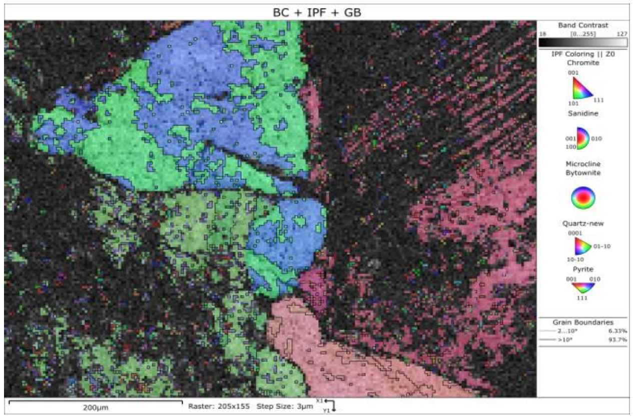

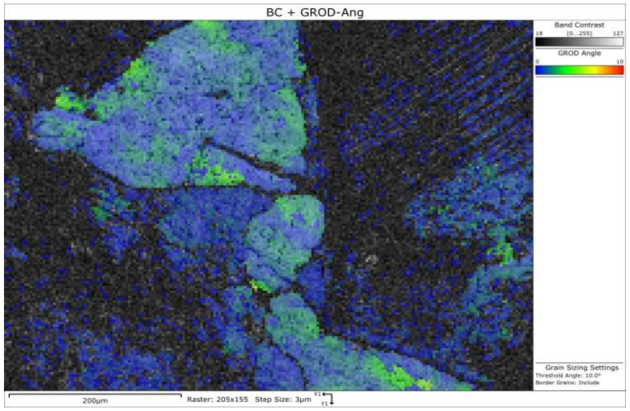

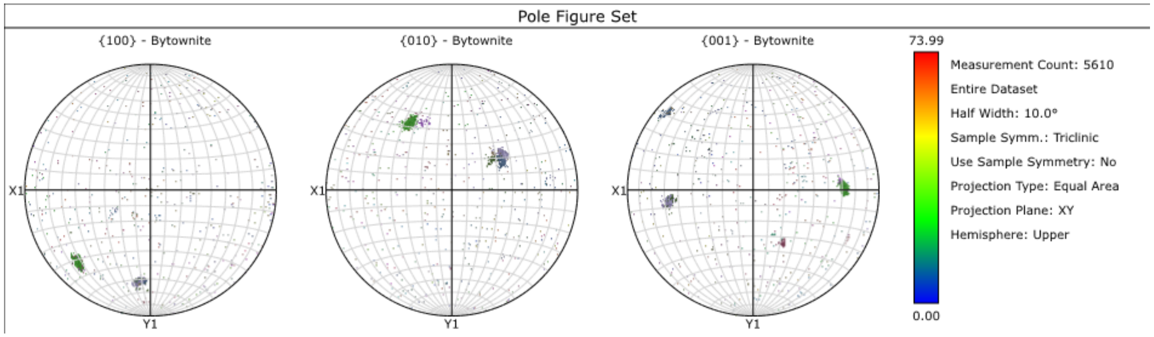

Measurement Count: 5610
Entire Dataset
Half Width: 10.0°
Sample Symm.: Triclinic
Use Sample Symmetry: No
Projection Type: Equal Area
Projection Plane: XY
Hemisphere: Upper

Table B - Analysis details and maps for example Dataset 2 from Sample CHX-1160.7

Dataset 2 details	
Pixel Count	445060
Raster	770x578
Step Size	0.5 µm
Acquisition Time	06:11:00
Speed of Acquisition	19.99 Hz
Zero Solution Count	316502
Hit Rate	28.89%

Phases in Dataset 2

Phases	Fraction
Zero solution	71.10%
Albite - mon	1.80%
Bytownite	26.10%
Quartz -new	0%
Sanidine	0.40%
Microcline	0.60%

Example maps:

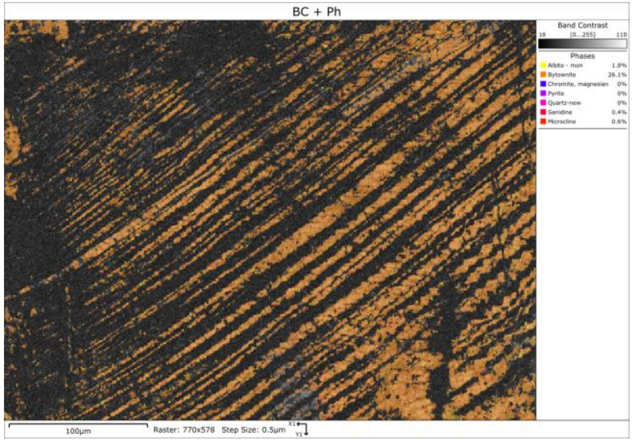
BC + Ph

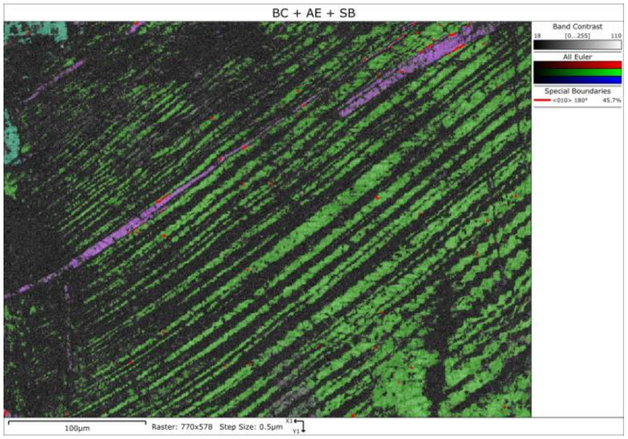
BC + AE + SB

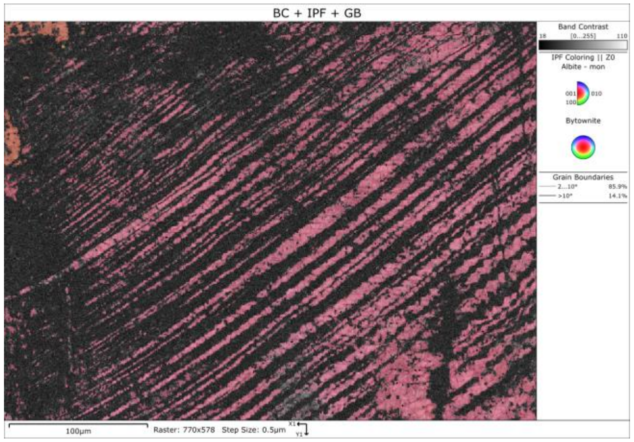
BC + IPF + GB

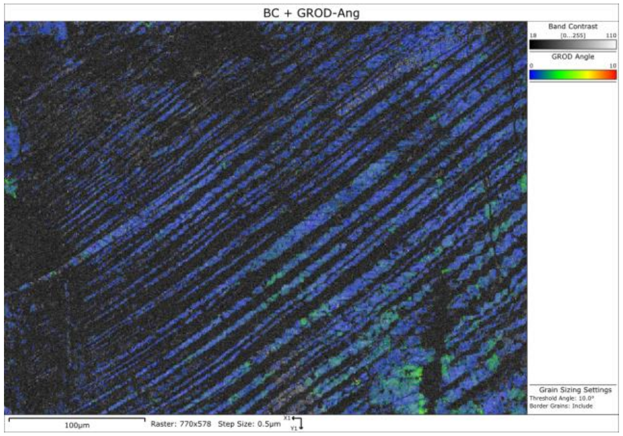
BC + GROD-Ang

Grain Sizing Settings
Threshold Angle: 10.0°
Border Grains: Include

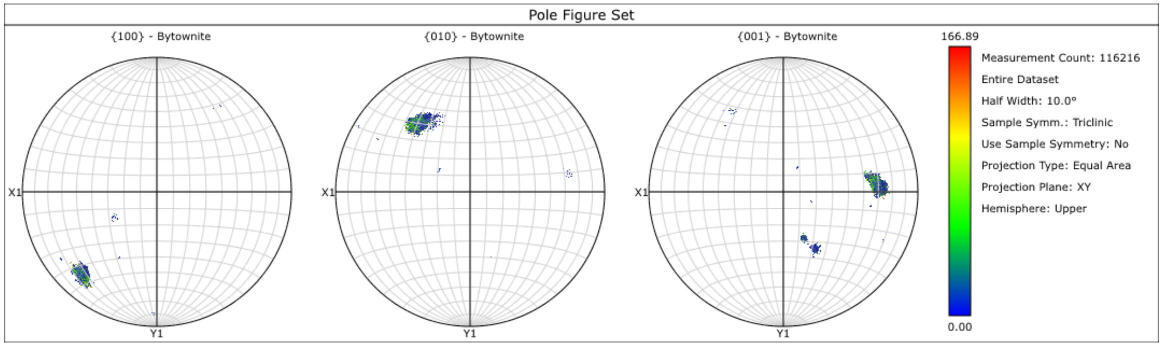
Pole Figure Set

Measurement Count: 116216
Entire Dataset
Half Width: 10.0°
Sample Symm.: Triclinic
Use Sample Symmetry: No
Projection Type: Equal Area
Projection Plane: XY
Hemisphere: Upper

6.5 Appendix E: EPMA Data

Table A – Beam Operating Conditions

Beam operating conditions and calibrations standards	
Accelerating voltage	15 KeV
Probe current	4 nA (condition 1) and 100 nA (condition 2)

Element	Standard
Na	Jadeite-BL7
Al	Jadeite-BL7
Si	Qz
Ca	Wollastonite-BL7
Mg	Spinel-BL8
K	Orthoclase-BL7
Sr	Celestite-Bl7
Ti	Rutile-BL8
Mn	PuMn -BL8
Fe	Fayalite
Ba	Barite-BL7

Table B – Raw EPMA data in wt. %

Raw data (wt. %)															
			Element (wt. %)												
Sample	Site	Point	Na	Si	Al	Ca	Mg	K	Sr	Ti	Mn	Fe	Ba	O	Total
CHX-1160.7	1	1	7.62	29.75	10.04	0.66	0.00	0.17	0.04	0.00	0.00	0.01	0.02	45.79	94.10
CHX-1160.7	1	2	7.87	30.63	10.83	0.99	0.00	0.18	0.06	0.00	0.01	0.03	0.01	47.72	98.34
CHX-1160.7	1	5	7.08	29.59	11.79	2.87	0.00	0.22	0.08	0.00	0.00	0.07	0.00	47.89	99.59
CHX-1160.7	1	6	6.85	29.09	11.90	3.09	0.02	0.33	0.13	0.00	0.01	0.12	0.01	47.49	99.03
CHX-1160.7	1	7	7.24	29.92	11.60	2.53	0.01	0.30	0.11	0.00	0.00	0.10	0.03	48.06	99.90
CHX-1160.7	1	3	7.82	31.09	11.20	1.20	0.00	0.29	0.07	0.00	0.01	0.04	0.01	48.68	100.41
CHX-1160.7	1	8	6.97	29.87	12.03	2.94	0.00	0.28	0.06	0.00	0.00	0.04	-0.02	48.41	100.58
CHX-1160.7	1	4	7.97	30.91	11.07	1.22	0.01	0.24	0.10	0.00	0.00	0.08	0.00	48.43	100.04
CHX-1160.7	2	1	6.96	29.68	12.31	3.10	0.02	0.20	0.13	0.00	0.00	0.05	0.03	48.51	100.98
CHX-1160.7	2	6	7.74	30.69	11.59	1.82	0.00	0.20	0.10	0.00	0.01	0.01	0.00	48.77	100.92
CHX-1160.7	2	7	7.86	30.61	11.46	1.85	0.00	0.19	0.09	0.00	-0.01	0.01	0.00	48.60	100.65
CHX-1160.7	2	2	6.85	29.61	12.63	3.50	0.01	0.17	0.17	0.00	0.00	0.10	0.03	48.85	101.91
CHX-1160.7	2	3	6.67	29.39	12.54	3.52	0.00	0.15	0.12	0.00	-0.01	0.04	0.02	48.42	100.86
CHX-1160.7	2	4	6.62	29.32	12.51	3.54	0.00	0.37	0.19	0.00	0.00	0.12	0.01	48.39	101.06
CHX-1160.7	2	5	6.69	29.38	12.34	3.35	0.00	0.36	0.17	0.00	0.00	0.12	0.03	48.26	100.70
CHX-1160.7	3	1	6.95	29.83	11.96	2.92	0.00	0.21	0.12	0.00	-0.01	0.08	0.00	48.29	100.34
CHX-1160.7	3	2	6.50	29.42	12.48	3.47	0.00	0.40	0.10	0.00	0.01	0.09	0.01	48.40	100.87
CHX-1160.7	3	3	6.71	29.32	12.42	3.84	0.00	0.23	0.13	0.00	0.00	0.11	0.01	48.42	101.17
CHX-1160.7	3	4	6.63	29.32	12.58	3.89	0.00	0.23	0.12	0.00	0.00	0.11	0.00	48.56	101.44
CHX-1160.7	3	5	6.58	29.08	12.49	3.69	0.00	0.23	0.12	0.00	0.00	0.12	-0.01	48.11	100.42
CHX-1160.7	3	6	6.78	29.45	12.30	3.32	0.01	0.36	0.11	0.00	-0.01	0.12	-0.01	48.32	100.76
CHX-1160.7	3	7	6.68	29.28	12.53	3.68	0.00	0.25	0.13	0.00	0.00	0.11	0.01	48.41	101.08
CHX-1160.7	3	8	6.67	29.47	12.35	3.67	0.00	0.30	0.13	0.00	0.00	0.12	0.02	48.48	101.21
CHX-1160.7	3	9	6.64	29.19	12.52	3.69	0.00	0.30	0.12	0.00	0.01	0.10	0.02	48.30	100.89
CHX-1160.7	3	10	6.99	29.46	12.21	3.21	0.03	0.74	0.12	0.00	0.00	0.13	0.04	48.38	101.31

CHX-1160.7	3	11	6.35	29.28	12.80	3.95	0.00	0.25	0.14	0.00	0.00	0.10	0.01	48.64	101.53
CHX-1160.7	3	12	7.06	29.37	11.97	3.10	0.00	0.10	0.10	0.00	0.00	0.08	0.01	47.88	99.68
CHX-1160.7	6	1a	6.47	29.36	12.24	3.32	0.00	0.30	0.10	0.00	-0.01	0.11	0.02	48.02	99.91
CHX-1160.7	6	1b	6.54	29.40	11.91	2.99	0.00	0.35	0.08	0.00	0.01	0.10	0.01	47.68	99.08
CHX-1160.7	6	1c	6.81	29.25	12.08	3.09	0.00	0.26	0.09	0.00	0.01	0.11	0.00	47.77	99.47
CHX-1160.7	6	2a	0.44	29.48	9.31	0.05	0.00	11.29	0.11	-0.05	0.00	0.06	0.47	44.41	95.57
CHX-1160.7	6	2b	0.40	29.50	9.54	0.02	0.00	11.46	0.07	-0.05	0.01	0.01	0.48	44.62	96.03
CHX-1160.7	6	2c	0.31	29.74	9.60	0.01	0.00	11.76	0.07	-0.03	0.00	0.01	0.26	44.96	96.68
CHX-1160.7	6	3a	6.99	29.71	11.56	2.42	- 0.01	0.21	0.11	0.00	0.00	0.09	0.01	47.63	98.74
CHX-1160.7	6	3b	6.77	29.20	11.79	2.93	0.00	0.22	0.10	0.00	0.00	0.09	0.01	47.37	98.46
CHX-1160.7	6	3c	6.88	29.50	11.93	2.86	0.00	0.20	0.10	0.00	0.00	0.08	0.01	47.85	99.41
CHX-1160.7	6	4a	0.30	29.81	9.56	0.03	0.00	11.77	0.08	-0.04	0.00	0.06	0.35	45.04	96.97
CHX-1160.7	6	4b	0.39	29.83	9.72	0.03	0.00	11.72	0.07	-0.04	0.00	0.05	0.31	45.22	97.31
CHX-1160.7	6	4c	0.49	29.97	9.46	0.02	0.00	11.48	0.07	-0.03	0.01	0.07	0.27	45.13	96.92
CHX-1160.7	6	5a	7.10	29.22	11.51	2.55	0.00	0.18	0.14	0.00	0.00	0.11	-0.01	47.11	97.91
CHX-1160.7	6	5b	7.52	30.92	11.27	1.31	0.00	0.13	0.21	0.00	0.00	0.05	0.02	48.46	99.87
CHX-1160.7	6	5c	8.04	31.06	10.83	0.94	0.00	0.09	0.12	0.00	-0.01	0.03	-0.01	48.23	99.32
CHX-1160.7	6	6a	0.28	30.06	9.65	0.02	0.00	11.76	0.03	-0.01	0.00	0.05	0.09	45.37	97.30
CHX-1160.7	6	6b	0.38	30.08	9.48	0.01	0.00	11.55	0.08	-0.01	0.01	0.05	0.07	45.24	96.93
CHX-1160.7	6	6c	0.47	30.07	9.60	0.01	0.00	11.54	0.09	-0.02	0.00	0.05	0.20	45.38	97.39
CHX-1160.7	7	1a	6.87	29.48	11.99	2.66	0.00	0.06	0.11	0.00	0.01	0.06	0.00	47.76	99.01
CHX-1160.7	7	1b	6.84	29.61	12.01	2.93	0.00	0.08	0.09	0.00	0.00	0.08	0.01	48.03	99.68
CHX-1160.7	7	1c	6.69	29.08	12.02	3.30	0.01	0.21	0.14	0.00	-0.01	0.11	0.01	47.57	99.13
CHX-1160.7	7	2a	0.44	29.77	9.45	0.03	0.00	11.38	0.10	-0.04	0.00	0.07	0.38	44.88	96.47
CHX-1160.7	7	2b	0.46	30.00	9.70	0.01	0.00	11.48	0.05	-0.02	0.00	0.07	0.21	45.36	97.31
CHX-1160.7	7	2c	0.44	29.70	9.46	0.03	0.00	11.35	0.04	-0.02	0.00	0.07	0.22	44.78	96.07
CHX-1160.7	7	3a	6.81	29.25	11.79	2.99	0.00	0.05	0.14	0.00	0.00	0.03	0.01	47.42	98.48
CHX-1160.7	7	3b	6.87	29.71	11.56	2.30	0.00	0.07	0.14	0.00	0.00	0.04	0.01	47.49	98.20
CHX-1160.7	7	3c	6.87	29.31	11.79	2.79	0.00	0.10	0.16	0.00	0.00	0.03	0.01	47.44	98.49

CHX-1160.7	7	4a	6.47	28.64	12.26	3.56	0.00	0.11	0.13	0.00	0.00	0.10	0.01	47.29	98.57
CHX-1160.7	7	4b	6.21	26.43	8.81	0.61	0.00	0.26	0.05	0.00	-0.01	0.01	0.00	40.42	82.80
CHX-1160.7	7	4c	8.03	30.92	10.52	0.69	0.02	0.19	0.04	0.00	0.00	0.06	0.00	47.73	98.21
CHX-1160.7	7	5a	7.00	29.74	12.08	2.79	0.00	0.08	0.12	0.00	0.00	0.08	0.01	48.24	100.13
CHX-1160.7	7	5b	7.20	30.05	11.80	2.45	0.00	0.09	0.11	0.00	-0.01	0.05	0.00	48.27	100.02
CHX-1160.7	7	5c	6.46	29.02	12.29	3.69	0.00	0.12	0.11	0.00	0.00	0.10	0.01	47.79	99.59
CHX-1160.7	7	6a	6.64	28.82	11.67	3.05	0.00	0.17	0.10	0.00	0.01	0.12	0.00	46.83	97.41
CHX-1160.7	7	6b	6.74	29.22	11.82	3.22	0.00	0.08	0.13	0.00	0.00	0.12	0.01	47.51	98.85
CHX-1160.7	7	6c	6.57	28.68	11.60	3.11	0.00	0.26	0.12	0.00	-0.01	0.13	0.01	46.63	97.11
CHX-1160.7	7	7a	0.34	29.56	9.49	0.04	0.00	11.43	0.05	-0.04	0.00	0.07	0.31	44.64	95.90
CHX-1160.7	7	7b	0.28	29.41	9.40	0.01	0.00	11.64	0.06	-0.04	0.00	0.05	0.42	44.39	95.60
CHX-1160.7	7	7c	0.47	29.53	9.56	0.01	0.00	11.41	0.04	-0.04	0.01	0.03	0.40	44.69	96.10
CHX-1160.7	11	1	8.35	30.87	11.03	1.15	0.00	0.14	0.11	0.00	0.00	0.07	0.00	48.42	100.15
CHX-1160.7	11	2	9.11	32.37	10.29	0.02	0.00	0.02	0.02	0.00	0.01	0.01	-0.02	49.23	101.06
CHX-1160.7	11	3	8.50	31.62	10.85	0.33	0.04	0.18	0.04	0.00	0.01	0.09	0.00	48.87	100.53
CHX-1160.7	11	4	8.98	32.29	10.22	0.06	-0.01	0.02	0.02	0.00	-0.01	0.01	0.00	49.04	100.62
CHX-1160.7	11	5	7.57	29.98	11.43	2.34	0.00	0.14	0.10	0.00	0.00	0.06	0.00	47.96	99.58
CHX-1199.6	5	1a	8.05	30.79	11.38	1.56	0.01	0.11	0.13	0.00	0.01	0.06	-0.01	48.70	100.80
CHX-1199.6	5	1b	8.43	31.93	10.97	0.68	0.00	0.09	0.12	0.00	0.00	0.05	0.01	49.39	101.67
CHX-1199.6	5	1c	8.26	31.45	11.12	0.92	0.05	0.42	0.17	0.00	0.00	0.13	0.00	49.16	101.68
CHX-1199.6	5	2a	7.36	29.68	11.68	2.46	0.00	0.26	0.04	0.00	0.00	0.08	-0.01	47.83	99.37
CHX-1199.6	5	2b	7.49	29.73	11.58	2.36	0.00	0.28	0.02	0.00	-0.01	0.09	0.01	47.80	99.34
CHX-1199.6	5	2c	7.55	31.09	11.58	1.75	0.00	0.36	0.02	0.00	-0.01	0.09	0.00	49.15	101.59
CHX-1199.6	5	2d	7.68	30.61	11.68	2.12	0.00	0.27	0.02	0.00	0.00	0.07	0.01	48.87	101.35
CHX-1199.6	5	2e	7.76	31.00	11.32	1.96	0.00	0.24	0.04	0.00	0.00	0.08	0.03	48.96	101.40
CHX-1199.6	5	3a	6.83	32.01	10.17	0.23	0.00	0.16	0.05	0.00	0.00	0.09	0.02	48.05	97.60
CHX-1199.6	5	3b	8.15	30.93	10.88	1.38	0.00	0.11	0.05	0.00	0.00	0.04	0.02	48.34	99.90
CHX-1199.6	5	3c	8.41	31.46	10.27	0.06	0.00	3.65	0.03	-0.01	0.00	0.04	0.05	48.69	102.66
CHX-1199.6	5	3d	8.63	31.90	10.61	0.60	0.00	0.13	0.08	0.00	0.01	0.05	0.02	49.08	101.09

CHX-1199.6	5	3e	8.59	31.71	10.84	0.82	0.00	0.14	0.08	0.00	0.00	0.04	0.00	49.14	101.34
CHX-1199.6	5	3f	8.34	31.44	10.90	0.95	0.00	0.26	0.08	0.00	0.00	0.07	0.00	48.89	100.94
CHX-1199.6	5	4a	0.55	30.42	9.68	0.03	0.00	13.24	0.00	0.00	0.01	0.05	0.03	46.20	100.21
CHX-1199.6	5	4b	0.46	30.51	9.77	0.02	0.00	13.58	0.02	0.00	0.00	0.05	0.00	46.43	100.85
CHX-1199.6	5	4c	0.34	30.31	9.73	0.03	0.00	13.59	0.03	0.00	0.00	0.03	0.07	46.11	100.23
CHX-1199.6	5	5a	0.92	30.27	9.75	0.01	0.00	13.39	0.02	0.00	0.00	0.06	0.03	46.25	100.71
CHX-1199.6	5	5b	0.51	30.45	9.55	0.01	0.00	13.53	0.01	0.00	0.00	0.06	0.00	46.16	100.30
CHX-1199.6	5	5c	0.44	30.30	9.65	0.01	0.00	13.74	0.04	0.00	0.00	0.05	0.03	46.10	100.35
CHX-1199.6	5	6a	6.26	30.89	11.27	1.80	0.00	0.15	0.03	0.00	0.00	0.09	-0.01	48.18	98.67
CHX-1199.6	5	6b	6.20	30.70	11.50	1.98	0.02	0.18	0.03	0.00	0.00	0.10	0.00	48.24	98.96
CHX-1199.6	5	6c	5.97	30.37	11.63	2.27	0.00	0.15	0.04	0.00	0.00	0.09	0.01	47.99	98.51
CHX-1199.6	7	1a	0.34	30.20	9.49	0.03	0.00	13.76	0.04	-0.02	0.00	0.09	0.17	45.84	99.96
CHX-1199.6	7	1b	0.28	30.39	9.56	0.03	0.00	13.79	0.04	-0.01	0.00	0.06	0.09	46.09	100.32
CHX-1199.6	7	1c	0.31	30.22	9.51	0.02	0.00	13.76	0.03	0.00	0.00	0.06	0.07	45.85	99.83
CHX-1199.6	7	1d	0.22	30.22	9.51	0.02	0.00	14.14	0.04	-0.01	0.01	0.04	0.11	45.89	100.19
CHX-1199.6	7	3a	8.58	31.78	10.62	0.70	-0.01	0.49	0.05	0.00	0.00	0.07	0.01	49.04	101.33
CHX-1199.6	7	3b	8.69	32.13	10.66	0.46	0.00	0.13	0.04	0.00	0.00	0.06	0.02	49.34	101.52
CHX-1199.6	7	3c	8.96	32.20	10.42	0.27	-0.01	0.08	0.05	0.00	0.01	0.04	0.01	49.23	101.26
CHX-1199.6	7	3d	8.78	31.95	10.57	0.48	0.00	0.12	0.07	0.00	0.01	0.18	0.00	49.14	101.30
CHX-1199.6	7	4a	7.62	30.66	11.31	2.26	0.00	0.32	0.01	0.00	0.01	0.09	0.01	48.64	100.93
CHX-1199.6	7	4b	7.69	30.66	11.60	2.21	0.00	0.33	0.01	0.00	0.01	0.09	-0.01	48.90	101.49
CHX-1199.6	7	4c	7.43	30.63	11.54	2.23	0.00	0.37	0.02	0.00	-0.01	0.09	-0.01	48.75	101.06
CHX-1199.6	7	4d	7.59	30.71	11.41	2.25	0.00	0.44	0.04	0.00	0.00	0.09	0.00	48.80	101.32
CHX-1199.6	7	2a	0.37	30.46	9.75	0.06	0.00	13.61	0.04	0.00	-0.01	0.06	0.04	46.33	100.70
CHX-1199.6	7	2b	0.45	30.26	9.69	0.07	0.00	13.65	0.04	0.00	0.00	0.10	0.04	46.12	100.43
CHX-1199.6	7	2c	0.99	30.29	9.64	0.05	0.00	13.57	0.03	0.00	0.01	0.06	0.01	46.25	100.89
CHX-1199.6	7	2d	0.50	30.52	9.60	0.03	0.00	13.53	0.03	0.00	0.01	0.05	0.01	46.29	100.58
CHX-1199.6	7	5a	7.30	30.06	11.91	2.83	0.00	0.10	0.08	0.00	0.00	0.06	0.01	48.56	100.90

CHX-1199.6	7	5b	7.42	30.25	11.95	2.72	0.00	0.09	0.07	0.00	0.00	0.06	0.00	48.81	101.36
CHX-1199.6	7	5c	7.14	30.12	12.21	2.89	0.00	0.20	0.08	0.00	0.01	0.10	-0.01	48.91	101.65
CHX-1199.6	7	5d	7.27	29.88	11.80	2.90	0.00	0.13	0.07	0.00	0.00	0.10	0.01	48.29	100.43
CHX-1199.6	7	6a	8.56	32.04	10.93	0.61	0.00	0.15	0.12	0.00	0.00	0.10	0.02	49.54	102.08
CHX-1199.6	7	6b	8.15	31.05	11.49	1.49	0.00	0.13	0.07	0.00	0.00	0.07	0.01	49.09	101.55
CHX-1199.6	7	6c	8.60	31.68	10.74	0.73	-0.01	0.10	0.05	0.00	0.01	0.06	-0.01	48.97	100.92
CHX-1199.6	7	6d	8.66	31.62	10.43	0.28	0.00	0.10	0.05	0.00	0.01	0.08	0.00	48.48	99.71
CHX-1199.6	7	7a	8.67	31.59	10.63	0.52	0.00	0.11	0.17	0.00	0.00	0.03	0.01	48.74	100.47
CHX-1199.6	7	7b	8.48	31.55	10.78	0.71	0.00	0.22	0.17	0.00	0.00	0.10	0.01	48.87	100.89
CHX-1199.6	7	7c	8.40	31.66	10.92	0.86	0.00	0.13	0.13	0.00	0.00	0.13	-0.01	49.14	101.36
CHX-1199.6	7	7d	8.65	31.84	10.92	0.86	0.00	0.16	0.11	0.00	0.00	0.12	0.00	49.43	102.09
CHX-1199.6	8	1a	7.21	30.03	12.04	2.71	0.00	0.20	0.06	0.00	0.00	0.09	0.00	48.59	100.94
CHX-1199.6	8	1b	7.76	30.48	11.46	2.19	0.00	0.14	0.06	0.00	0.00	0.04	-0.01	48.54	100.66
CHX-1199.6	8	1c	7.61	30.63	11.67	2.29	0.00	0.18	0.05	0.00	0.00	0.08	0.00	48.91	101.41
CHX-1199.6	8	1d	7.48	30.47	11.58	2.39	0.00	0.22	0.05	0.00	-0.01	0.09	-0.01	48.66	100.93
CHX-1199.6	8	2a	0.24	30.07	9.84	0.02	0.00	13.71	0.04	-0.04	0.00	0.06	0.34	45.94	100.22
CHX-1199.6	8	2b	0.40	30.28	9.59	0.02	0.00	13.53	0.05	-0.02	0.00	0.05	0.17	45.98	100.06
CHX-1199.6	8	2c	0.56	30.40	9.49	0.04	0.00	13.46	0.05	-0.01	0.01	0.06	0.10	46.09	100.26
CHX-1199.6	8	2d	0.57	30.35	9.57	0.04	0.00	13.56	0.04	0.00	0.00	0.06	0.05	46.11	100.35
CHX-1199.6	8	3a	8.73	32.00	10.72	0.66	0.00	0.10	0.10	0.00	0.00	0.02	0.00	49.33	101.64
CHX-1199.6	8	3b	8.92	31.94	10.61	0.43	0.00	0.19	0.04	0.00	0.01	0.12	0.01	49.19	101.45
CHX-1199.6	8	3c	8.87	32.24	10.40	0.19	0.00	0.13	0.09	0.00	0.02	0.05	0.01	49.21	101.20
CHX-1199.6	8	3d	8.56	31.73	11.07	0.31	0.00	0.29	0.05	0.00	0.00	0.16	-0.01	49.21	101.38
CHX-1199.6	8	4a	8.77	32.26	10.58	0.48	0.00	0.13	0.09	0.00	0.00	0.12	0.01	49.49	101.95
CHX-1199.6	8	4b	8.56	32.02	10.70	0.44	-0.01	0.10	0.11	0.00	0.01	0.14	-0.01	49.23	101.30
CHX-1199.6	8	4c	8.58	32.07	10.81	0.59	0.00	0.18	0.10	0.00	0.02	0.20	-0.02	49.49	102.01
CHX-1199.6	8	4d	8.65	32.03	10.82	0.44	0.00	0.41	0.10	0.00	0.00	0.25	0.01	49.47	102.18
CHX-1199.6	8	5a	7.92	30.26	11.24	1.74	0.00	0.15	0.04	0.00	0.01	0.08	0.02	47.99	99.44

CHX-1199.6	8	5b	8.21	31.01	10.83	0.99	0.01	0.19	0.04	0.00	0.00	0.09	-0.01	48.29	99.65
CHX-1199.6	8	5c	8.25	31.17	10.99	1.37	0.01	0.17	0.05	0.00	-0.01	0.10	0.00	48.79	100.89
CHX-1199.6	8	5d	7.85	30.87	11.41	1.79	0.00	0.24	0.06	0.00	0.01	0.11	0.01	48.87	101.23
CHX-1199.6	8	6a	7.83	30.81	11.37	1.81	0.00	0.31	0.05	0.00	0.00	0.09	0.01	48.76	101.03
CHX-1199.6	8	6b	7.27	30.33	11.22	2.14	0.00	0.40	0.06	0.00	0.00	0.09	0.01	48.05	99.57
CHX-1199.6	8	6c	7.43	30.47	11.62	2.47	0.02	0.19	0.06	0.00	0.01	0.10	0.00	48.72	101.08
CHX-1199.6	8	6d	7.50	30.44	11.58	2.19	0.01	0.22	0.03	0.00	0.00	0.09	0.00	48.55	100.60
CHX-1199.6	8	7a	0.49	30.55	9.61	0.02	0.00	13.38	0.04	-0.02	0.00	0.02	0.16	46.29	100.55
CHX-1199.6	8	7b	0.64	30.66	9.66	0.03	0.00	12.14	0.04	-0.02	0.01	0.05	0.18	46.28	99.68
CHX-1199.6	8	7c	0.60	30.27	9.67	0.04	0.00	13.35	0.04	0.00	0.00	0.06	0.02	46.07	100.13
CHX-1199.6	8	7d	0.45	30.35	9.50	0.08	0.00	13.85	0.04	-0.01	0.00	0.14	0.10	46.10	100.58
CHX-1216.5	1	1a	0.22	0.47	0.29	0.13	0.00	0.01	0.02	0.00	0.01	0.01	0.03	48.17	100.00
CHX-1216.5	1	1b	0.23	0.47	0.29	0.13	0.00	0.01	0.02	0.00	0.01	0.01	0.03	48.46	100.65
CHX-1216.5	1	1c	0.23	0.46	0.29	0.13	0.00	0.01	0.02	0.00	0.01	0.01	0.03	47.86	99.54
CHX-1216.5	1	2a	0.24	0.48	0.27	0.07	0.00	0.01	0.02	0.00	0.01	0.01	0.03	48.43	99.84
CHX-1216.5	1	2b	0.20	0.46	0.30	0.06	0.00	0.02	0.02	0.00	0.01	0.01	0.03	46.31	95.19
CHX-1216.5	1	2c	0.23	0.47	0.28	0.06	0.00	0.02	0.02	0.00	0.01	0.01	0.03	48.56	101.02
CHX-1216.5	1	3a	0.02	0.46	0.25	0.01	0.00	0.31	0.02	0.00	0.01	0.01	0.04	45.51	98.45
CHX-1216.5	1	3b	0.01	0.46	0.25	0.01	0.00	0.31	0.02	0.00	0.01	0.01	0.03	45.82	98.95
CHX-1216.5	1	3c	0.01	0.46	0.25	0.01	0.00	0.31	0.02	0.00	0.01	0.01	0.03	45.58	98.39
CHX-1216.5	1	4a	0.22	0.46	0.28	0.13	0.00	0.01	0.02	0.00	0.01	0.01	0.03	47.57	98.87
CHX-1216.5	1	4b	0.22	0.47	0.28	0.13	0.00	0.01	0.02	0.00	0.01	0.01	0.03	47.92	99.38
CHX-1216.5	1	4c	0.22	0.46	0.28	0.13	0.00	0.01	0.02	0.00	0.01	0.01	0.03	47.61	98.78
CHX-1216.5	1	5a	0.01	0.45	0.25	0.01	0.00	0.30	0.02	0.00	0.01	0.01	0.03	44.81	96.36
CHX-1216.5	1	5b	0.01	0.45	0.25	0.01	0.00	0.30	0.02	0.00	0.01	0.01	0.03	44.79	96.51
CHX-1216.5	1	5c	0.01	0.45	0.25	0.01	0.00	0.30	0.02	0.00	0.01	0.01	0.03	44.87	96.46
CHX-1216.5	1	6a	0.24	0.48	0.27	0.07	0.00	0.01	0.02	0.00	0.01	0.01	0.03	47.84	98.53
CHX-1216.5	1	6b	0.22	0.46	0.28	0.06	0.00	0.01	0.02	0.00	0.01	0.01	0.03	45.82	93.83
CHX-1216.5	1	6c	0.23	0.47	0.27	0.08	0.00	0.01	0.02	0.00	0.01	0.01	0.03	47.61	97.92
CHX-1216.5	1	7a	0.01	0.45	0.25	0.01	0.00	0.31	0.02	0.00	0.01	0.01	0.03	44.82	96.90

CHX-1216.5	1	7b	0.01	0.45	0.25	0.01	0.00	0.30	0.02	0.00	0.01	0.01	0.03	44.66	96.18
CHX-1216.5	1	7c	0.01	0.45	0.25	0.01	0.00	0.31	0.02	0.00	0.01	0.01	0.03	44.75	96.51
CHX-1216.5	1	8a	0.24	0.47	0.27	0.08	0.00	0.01	0.02	0.00	0.01	0.01	0.03	47.86	98.97
CHX-1216.5	1	8b	0.23	0.47	0.27	0.07	0.00	0.01	0.03	0.00	0.01	0.01	0.03	47.04	96.89
CHX-1216.5	1	8c	0.24	0.47	0.27	0.07	0.00	0.01	0.02	0.00	0.01	0.01	0.03	47.86	98.69
CHX-1216.5	2	1a	0.22	0.46	0.28	0.13	0.00	0.01	0.02	0.00	0.01	0.01	0.03	47.33	98.11
CHX-1216.5	2	1b	0.22	0.46	0.28	0.13	0.00	0.01	0.02	0.00	0.01	0.01	0.03	47.70	99.05
CHX-1216.5	2	1c	0.22	0.46	0.28	0.13	0.00	0.01	0.02	0.00	0.01	0.01	0.03	47.74	99.04
CHX-1216.5	2	2a	0.02	0.46	0.25	0.01	0.00	0.30	0.02	0.00	0.01	0.01	0.03	45.54	97.90
CHX-1216.5	2	2b	0.02	0.46	0.25	0.01	0.00	0.30	0.02	0.00	0.01	0.01	0.03	45.23	97.19
CHX-1216.5	2	2c	0.01	0.46	0.25	0.01	0.00	0.30	0.02	0.00	0.01	0.01	0.03	45.16	97.12
CHX-1216.5	2	3a	0.22	0.47	0.29	0.13	0.00	0.01	0.02	0.00	0.01	0.01	0.03	48.06	99.67
CHX-1216.5	2	3b	0.22	0.46	0.28	0.13	0.00	0.01	0.02	0.00	0.01	0.01	0.03	47.55	98.74
CHX-1216.5	2	3c	0.22	0.47	0.28	0.12	0.00	0.01	0.02	0.00	0.01	0.01	0.03	47.68	98.67
CHX-1216.5	2	4a	0.22	0.47	0.28	0.08	0.00	0.01	0.02	0.00	0.01	0.01	0.03	48.15	98.98
CHX-1216.5	2	4b	0.22	0.47	0.28	0.13	0.00	0.01	0.02	0.00	0.01	0.01	0.03	47.62	98.85
CHX-1216.5	2	4c	0.22	0.46	0.29	0.13	0.00	0.01	0.02	0.00	0.01	0.01	0.03	48.05	99.75
CHX-1216.5	2	5a	0.01	0.45	0.25	0.01	0.00	0.31	0.02	0.00	0.01	0.01	0.03	44.86	96.49
CHX-1216.5	2	5b	0.01	0.46	0.25	0.01	0.00	0.30	0.02	0.00	0.01	0.01	0.03	45.59	97.91
CHX-1216.5	2	5c	0.01	0.45	0.25	0.01	0.00	0.31	0.02	0.00	0.01	0.01	0.03	44.40	95.59
CHX-1216.5	2	6a	0.24	0.48	0.27	0.05	0.00	0.01	0.02	0.00	0.01	0.01	0.03	49.01	100.77
CHX-1216.5	2	6b	0.24	0.48	0.27	0.05	0.00	0.01	0.02	0.00	0.01	0.01	0.03	48.70	100.10
CHX-1216.5	2	7a	0.24	0.48	0.27	0.04	0.00	0.01	0.02	0.00	0.01	0.01	0.03	48.64	99.90
CHX-1216.5	2	7b	0.24	0.48	0.27	0.05	0.00	0.01	0.02	0.00	0.01	0.01	0.03	48.38	99.49
CHX-1216.5	3	1a	6.85	29.85	11.62	0.39	0.09	1.81	0.07	0.00	0.02	0.26	0.01	47.41	98.39
CHX-1216.5	3	1b	8.43	31.14	10.22	0.34	0.00	0.09	0.15	0.00	0.01	0.11	0.00	47.72	98.20
CHX-1216.5	3	1c	7.52	29.97	11.07	0.32	0.07	1.88	0.12	0.00	0.02	0.24	0.03	47.26	98.50
CHX-1216.5	3	2a	0.80	28.60	9.53	0.04	0.00	10.31	0.19	-0.17	0.01	0.07	1.60	43.59	94.56
CHX-1216.5	3	2b	0.48	28.86	9.74	0.02	0.00	11.00	0.12	-0.19	0.00	0.07	1.77	44.09	95.96
CHX-1216.5	3	2c	0.58	29.05	9.66	0.04	0.00	11.17	0.17	-0.19	0.01	0.07	1.77	44.32	96.64

CHX-1216.5	3	3a	8.28	30.71	10.52	0.40	0.01	0.38	0.08	0.00	0.01	0.11	0.01	47.53	98.04
CHX-1216.5	3	3b	8.14	30.42	10.63	0.78	0.00	0.22	0.09	0.00	0.01	0.07	0.01	47.35	97.71
CHX-1216.5	3	3c	7.83	29.83	10.73	1.29	0.00	0.13	0.08	0.00	0.00	0.04	0.01	46.82	96.74
CHX-1216.5	3	4a	0.74	29.44	9.63	0.06	0.00	10.93	0.09	-0.14	0.00	0.06	1.24	44.71	96.76
CHX-1216.5	3	4b	0.50	29.64	9.98	0.09	0.00	11.22	0.07	-0.14	0.01	0.19	1.22	45.27	98.04
CHX-1216.5	3	4c	0.52	29.34	9.77	0.06	0.00	11.04	0.09	-0.11	0.01	0.13	1.05	44.69	96.59

6.6 Appendix F: Conference abstracts generated by this project

Submitted for the 84th Annual Meeting of the Meteoritical Society 2022

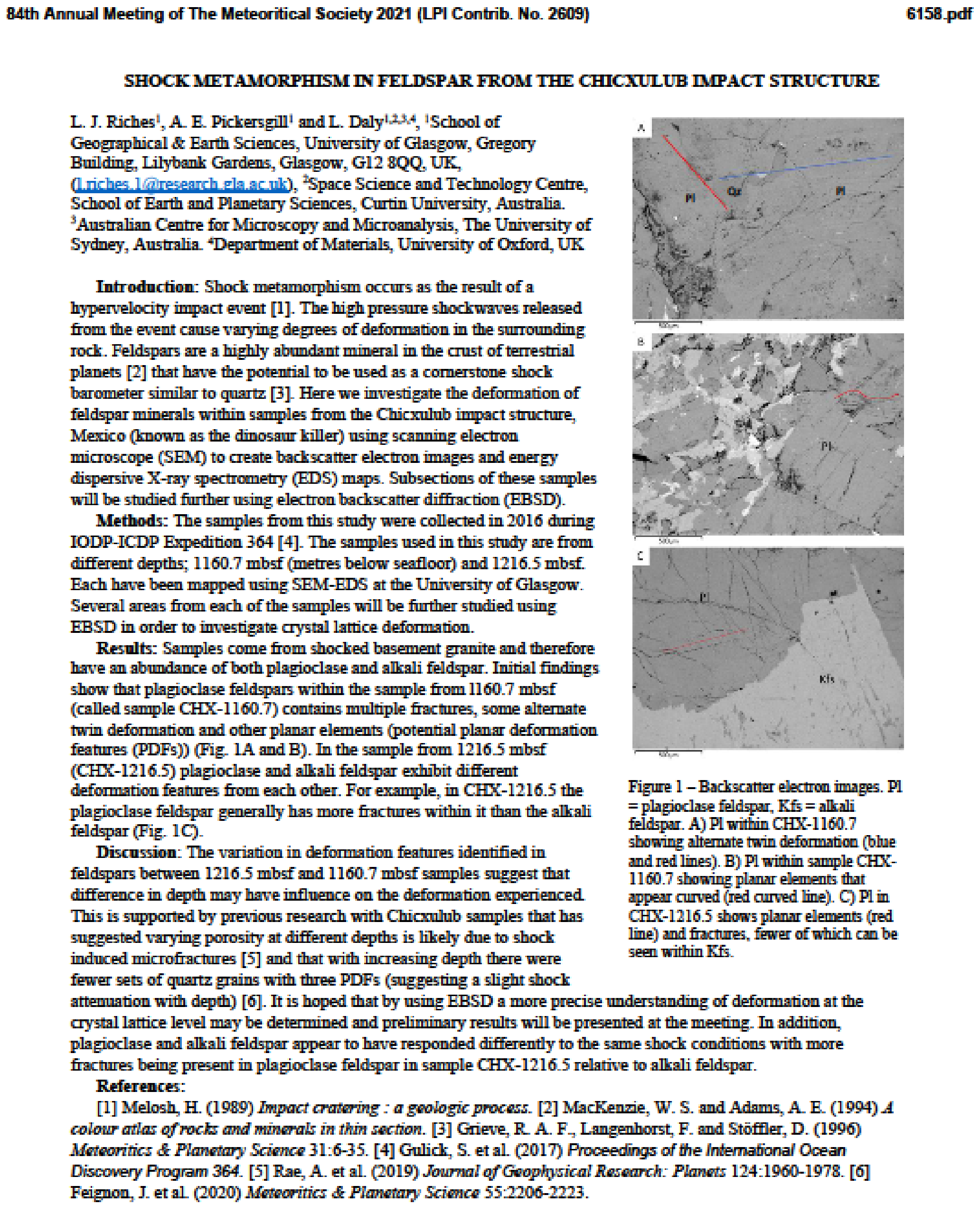

84th Annual Meeting of The Meteoritical Society 2021 (LPI Contrib. No. 2609) **6158.pdf**

SHOCK METAMORPHISM IN FELDSPAR FROM THE CHICXULUB IMPACT STRUCTURE

L. J. Riches[1], A. E. Pickersgill[1] and L. Daly[1,2,3,4], [1]School of Geographical & Earth Sciences, University of Glasgow, Gregory Building, Lilybank Gardens, Glasgow, G12 8QQ, UK, (l.riches.1@research.gla.ac.uk), [2]Space Science and Technology Centre, School of Earth and Planetary Sciences, Curtin University, Australia. [3]Australian Centre for Microscopy and Microanalysis, The University of Sydney, Australia. [4]Department of Materials, University of Oxford, UK

Introduction: Shock metamorphism occurs as the result of a hypervelocity impact event [1]. The high pressure shockwaves released from the event cause varying degrees of deformation in the surrounding rock. Feldspars are a highly abundant mineral in the crust of terrestrial planets [2] that have the potential to be used as a cornerstone shock barometer similar to quartz [3]. Here we investigate the deformation of feldspar minerals within samples from the Chicxulub impact structure, Mexico (known as the dinosaur killer) using scanning electron microscope (SEM) to create backscatter electron images and energy dispersive X-ray spectrometry (EDS) maps. Subsections of these samples will be studied further using electron backscatter diffraction (EBSD).

Methods: The samples from this study were collected in 2016 during IODP-ICDP Expedition 364 [4]. The samples used in this study are from different depths; 1160.7 mbsf (metres below seafloor) and 1216.5 mbsf. Each have been mapped using SEM-EDS at the University of Glasgow. Several areas from each of the samples will be further studied using EBSD in order to investigate crystal lattice deformation.

Results: Samples come from shocked basement granite and therefore have an abundance of both plagioclase and alkali feldspar. Initial findings show that plagioclase feldspars within the sample from 1160.7 mbsf (called sample CHX-1160.7) contains multiple fractures, some alternate twin deformation and other planar elements (potential planar deformation features (PDFs)) (Fig. 1A and B). In the sample from 1216.5 mbsf (CHX-1216.5) plagioclase and alkali feldspar exhibit different deformation features from each other. For example, in CHX-1216.5 the plagioclase feldspar generally has more fractures within it than the alkali feldspar (Fig. 1C).

Figure 1 – Backscatter electron images. Pl = plagioclase feldspar, Kfs = alkali feldspar. A) Pl within CHX-1160.7 showing alternate twin deformation (blue and red lines). B) Pl within sample CHX-1160.7 showing planar elements that appear curved (red curved line). C) Pl in CHX-1216.5 shows planar elements (red line) and fractures, fewer of which can be seen within Kfs.

Discussion: The variation in deformation features identified in feldspars between 1216.5 mbsf and 1160.7 mbsf samples suggest that difference in depth may have influence on the deformation experienced. This is supported by previous research with Chicxulub samples that has suggested varying porosity at different depths is likely due to shock induced microfractures [5] and that with increasing depth there were fewer sets of quartz grains with three PDFs (suggesting a slight shock attenuation with depth) [6]. It is hoped that by using EBSD a more precise understanding of deformation at the crystal lattice level may be determined and preliminary results will be presented at the meeting. In addition, plagioclase and alkali feldspar appear to have responded differently to the same shock conditions with more fractures being present in plagioclase feldspar in sample CHX-1216.5 relative to alkali feldspar.

References:

[1] Melosh, H. (1989) *Impact cratering : a geologic process.* [2] MacKenzie, W. S. and Adams, A. E. (1994) *A colour atlas of rocks and minerals in thin section.* [3] Grieve, R. A. F., Langenhorst, F. and Stöffler, D. (1996) *Meteoritics & Planetary Science* 31:6-35. [4] Gulick, S. et al. (2017) *Proceedings of the International Ocean Discovery Program 364.* [5] Rae, A. et al. (2019) *Journal of Geophysical Research: Planets* 124:1960-1978. [6] Feignon, J. et al. (2020) *Meteoritics & Planetary Science* 55:2206-2223.

Shock deformation in feldspar: Partial amorphisation in feldspar twins

L. J. Riches[1], A. E. Pickersgill[2] and L. Daly[1,3,4,5], [1]School of Geographical & Earth Sciences, University of Glasgow, Gregory Building, Lilybank Gardens, Glasgow, G12 8QQ, UK, (l.riches.1@research.gla.ac.uk),), [2]NERC Argon Isotope Facility, Scottish Universities Environmental Research Centre (SUERC), UK, [3]Australian Centre for Microscopy and Microanalysis, The University of Sydney, Australia. [4]Department of Materials, University of Oxford, UK

Introduction: The formation of hypervelocity impact structures causes shock deformation in the impacted material [1,2]. In this study, samples from the Chicxulub impact structure (Yucatán Peninsula, Mexico) have been investigated to study shock deformation in feldspar. Due to its high abundance [3], feldspar can be a useful tool in shock barometry. Feldspar from both the plagioclase and alkali feldspar series were identified in these samples with Na-rich plagioclase in particular containing more shock related deformation features than K-rich feldspar. These deformation features have since been investigated using the crystallographic technique electron backscatter diffraction (EBSD) and chemical changes within these microstructures have been investigated by energy dispersive X-ray spectroscopy (EDS) and electron probe microanalysis (EPMA).

Methods: The Chicxulub samples were collected in 2016 during the IODP-ICDP Expedition 364 [4]. Three samples were studied in this project (collected from depths 1160.7, 1199.6 and 1216.5 mbsf (metres below seafloor)). These samples have been analysed using optical microscopy, scanning electron microscopy (SEM), including backscatter electron (BSE) imaging and EDS mapping at the University of Glasgow. One sample (CHX_1160.7) was also analysed using EBSD at the University of Glasgow and EPMA collected at the University of Edinburgh.

Results: CHX-1160.7 was found to contain planar features in Na-rich feldspar. EBSD analysis of the areas containing planar features revealed that in some areas they were partially amorphized twins, alternating between amorphous and crystalline twins, evidenced by non-indexed and indexed llamellar regions in EBSD maps (Fig 1A). Interestingly, the chemistry of these partially amorphous twins is different from the neighbouring crystalline twins: the Ca content (which overall is no more than ~2.5 at. %) is ~1 at. % lower in the partially amorphous twins (i.e., more deformed twins have less Ca). When comparing the deformation features found in the Na-rich feldspar to K-rich feldspar, there were notably more deformation microstructures found in the Na-rich than the K-rich feldspar. The K-rich feldspar contained few deformation microstructures beyond fractures.

Discussion: This alternate twin deformation has been identified in shocked feldspar before [5,6], although the role of low level variations of Ca content in Na-rich feldspar twins that have been shocked has not been discussed. Based on the findings from this investigation it seems likely that partial amorphisation of alternating twins has influenced the Ca concentration post shock. It is also clear from these findings that Na-rich feldspar is more susceptible to shock than K-rich feldspar.

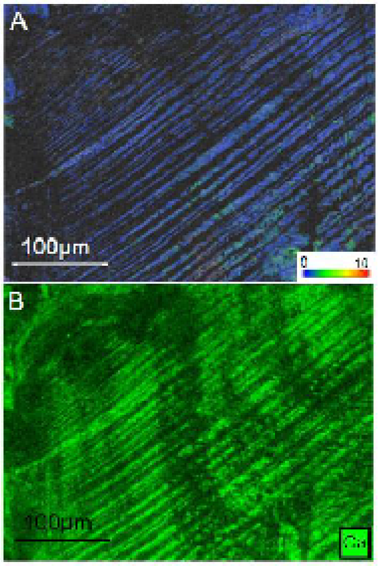

Figure 1 – A) GROD angle EBSD map showing the misorientation of an area within a Na-rich feldspar in sample CHX-1160.7. B) A false colour EDS map showing the distribution of Ca across the same area of Na-rich feldspar.

References: [1] Melosh, H. (1989) *Impact cratering: a geologic process.* [2] French, B & Koeberl, C. (2010) *Earth Science Reviews* 98:1-2. [3] MacKenzie, W. S. and Adams, A. E. (1994) *A colour atlas of rocks and minerals in thin section.* [4] Gulick, S. et al. (2017) *Proceedings of the International Ocean Discovery Program 364.* [5] Stöffler, D. (1966) *Contributions to mineralogy and petrology* 12:15–24. [6] Pickersgill, A, E. et al. (2015) *Meteoritics & Planetary Science 50:*1546–1561.

Submitted for the 3rd British Planetary Science Conference 2022

Shock deformation in feldspar in the Chicxulub impact structure

L. J. Riches[1], A. E. Pickersgill[2] and L. Daly[1,3,4,5], [1]School of Geographical & Earth Sciences, University of Glasgow, Gregory Building, Lilybank Gardens, Glasgow, G12 8QQ, UK, (l.riches.1@research.gla.ac.uk),), [2]NERC Argon Isotope Facility, Scottish Universities Environmental Research Centre (SUERC), UK, [3]Australian Centre for Microscopy and Microanalysis, The University of Sydney, Australia. [4]Department of Materials, University of Oxford, UK

Shock deformation is caused by a hypervelocity impact of two planetary bodies [1,2]. Shock barometry is the process of determining pressure to which material was exposed during impact. Feldspar group minerals are valuable tools in shock barometry due to their high abundance in Earth's crust [3]. Both Na-rich and K-rich feldspars from the Chicxulub impact structure have been analysed in this study. Shock deformation features have been characterised within these samples using a range of methods, primarily electron backscatter diffraction (EBSD).

Three samples were analysed in this study from the Chicxulub impact structure The samples were collected in 2016 during the IODP-ICDP Expedition 364 [4]. The three samples were collected from between 1160.7 and 1216.5 mbsf (metres below the seafloor) and were analysed using a range of methods. These methods were scanning electron microscopy (SEM), including backscatter electron (BSE) imaging and EDS mapping and optical microscopy (all at the University of Glasgow) and electron probe microanalysis (EPMA) which was carried out at the university of Edinburgh). One of the samples in this study was analysed further using EBSD to further investigate the shock microstructures found.

The Na-rich feldspar was found to contain more evidence of deformation than the K-rich feldspar in the same samples. One key feature found in Na-rich feldspar was the presence of partially amorphised alternating twins. Several EBSD maps showed alternating indexed and unindexed twins. The crystalline set of twins contain a low level of Ca (no more than ~2.5 at. %) however, the partially amorphous twins that alternate with these crystalline twins contain even less Ca (~1 at. %).

Deformation in alternating twins has been found in previous research [5,6]. The variation of Ca content across this alternate twin deformation in Na-rich feldspars has however not been as discussed before. Based on the evidence in this study it has been deemed more likely that this change in Ca content is due to partial amorphisation influencing Ca levels post shock.

References: [1] Melosh, H. (1989) *Impact cratering: a geologic process.* [2] French, B & Koeberl, C. (2010) *Earth Science Reviews* 98:1-2. [3] MacKenzie, W. S. and Adams, A. E. (1994) *A colour atlas of rocks and minerals in thin section.* [4] Gulick, S. et al. (2017) *Proceedings of the International Ocean Discovery Program 364. [5]* Stöffler, D. (1966) *Contributions to mineralogy and petrology* 12:15–24. [6] Pickersgill, A, E. et al. (2015) *Meteoritics & Planetary Science 50:*1546–1561.

6.7 Appendix G: Additional Optical Images

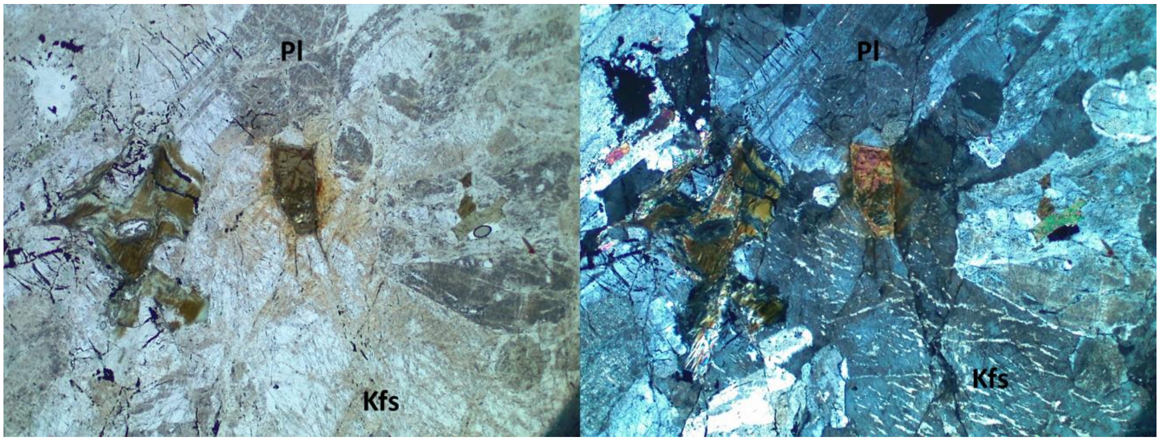

Figure 6.3 - Optical microscope images of an area from Sample CHX-1199.6. Pl = plagioclase feldspar and Kfs = K-rich feldspar. Right image is in PPL and left image is in XPL.

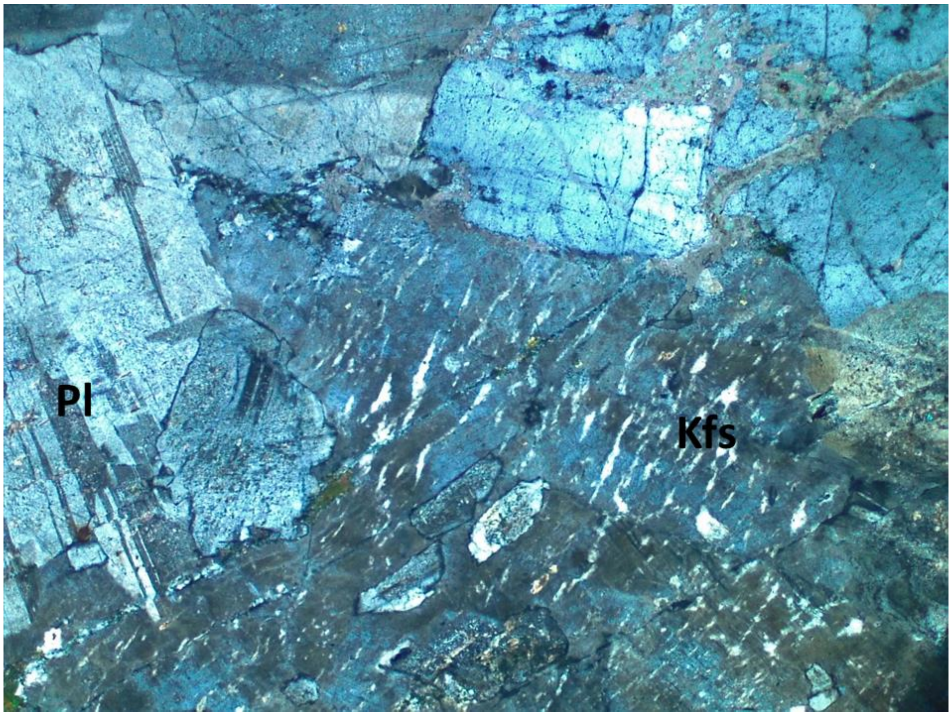

Figure 6.4 - XPL image of an area in Sample CHX-1216.5. Pl = plagioclase and Kfs = K-rich feldspar.

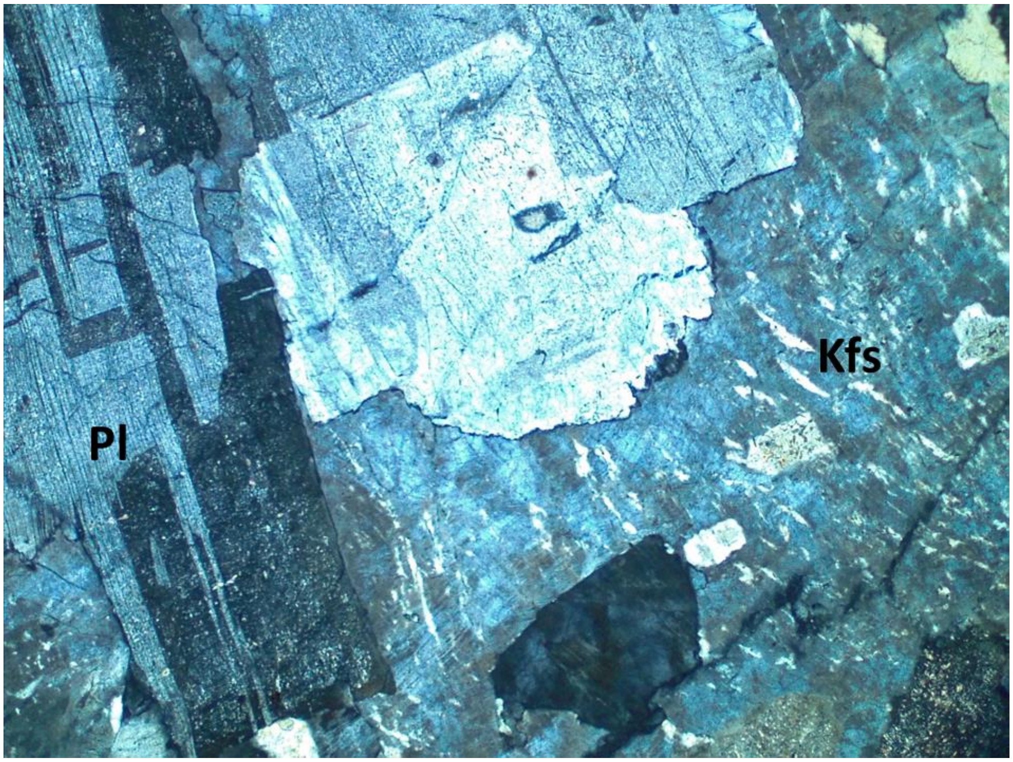

Figure 6.5 - XPL image of an area of Sample CHX-1216.5. Pl = plagioclase feldspar and Kfs - K-rich feldspar.

References

Albin, E. F., King, David. T. J., Jaret, S. J., Harris, R., & Jarrett, Robert. E. (2009, March). Alternate Twin Deformation in Plagioclase: Possible Evidence of Shock Deformation in Charnockitic Rocks Associated with the Woodbury Structure. *40th Lunar and Planetary Science Conference - Abstract #2544*.

Alvarez, L. W., Alvarez, W., Asaro, F., & Michel, H. v. (1980). Extraterrestrial Cause for the Cretaceous-Tertiary Extinction. *Science*, *208*(4448). https://doi.org/10.1126/science.208.4448.1095

Alvarez, W., Claeys, P., & Kieffer, S. W. (1995). Emplacement of Cretaceous-Tertiary Boundary Shocked Quartz from Chicxulub Crater. *Science*, *269*(5226), 930–935. https://doi.org/10.1126/science.269.5226.930

Bischoff, A., & Stöffler, D. (1984). Chemical and structural changes induced by thermal annealing of shocked feldspar inclusions in impact melt rocks from Lappajärvi Crater, Finland. *Journal of Geophysical Research*, *89*(S02), B645. https://doi.org/10.1029/JB089iS02p0B645

Bohor, B. F. (1990). Shock-induced microdeformations in quartz and other mineralogical indications of an impact event at the Cretaceous-Tertiary boundary. *Tectonophysics*, *171*(1–4), 359–372. https://doi.org/10.1016/0040-1951(90)90110-T

Cavosie, A. J., Timms, N. E., Ferrière, L., & Rochette, P. (2018). FRIGN zircon—The only terrestrial mineral diagnostic of high-pressure and high-temperature shock deformation. *Geology*, *46*(10), 891–894. https://doi.org/10.1130/G45079.1

Chao, E. C. T. (1966). Impact Metamorphism. *US Geological Survey Astrogeological Studies Annual Progress Report*, 135–164.

Chen, M., & el Goresy, A. (2000). The nature of maskelynite in shocked meteorites: not diaplectic glass but a glass quenched from shock-induced dense melt at high pressures. *Earth and Planetary Science Letters*, *179*(3–4). https://doi.org/10.1016/S0012-821X(00)00130-8

Cherniak, D. J., & Watson, E. B. (2019). Ca diffusion in K-Feldspar. *Lithos*, *348–349*, 105200. https://doi.org/10.1016/j.lithos.2019.105200

Cintala, M. J., & Grieve, R. A. F. (1998). Scaling impact melting and crater dimensions: Implications for the lunar cratering record. *Meteoritics & Planetary Science*, *33*(4), 889–912. https://doi.org/10.1111/j.1945-5100.1998.tb01695.x

Cockell, C. S., Lee, P., Osinski, G., Horneck, G., & Broady, P. (2002). Impact-induced microbial endolithic habitats. *Meteoritics & Planetary Science*, *37*(10). https://doi.org/10.1111/j.1945-5100.2002.tb01029.x

Cox, M. A., Erickson, T. M., Schmieder, M., Christoffersen, R., Ross, D. K., Cavosie, A. J., Bland, P. A., & Kring, D. A. (2020). High-resolution microstructural and compositional analyses of shock deformed apatite from the peak ring of the Chicxulub impact crater. *Meteoritics & Planetary Science*, *55*(8). https://doi.org/10.1111/maps.13541

Daly, L., Bland, P. A., Dyl, K. A., Forman, L. v., Saxey, D. W., Reddy, S. M., Fougerouse, D., Rickard, W. D. A., Trimby, P. W., Moody, S., Yang, L., Liu, H., Ringer, S. P., Saunders, M., & Piazolo, S. (2017). Crystallography of refractory metal nuggets in carbonaceous chondrites: A transmission Kikuchi diffraction approach. *Geochimica et Cosmochimica Acta*, *216*, 42–60. https://doi.org/10.1016/j.gca.2017.03.037

Daly, L., Lee, M. R., Piazolo, S., Griffin, S., Bazargan, M., Campanale, F., Chung, P., Cohen, B. E., Pickersgill, A. E., Hallis, L. J., Trimby, P. W., Baumgartner, R., Forman, L. v., & Benedix, G. K. (2019). Boom boom pow: Shock-facilitated aqueous alteration and evidence for two shock events in the Martian nakhlite meteorites. *Science Advances*, *5*(9). https://doi.org/10.1126/sciadv.aaw5549

Daniel, I., Gillet, P., McMillan, P. F., Wolf, G., & Verhelst, M. A. (1997). High-pressure behavior of anorthite: Compression and amorphization. *Journal of Geophysical Research: Solid Earth*, *102*(B5), 10313–10325. https://doi.org/10.1029/97JB00398

DePalma, R. A., Smit, J., Burnham, D. A., Kuiper, K., Manning, P. L., Oleinik, A., Larson, P., Maurrasse, F. J., Vellekoop, J., Richards, M. A., Gurche, L., & Alvarez, W. (2019). A seismically induced onshore surge deposit at the KPg boundary, North Dakota. *Proceedings of the National Academy of Sciences*, *116*(17), 8190–8199. https://doi.org/10.1073/pnas.1817407116

Dressler, B. (1990). Shock metamorphic features and their zoning and orientation in the Precambrian rocks of the Manicouagan Structure, Quebec, Canada. *Tectonophysics*, *171*(1–4). https://doi.org/10.1016/0040-1951(90)90101-D

Duff, D. (1993). *Holmes Principles of Physical Geology* (4th ed.). Chapman & Hall.

Feignon, J., FerriÈre, L., Leroux, H., & Koeberl, C. (2020). Characterization of shocked quartz grains from Chicxulub peak ring granites and shock pressure estimates. *Meteoritics & Planetary Science*, *55*(10). https://doi.org/10.1111/maps.13570

Ferrière, L., Koeberl, C., Ivanov, B. A., & Reimold, W. U. (2008). Shock Metamorphism of Bosumtwi Impact Crater Rocks, Shock Attenuation, and Uplift Formation. *Science*, *322*(5908), 1678–1681. https://doi.org/10.1126/science.1166283

French B. M. (1998). Traces of Catastrophe A Handbook of Shock-Metamorphic Effects in Terrestrial Meteorite Impact Structures. *LPI Contribution No. 954, Lunar and Planetary Institute, Houston.*, 120.

French, B. M., & Koeberl, C. (2010). The convincing identification of terrestrial meteorite impact structures: What works, what doesn’t, and why. *Earth-Science Reviews*, *98*(1–2). https://doi.org/10.1016/j.earscirev.2009.10.009

Fritz, J., Assis Fernandes, V., Greshake, A., Holzwarth, A., & Böttger, U. (2019). On the formation of diaplectic glass: Shock and thermal experiments with plagioclase of different chemical compositions. *Meteoritics & Planetary Science*, *54*(7). https://doi.org/10.1111/maps.13289

Glikson, A. Y. (2013). Precambrian Asteroid Impacts. In *The Asteroid Impact Connection of Planetary Evolution* (pp. 67–89). https://doi.org/10.1007/978-94-007-6328-9_8

Goldstein, J. I., Newbury, D. E., Echlin, P., Joy, D. C., Romig, A. D., Lyman, C. E., Fiori, C., & Lifshin, E. (1992). *Scanning Electron Microscopy and X-Ray Microanalysis*. Springer US. https://doi.org/10.1007/978-1-4613-0491-3

Goltrant, O., Cordier, P., & Doukhan, J.-C. (1991). Planar deformation features in shocked quartz; a transmission electron microscopy investigation. *Earth and Planetary Science Letters*, *106*(1–4), 103–115. https://doi.org/10.1016/0012-821X(91)90066-Q

Goltrant, O., Leroux, H., Doukhan, J.-C., & Cordier, P. (1992). Formation mechanisms of planar deformation features in naturally shocked quartz. *Physics of the Earth and Planetary Interiors*, *74*(3–4). https://doi.org/10.1016/0031-9201(92)90012-K

Götze, J., & Kempe, U. (2009). Physical Principles of Cathodoluminescence (CL) and its Applications in Geosciences. In *Cathodoluminescence and its Application in the Planetary Sciences* (pp. 1–22). Springer Berlin Heidelberg. https://doi.org/10.1007/978-3-540-87529-1_1

Grieve, R. A. F., Langenhorst, F., & Stöffler, D. (1996). Shock metamorphism of quartz in nature and experiment: II. Significance in geoscience*. *Meteoritics & Planetary Science*, *31*(1), 6–35. https://doi.org/10.1111/j.1945-5100.1996.tb02049.x

Grieve, R. A. F., Reny, G., Gurov, E. P., & Ryabenko, V. A. (1987). The melt rocks of the Boltysh impact crater, Ukraine, USSR. *Contributions to Mineralogy and Petrology*, *96*(1), 56–62. https://doi.org/10.1007/BF00375525

Grieve, R. A. F., & Robertson, P. B. (1979). The terrestrial cratering record. *Icarus*, *38*(2), 212–229. https://doi.org/10.1016/0019-1035(79)90179-9

Grieve, R., & Therriault, A. (2000). Vredefort, Sudbury, Chicxulub: Three of a Kind? *Annual Review of Earth and Planetary Sciences*, *28*(1). https://doi.org/10.1146/annurev.earth.28.1.305

Gulick, S., Morgan, J., Mellett, C. L., Green, S. L., Bralower, T., Chenot, E., Christeson, G., Claeys, P., Cockell, C., Coolen, M. J. L., Ferrière, L., Gebhardt, C., Goto, K., Jones, H., Kring, D., Lofi, J., Lowery, C., Ocampo-Torres, R., Perez-Cruz, L., … Zylberman, W. (2017). *Expedition 364 summary*. https://doi.org/10.14379/iodp.proc.364.101.2017

Haldar, S. K., & Tišljar, J. (2014). Basic Mineralogy. In *Introduction to Mineralogy and Petrology* (pp. 39–79). Elsevier. https://doi.org/10.1016/B978-0-12-408133-8.00002-X

Hammond, C. (2015). *The Basics of Crystallography and Diffraction*. Oxford University Press. https://doi.org/10.1093/acprof:oso/9780198738671.001.0001

Hildebrand, A. R., Penfield, G. T., Kring, D. A., Pilkington, M., Camargo Z., A., Jacobsen, S. B., & Boynton, W. v. (1991). Chicxulub Crater: A possible Cretaceous/Tertiary boundary impact crater on the Yucatán Peninsula, Mexico. *Geology*, *19*(9). https://doi.org/10.1130/0091-7613(1991)019<0867:CCAPCT>2.3.CO;2

Hildebrand, A. R., Pilkington, M., Connors, M., Ortiz-Aleman, C., & Chavez, R. E. (1995). Size and structure of the Chicxulub crater revealed by horizontal gravity gradients and cenotes. *Nature*, *376*(6539). https://doi.org/10.1038/376415a0

Holm, S., Alwmark, C., Alvarez, W., & Schmitz, B. (2011). Shock barometry of the Siljan impact structure, Sweden. *Meteoritics & Planetary Science*, *46*(12). https://doi.org/10.1111/j.1945-5100.2011.01303.x

Holm-Alwmark, S., Rae, A. S. P., Ferrière, L., Alwmark, C., & Collins, G. S. (2017a). Combining shock barometry with numerical modeling: Insights into complex crater formation-The example of the Siljan impact structure (Sweden). *Meteoritics & Planetary Science*, *52*(12). https://doi.org/10.1111/maps.12955

Holm-Alwmark, S., Rae, A. S. P., Ferrière, L., Alwmark, C., & Collins, G. S. (2017b). Combining shock barometry with numerical modeling: Insights into complex crater formation-The example of the Siljan impact structure (Sweden). *Meteoritics & Planetary Science*, *52*(12), 2521–2549. https://doi.org/10.1111/maps.12955

Hörz, F., & Quaide, W. L. (1973). Debye-scherrer investigations of experimentally shocked silicates. *The Moon*, *6*(1–2), 45–82. https://doi.org/10.1007/BF02630652

Jaret, S. J., Johnson, J. R., Sims, M., DiFrancesco, N., & Glotch, T. D. (2018). Microspectroscopic and Petrographic Comparison of Experimentally Shocked

Albite, Andesine, and Bytownite. *Journal of Geophysical Research: Planets*, *123*(7). https://doi.org/10.1029/2018JE005523

Jaret, S. J., Kah, L. C., & Harris, R. S. (2014). Progressive deformation of feldspar recording low-barometry impact processes, Tenoumer impact structure, Mauritania. *Meteoritics & Planetary Science*, *49*(6). https://doi.org/10.1111/maps.12310

Johnson, B. C., & Bowling, T. J. (2014). Where have all the craters gone? Earth's bombardment history and the expected terrestrial cratering record. *Geology*, *42*(7), 587–590. https://doi.org/10.1130/G35754.1

Johnson, J. R. (2012). Thermal infrared spectra of experimentally shocked andesine anorthosite. *Icarus*, *221*(1), 359–364. https://doi.org/10.1016/j.icarus.2012.08.012

Jung, H., Katayama, I., Jiang, Z., Hiraga, T., & Karato, S. (2006). Effect of water and stress on the lattice-preferred orientation of olivine. *Tectonophysics*, *421*(1–2). https://doi.org/10.1016/j.tecto.2006.02.011

Karato, S., Jung, H., Katayama, I., & Skemer, P. (2008). Geodynamic Significance of Seismic Anisotropy of the Upper Mantle: New Insights from Laboratory Studies. *Annual Review of Earth and Planetary Sciences*, *36*(1). https://doi.org/10.1146/annurev.earth.36.031207.124120

Kovaleva, E., & Habler, G. (2019). Spatial distribution of zircon with shock microtwins in pseudotachylite-bearing granite gneisses, Vredefort impact structure, South Africa. *Journal of Structural Geology*, *129*, 103890. https://doi.org/10.1016/j.jsg.2019.103890

Kring, D. A. (2005). Hypervelocity collisions into continental crust composed of sediments and an underlying crystalline basement: comparing the Ries (∼24 km) and Chicxulub (∼180 km) impact craters. *Geochemistry*, *65*(1). https://doi.org/10.1016/j.chemer.2004.10.003

Kubo, T., Kimura, M., Kato, T., Nishi, M., Tominaga, A., Kikegawa, T., & Funakoshi, K. (2010). Plagioclase breakdown as an indicator for shock conditions of meteorites. *Nature Geoscience*, *3*(1), 41–45. https://doi.org/10.1038/ngeo704

Lambert, P., & Grieve, R. A. F. (1984). Shock experiments on maskelynite-bearing anorthosite. *Earth and Planetary Science Letters*, *68*, 159–171.

Langenhorst, F., & Deutsch, A. (1994). Shock experiments on pre-heated α- and β-quartz: I. Optical and density data. *Earth and Planetary Science Letters*, *125*(1–4). https://doi.org/10.1016/0012-821X(94)90229-1

Larsson, D., Grönvold, K., Oskarsson, N., & Gunnlaugsson, E. (2002). Hydrothermal alteration of plagioclase and growth of secondary feldspar in the Hengill Volcanic Centre, SW Iceland. *Journal of Volcanology and Geothermal Research*, *114*(3–4), 275–290. https://doi.org/10.1016/S0377-0273(01)00267-0

Lee, M. R., Parsons, I., Edwards, P. R., & Martin, R. W. (2007). Identification of cathodoluminescence activators in zoned alkali feldspars by hyperspectral imaging and electron-probe microanalysis. *American Mineralogist*, *92*(2–3), 243–253. https://doi.org/10.2138/am.2007.2160

Levinson, A. A., & Taylor, S. R. (1971). THE MINERALS. In *Moon Rocks and Minerals* (pp. 45–96). Elsevier. https://doi.org/10.1016/B978-0-08-016669-8.50010-6

Lewis, J. A., & Jones, R. H. (2019). Primary feldspar in the Semarkona LL3.00 chondrite: Constraints on chondrule formation and secondary alteration. *Meteoritics & Planetary Science*, *54*(1), 72–89. https://doi.org/10.1111/maps.13194

Luu, V. N., Murakami, K., Samouh, H., Maruyama, I., Ohkubo, T., Tom, P. P., Chen, L., Kano, S., Yang, H., Abe, H., Suzuki, K., & Suzuki, M. (2021). Changes in properties of alpha-quartz and feldspars under 3 MeV Si-ion irradiation. *Journal of Nuclear Materials*, *545*. https://doi.org/10.1016/j.jnucmat.2020.152734

MacKenzie, W. S., & Adams, A. E. (1994). *A Colour Atlas of Rocks and Minerals in Thin Section*. CRC Press - Taylor & Francis Group.

McLaren, S., & Reddy, S. M. (2008). Automated mapping of K-feldspar by electron backscatter diffraction and application to 40Ar/39Ar dating. *Journal of Structural Geology*, *30*(10). https://doi.org/10.1016/j.jsg.2008.05.008

Morgan, J., Warner, M., the Chicxulub Working Group, Brittan, J., Buffler, R., Camargo, A., Christeson, G., Denton, P., Hildebrand, A., Hobbs, R., Macintyre, H., Mackenzie, G., Maguire, P., Marin, L., Nakamura, Y., Pilkington, M., Sharpton, V., Snyder, D., Suarez, G., & Trejo, A. (1997). Size and morphology of the Chicxulub impact crater. *Nature*, *390*(6659). https://doi.org/10.1038/37291

Morgan, J. v., Gulick, S. P. S., Bralower, T., Chenot, E., Christeson, G., Claeys, P., Cockell, C., Collins, G. S., Coolen, M. J. L., Ferrière, L., Gebhardt, C., Goto, K., Jones, H., Kring, D. A., le Ber, E., Lofi, J., Long, X., Lowery, C., Mellett, C., … Zylberman, W. (2016). The formation of peak rings in large impact craters. *Science*, *354*(6314), 878–882. https://doi.org/10.1126/science.aah6561

Mukai, H., Austrheim, H., Putnis, C. v., & Putnis, A. (2014). Textural Evolution of Plagioclase Feldspar across a Shear Zone: Implications for Deformation Mechanism and Rock Strength. *Journal of Petrology*, *55*(8). https://doi.org/10.1093/petrology/egu030

Nolze, G. (2015). Euler angles and crystal symmetry. *Crystal Research and Technology*, *50*(2). https://doi.org/10.1002/crat.201400427

Okrusch, M., & Frimmel, H. E. (2020). *Mineralogy*. Springer Berlin Heidelberg. https://doi.org/10.1007/978-3-662-57316-7

Ostertag, R. (1983). Shock experiments on feldspar crystals. *Journal of Geophysical Research*, *88*(S01). https://doi.org/10.1029/JB088iS01p0B364

Ostertag, R., & Stöffler, D. (1982). Thermal annealing of experimentally shocked feldspar crystals. *Journal of Geophysical Research*, *87*(S01), A457. https://doi.org/10.1029/JB087iS01p0A457

Oxford Instruments NanoAnalysis. (2020). Generating Orientation Maps to Present EBSD Data. *AZoM*.

Oxford Instruments Plc. (2021). *https://www.ebsd.com/solving-problems-with-ebsd/microstructure-visualization-in-sem*.

Parsons, I., Fitz Gerald, J. D., & Lee, M. R. (2015). Routine characterization and interpretation of complex alkali feldspar intergrowths. *American Mineralogist*, *100*(5–6), 1277–1303.

Parsons, I., & Lee, M. R. (2009). Mutual replacement reactions in alkali feldspars I: microtextures and mechanisms. *Contributions to Mineralogy and Petrology*, *157*(5), 641–661. https://doi.org/10.1007/s00410-008-0355-4

Parsons, I., Thompson, P., Lee, M. R., & Cayzer, N. (2005). Alkali Feldspar Microtextures as Provenance Indicators in Siliciclastic Rocks and Their Role in Feldspar Dissolution During Transport and Diagenesis. *Journal of Sedimentary Research*, *75*(5), 921–942. https://doi.org/10.2110/jsr.2005.071

Pickersgill*, A. E., Jaret, S. J., Pittarello, L., Fritz, J., & Harris, R. S. (2021). Shock effects in feldspars: An overview. In *Large Meteorite Impacts and Planetary Evolution VI* (pp. 507–535). Geological Society of America. https://doi.org/10.1130/2021.2550(23)

Pickersgill, A. E., Osinski, G. R., & Flemming, R. L. (2015). Shock effects in plagioclase feldspar from the Mistastin Lake impact structure, Canada. *Meteoritics & Planetary Science*, *50*(9), 1546–1561. https://doi.org/10.1111/maps.12495

Pittarello, L., Daly, L., PickersgilL, A. E., Ferrière, L., & Lee, M. R. (2020). Shock metamorphism in plagioclase and selective amorphization. *Meteoritics & Planetary Science*, *55*(5). https://doi.org/10.1111/maps.13494

Pittarello, L., Ferrière, L., Feignon, J., Osinski, G. R., & Koeberl, C. (2020). Preferred orientation distribution of shock-induced planar microstructures in quartz and feldspar. *Meteoritics & Planetary Science*, *55*(5). https://doi.org/10.1111/maps.13490

Pittarello, L., Fritz, J., Roszjar, J., Lenz, C., Chanmuang N., C., & Koeberl, C. (2020). Partial amorphization of experimentally shocked plagioclase: A spectroscopic study. *Meteoritics & Planetary Science*, *55*(3), 669–678. https://doi.org/10.1111/maps.13445

Pittarello, L., Schulz, T., Koeberl, C., Hoffmann, J. E., & Münker, C. (2013). Petrography, geochemistry, and Hf-Nd isotope evolution of drill core samples and target rocks from the El’gygytgyn impact crater, NE Chukotka, Arctic Russia. *Meteoritics & Planetary Science*, *48*(7). https://doi.org/10.1111/maps.12088

Plasmaterials. (2016, August 1). *Converting Atomic Percent to Weight Percent and Vice Versa*. https://www.plasmaterials.com/converting-atomic-percent-to-weight-percent-and-vice-versa/

Pope, K. O., Ocampo, A. C., Kinsland, G. L., & Smith, R. (1996). Surface expression of the Chicxulub crater. *Geology*, *24*(6). https://doi.org/10.1130/0091-7613(1996)024<0527:SEOTCC>2.3.CO;2

Prior, D. J., Mariani, E., & Wheeler, J. (2009). EBSD in the Earth Sciences: Applications, Common Practice, and Challenges. In *Electron Backscatter Diffraction in Materials Science*. Springer US. https://doi.org/10.1007/978-0-387-88136-2_26

Qin, F., & Beckingham, L. E. (2019). Impact of image resolution on quantification of mineral abundances and accessible surface areas. *Chemical Geology*, *523*, 31–41. https://doi.org/10.1016/j.chemgeo.2019.06.004

Reed, S. J. B. (2005a). Introduction. In *Electron Microprobe Analysis and Scanning Electron Microscopy in Geology* (pp. 1–6). Cambridge University Press. https://doi.org/10.1017/CBO9780511610561.002

Reed, S. J. B. (2005b). Scanning electron microscopy. In *Electron Microprobe Analysis and Scanning Electron Microscopy in Geology* (pp. 41–75). Cambridge University Press. https://doi.org/10.1017/CBO9780511610561.005

Renne, P. R., Deino, A. L., Hilgen, F. J., Kuiper, K. F., Mark, D. F., Mitchell, W. S., Morgan, L. E., Mundil, R., & Smit, J. (2013). Time Scales of Critical Events Around the Cretaceous-Paleogene Boundary. *Science*, *339*(6120). https://doi.org/10.1126/science.1230492

Rubin, A. E. (2015). Maskelynite in asteroidal, lunar and planetary basaltic meteorites: An indicator of shock pressure during impact ejection from their parent bodies. *Icarus*, *257*, 221–229. https://doi.org/10.1016/j.icarus.2015.05.010

Ruzicka, A. M., & Hugo, R. C. (2018). Electron backscatter diffraction (EBSD) study of seven heavily metamorphosed chondrites: Deformation systematics and variations in pre-shock temperature and post-shock annealing. *Geochimica et Cosmochimica Acta*, *234*. https://doi.org/10.1016/j.gca.2018.05.014

Ryder, G. (1990). Lunar samples, lunar accretion and the early bombardment of the Moon. *Eos, Transactions American Geophysical Union*, *71*(10), 313. https://doi.org/10.1029/90EO00086

Singleton, A. C., Osinski, G. R., McCausland, P. J. A., & Moser, D. E. (2011). Shock-induced changes in density and porosity in shock-metamorphosed crystalline rocks, Haughton impact structure, Canada. *Meteoritics & Planetary Science*, *46*(11). https://doi.org/10.1111/j.1945-5100.2011.01290.x

Stöffler, D. (1971). Progressive metamorphism and classification of shocked and brecciated crystalline rocks at impact craters. *Journal of Geophysical Research*, *76*(23). https://doi.org/10.1029/JB076i023p05541

Stöffler, D. (1984). Glasses formed by hypervelocity impact. *Journal of Non-Crystalline Solids*, *67*(1–3). https://doi.org/10.1016/0022-3093(84)90171-6

Stöffler, D., Artemieva, N. A., Ivanov, B. A., Hecht, L., Kenkmann, T., Schmitt, R. T., Tagle, R. A., & Wittmann, A. (2004). Origin and emplacement of the impact formations at Chicxulub, Mexico, as revealed by the ICDP deep drilling at Yaxcopoil-1 and by numerical modeling. *Meteoritics & Planetary Science*, *39*(7). https://doi.org/10.1111/j.1945-5100.2004.tb01128.x

Stöffler, D., Hamann, C., & Metzler, K. (2018). Shock metamorphism of planetary silicate rocks and sediments: Proposal for an updated classification system. *Meteoritics & Planetary Science*, *53*(1). https://doi.org/10.1111/maps.12912

Stöffler, D., & Langenhorst, F. (1994). Shock metamorphism of quartz in nature and experiment: I. Basic observation and theory*. *Meteoritics*, *29*(2). https://doi.org/10.1111/j.1945-5100.1994.tb00670.x

Stöffler, Dieter. (1966). Zones of impact metamorphism in the crystalline rocks of the Nördlinger Ries crater. *Contributions to Mineralogy and Petrology*, *12*(1), 15–24.

Svensson, N.-B. (1971). Probable Meteorite Impact Crater in Central Sweden. *Nature Physical Science*, *229*(3). https://doi.org/10.1038/physci229090a0

Timms, N. E., Kirkland, C. L., Cavosie, A. J., Rae, A. S. P., Rickard, W. D. A., Evans, N. J., Erickson, T. M., Wittmann, A., Ferrière, L., Collins, G. S., & Gulick, S. P. S. (2020).

Shocked titanite records Chicxulub hydrothermal alteration and impact age. *Geochimica et Cosmochimica Acta*, *281*, 12–30. https://doi.org/10.1016/j.gca.2020.04.031

Timms, N. E., Pearce, M. A., Erickson, T. M., Cavosie, A. J., Rae, A. S. P., Wheeler, J., Wittmann, A., Ferrière, L., Poelchau, M. H., Tomioka, N., Collins, G. S., Gulick, S. P. S., Rasmussen, C., & Morgan, J. v. (2019). New shock microstructures in titanite (CaTiSiO5) from the peak ring of the Chicxulub impact structure, Mexico. *Contributions to Mineralogy and Petrology*, *174*(5). https://doi.org/10.1007/s00410-019-1565-7

Trefil, J. S., & Raup, D. M. (1990a). Crater Taphonomy and Bombardment Rates in the Phanerozoic. *The Journal of Geology*, *98*(3). https://doi.org/10.1086/629411

Trefil, J. S., & Raup, D. M. (1990b). Crater Taphonomy and Bombardment Rates in the Phanerozoic. *The Journal of Geology*, *98*(3), 385–398.

Trepmann, C. A. (2008). Shock effects in quartz: Compression versus shear deformation — An example from the Rochechouart impact structure, France. *Earth and Planetary Science Letters*, *267*(1–2), 322–332. https://doi.org/10.1016/j.epsl.2007.11.035

Urrutia-Fucugauchi, J., Marin, L., & Trejo-Garcia, A. (1996). UNAM Scientific Drilling Program of Chicxulub Impact Structure-Evidence for a 300 kilometer crater diameter. *Geophysical Research Letters*, *23*(13). https://doi.org/10.1029/96GL01566

van der Plas, L. (Ed.). (1966). *Chapter 9 Twinning of Feldspars* (pp. 145–167). https://doi.org/10.1016/S0070-4571(08)70643-5

Vermeesch, P. M., & Morgan, J. v. (2004). Chicxulub central crater structure: Initial results from physical property measurements and combined velocity and gravity modeling. *Meteoritics & Planetary Science*, *39*(7). https://doi.org/10.1111/j.1945-5100.2004.tb01127.x

Walther, John. v. (2005). *Essentials of Geochemistry*. Jones and Bartlett Publishers.

Wang, Y., Lesher, C. M., Lightfoot, P. C., Pattison, E. F., & Golightly, J. P. (2018). Shock metamorphic features in mafic and ultramafic inclusions in the Sudbury Igneous Complex: Implications for their origin and impact excavation. *Geology*, *46*(5). https://doi.org/10.1130/G39913.1

White, L. F., Kizovski, T. v., Tait, K. T., Langelier, B., Gordon, L. M., Harlov, D., & Norberg, N. (2018). Nanoscale chemical characterisation of phase separation, solid state transformation, and recrystallization in feldspar and maskelynite using atom probe tomography. *Contributions to Mineralogy and Petrology*, *173*(10), 87. https://doi.org/10.1007/s00410-018-1516-8

Wittmann, A., Kenkmann, T., Schmitt, R. T., & Stöffler, D. (2006). Shock-metamorphosed zircon in terrestrial impact craters. *Meteoritics & Planetary Science*, *41*(3). https://doi.org/10.1111/j.1945-5100.2006.tb00472.x

Xie, T., Osinski, G. R., & Shieh, S. R. (2020). Raman study of shock features in plagioclase feldspar from the Mistastin Lake impact structure, Canada. *Meteoritics & Planetary Science*, *55*(7), 1471–1490. https://doi.org/10.1111/maps.13523

Xie, T., Osinski, G. R., & Shieh, S. R. (2021). Raman study of shock effects in lunar anorthite from the Apollo missions. *Meteoritics & Planetary Science*, *56*(9), 1633–1651. https://doi.org/10.1111/maps.13728

Yin, F., & Dai, D. (2020). A Study of Shock-Metamorphic Features of Feldspars from the Xiuyan Impact Crater. *Minerals*, *10*(3). https://doi.org/10.3390/min10030231

Zolensky, M. E., Abreu, N. M., Velbel, M. A., Rubin, A., Chaumard, N., Noguchi, T., & Michikami, T. (2018). Physical, Chemical, and Petrological Characteristics of Chondritic Materials and Their Relationships to Small Solar System Bodies. In *Primitive Meteorites and Asteroids* (pp. 59–204). Elsevier. https://doi.org/10.1016/B978-0-12-813325-5.00002-1